

Synthesis and Characterization of Functionalized Spacer Cations for the Incorporation in Layered Perovskites

Présentée le 31 août 2023

Faculté des sciences de base
Laboratoire d'ingénierie moléculaire des nanomatériaux optoélectroniques
Programme doctoral en chimie et génie chimique

pour l'obtention du grade de Docteur ès Sciences

par

Simon NUSSBAUM

Acceptée sur proposition du jury

Prof. O. Kröcher, président du jury
Prof. K. Sivula, Dr J. H. Yum, directeurs de thèse
Prof. M. Saliba, rapporteur
Prof. L. Dou, rapporteur
Prof. F. Nüesch, rapporteur

*I would rather have questions that can't be answered
than answers that can't be questioned.*
— Richard P. Feynman

To my parents...

Acknowledgements

I acknowledge everyone taking the time to read the following work, in which the results of the last four years' hard work, sweat, blood, and tears are aggregated. First, I want to thank my KEPCO and the funding body for their financial support enabling to conduct my research. I would like to express my gratitude to my thesis director, Prof. Dr. Kevin Sivula, and co-director, Dr. Jun Ho Yum, for accepting me as a master's and doctoral student. I enjoyed the work in an exciting multidisciplinary and international research group. Their assistance in conducting the measurements and designing the experiments helped me to proceed in my studies and significantly shaped the quality of this work.

I want to extend my gratitude to Prof. Dr. Michael Saliba, Prof. Dr. Letian Dou, Prof. Dr. Frank Nüesch, and Prof. Dr. Oliver Kröcher for serving as the jury members for my thesis defense and their provided suggestions for improvements.

I'm incredibly thankful to previous supervisors and professors for shaping my early career track as a scientist and advising me in various research projects. Mainly, I thank Dr. Nikita Drigo, who opened the door for me to pursue my scientific career in organic chemistry and organic electronics. His recommendations led me to conduct my master's thesis in the Laboratory for Molecular Engineering of Optoelectronic Nanomaterials (LIMNO), which ultimately led to the results presented in this work.

As collaborations with people from other fields is crucial in research, I want to express my exceptional gratitude to all my collaborators at EPFL, in specific Dr. Etienne Socie and Dr. George Fish for their indispensable contribution and help with transient absorption measurements and Dr. Pascal Schouwink and Dr. Mounir Mensi for their professional support in the characterization of my samples.

During my doctoral studies, I had the opportunity to conduct parts of my research at the Institute for Solar Fuels at the Helmholtz Zentrum für Energie und Materialien in Berlin (HZB) supported by the EPFL Doc.mobility program. Special thanks to Dr. Dennis Friedrich, who supervised me during the stay and gave me important insight into time-resolved microwave conductivity measurements. I'm specifically grateful to Markus, Jonathan, and Orestis for the interesting discussions and their help. Without their help and the fun nights with all the other people from HZB, the stay in Berlin would not have been as enjoyable as I had the chance to experience it.

I would like to thank all LIMNO group members and all visitors and master's students for the interesting and inspiring discussions. During my studies, I was always thankful to share my office with Connor Firth, and (unfortunately only for a short time) Adélie Ollivier who created a comfortable environment in the office. We were indeed the coolest office in the group, nay on the whole campus. Many thank to my dear colleagues and former master's students Haiying Hu, Raluca Kessler, Colin Jeanguenat, Nicolas Diercks, Benjamin Goldman, Luc Monier, YeonJu Kim, Dan Zhang, Dr. Arvinth Sekar, Dr. Yoengpeng Liu, Dr. Barbara Primera Darwich, Dr. Rebekah

Acknowledgements

Wells and Dr. Marina Caretti for their collaboration in the laboratory and many activities out of the laboratory. Moreover, I'm happy for their decency not to burn down the lab during my era as CoSec. An honorable mention goes out to Dr. Nukorn Plainpan for his suffering and endurance during the many hikes together. May he once speed up and catch up with my walking pace. I thank Prof. Dr. Han Hee Cho, Dr. Liang Yao, Dr. Emeline Rideau, and Dr. Parnian Ferdowsi for their rich knowledge and research experience, which have proven indispensable during my studies.

Besides my coworkers already mentioned, this work would not be finished without the help of my family and friends, who provided strong support in times of doubt, concerns, and pandemic-induced loneliness. Their opinions are highly regarded and will be valued in the future. Thank you very much!

Lausanne, July 26, 2023

- S.N.

Abstract

Layered hybrid organic-inorganic perovskite (LHOIP) materials are an emerging class of semiconductors endorsed as a more stable alternative compared to the more widely investigated 3D hybrid organic-inorganic halide perovskites (HOIP). Consisting of alternating slabs of inorganic layers separated by layers of organic spacer cations, their optoelectronic properties are determined by quantum and dielectric confinement effects resulting in materials with high exciton binding energies and charge carrier anisotropy. Considering aliphatic spacer cations, such as *n*-butylammonium (BA) or phenylethylammonium (PEA), the spacer cations act mainly structurally, and the optoelectronic properties are determined by the distortions of the inorganic octahedral Pb-I-network. Recent reports have discovered that the incorporation of organic semiconducting spacer cations into the layered perovskite structure is an interesting approach to tuning the optoelectronic properties. While aliphatic spacer cations create a quantum well structure due to a mismatch between their HOMO and LUMO energy levels and the valence band (VB) and conduction band (CB) of the inorganic layer, respectively, semiconducting organic chromophores can contribute to the electronic structure, thus potentially breaking the quantum confinement. For example, by incorporating electron-accepting spacer cations, type II organic-inorganic nano-heterostructures can be formed, where the excited electrons are transferred from the inorganic layer to the organic spacer chromophore. The possibility to modify the localization of the electrons and holes opens the door for a wide range of applications, such as in LED and solar cell devices. However, incorporating organic spacer cations remains challenging due to their large size. In this work, novel spacer cations for the formation of layered perovskite materials are investigated.

Focusing on novel spacer cations based on naphthalene diimide (NDI) chromophore and NDI derivatives, critical aspects for the layered perovskite formation are analyzed. We further investigate the electron transfer mechanism from the inorganic layer to the NDI spacer cation by time-resolved photoluminescence and transient absorption (TA) spectroscopy showing electron transfer on a sub-picosecond timescale. The formation of long-lived charge-separated states and their potential implication in the exciton dissociation were studied by time-resolved microwave conductivity (TRMC) measurements. Modifying NDI spacer cations and synthesizing a core substituted derivative, a visible-light absorbing spacer cation was incorporated into a layered perovskite structure. Selectively exciting the spacer cation and tuning the CB and VB of the inorganic layer by forming a mixed halide octahedral perovskite network, we were able to further study electronic interactions between the organic and inorganic layers in the semiconducting material.

Keywords: Hybrid Organic-Inorganic Halide Perovskite, HOIPS, Layered Perovskites, Organic Semiconductor Incorporated Perovskites, OSiP, Nanoscale Heterostructures, Semiconductor Design, Photovoltaics

Zusammenfassung

Geschichtete (layered) organisch-anorganische Perowskite sind eine aufstrebende Klasse von Halbleitern, die eine stabilere Alternative zu den klassischen drei-dimensionalen organisch-anorganisch ABX_3 Perowskiten darstellen. Solche Halbleiter bestehen aus Schichten anorganischer Perowskitstrukturen, die durch organische Barrierektionen (spacer cations) auseinandergehalten werden. Die optoelektronischen Eigenschaften werden dabei durch Quanteneffekte und dielektrische Effekte bestimmt, was zu einer hohen Exzitonen-Bindungsenergie und anisotropen Mobilität der Ladungsträger führt. In Leuchtdioden und Solarzellen sind geschichtete Perowskite deshalb nur in gemischten Systemen mit 3D Perowskiten und quasi-2D Perowskiten verwendbar. Bei Barrierektionen wie n-Butylammonium (BA) oder Phenylethylammonium (PEA) wirkt das Barrierektion hauptsächlich strukturell, wobei die optoelektronischen Eigenschaften durch strukturelle Modifikationen der anorganischen Pb-X-Schicht bestimmt werden.

Kürzlich publizierte Berichte über geschichtete Perowskite, wo organische halbleitende Molekülkationen als Barrierektionen eingesetzt werden, beleuchten einen interessanten Ansatz um die optoelektronischen Eigenschaften des Halbleiters durch elektronische Eigenschaften der Barrierektionen zu steuern. Im Gegensatz zu aliphatischen Barrierektionen, bei denen sich die HOMO- und LUMO-Energieniveaus des Barrierektions von dem Valenzband und Leitungsband der anorganischen Schicht stark unterscheiden und eine Quantentopfstruktur (quantum well) bilden, können organische Halbleiter zur elektronischen Struktur des geschichteten Perowskiten beitragen und damit möglicherweise die Quanteneffekte reduzieren. Die Einbindung von Chromophoren welche Elektronen akzeptieren können, führt zur Bildung einer künstlichen Nanoheterostruktur vom Typ II. Solche Heterostrukturen ermöglichen es den angeregten Elektronen von der anorganischen Schicht auf das organisch halbleitende Barrierechromophor zu transferieren. Die Möglichkeit, Elektronen und Löcher in der organischen wie anorganischen Schicht zu lokalisieren stellt eine interessante Strategie dar die starken Coulomb-Interaktionen zwischen Elektron und Löchern zu reduzieren. Solche Materialien können in Leuchtdioden und Solarzellen eingesetzt werden. Die Einbindung solcher Barrierektionen basierend auf organischen Halbleitern bleibt jedoch aufgrund der verschiedenen molekularen Interaktionen und der Grösse solcher Moleküle limitiert.

In dieser Arbeit werden neuartige Barrierektionen synthetisiert und untersucht. Basierend auf Naphthalindiimidchromophore und deren Derivaten werden Schlüsselaspekte der Perowskitbildung erläutert. Dabei wird gezeigt, dass die Länge der Kohlenstoffkette, welche das Kation am Perowskiten verbindet einen entscheidenden Einfluss auf die Formbarkeit und das Kristallwachstum bestimmt. Basierend auf der Typ II Heterostruktur wird die Dynamik des Elektrontransfers von der anorganischen Schicht zum halbleitenden Barrierektion mittels zeitaufgelöster Photolumineszenz- und Transientenabsorptionsspektroskopie (TA) untersucht. Die Bildung von langlebigen freien Ladungsträger und deren Auswirkung auf die Exzitonendissoziation wurden durch zeitaufgelöste Mikrowellenabsorptionsmessungen untersucht.

Zusammenfassung

Schlagwörter: Perowskite, Layered Perowskite, Organische Halbleiter in Layered Perowskite, Heterostrukturen, Halbleitersynthese, Solarzellen

Contents

Acknowledgements	i
Abstract (English/German)	iii
List of figures	ix
List of tables	xvii
1 Introduction	1
1.1 Abstract	1
1.2 The Silicon Age	2
1.3 The Need for New Semiconducting Materials	4
1.4 Emerging Novel Semiconducting Materials for Optoelectronic Applications	5
1.4.1 Organic Semiconducting Materials	5
1.4.2 Hybrid Organic-Inorganic Perovskite Structure and Properties	8
1.4.3 Layered Perovskite Semiconductors	9
1.5 Properties of Layered Perovskite Materials and Quasi-Layered Perovskite Materials Incorporating Aliphatic Spacer Cations	11
1.5.1 Charge Carrier Properties in Quasi-Layered Poly-Dispersed Thin Films	13
1.6 Tuning Optoelectronic Properties by Structure Modifications	16
1.7 Tuning the Dielectric Screening in Layered Perovskite Materials with Functional- ized Spacer Cations	17
1.8 Tuning the Properties by Incorporation of Semiconducting Spacer Cations	19
1.9 Research Motivation	22
1.10 Thesis Outline	23
2 Characterization Techniques	25
2.1 Abstract	25
2.2 Interaction of Matter with Electromagnetic Irradiation for Structural, Optical and Electronic Characterization of Materials	26
2.2.1 Structural Characterization of Crystalline Phase by X-ray Diffraction	27
2.2.2 Grazing-Incidence Wide-Angle X-Ray Scattering (GIWAXS)	29
2.2.3 Visible light Absorption and Emission Spectroscopy	31
2.2.4 Sheet Conductivity <i>via</i> Time-Resolved Microwave Conductivity Measurement	33
2.3 Electronic Characterization <i>via</i> Space-Charge-Limited Current	34
3 Tuning Naphthalene Diimide Spacer Cations for the Incorporation into a Layered RP Phase Perovskite Structure	39
3.1 Abstract	39

Contents

3.2	Introduction	40
3.3	Experimental	42
3.4	Results and Discussion	44
3.5	Conclusion	55
4	Photogenerated Charge Transfer in Dion-Jacobson Type Layered Perovskite Based on Naphthalene Diimide	59
4.1	Abstract	59
4.2	Introduction	60
4.3	Experimental	62
4.4	Results and Discussion	64
4.5	Conclusion	74
5	Free Charge Carrier Generation by Visible-light-absorbing Chromophore Spacer in Ruddlesden-Popper Type Perovskites	77
5.1	Abstract	77
5.2	Introduction	78
5.3	Experimental	80
5.4	Results and Discussion	81
5.5	Conclusion	92
6	Conclusion and Outlook	95
	Bibliography	102
A	Appendix: Tuning Naphthalene Diimide Spacer Cations for the Incorporation into a Layered RP Phase Perovskite Structure	A1
B	Appendix: Photogenerated Charge Transfer in Dion-Jacobson Type Layered Perovskite Based on Naphthalene Diimide	B1
C	Appendix: Free Charge Carrier Generation by Visible Light Absorbing Chromophore Spacer in Ruddlesden-Popper Type Perovskites	C1
D	Appendix: Conclusion and Outlook — Synthesis of a High-Dipole Spacer Cation	D1
E	Appendix: Conclusion and Outlook – Synthesis of Isoindigo-based Spacer Cations	E1
F	Appendix: Conclusion and Outlook -Incorporation of Organic-Charge Transfer Complexes in the Organic Layer	F1

List of Figures

1.1	a) Simplified electronic structure of metals, semiconductors, and insulators. b) Schematic illustration of a p-n junction as found in commercial Si-based solar cells under light illumination.	2
1.2	a) π - and σ -bonding arising from the p and sp^2 hybridized atomic orbitals in ethylene. b) Increasing the number of double bonds in molecules, and increased molecular packing of the organics in solid states lead to a quasi-continuous energy-states.	6
1.3	a) Charge carrier hopping in organic semiconductors. The blue curve indicates the density of states distribution. b) Schematic illustration of the architecture of a bulk heterojunction (BHJ). c) The pillar shaped system represents the ideal case for efficient charge dissociation.	7
1.4	a) Structure of hybrid organic-inorganic halide perovskite, and b) chemical structure of methylammonium (MA^+) and formamidinium (FA^+).	8
1.5	a) Structure of layered perovskite materials incorporating monocations and dications into the octahedral framework and b) view along c-axis for $\frac{1}{2}$, $\frac{1}{2}$, and $\frac{1}{2}$, 0, and 0, 0 shifts.	10
1.6	a) Quantum well structure formed by incorporating aliphatic spacer cations, and b) resulting orientation in thin film with respective in-plane and out-of-plane direction.	12
1.7	a) UV-vis absorption and PL-emission spectra of $(PEA)_2PbI_4$ show characteristic excitonic absorption band at around 500 nm as a result of the strong quantum and dielectric confinement effects. Scheme b) illustrates the effect of the exciton binding energy on the absorption spectra and observed excitonic band.	13
1.8	a) Effect of the quantum well width on the stability and band gap. b) Crystal growth mechanism upon additive engineering to avoid nucleation inside the solvent to obtain oriented layered perovskite thin films reproduced from ref. 84 (copyright ©2020, the author(s)).	14
1.9	Structure of a) $\langle 100 \rangle$, b) $\langle 110 \rangle$, and c) $\langle 111 \rangle$ perovskites. d) Corrugated structure of $\langle 110 \rangle$ perovskites. e) Distortions of the inorganic framework in $\langle 100 \rangle$ -layered perovskites leads to modification of the optoelectronic properties of the material.	16
1.10	a) Effect of the dielectric constant of the spacer cation on the exciton binding energy of the layered perovskite. Figure is reproduced from ref. 85 (copyright ©2018, the author(s)). b) The increase in relative permittivity of the spacer cation results in reduced exciton binding energies. c) Previously investigated high-dipole spacer cations by Queloz <i>et al.</i> from ref. 115.	18

List of Figures

1.11	Energy band alignment in layered perovskite materials forming quantum wells (type I heterostructures). By incorporating electron accepting donor or acceptor chromophores type II nano-heterostructure can be formed as proposed by Gao <i>et al.</i> in ref. 123.	19
1.12	Energy transfer from the inorganic layer to the naphthalene chromophore <i>via</i> a triplet injection as reported by Ema <i>et al.</i> in ref. 127.	20
2.1	The electromagnetic spectrum from high energy photons to low energy energy photons.	26
2.2	Illustration of the X-ray diffraction principle with respective X-ray incident and reflection angle Θ	28
2.3	a) Experimental setup of grazing-incidence wide-angle X-ray scattering measurements. Resulting GIWAXS image of b) perovskite layers oriented parallel to the substrate. c) With increasing anisotropy the spots become circular. d) GIWAXS image of perovskite layer orientated perpendicular to the substrate.	29
2.4	Jablonski diagram of different electronic process upon absorption. ISC denotes the intersystem crossing process populating an excited triplet state causing long-lived phosphorescence due to spin-flip. Shorter-lived Fluorescence is due to S_1 to S_0 transitions.	31
2.5	Systematic presentation of transient absorption measurements including possible photo-physical process resulting in observable TA features. Figure was adapted from ref. 161.	32
2.6	Time-resolved microwave conductivity setup and microwave cavity.	33
2.7	a) Illustration of charge carrier transport through the semiconductor sandwiched between two electron-selective contacts. b) Current-Voltage log-log curve showing the ohmic region, trap filling region (TFR) and region dominated by space-charge-limited current.	36
3.1	a) Band alignment of the type II heterostructure structure indicated based on computational studies from ref. 171. b) Schematic description of the layered perovskite structure and chemical structure of the investigated NDI-based spacer cations.	40
3.2	a) Synthetic procedure for the thin film fabrication. The spin-coating of the precursor solution containing NDI-E and PbI_2 (2:1 molar ratio) results in a film with the absorption spectrum displayed in b) . The visible-light absorbance of the thin films after annealing c) and XRD d) show characteristic features for RP LHOIP. . .	44
3.3	Grazing-incidence wide-angle X-ray scattering for the $(NDI-E)_2PbI_4$ a) , $(NDI-b)_2PbI_4$ b) , and $(NDI-H)_2PbI_4$ c) thin film.	46
3.4	a) Representative illustration of the <i>in-situ</i> absorption spectroscopy measurements to track the evolution of the thin film formation. b) Resulting curve when the temperature is gradually increased at a rate of 0.25 K s^{-1}	47
3.5	a) Fit Avrami model to crystal phase formation under isothermal conditions. b) Proposed crystal growth mechanism based on the obtained Avrami-coefficients n . . .	49

3.6	a) Illustration of the electronic structure and electron transfer in the type II heterostructure. b) PL decay dynamics determined by FLUPS.	50
3.7	Transient absorption spectra of a) NDI-E, b) NDI-B, and c) NDI-H. d) Corresponding GSB dynamics with tri-exponential fit.	51
3.8	a) TRMC transient for (NDI) ₂ PbI ₄ and (PEA) ₂ PbI ₄ based perovskite thin films, and b) extracted peak mobility at different excitation intensities assuming $\phi = 1$	53
3.9	a) Visible light absorption spectra of NDI-based quasi-layered films based ($\langle n \rangle = 5$), and b) XRD of the investigated films.	55
4.1	a) Chemical structure of NDIC2 and the herein investigated NDI-dB and NDI-dH. b) Reported crystal structure of the lead-iodide nanowire obtained when NDIC2 is incorporation. Reproduced from ref. 174 with permission from The Royal Society of Chemistry. c) Schematic illustration of the desired (2D) layered perovskite structure.	61
4.2	a) Visible light absorption and PL steady-state spectra, and b) XRD of the (NDI-dH)PbI ₄ . XRD was recorded with a monochromated Cu-K α_1 X-ray source. c) Transient absorption spectral slices, and d) Ultrafast PL and GSB dynamics of the (NDI-dH)PbI ₄ films based on fluorescence up-conversion spectroscopy (FLUPS) and TA, respectively.	64
4.3	a) Illustration of the fp-TRMC setup measuring the mobilities of free charge carriers along the axis parallel to the substrate and b) fp-TRMC transient of (NDI-dH)PbI ₄ (closed black circles) and (BA) ₂ PbI ₄ (closed red circles) with the obtained mobilities in the inset of the figure. Samples were excited at 420 nm. Decay time constants τ_1 c) , and τ_2 d) at different absorbed photon flux.	66
4.4	Transient obtained from optical-pump terahertz-probe spectroscopy (OPTP). The sample was pumped at 400 nm.	67
4.5	a) Schematic illustration of the quasi-layered perovskite materials incorporating NDI-dH. The Energy levels of the inorganic layer as based on ref. 95. b) Visible light absorbance of $\langle n \rangle = 1$, $\langle n \rangle = 2$ and $\langle n \rangle = 3$ thin films and c) transient absorption slices of $\langle n \rangle = 3$ film.	68
4.6	Transient absorption slices of the a) $\langle n \rangle = 4$ and b) $\langle n \rangle = 5$ thin films. GSB minima shifts from 667 nm to 682 nm with increasing n . GSB for MAPbI ₃ is reported above 700 nm. ^[172]	69
4.7	a) GIWAXS with incident angle $\alpha = 2.0^\circ$ using a K α_1 X-ray source and b) XRD of (NDI-dH)MA ₄ Pb ₅ I ₁₆ spin-coated using the optimized conditions.	70
4.8	a) Visible light absorption spectra of optimized NDI-dH ($\langle n \rangle = 5$) and 3D MAPbI ₃ . b) PL spectra of NDI-dH ($\langle n \rangle = 5$, optimized) excited at 350, 500, and 600 nm. c) Stability of the NDI-dH and BA-based films ($\langle n \rangle = 5$) when stored under ambient conditions. The BA-based quasi-layered films were formed using the same conditions as for the space-charge limited current.	71

List of Figures

4.9	a) Device architecture of the SCLC device setup for electron mobility. b) Cross-section electron micrographs for different thickness of NDI-dH $\langle n \rangle = 5$ films. Typical current-voltage (I - V) curve of the electron-only space-charge-limited current (SCLC) of c) NDI-dH ($\langle n \rangle = 5$) and d) BA ($\langle n \rangle = 5$) thin films. e) Obtained electron mobilities for BA and NDI based devices. f) XRD of the $\langle n \rangle = 5$ BA film. XRD were performed using a Cu- $K\alpha_1$ X-ray source.	72
5.1	Electronic structure of a) layered perovskite incorporating simple aliphatic spacer cations and b) incorporating organic semiconducting spacer cations.	78
5.2	a) Structure of PDI-H and b) visible light absorption spectra of the PDI-H cation as-spin coated on a glass substrate and PbI_2 :PDI-H precursor solution spin-coated and annealed at 200 °C for 10 minutes. c) XRD of the PbI_2 :PDI-H thin film shows no indication for the formation of a layered perovskite structure.	81
5.3	a) Chemical structure of NDI-DAE and aimed crystal structure of the Layered perovskite material. b) Visible light absorption of the NDI-DAE cation and $(\text{NDI-DAE})_2\text{PbI}_4$ LHOIP and PL of $(\text{NDI-DAE})_2\text{PbI}_4$, and c) XRD of the $(\text{NDI-DAE})_2\text{PbI}_4$. d) The required annealing temperature for the formation of $(\text{NDI-DAE})_2\text{PbI}_4$ in comparison to $(\text{NDI-B})_2\text{PbI}_4$	82
5.4	TRMC transient of $(\text{NDI-DAE})_2\text{PbI}_4$ when excited at 420 nm and 540 nm.	84
5.5	a) Visible light absorption, b) XRD and c) PL emission spectrum of mixed halide LHOIPs of the general formula $(\text{BA})_2\text{Pb}(\text{I}_{1-x}\text{Br}_x)_4$	86
5.6	a) Sum mobilities of $(\text{BA})_2\text{Pb}(\text{I}_{1-x}\text{Br}_x)_4$ thin films determined by fp-TRMC assuming $\phi = 1$. b) The trend in TRMC sum mobilities can be rationalized by previously reported inhomogeneity hampering the charge carrier mobility through the inorganic layer.	87
5.7	a) Visible light absorbance of NDI-DAE-I, NDI-DAE-mix and NDI-DAE-Br thin films as well the visible light absorbance of the spacer chromophore. b) PL emission of the corresponding thin films excited at 400 nm. The PL quenching of the NDI-DAE-mix and NDI-DAE-I films is potentially due to the type II heterostructure arrangement where the PL is quenched due to hole transfer to the organic chromophore to the NDI-DAE chromophore to the inorganic layer.	88
5.8	Schematic presentation of the energetic structure of a) a type II heterostructure, and b) . inverted type I heterostructure. c) Illustration of conduction and valence band energy levels of NDI-DAE respective to $(\text{BA})_2\text{PbI}_4$ and $(\text{BA})_2\text{PbBr}_4$ determined by Ultraviolet photoelectron spectroscopy (UPS). d) TA slices of NDI-DAE-mix after photoexcitation at 525 nm.	89
5.9	a) Peak photoconductivity at various wavelength for NDI-DAE-mix normalized by incident light intensity but not absorbance. b) Transient of the free charge carrier dynamics when excited at 420 and 520 nm at $3 \cdot 10^{13}$ absorbed photons per cm^2 . The inset shows the photoconductivity at different absorbed photon flux. The error bars are calculated based on uncertainties given by the photon fluence.	90

5.10	a) Transient of (NDI-DAE) ₂ PbBr ₄ when excited at 500 nm, and b) resulting mobilities. The error bars are calculated based on uncertainties given by the photon fluence.	91
A.1	Synthetic scheme of NDI-based spacer cations	A1
A.2	Visible light absorption spectra a) and XRD b) of the as-spin coated (NDI-E) ₂ PbI ₄ , (NDI-B) ₂ PbI ₄ , and (NDI-H) ₂ PbI ₄ films.	A4
A.3	Cyclic voltammogram of NDI-E in DCM using Ferrocene as internal standard to measure oxidation potential of the spacer cation. Measurement was performed on Boc-protected NDI-E to prevent reduction of the I ⁻ ion.	A4
A.4	Integrated and normalized azimuthal angle (ϕ) derived from grazing-incidence small-angle X-ray scattering measurements.	A5
A.5	Setup of the FTO-coated window for <i>in-situ</i> UV-vis absorption measurements. The temperature of the window was controlled <i>via</i> a feedback loop with a temperature sensor directly on the window.	A6
A.6	Evolution of the conversion coefficient at different absorption wavelength. The data was obtained by annealing NDI-E based films on a hot plate and measure full spectra after certain periods of time.	A6
A.7	Evolution of conversion coefficient (α) over annealing of (NDI-H) ₂ PbI ₄	A7
A.8	a) XRD and b) visible light absorption spectra of NDI-H annealed at 220 °C.	A7
A.9	Temporal- and spectral dependent PL-intensity of (NDI-E) ₂ PbI ₄ , (NDI-B) ₂ PbI ₄ , and (NDI-H) ₂ PbI ₄ excited at 400 nm.	A8
A.10	Decay associated spectra resulting from the global analysis of the ground state bleach.	A9
A.11	fp-TRMC transient of (NDI) ₂ PbI ₄ on logarithmic scale excited at 420 nm. NDI-based perovskites where excited with $2 \cdot 10^{13}$ photons per cm ²	A10
A.12	Visible light absorption of quasi-layered films with a) $\langle n \rangle = 2$ and b) $\langle n \rangle = 3$	A10
A.13	Absorption spectra of thin film of quasi-layered perovskite aimed for the phase (NDI-E) ₂ MA ₄ Pb ₅ I ₁₆ at various solvent (DMSO and DMF) and annealing temperatures.	A10
A.14	¹ H-NMR of NDI-E-Boc (top), ¹³ C-NMR of NDI-E-Boc (center), and ¹ H-NMR of NDI-B-Boc (bottom) recorded in chloroform-d.	A11
A.15	¹³ C-NMR of NDI-B-Boc (top), ¹ H-NMR of NDI-H-Boc (center), and ¹³ C-NMR of NDI-H-Boc (bottom) recorded in chloroform-d.	A12
A.16	¹ H-NMR of NDI-E (top), ¹³ C-NMR of NDI-E (center), and ¹ H-NMR of NDI-B (bottom) recorded in DMSO-d ₆	A13
A.17	¹³ C-NMR of NDI-B (top), ¹ H-NMR of NDI-H (center), and ¹³ C-NMR of NDI-H (bottom) recorded in DMSO-d ₆	A14
B.1	a) PL-intensity of (NDI-dB)PbI ₄ , (NDI-dH)PbI ₄ , and (BA) ₂ PbI ₄ excited at 400 nm (3 nm slit). The PL-intensity is normalized to the absorbed photons at 400 nm, b) Zoom of Figure a.	B4

List of Figures

B.2	a) UV-vis absorbance and b) XRD of NDI-dH and NDI-dB based ($n = 1$) layered perovskite thin films.	B4
B.3	a) Image from optical microscope of (NDI-dB)PbI ₄ , and b) (NDI-dH)PbI ₄	B5
B.4	a) Ground state bleach (GSB) dynamics at 507 nm for (NDI-dH)PbI ₄ films and b) GSB at 507 nm at different photon flux.	B5
B.5	XRD of NDI-dH based perovskites $n = 1$ -3 thin films.	B5
B.6	a) TA slices of $\langle n \rangle = 2$ film and b) GSB decay and fit of the $n = 2$ and $n = 3$ phase. .	B6
B.7	UV-vis absorbance of un-optimized $\langle n \rangle = 4$ and $\langle n \rangle = 5$ films.	B6
B.8	Ground state decay fit for a) $n = 4$ and b) $n = 5$ films.	B6
B.9	GIWAXS of thin film using various amounts of NH ₄ SCN in the precursor solution. The percentage are referred to as molar percentage of the PbI ₂	B7
B.10	Obtained Impedance spectrum of NDI-dH based perovskite ($n = 5$). For the measurement the NDI-dH film was spin-coated on FTO and gold electrodes (0.16 cm ²) were evaporated on top.	B8
B.11	I-V curve for NDI-dH $\langle n \rangle = 5$ using pulsed SCLC measurements for different dwell times.	B8
B.12	¹ H-NMR of NDI-dH-Boc (top), ¹³ C-NMR of NDI-dH-Boc (center), and ¹ H-NMR of NDI-dB-Boc (bottom) in CDCl ₃	B9
B.13	¹³ C-NMR of NDI-dB-Boc in CDCl ₃ (top), ¹ H-NMR of NDI-dH (center), and ¹³ C-NMR of NDI-dH in DMSO-d ₆ (bottom).	B10
B.14	¹ H-NMR of NDI-dB (top), and ¹³ C-NMR of NDI-dB in DMSO-d ₆ (bottom).	B11
C.1	Schematic procedure for the synthesis of PDI-H.	C1
C.2	UV-vis of PDI-H in DMF at different concentration showing aggregation in the precursor solution.	C6
C.3	PL-intensity of the (NDI-DAE) ₂ PbI ₄	C7
C.4	UV-vis a) and XRD b) of NDI-DAE with a hexyl based alkane chain incorporated into a layered perovskite structure.	C7
C.5	UV-vis of NDI-DAE with a ethyl based alkane chain.	C8
C.6	UPS spectra of NDI-DAE chromophore spin-coated on FTO coated glass substrate. $E_{HOMO} = -6.08$ eV.	C8
C.7	UPS spectra of (BA) ₂ PbI ₄ chromophore spin-coated on FTO coated glass substrate $E_{VB} = -5.76$ eV.	C9
C.8	UPS spectra of (BA) ₂ PbBr ₄ chromophore spin-coated on FTO coated glass substrate $E_{VB} = -6.14$ eV.	C9
C.9	XRD of NDI-DAE-I, NDI-DAE-mix and NDI-DAE-Br.	C10
C.10	PL emission of (NDI-DAE) ₂ PbI ₄ when excited at 480 nm.	C10
C.11	a) TRMC transient of (NDI-DAE) ₂ Pb(I _{0.5} Br _{0.5}) ₄ excited at 420 nm and 520 nm and the Transient of (NDI-DAE) ₂ PbBr ₄ (yellow dots). b) Obtained peak mobility assuming $\phi = 1$	C11

C.12	Overlap of the TRMC transient of of the NDI-DAE chromophore cation spin-coated on quartz substrate (NDI-DAE-chromophore) and (NDI-DAE) ₂ PbBr ₄ excitedt at 500 nm.	C11
C.13	¹ H-NMR of PDI-C5-sym in Chloroform-d.	C11
C.14	¹ H-NMR of PDI-H-Boc (top), ¹³ C-NMR of PDI-H-Boc in CDCl ₃ (center), and ¹ H-NMR of PDI-H in DMSO-d ₆ (bottom). Around 5 %v/v of Toluene-d ₈ was added to the DMSO to obtain better NMR coupling.	C12
C.15	¹ H-NMR of NDI-DAE-E-Boc in CDCl ₃ (top), ¹³ C-NMR of NDI-DAE-E-Boc in CDCl ₃ (center), and ¹ H-NMR of NDI-DAE-Boc in CDCl ₃ (bottom).	C13
C.16	¹³ C-NMR of NDI-DAE-Boc in CDCl ₃ (top), and ¹ H-NMR of NDI-DAE-H-Boc in CDCl ₃ (center), ¹ H-NMR of NDI-DAE-E in DMSO-d (bottom).	C14
C.17	¹³ C-NMR of NDI-DAE-E in DMSO-d ₆ (top), ¹ H-NMR of NDI-DAE in DMSO-d ₆ (center), ¹³ C-NMR of NDI-DAE in DMSO-d ₆ (bottom).	C15
C.18	¹ H-NMR of NDI-DAE-H in DMSO-d ₆	C16
D.1	Chemical structure of the investigated MN-PEA spacer cation and calculated dipole moment of the MN-PEA core.	D1
D.2	a) Visible-light absorption spectrum of (MN-PEA) ₂ PbI ₄ . b) Orientation of the aromatic spacer cation and (F-PEA) ₂ PbI ₄ based on sc-XRD.	D3
D.3	NMR of the MN-PEAI cation in DMSO and NMR of the redissolved (MN-PEA) ₂ PbI ₄ in DMSO.	D4
D.4	a) TRMC mobilities at various absorbed photon flux after photoexcitation at 420 nm, and b) corresponding TRMC transient.	D5
E.1	a) UV-Vis absorption spectra and b) XRD spectra of Isoindigo-based quantum well structure.	E1
E.2	Synthetic scheme for the synthesis of Isoindigo-based dications.	E2
E.3	Synthetic scheme for the synthesis of Isoindigo-based monocations.	E4
F.1	Formation of organic charge-transfer complex in solution formed by naphthalene diimide and pyrene and naphthalene diimide:pyrene (1:1 molar ratio, center) in DCM.	F1
F.2	a) UV-vis absorption spectra and b) XRD TCBQ-Naphthalene organic charge-transfer perovskites following the same synthetic conditions as ref. 149.	F2
F.3	a) TRMC transient of TCBQ charge transfer after photoexcitation at 420 nm, and b) mobilities for x = 1.0 under assumption $\phi = 1$	F2
F.4	¹ H-NMR of Naphthalene-C3-Boc in CDCl ₃	F3
F.5	¹³ C-NMR of Naphthalene-C3-Boc in CDCl ₃ (top), and ¹ H-NMR of Naphthalene-C3-salt in DMSO-d ₆ (center), and ¹³ C-NMR of Naphthalene-C3-salt in DMSO-d (bottom).	F4

List of Tables

1.1	Eigenwert determined for the 3D and 2D hydrogen model where $N = 0, 1, 2, \dots$ and R is the Rydberg constant.	13
3.1	Decay time constants of the absorption bleach for the investigated thin films derived from tri-exponential displayed in Figure 3.7d.	52
4.1	Fit GSB decay dynamic for the investigated films.	69
A.1	Determined LUMO level of NDI-E-Boc based on CV. HOMO was derived from the optical band gap.	A4
A.2	Decay dynamics of free charge carrier decay. NDI-based perovskites where excited at 420 nm with $2 \cdot 10^{13}$ photons per cm^2	A9

Chapter 1

Introduction

1.1 Abstract

This Chapter discusses the properties of semiconductors and their application in optoelectronic and electronic devices. Considering the existing limitation related to processability, bio-compatibility, tunability, and materials flexibility, it is shown that the development of new semiconducting materials is necessary to expand semiconductors to new fields of application such as spintronics, photodetection, photovoltaics, and bio-electronics. Based on two emerging classes of semiconductors, organic semiconductors and hybrid organic-inorganic perovskite semiconductors (HOIPS), key aspects of their electronic properties are presented, highlighting the advantages and limitations of these materials. The second part of this chapter focuses on a subclass of HOIPS, namely layered hybrid organic-inorganic perovskite semiconductors (LHOIPS), which have the potential to overcome the limited structural stability found in HOIPS materials. By introducing the concept of quantum and dielectric confinement, a brief introduction to quasi-layered perovskite and their electronic structure in poly-dispersed thin films is given. Additionally, taking a step back, a brief literature overview on the possibility of tuning the optoelectronic properties of LHOIPs by the design of the spacer cation is given. More specifically, the prospects of tuning the electronic structure by the incorporation of spacer cations based on organic semiconducting building blocks are presented. Organic semiconductors incorporated into perovskite materials provide an interesting subclass of LHOIPs for the application in optoelectronic devices.

The herein presented review is aimed for future publication.

1.2 The Silicon Age

Since the development of the transistor in 1947, semiconducting materials have been an essential part of crucial components in many modern electronic devices. They are important building blocks in computers, cars, microwaves, and mobile phones.^[1] The development of the internet and the widespread use of personal computers in the last 30 years would not have been possible without the properties of semiconductors.^[2] Indeed, the impact of the internet on culture, society and politics, and novel technological advances lead some commentators to refer to the current information-driven era as the silicon age.^[3] In general, the electronic properties of semiconducting materials that are crucial for their application in electronic devices lay somewhere between insulators and conductors. These properties are determined by the material's electronic structure. Unlike conductors such as metals, where the valence electrons behave like an electron cloud in the lattice with a continuum of possible energy states, semiconducting materials possess a distinct valence band (VB) and conduction band (CB) separated by a band gap of non-allowed energy states, as illustrated in Figure 1.1a. Compared to insulators, the band gap in the semiconductor is small (less than 3 eV), and the conduction band is partially filled by thermally excited electrons allowing charge transport through the material.^[4,5]

Although this partially filled conduction band makes semiconductors inferior to metals regarding their electronic conductivity, charge carrier transport in a semiconductor can be altered by deliberately inducing impurities into the material structure. As new states are formed close to the valence band or conduction band, the band structure shifts, and charge carrier conductance is altered. Incorporating electron-accepting (atoms with a lower number of valence electrons than the atoms of the host material) or electron-donating (atoms with a higher number of valence electrons than the atoms of the host material) dopants allow the formation of p-type

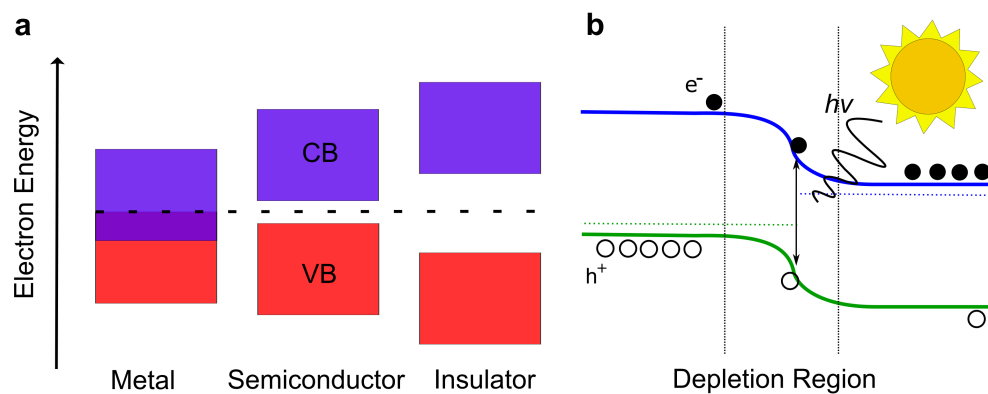


Figure 1.1 – **a)** Simplified electronic structure of metals, semiconductors, and insulators. **b)** Schematic illustration of a p-n junction as found in commercial Si-based solar cells under light illumination.

and n-type extrinsic semiconductors, respectively. While in p-type semiconductors holes are the majority charge carriers and electrons are the minority charge carriers, electrons are the majority carrier in n-type semiconductors.^[6] A key aspect of semiconductors is the dependency of their electronic properties on environmental factors. The transfer of electrons from the VB to the CB by photoexcitation, thermal excitation, or by applying voltage increases the population of electrons in the conduction band, altering the resistivity of the materials. These electronic transitions from the VB to the CB or relaxation from the CB to the VB are the fundamental processes in many optoelectronic devices such as light-emitting diodes (LEDs) and photo resistors.^[7]

In the wake of the current energy crisis and global climate change caused by the emission of CO₂ resulting from the burning of fossil fuels, the application of semiconductors as light-harvesting material for light-to-electricity conversion in solar cell devices gained particular interest in research. Considering the average terrestrial solar irradiance of around 1'000 Wm⁻², the sunlight reaching the earth's surface provides an effectively unlimited clean energy source.^[8] Harvesting green solar energy by light-to-electricity conversion is an essential pillar of the future energy strategy outlined in the current European Union's green deal energy strategy.^[9] Light-to-electricity conversion in solar cell devices is based on the photovoltaic effect in narrow-gap semiconducting materials. When the semiconductor absorbs incident photons with higher energy than the band gap, an electron from the VB is promoted to the CB, leaving behind an absence of an electron (hole) in the VB. Electrons that are well in the conduction band lose their energy by generating phonons until these electrons have energetically reached the lower edge of the conduction band. The created electron-hole pairs have a relatively long lifetime of up to 10⁻³ seconds. This allows the conversion from electron energy to electrical energy *via* the separation and subsequent injection of both electrons and holes into an electrical grid.^[10] However, the absorption of a photon alone does not necessarily lead to the formation of a free charge carrier (separated electron and holes), as, depending on the material, an exciton (an electron and hole pair in a bound state) formed by the absorption of a photon has to overcome the coulomb forces between the electron and hole, commonly denoted as the exciton binding energy.^[11] A low exciton binding energy close to $k_b T$ (0.026 eV at room temperature, where k_b is the Boltzmann constant), as found in high-dielectric materials, allows efficient dissociation and charge carrier generation at room temperature, and free charge carriers can be separated and collected at carrier-selective electrodes. In the most common type of commercially available solar cells, devices that are based on semiconducting silicon (Si) as a light-harvesting material, these selective electrodes are formed by n-type and p-type crystalline or amorphous silicon with an overall thickness of several micrometers. Electrons are injected into the n-type silicon layer, whereas the holes are injected into the p-type semiconductor, as shown in Figure 1.1b. The electric field in the depletion region constitutes only around 1% of the total semiconductor^[12] and is arguably less crucial for the free charge carrier generation in high-dielectric materials with low

exciton binding energies where free charge carriers thermally dissociate at room temperature. On the other hand, in low-dielectric materials, the exciton binding energy is too high to facilitate thermal charge dissociation. In these materials, electron-hole pairs would recombine within the bulk of the material. Charge carrier dissociation in low-dielectric materials such as organic semiconductors (see section 1.4.1), in contrast, happens mainly at the donor-acceptor interface, making optimal contacts between p- and n-type semiconductors crucial for efficient device operation.

1.3 The Need for New Semiconducting Materials

Considering the wide application of semiconducting materials, it may appear surprising that, as of today, the industry is relatively conservative regarding the choice of semiconducting materials, relying mainly on inorganic germanium, gallium arsenide, silicon, or metal oxide semiconductors. Referring to the previous section, silicon (Si)-based materials, for example, highly dominate the solar cell devices market, where amorphous or crystalline silicon solar cells make up to 90% of the market share.^[13] Nevertheless, these materials often require energy-intensive fabrication steps. Silicon wafers must have a high purity ($>99.9999\%$), resulting in an energy-intensive production.^[14] The high temperature in the fabrication process makes cheap solution-based roll-to-roll fabrication methods hard to implement for these materials and widely limits the application of different temperature-sensitive substrates.^[15]

Ultimately, silicon and other semiconductors will reach their physical limits for further enhancing the performance of electronic devices, which require even further miniaturization. For instance, the indirect band gap of semiconducting silicon reduces the material's light absorptance. This becomes particularly problematic in solar cell devices that require a relatively thick wafer of several micrometers to effectively absorb enough photons to generate electricity efficiently.^[16] Because of this, the devices become heavy and brittle, limiting the application in lightweight devices. Even though silicon-based materials have a band gap of around 1.1 eV, which is close to the optimal band gap to obtain a theoretical solar-to-electricity conversion efficiency given by the Shockley-Queisser limit of around 33% in single junction solar cells, the band gap of Si is relatively fixed and difficult to alter. Materials with tunable band gaps offer the possibility to design colorful photoabsorbers for implementation in more integrated systems. Photoabsorbers with a large band gap could also be used as a top layer in tandem-solar cells, allowing them to overcome the Shockley-Queisser limit in single-junction devices and enhancing the solar-to-electricity efficiency. Moreover, the price of electricity produced by solar energy strongly depends on the device's efficiency due to fixed module integration costs. Implementing more efficient solar cell devices is a promising strategy to make solar energy cheaper.^[17,18]

1.4. Emerging Novel Semiconducting Materials for Optoelectronic Applications

Despite the emphasis here on semiconductors for application in energy devices such as solar cells — undoubtedly an important driving force for the development of new materials — new emerging fields such as spintronics or organic bio-electronics require materials that possess properties, such as structural flexibility or bio-compatibility, which are not fulfilled by existing inorganic semiconducting materials or are challenging to produce by existing fabrication processes. While today the semiconducting industry heavily relies on a top-down design approach (e.g., photolithography or e-beam lithography), further development of new semiconducting materials has to focus more on bottom-up approaches. Engineering the semiconducting material to this specific requirement in combination with cheap and large-scale solvent-based fabrication processes provides an exciting opportunity to further advance the large field of semiconducting materials.

1.4 Emerging Novel Semiconducting Materials for Optoelectronic Applications

The research for new semiconducting materials for various applications has yielded a wide range of novel materials with promising properties. While some materials have obtained tremendous interest, such as 2D materials like graphene — for which Andre Geim and Konstantin Novoselov were honored with the Nobel prize in 2010 ^[19,20] — a complete discussion of all these materials would vastly exceed the scope of this thesis. In the following, the discussion will be limited to two emerging classes of semiconductors widely studied in chemistry. Firstly, semiconductors consisting mainly of carbon-based organic materials will be discussed. These materials have a high degree of variability and tunability by molecular engineering, which makes them promising for a wide field of applications and have already seen commercialization for specific applications. The second class of materials that will be discussed in the following is hybrid organic-inorganic perovskite (HOIP) semiconductors. This discussion focuses on the electronic and optical properties rather than the synthetic aspects, which will only be addressed when the understanding requires so.

1.4.1 Organic Semiconducting Materials

Organic semiconductors combine the optoelectronic properties of inorganic semiconductors with organic materials' tunability and chemical flexibility. ^[5] The semiconducting properties arise from the atomic and molecular orbitals of the carbon atoms. Considering atomic carbon, the valence electrons are located in the 2s (2 electrons) and the 2p (2 electrons) orbitals. However,

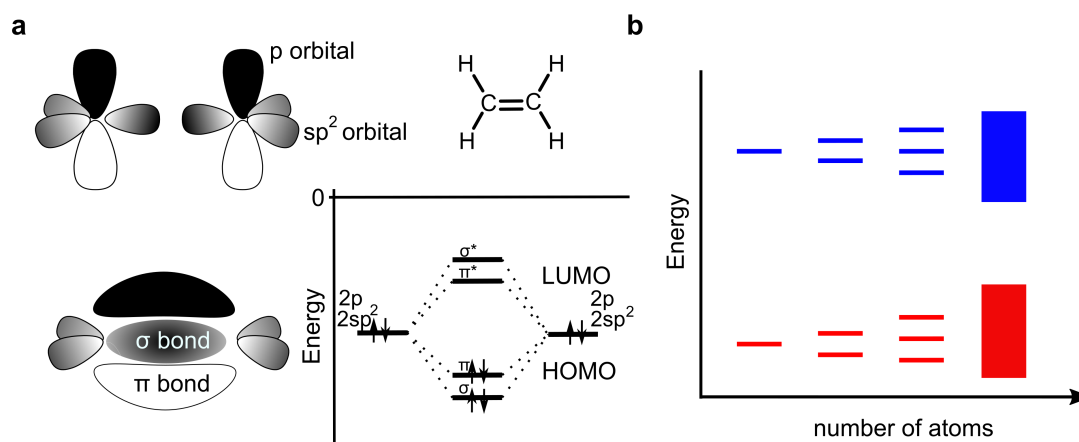


Figure 1.2 – **a)** π - and σ -bonding arising from the p and sp^2 hybridized atomic orbitals in ethylene. **b)** Increasing the number of double bonds in molecules, and increased molecular packing of the organics in solid states lead to a quasi-continuous energy-states.

when carbon is bonded to hydrogen or other carbon atoms, the $2s$ and $2p$ orbitals undergo hybridization, forming four sp^3 hybridized atomic orbitals. The four equivalent hybrid atom orbitals give rise to tetrahedral molecular structures found in, for example, methane molecules. In carbon double-bonds, the valence orbitals in the carbon are sp^2 -hybridized, leading to one available p -orbital with distinct energy levels from the sp^2 orbitals.^[11,21] While the sp^2 orbitals of the carbon form a σ -bond with each other, the p -orbitals form π -bonds. Energetically, the π -bonds are less favored compared to σ -bonds, leading to the localization of the valence electrons in the highest occupied molecular orbital (HOMO) made from π -orbitals, while the π^* -anti-bonding orbitals build the lowest unoccupied molecular orbital (LUMO), as shown in Figure 1.2a. By increasing the conjugation in the π -system, the difference between the HOMO and LUMO energy levels decreases, leading to organic molecules with visible light absorption properties as found in many organic chromophores. While in single molecules the HOMO and LUMO are still discrete energy levels, when packing organic molecules in solid matter, the orbitals of different molecules start to interact, and with increasing density, the discrete states start to become a quasi-continuous band of energy levels as displayed in Figure 1.2b.

Despite the similarities in the electronic structure, there are clear differences between organic and inorganic semiconductors. While in inorganic semiconductors individual atoms are held together by ionic or covalent forces, strong van-der-Waals, and π - π interactions are formed between organic molecules or polymers in organic semiconductors, which play a crucial role in the charge carrier transport through the material. Charge carrier transport in organic semiconductors differs from the band-like transport in Si-based semiconductors and is described as an array of hopping-like processes (polaron-transport), as displayed in Figure 1.3a.^[22,23] Such charge carrier properties suggest that the material's disorder can substantially impact the

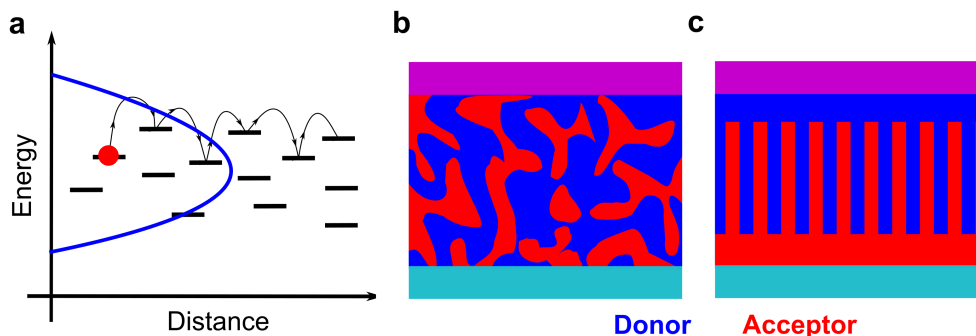


Figure 1.3 – **a)** Charge carrier hopping in organic semiconductors. The blue curve indicates the density of states distribution. **b)** Schematic illustration of the architecture of a bulk heterojunction (BHJ). **c)** The pillar shaped system represents the ideal case for efficient charge dissociation.

charge carrier mobility where highly ordered systems achieve more band-like transport and show enhanced charge carrier mobility. Achieving organic semiconductors with high ordering and high charge carrier mobility can be challenging and is strongly impacted by the deposition methods, making charge carrier transport a limitation in their application in optoelectronic devices.

Organic semiconductors have attracted attention for their application in light-emitting diodes, which have been commercialized in recent years. The thin film fabrication process on polymeric substrate allows cheap production of bendable LED displays. A key characteristic of organic semiconducting materials is their relatively low dielectric constant, which results in strong exciton binding energies. By synthesizing visible-light absorbing organic molecules or polymers, organic semiconductors can also be implemented in solar cell devices allowing the fabrication of lightweight devices. However, the low dielectric constant is disadvantageous for solar cell applications where efficient electron-hole separation is needed. As low dielectric materials screen the electron-hole interactions less efficiently, the formation of strongly bound electron-hole pairs (Frenkel excitons) with low diffusion lengths, which are hard to separate into free charge carriers, is favored.^[24,25] To mitigate the high exciton binding energies, the electron-hole pair can be separated at the interface of two organic semiconductors by forming a type II heterojunction. This can be achieved by depositing an electron-donor on top of an electron-acceptor organic semiconductor. In the case of a single junction architecture, which resembles the device architecture of p-n junctions in silicon solar cell devices, charge separation is still limited by the short exciton diffusion length of the excitons through the bulk material. Efficient charge separation can only occur for distances between donor and acceptor domain sizes close to the exciton diffusion length of 10-50 nm.^[26,27] To reduce the size of the bulk material and increase the charge separation efficiency, a bulk heterojunction (BHJ) of a blended mixture

of donor and acceptor polymer forming an interconnected continuous network is targeted to achieve high-performing organic solar cells.^[28] An important factor in achieving such high efficiencies is the optimal blending reducing the domain size to only a few nanometers while still forming a continuous network for good charge carrier transport. In the ideal case, a pillar-like structure, as illustrated in Figure 1.3c, allows optimized charge separation and charge transport. However, bulk heterojunction systems containing all polymer are anisotropic, and controlling the orientation and crystallinity of donor and acceptor is challenging to achieve.

1.4.2 Hybrid Organic-Inorganic Perovskite Structure and Properties

While organic semiconductors were successfully implemented in LED devices, the development of efficient organic-based solar cell devices was eclipsed by the rise of hybrid organic-inorganic perovskite-based semiconductors (HOIPs). The perovskite structure consists of a class of materials with the general formula ABX_3 where the A-site is a monovalent cation, B is a divalent metal cation, and X is a halide. The formability of a perovskite structure is described by the Goldschmidt tolerance factor (t) defined as:

$$t = \frac{r_A + r_X}{\sqrt{2}(r_B + r_X)} \quad (1.1)$$

where r_A , r_B , and r_X are the ionic radius of the A-site, B-site, and halide, respectively.^[29,30] As illustrated in Figure 1.4a, a cubic perovskite structure is formed when the tolerance factor is between 0.8 and 1.1. In the most widely employed HOIP materials for the application in solar cell devices, Cs^+ methylammonium (MA^+) or formamidinium (FA^+) (chemical structures are shown in Figure 1.4b) are used as an A-site, while Pb^{2+} or Sn^{2+} are used as B-site, forming a hybrid organic-inorganic perovskite (HOIP) structure. As the precursors of HOIPs are soluble

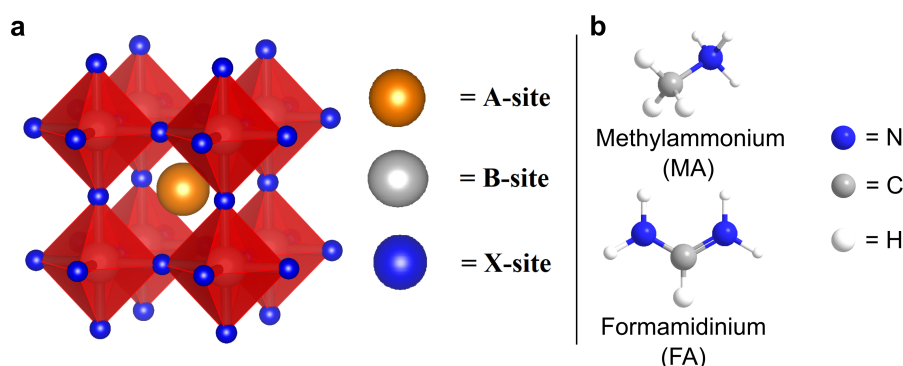


Figure 1.4 – **a**) Structure of hybrid organic-inorganic halide perovskite, and **b**) chemical structure of methylammonium (MA^+) and formamidinium (FA^+).

1.4. Emerging Novel Semiconducting Materials for Optoelectronic Applications

in Dimethylsulfoxide (DMSO) or N,N-Dimethylformamide (DMF), thin films can be easily formed by solvent-based fabrication methods, such as spin-coating or doctor blade coating, at relatively low temperatures.^[31,32] Additionally, compositional engineering can easily tune the optoelectronic properties of the material.^[33–35] As the band structure is determined by the p-orbitals of the halide (VB) and the overlap of 6p orbitals of lead and p orbitals of the halide (CB), replacing iodide with bromide shifts the CB and VB energies and increases the band gap.^[36] Although the A-site cation does not contribute electronically to the perovskites, tilting of the Pb-X octahedra induced by the A-site can further tune the electronic structure of the material.^[37,38] The high visible-light absorption, the low exciton binding energy of a few meV, and the high charge carrier diffusion length^[39] of methylammonium and formamidinium-based lead-halide perovskites (MAPbI₃ or FAPbI₃), for example, make these materials suitable for the applications in solar cell devices, reaching power conversion efficiencies of more than 25.7%, which is comparable to the efficiencies obtained in silicon-based solar cells.^[40,41] Furthermore, the high tunability and processability, along with the straightforward synthesis of lead-halide perovskite-based nanoparticles of various band gaps, make these materials attractive for a wide range of applications, such as photodetectors and LEDs.^[42] However, the large-scale applications and commercialization of perovskite semiconductors remain hampered by the low stability of the materials under operational conditions. HOIPs can undergo thermal, light, and moisture-induced decomposition under working conditions forming PbI₂.^[43,44] Although moisture and thermal stability can be improved by compositional engineering and device encapsulation,^[45] material decomposition remains a substantial drawback for all HOIP semiconductors.

1.4.3 Layered Perovskite Semiconductors

Due to the low intrinsic stability of hybrid organic-inorganic lead-halide-based perovskites, focus of researchers has shifted in the last few years towards the synthesis and characterization of so-called layered (LHOIP) and quasi-layered perovskite materials as a stable alternative to HOIPs. Layered perovskite materials are formed by replacing the A-site cation partially or completely with a bulky organic aliphatic spacer cation. As the spacer cations are too large to fit into the octahedral cage, a new phase is formed where the octahedral framework is separated along a particular crystalline direction forming layers of alternating organic-inorganic slabs, as illustrated in Figure 1.5a.^[46–49] In the simplest case, the spacer cation is an aliphatic ammonium anion or a cyclic (aromatic or aliphatic) molecule with an alkyl linker chain bearing ammonium group that connects the spacer to the inorganic slab.^[50] The spacer head that connects the inorganic layer with the organic molecule consists commonly of a primary ammonium group. Some reports have explored substitutions at the amino position to form secondary or tertiary amines.^[51,52] However, these modifications make the spacer cation less prone to form a layered

perovskite structure as the amino group becomes too large to fit into the inorganic pocket destabilizing the layered structure. Due to the hydrophobic character of typical spacer cations such as *n*-butylammonium (BA) and phenylethylammonium (PEA) and the increased formation energy compared to the "conventional" three-dimensional (3D) ABX₃ perovskites, these materials have higher moisture resistivity and thermal stability.^[48,53,54]

As shown in Figure 1.5a, the incorporation of monocations results in a structure where a bi-layer of organic spacer cations separates the inorganic slabs. In contrast, the inorganic slabs are held apart by a monolayer of organic spacers when a dication is incorporated. The layered phases that are formed based on the valency of the spacer cations are commonly referred to as Ruddlesden-Popper (RP) type perovskite for monocations with the general structure A₂PbX₄, and Dion-Jacobson (DJ) type perovskites for dications, with the general structure APbX₄. The nomenclature of LHOIPs is rooted in the nomenclature of oxide perovskites and is based on the distinct structural feature with respect to the displacement of adjacent perovskite slabs. In the RP phase, adjacent octahedral layers are shifted by the length of half a unit-cell length (denoted as $\frac{1}{2}, \frac{1}{2}$ shift), while no or only a $\frac{1}{2}, 0$ shift can be observed for DJ phases, as illustrated in Figure 1.5b.^[55] Because of the structural flexibility of the spacer dication often based on aliphatic alkyl chains, proper DJ phases in the structural sense where no shift of the adjacent slabs can be found, remain relatively rarely observed, and perovskite phases that can be assigned to the RP phase constitute the majority of investigated LHOIPs. In this work, independently of the relative

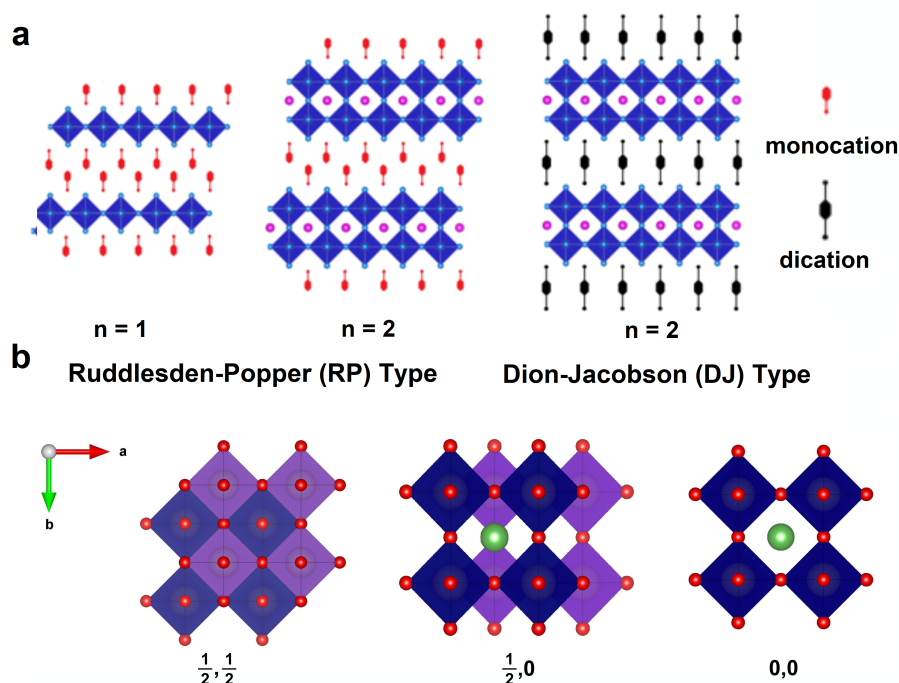


Figure 1.5 – **a)** Structure of layered perovskite materials incorporating monocations and dications into the octahedral framework and **b)** view along c-axis for $\frac{1}{2}, \frac{1}{2}$, and $\frac{1}{2}, 0$, and $0, 0$ shifts.

1.5. Properties of Layered Perovskite Materials and Quasi-Layered Perovskite Materials Incorporating Aliphatic Spacer Cations

displacement of the octahedral layers, LHOIP based on monovalent spacers are referred to as RP phase, while materials incorporating dications are denoted as DJ phase.

Similarly to ABX_3 perovskites, LHOIP materials show high tunability by compositional engineering. By mixing small organic cations (A') and spacer cations (A) quasi-layered perovskites with the general formula $A_2(A')_{n-1}Pb_nI_{3n+1}$ (RP phase) and $A(A')_{n-1}B_nX_{3n+1}$ can be formed where B is a divalent metal cation (e.g., Pb^{2+}) and X is a halide anion. With increasing n , the size of the inorganic slab becomes wider, as shown in Figure 1.5a, tuning the optoelectronic properties of the material. Additionally, as the band edges are composed of contributions from the halide and lead atomic orbitals, layered perovskite materials can be tuned by the halide composition.^[56]

The high tunability and hydrophobic character of the spacer cation render layered and quasi-layered perovskites interesting materials for applications in optoelectronic devices such as solar cell devices,^[57–62] (LEDs),^[63] photodetectors,^[64] and field effect transistors (FET).^[65–67] For example, Grancini *et al.* reported one-year stable perovskite solar cells by engineering a 3D/2D interface where the 2D layer acts as a moisture barrier.^[68] However, especially for the application as light harvesting materials, layered and quasi-layered perovskite semiconductors are still lagging behind the performance of less stable 3D perovskite materials due to their anisotropic character and less suitable optoelectronic properties. In the following, the intrinsic and extrinsic optoelectronic properties of layered perovskite materials will be addressed. This will be followed by a discussion of electronic interactions in quasi-layered perovskite phases. Finally, the possibilities of tuning the perovskite materials by spacer cation design will be outlined.

1.5 Properties of Layered Perovskite Materials and Quasi-Layered Perovskite Materials Incorporating Aliphatic Spacer Cations

Let us consider a simple layered perovskite structure with $n = 1$ of the general structure A_2PbX_4 or $APbX_4$ where A is an aliphatic spacer cation. If we compare the HOMO and LUMO levels of the organic spacer with the CB and VB of the inorganic perovskite slabs, we obtain an electronic structure where the electronic level of the organic cation's LUMO is far higher than the CB minimum of the perovskite layer. Additionally, the HOMO of the organic layer is energetically far below the VB maximum of the layered perovskite structure. The electronic mismatch between organic and inorganic layers causes the formation of a quantum well structure where the isolating organic spacer cation acts as the walls of the well, as illustrated in Figure 1.6a.^[69] The distinct pseudo-two-dimensional (2D) structure of layered perovskite materials has implications for the optoelectronic properties and, subsequently, on the application in optoelectronic devices. As illustrated in Figure 1.6b, charge carrier mobility through the organic layer is hampered compared

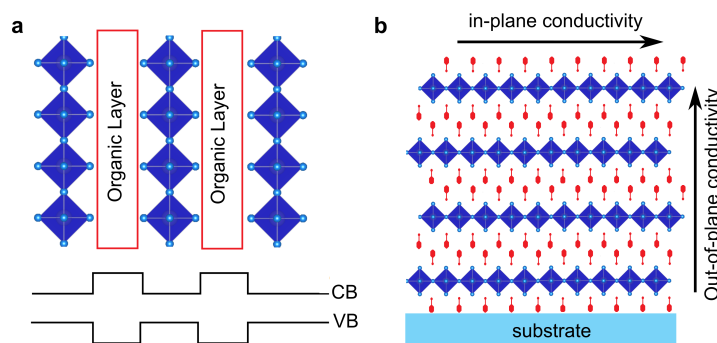


Figure 1.6 – **a)** Quantum well structure formed by incorporating aliphatic spacer cations, and **b)** resulting orientation in thin film with respective in-plane and out-of-plane direction.

to the charge carrier mobility along the inorganic layer due to the anisotropy of the 2D system. Differences of several orders of magnitude were found with mobilities along the inorganic slabs comparable with the mobility of 3D HOIPs.^[70] Notably, out-of-plane conductivity is enhanced by decreasing the barrier size by incorporating a shorter spacer cation reducing the distance between adjacent inorganic slabs.^[71,72] The anisotropic charge carrier properties constitute a crucial limitation for applying LHOIPs in optoelectronic devices. This limitation is further amplified by the preferentially oriented structure observed in most commonly investigated materials, where the inorganic layers lay parallel to the substrate when deposited by spin-coating or doctor-blading methods. Besides that, the optoelectronic features are affected by strong quantum confinement effects due to the electronic mismatch between the electronic structure of the spacer cation and the inorganic perovskite layer, as illustrated in Figure 1.6.^[73]

Shinada *et al.* have previously estimated the impact of the quantum confinement on the exciton binding energy by considering a two-dimensional hydrogen model for semiconductors and comparing it with the hydrogen model of the three-dimensional situation.^[74] By solving the Eigenwert equation with the adapted two-dimensional Hamiltonian, the energy levels can be calculated based on the equations displayed in Table 1.1. where R is the Rydberg constant and $N = 0, 1, 2, \dots$. Comparing the case for 2D and 3D semiconductors, the main difference is in the denominator of the Eigenvalue, where in the 2D case, the denominator is $(N + \frac{1}{2})^2$ instead of N^2 , and N starts from 0. Assuming $E = 0$ to be the energy of a free electron state, an increase of the exciton binding energy by a factor of 4 is expected when moving from a 3D to a 2D semiconductor.^[75,76] Experimental results, however, reveal an exciton binding energy of more than 310 meV^[73,77,78] in $(\text{BA})_2\text{PbI}_4$, which is more than 20 times higher than determined in the 3D non-layered structure. While the assumption of a 2D hydrogen model might be an oversimplification of the real world as, for example, tunneling processes are not taken into account, it is widely accepted that the observed mismatch between the calculated theoretical and measured exciton binding energy

1.5. Properties of Layered Perovskite Materials and Quasi-Layered Perovskite Materials Incorporating Aliphatic Spacer Cations

Table 1.1 – Eigenwert determined for the 3D and 2D hydrogen model where $N = 0, 1, 2, \dots$ and R is the Rydberg constant.

3D	2D
$E_N^{3D} = -\frac{R}{N^2}$	$E_N^{2D} = -\frac{R}{(N+\frac{1}{2})^2}$

is a result of additional dielectric confinement effects as the relative permittivity of the spacer cation is lower than the relative permittivity of the inorganic slabs.^[79] The mismatch results in a poor dielectric screening of the electron-hole pair, reducing the Bohr radius and increasing the exciton binding energy even further. While quantum and dielectric confinement effects cause a large increase of the exciton binding energy,^[80] the formation of a layered perovskite is manifested by a characteristic excitonic absorption band at around 500 - 525 nm (2.4 eV)^[81] and strong photoluminescence emission at around 525 nm, as observed in phenylethylammonium based (PEA)₂PbI₄ layered perovskite materials displayed in Figure 1.7a and b.

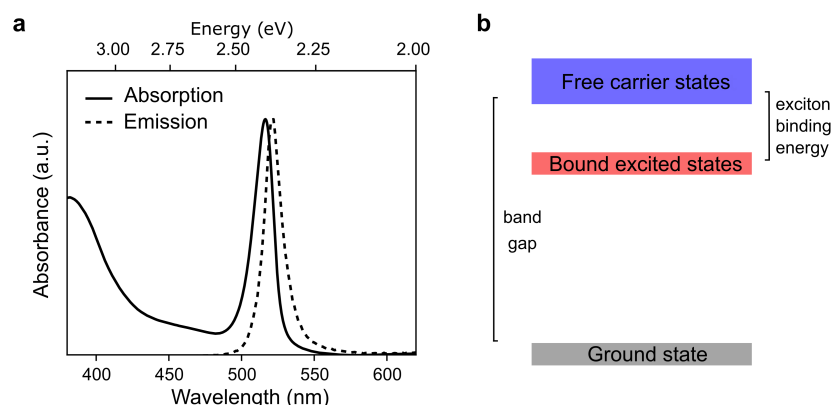


Figure 1.7 – **a)** UV-vis absorption and PL-emission spectra of (PEA)₂PbI₄ show characteristic excitonic absorption band at around 500 nm as a result of the strong quantum and dielectric confinement effects. Scheme **b)** illustrates the effect of the exciton binding energy on the absorption spectra and observed excitonic band.

1.5.1 Charge Carrier Properties in Quasi-Layered Poly-Dispersed Thin Films

In contrast to the more conventional ABX₃ HOIPs, pure LHOIP semiconductors of the general formula A₂PbX₄ and APbX₄ ($n = 1$), where A is the spacer cation, and X is a halide anion, are rarely reported for optoelectronic application in general and solar cell devices in particular. The large

band gap for visible-light harvesting and high exciton binding energy compared to conventional HOIP materials make charge separation in solar cell devices challenging. Moreover, in most cases of thin film samples, the inorganic slabs lay parallel to the substrate, preventing efficient charge transfer through the film and thus limiting the application in devices where the material is sandwiched between two electrodes.^[82] The most straightforward approach to tuning the electronic structure and charge carrier properties is the formation of quasi-layered materials by mixing small A'-site cations and spacer cations in the specific stoichiometric ratios leading to quasi-layered phases of the general formula $A_2A'_{n-1}Pb_nX_{3n+1}$ and $AA'_{n-1}Pb_nX_{3n+1}$, where A' cation is small enough to fit into the octahedral cage. These materials are characterized by the quantum well width denoted by the number (n) of lead-halide octahedra in the inorganic layers. As illustrated in Figure 1.8a, with increasing well size, quantum and dielectric confinements are reduced while stability is diminished but still superior to the stability of 3D HOIPs. Quasi-layered perovskite materials have shown significant advances in stability, making these materials interesting for applications in solar cell devices. Moreover, they are currently under investigation for the application in light-emitting diodes (LEDs).^[83]

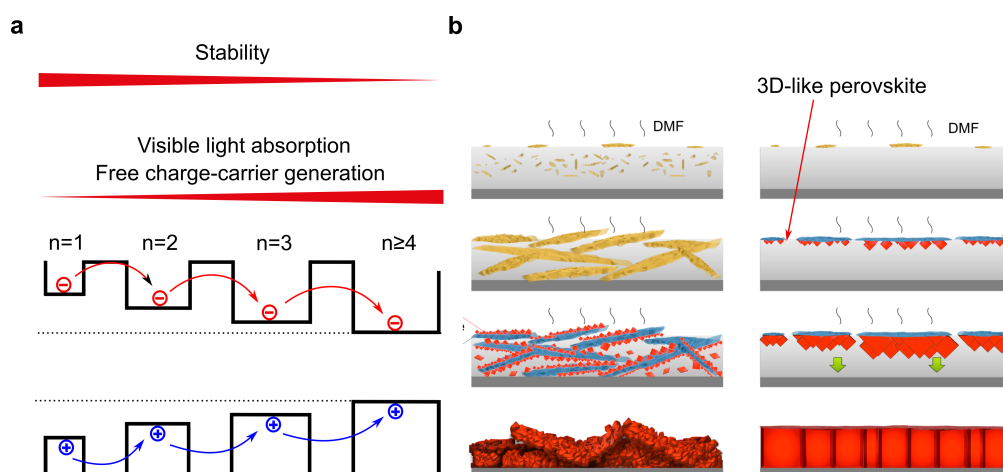


Figure 1.8 – **a)** Effect of the quantum well width on the stability and band gap. **b)** Crystal growth mechanism upon additive engineering to avoid nucleation inside the solvent to obtain oriented layered perovskite thin films reproduced from ref. 84 (copyright ©2020, the author(s)).

Besides the reduced dielectric and quantum confinement effects, poly-dispersed multi-well systems are more randomly oriented, and crystal orientation can easier tuned by solvent engineering such that the inorganic layers lay perpendicular to the substrate, acting as charge carrier channels between the electrodes.^[84,85] However, in contrast to 3D perovskite materials, in quasi-layered perovskite thin films, multiple quantum well phases with different n are usually formed where the overall optoelectronic properties are affected by the distribution of the poly-dispersed quantum well affected by the processing conditions.^[60,86,87] During the crystallization

1.5. Properties of Layered Perovskite Materials and Quasi-Layered Perovskite Materials Incorporating Aliphatic Spacer Cations

process, the formation kinetics and order, governed by the formation energy, are different for the various n phases, where low n phases tend to have a lower formation energy than high n phases.^[88–91] As such, during the formation of a thin film intended to form $(\text{BA})_2(\text{MA})_3\text{Pb}_4\text{I}_{13}$ ($n = 4$), the rapid formation of MAPbI_3 results in the depletion of the MA^+ in the coated residual film and enforcing the formation of low n -value phases.^[63,92] As a result, lower n phases, which can obstruct the charge carrier transport through the film, are found to be formed closer to the substrate, while 3D MAPbI_3 forms at the solvent-air interface.^[93] Moreover, given the relative energy level of the different quantum-well phases, electrons and holes can funnel from low n -value phases towards phases with wider quantum well width upon excitation, as illustrated in Figure 1.8a. Charge carrier funneling is a major issue in LEDs and PV devices, hampering the performance of such materials.^[94] The formation of a homogeneous energy landscape was suggested to be most favorable for the application in solar cell devices.^[95]

Therefore, understanding the detailed crystal growth mechanism is crucial to obtain preferential orientation where the inorganic layers lay perpendicular to the substrate and allow efficient charge carrier transport through the film. The retardation of the crystal phase formation was suggested to be crucial to tune the thin film phase distribution.^[96] As such, additive engineering with NH_4SCN or NH_4Cl was reported to allow the control of the crystallization mechanism by preventing the nucleation on the bulk of the film and favoring oriented crystal growth initiated at the solvent-air interface to the substrate, as illustrated in Figure 1.8b.^[97,98] He et al. reported direct modifications of the spacer cations to retard the formation of lower n phases replacing BA with meta-(aminomethyl) piperidinium cations to obtain a more homogeneous energy landscape.^[95] Moreover, recent reports indicate the formation of pure $n = 5$ quasi-layered perovskite when n -butylammonium iodide was replaced with n -butylammonium acetate.^[99] However, these strategies are only effective across a narrow range of spacer cations and targeted quantum well sizes.

More recently, research focused on tuning the optical properties in quasi-layered perovskite materials by designing novel spacer cations to modify charge transport, stability, and phase distribution.^[54,95,100] However, the formation of poly-dispersed thin films still challenges the understanding of the structure-properties relationship. Although quasi-layered perovskite single crystals with the general formula $(\text{A})_n\text{A}'_{n-1}\text{Pb}_n\text{I}_{3n+1}$ with $n = 1, 2, 3$ were reported based on BA and PEA spacer cations,^[101–103] the formation of quasi-layered single crystals and study of these materials remains scarce. In this context, the investigation of pure phase $n = 1$ layered perovskite materials remains a more accessible approach to understanding the effect of the spacer cation on the optoelectronic properties. Understanding the effect of the spacer cations on the optoelectronic properties of $n = 1$ LHOIPs remains of fundamental interest for the understanding and tailoring of LHOIP materials.^[104,105]

1.6 Tuning Optoelectronic Properties by Structure Modifications

While for the application in optoelectronic devices quasi-layered thin films are widely investigated, recent research has focused on tuning the optoelectronic structure of the materials by functionalizing the spacer cation.^[105] If we again consider a layered perovskite semiconductor with an aliphatic or small aromatic spacer cation forming a quantum well structure, the optoelectronic properties are only determined by the electronic structure of the inorganic slab and influenced by dielectric and quantum confinement effects. As such, similarly to 3D HOIPs, the band edges of the inorganic layer can be modified by changing the halide resulting in an increase of the band gap energy when replacing iodide with bromide.^[106] Because the spacer does not interact electronically with the inorganic perovskite layer, modifying the aliphatic spacer affects only the optoelectronic structure *via* structural modification of the octahedral framework. The structure-properties relationship has been studied in various layered perovskite systems.^[107–111]

Taking a step back, considering layered perovskite materials as a crystal structure of alternating layers where the spacer cation slices the inorganic layers, based on the crystallographic slicing direction of the 3D structure illustrated in Figure 1.9a-c ($\langle 100 \rangle$, $\langle 110 \rangle$ or $\langle 111 \rangle$), different layered crystal structures with distinct optoelectronic properties can be distinguished.^[48]

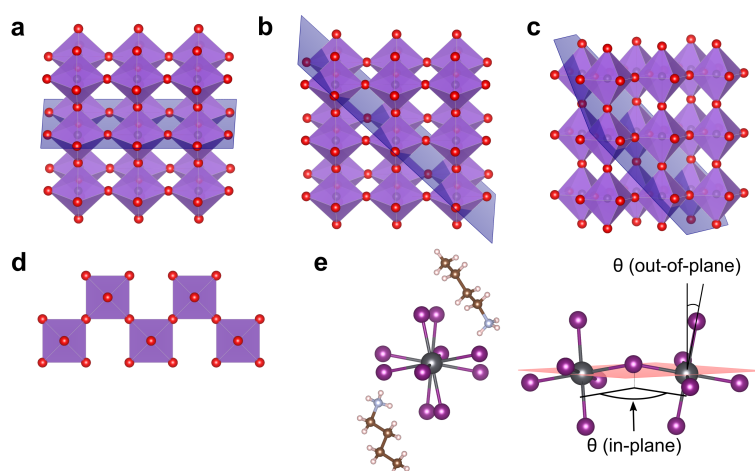


Figure 1.9 – Structure of **a)** $\langle 100 \rangle$, **b)** $\langle 110 \rangle$, and **c)** $\langle 111 \rangle$ perovskites. **d)** Corrugated structure of $\langle 110 \rangle$ perovskites. **e)** Distortions of the inorganic framework in $\langle 100 \rangle$ -layered perovskites leads to modification of the optoelectronic properties of the material.

While RP and DJ phases are specific subclasses of the most common $\langle 100 \rangle$ layered perovskite structure, $\langle 110 \rangle$ layered perovskite structures such as (EDBE)[PbBr_{4-x}Cl_x] based on the 2,2'-(ethylenedioxy)bis(ethylammonium) cation (EDBE) are mainly formed in the presence of strong hydrogen bonds between adjacent spacer cations.^[107–109] The strong hydrogen bonds result in a crystal structure where the octahedral framework is corrugated, as illustrated in Figure 1.9d.

1.7. Tuning the Dielectric Screening in Layered Perovskite Materials with Functionalized Spacer Cations

Although the structural distortion leads to absorption properties similar to the $\langle 100 \rangle$ sliced layered perovskites, self-trapping leads to broad photoluminescence emission.^[107] While the $\langle 111 \rangle$ and the $\langle 110 \rangle$ layered structures are less common than the $\langle 100 \rangle$ structures and are therefore considered a more exceptional case of structure modulation of layered perovskite semiconductors, octahedral distortion of the Pb-I-Pb framework, as illustrated in Figure 1.9e, also affects the optoelectronic properties in $\langle 100 \rangle$ perovskites. A systematic investigation of the octahedral distortion and its effect on excitonic absorption band position was reported by Ishihara *et al.*. However, no clear relationship has been found between octahedral distortions and excitonic absorption band position.^[110] A more comprehensive study on phenyl-based spacer cations of various amine-bearing linker chain lengths was presented by Kamminga *et al.*, where systematically increasing the phenyl alkylammonium chains length induces a blueshift in the photoluminescence. The induced structural distortion by incorporating a larger spacer cation caused the reorganization of the structure to include face-sharing as well as corner-sharing PbI_6 -octahedral, altering the band structure of the material.^[111] Moreover, Li *et al.* showed differences in in-plane charge carrier mobilities determined by optical-pump terahertz-probe spectroscopy arise from local chain distortion.^[112]

1.7 Tuning the Dielectric Screening in Layered Perovskite Materials with Functionalized Spacer Cations

Besides the strong quantum confinement effect, the optoelectronic properties of LHOIP materials are largely determined by dielectric confinement effects, as outlined in section 1.4. Tuning the dielectric constant of the layered perovskite material alters the optoelectronic properties of the material affecting the exciton binding energies. Indeed, considering that the exciton binding energy depends on the Coulombic interaction between electrons and holes, the Coulombic capture radius r is given by:^[113]

$$r^2 = \frac{e^2}{4\pi\epsilon k_b T} \quad (1.2)$$

where e is the elemental charge, $k_b T$ is the Boltzmann constant at temperature T . Equation 1.2 highlights the importance of the permittivity of the material on the physical separation required to overcome this radius. The properties of the spacer cation can be used to tune the dielectric confinement. Reducing the inter-lattice distance RP phase by incorporating short alkyl chain spacers or even more so in DJ phase perovskites, for example, enhances the dielectric screening of adjacent inorganic slabs, mitigating the quantum confinement effects and reducing the

out-of-plane resistivity.^[71,72] Moreover, reducing the material's overall relative permittivity by incorporating polarizable spacer cations such as ethanol ammonium-based spacers improving the dielectric screening of photoexcited electron-hole pair in the inorganic layer, reducing the exciton binding energy, as illustrated in Figure 1.10a and b, as it has been reported.^[114]

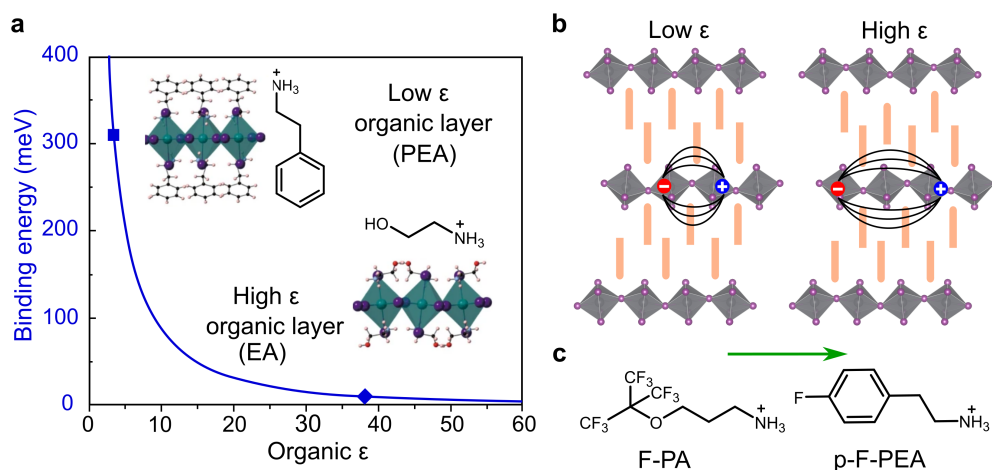


Figure 1.10 – **a)** Effect of the dielectric constant of the spacer cation on the exciton binding energy of the layered perovskite. Figure is reproduced from ref. 85 (copyright ©2018, the author(s)). **b)** The increase in relative permittivity of the spacer cation results in reduced exciton binding energies. **c)** Previously investigated high-dipole spacer cations by Quelo *et al.* from ref. 115.

More recently, several reports have investigated the effect of the dipole moment of the spacer cation on the charge carrier mobility and charge separation efficiency. Experimental studies based on p-F-PEA (chemical structure illustrated in Figure 1.10c) in quasi-layered ($n \approx 4$) perovskite materials suggest improved charge separation mainly due to enhanced transport through the inorganic layer.^[98,115–117] However, due to charge carrier funneling and various phase distributions in different thin film, it remains unknown whether improved photovoltaic performances are due to differences in phase distribution or intrinsically improved charge carrier transport. More interestingly, Xu *et al.* reported improved charge separation properties at a 3D/2D interface, with the 2D layer being a 2,2,2-trifluoroethylamine (FEA) based layered perovskite $(\text{FEA})_2\text{PbI}_4$. Moreover, the spacer cation is a potential potent passivation agent.^[118] It remains unknown if a high-dipole spacer cation can assist charge separation in $(\text{A})_2\text{PbI}_4$ perovskite. However, Quelo *et al.*, for example, reported long-lived charge carriers due to a photoinduced Stark effect when F-PA spacer cations were intercalated in the perovskite framework. It remains unclear if such a photoinduced Stark effect is due to the dipole moment of the spacer cation.^[119]

1.8 Tuning the Properties by Incorporation of Semiconducting Spacer Cations

While incorporating polarizable spacer cations can reduce the exciton binding energy, the layered perovskite structure still forms a quantum well structure where the HOMO and LUMO levels of the spacer cations strongly mismatch the CB and VB of the inorganic perovskite layer, respectively. However, incorporating spacer cations containing a chromophore core with HOMO-LUMO energy levels similar to the CB and VB of the inorganic slabs, orbital interactions occur between the spacer cation and the inorganic layer. A set of novel semiconducting materials can be obtained where the quantum confinement of the layered perovskite materials is mitigated.^[120,121] The distinct electronic properties derived from the synergy of the organic and inorganic components make them a new class of semiconductor,^[121] often denoted as Organic Semiconductor-Incorporated (OSiP).^[122]

Depending on the relative position of the spacer chromophore cation's HOMO and LUMO energy levels, two types of such heterostructures can be distinguished and are displayed in Figure 1.11.^[123,124] The quantum well formed by aliphatic spacer cations is denoted as type I heterostructure, where the excitons are located in the inorganic layer. An inverted type I heterostructure can be formed when the HOMO and LUMO energy levels are located between the CB and VB of the inorganic layer. In the case of an electron-accepting or electron-donating spacer cation, the CB and VB of the inorganic are offset relative to the organic chromophore's HOMO and LUMO energy levels, forming a structure that can be denoted as a type II heterostructure.^[125]

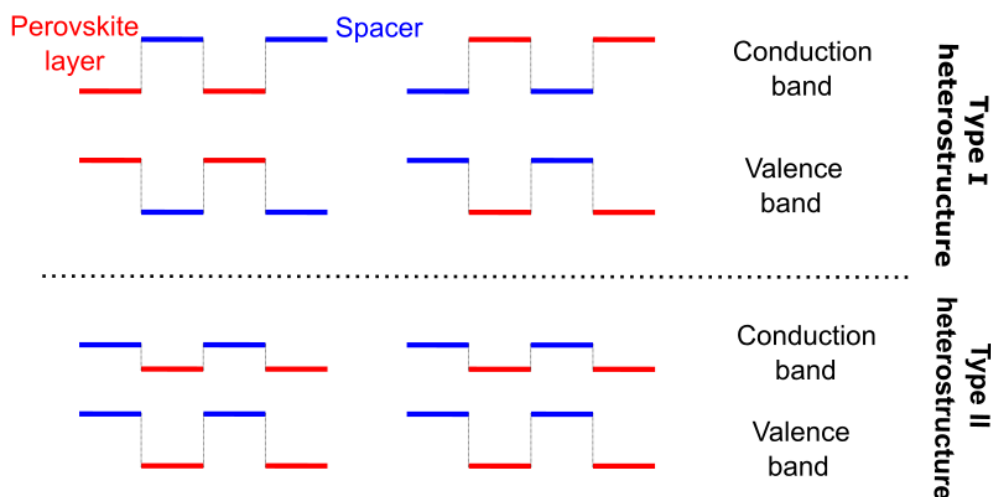


Figure 1.11 – Energy band alignment in layered perovskite materials forming quantum wells (type I heterostructures). By incorporating electron accepting donor or acceptor chromophores type II nano-heterostructure can be formed as proposed by Gao *et al.* in ref. 123.

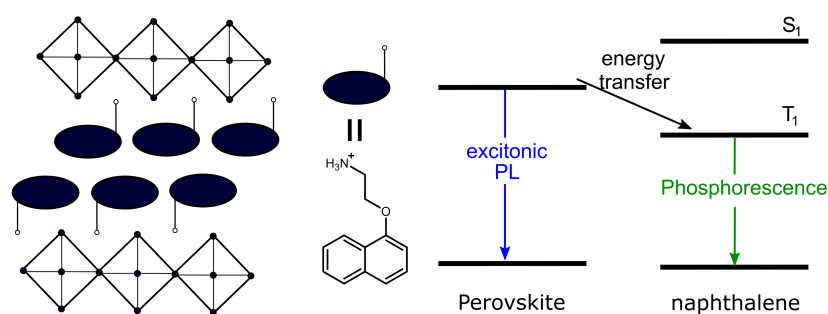


Figure 1.12 – Energy transfer from the inorganic layer to the naphthalene chromophore *via* a triplet injection as reported by Ema *et al.* in ref. 127.

Depending on the relative position of the energy levels, several interesting electronic effects are implied. In the case where the HOMO and LUMO of the spacer cations closely match the VB and CB of the perovskite layer, respectively, the out-of-plane conductivity can be strongly enhanced, as demonstrated in layered perovskites incorporating naphthalene and perylene-based spacer cations by Passarelli and co-workers.^[46] Matching the energy level of the spacer cation is an interesting approach in pure $n = 1$ layered perovskite films to enhance through-film charge carrier transfer, however, improvements in charge carrier transfer is limited to pure layered perovskite systems and can not expand to quasi-layered multiphase films, as the energy levels of the CB and VB strongly change with the size of the quantum well.^[95]

Incorporating electron-accepting or electron-donating spacer cations with low-lying LUMOs or high-lying HOMOs, respectively, forming type II heterostructures allows to control the localization of the electrons and holes upon photoexcitation and can be formed in pure $n = 1$ thin films and poly-dispersed quasi-layered films. Studies on electron and charge transfers were already conducted in the early stage of LHOIP research. Initial studies by Era *et al.* and Ema *et al.* suggest efficient energy transfer between the inorganic layer to the triplet states of a naphthalene-based spacer resulting in strong photoluminescence under cryogenic conditions, as illustrated in Figure 1.12.^[126,127] Since then, energy transfer in tetrazine^[128] and naphthalene-based systems have been intensively studied.^[129–132] Moreover, long-lived phosphorescence at room temperature has been recently reported by Hu *et al.* by reducing non-radiative relaxation of triplet excitons incorporating a mixture of phenylethylammonium and dithiophene ammonium-based spacers making these materials an interesting class of material for the application in light-emitting devices.^[133,134] Further, energy transfer from the inorganic perovskite layer to the organic spacer was studied in quasi-layered thin films recently.^[135] While such triplet injection and long-lived photoluminescence from the organic cation is of potential interest for the application in light-emitting diodes (LEDs), the organic-inorganic donor-acceptor interface might provide a powerful tool to mitigate high exciton binding energies and enhance

1.8. Tuning the Properties by Incorporation of Semiconducting Spacer Cations

charge separation in layered perovskites *via* the formation of long-lived charge-transfer excitons. Indeed, the formation of long-lived charge-separated states has previously been obtained in the group of Dou using thiophene-based spacer cations in lead-iodide LHOIPs.^[136] Additionally, reports on carbazole^[137,138] and thiophene-based^[136,139] cations incorporated into layered perovskites suggest such a hole and electron transfer, respectively.

Given the alternating structure of donor and acceptor domains, the resulting LHOIP structure with incorporated organic semiconducting building blocks can be understood electronically as a nano-heterojunction similarly employed in bulk-heterojunction organic solar cells where nanoscale domains of organic electron donating and accepting domains assist the charge separation, overcoming the strong coulomb interactions between the poorly screened electrons and holes in low dielectric organic materials. The here outlined concept, however, has some critical advantages over pure organic heterostructure systems as the strong ionic interactions and the self-assembling process during the thin film preparation enable to obtain ordered and oriented materials, where the perovskite layers may act as a templating scaffold. Additionally, the inorganic perovskitoid layer provides materials that can be easily modified by compositional engineering, tuning the electronic structure and band-alignment with respect to the HOMO-LUMO energy levels of the organic chromophore layer.

While combining semiconducting organic building blocks with the structure of layered perovskites and spacer cation engineering opens the door to a whole batch of novel, stable, and tunable semiconducting materials for various applications,^[122,140] only few semiconducting spacer cations, mainly based on oligothiophenes,^[139] were reported mainly due to the size constraint and various inter-molecular interactions which can hamper the incorporation of a wide range of spacer cations into a layered perovskite crystalline phase.^[141–144] Researchers mainly turned to perovskite nanoparticles coated with organic semiconducting ligands to study electronic interactions between perovskite and organic chromophores.^[145–147] While electron and hole transfer has been demonstrated in CsPbBr₃ nanoplatelet systems coated with perylene diimide-based ligands, such systems are not truly LHOIP materials and further lack the possibility of investigation by electrode-based characterization methods.^[148]

A novel approach combining dielectric screening and incorporation of semiconducting spacer cations is the formation of organic charge-transfer complexes in the organic layer by co-incorporating donor and acceptor organic molecules.^[149] As the charges are displaced in the organic layer, the electron-hole pair formed in the inorganic layer is better screened, reducing the exciton binding energy. Additionally, such an approach is also suitable to make the organic layer more visible-light absorbing, enhancing the material's absorptivity where the organic charge-transfer complex can potentially inject charges into the inorganic layer.^[150]

1.9 Research Motivation

Given the promising properties of layered perovskite materials in terms of tunability, stability, and potential application in optoelectronic devices, LHOIPs are an exciting class of semiconductors. However, the high exciton binding energy due to quantum and dielectric confinement imposes challenges to applying these materials in optoelectronic devices such as solar cells. While these challenges have been addressed so far mainly by forming quasi-layered perovskite materials, LHOIPs have shown to be highly versatile by functionalizing the spacer cations where dielectric and structural effects can tune the optoelectronic properties of these materials. Combining the rich toolbox of organic chemistry with the facile synthesis of LHOIPs opens the door for a whole batch of new semiconductors. Understanding and rationalizing the effects of the spacer cation on the crystal structure and optoelectronic properties remains crucial for designing new semiconducting LHOIPs.

An interesting subclass of LHOIPs can be formed by incorporating organic semiconducting spacer cations into a layered perovskite structure. Aligning the HOMO and LUMO levels of the organic spacer with the VB and CB of the perovskite layer allows for the mitigation of the effects of the quantum well structure. For example, incorporating electron-accepting or electron-donating organic semiconductors results in the formation of type II heterostructure systems. In such type II heterostructure systems, excitons created upon photoexcitation are not only confined in the inorganic layer but the electrons and holes can be localized in different layers. Forming charge-transfer excitons provide an interesting strategy to enhance charge separation in LHOIPs. Moreover, energy transfer from the inorganic layer to the organic spacer chromophore opens the door to novel strategies for designing novel materials for LEDs.

Although OSiPs show interesting electronic properties, the incorporation of novel bulky semiconducting spacer cations remains rarely reported, and design rules concerning the incomparability of such spacers are scarce. Additionally, when it comes to the photo-physical properties, crucial questions still need to be answered. To date, the nature of potential charge carrier transport in the organic layer — hopping-like transport as in organic semiconductors or band-like transport — remains unknown. Moreover, the light absorption of a spacer cation chromophore assisting the light-harvesting process and generation of free charge carriers in layered perovskites has yet to be reported.

In the following work, we study the synthesis and incorporation of novel semiconducting spacer cations into LHOIPs. Studying various structural parameters of the spacer cations and their effect on the optoelectronic structure, we aim to provide further synthetic guidelines for designing novel spacer cations.

1.10 Thesis Outline

While Chapter 1 gives a broad overview of the state-of-the-art materials and properties of layered perovskite semiconductors, Chapter 2 briefly describes the characterization methods used in this work.

In Chapter 3, the incorporation of monovalent naphthalene diimide-based spacer cations into RP phase structures is explored, and the optoelectronic properties are investigated. Particular attention is given to the effect of the amine-bearing alkyl chain length on the incorporation and crystal growth of the RP phase, and a general synthetic guideline for the incorporation into a layered perovskite material is proposed.

Following these guidelines, we expand the effect on the alkyl chain to DJ-type perovskite materials and first incorporate divalent NDI-based spacer cations in Chapter 4. We shortly underline the advantages of employing a spacer dication over the formation of RP phase perovskites. By increasing the n -number, we investigate the effect of the increased quantum well width size on the electron transfer dynamics and the generation of charge transfer excitons.

Chapter 5 discusses a strategy to enhance the visible light absorbance of the spacer cation and potential challenges concerning the ability to incorporate large aromatic spacers. Moreover, possible electronic interactions between the organic and inorganic layers are investigated in mixed-halide LHOIPs, demonstrating that a visible light-absorbing spacer cation may contribute to the light-harvesting in layered perovskite materials.

Finally, in Chapter 6, current and future work and research questions that remain to be addressed will be presented.

Chapter 2

Characterization Techniques

2.1 Abstract

The interaction of electromagnetic radiation with matter is the fundamental principle of modern characterization techniques. In this chapter, we first introduce the concept of photons, photon energy, and electromagnetic spectra. By briefly elucidating different interactions between photons with matter, starting from high-energy photons and moving toward low-energy electromagnetic waves, we elucidate how these interactions are used to investigate semiconducting materials' structural and electronic properties.

We discuss the structural characterization of solid materials by X-ray diffraction methods and briefly introduce how to obtain orientation parameters from grazing-incidence wide-angle X-ray scattering (GIWAXS) experiments. Moving to visible light, we discuss the possibility of investigating the evolution of electrons and holes over time *via* transient absorption (TA) spectroscopy and photoluminescence (PL) emission spectroscopy. While TA and PL spectroscopy can not distinguish between bound and free electron holes by reducing the photon energy of the probe into the microwave frequency, the evolution of photogenerated free charge carriers and their dynamic can be studied by time-resolved microwave conductivity (TRMC) measurements. The last section discusses the fundamentals of electrode-based characterization methods, namely space-charge-limited current measurements.

The chapter aims to give a broad understanding of the employed methods and a brief guideline for interpreting the results shown in this work.

2.2 Interaction of Matter with Electromagnetic Irradiation for Structural, Optical and Electronic Characterization of Materials

In the previous chapter, the interaction of semiconductors and matter in general with electromagnetic (EM) radiation (photons) has been briefly discussed in the context of the visible light-harvesting process in solar cell devices and photo-detectors. While visible light with wavelengths in the range between 400 and 800 nm makes up a large portion of the solar spectrum and is essential for the light-harvesting in solar cell devices, EM waves with higher or lower photon energies play a crucial role in spectroscopic techniques for the characterization of solid-state matter. Moreover, photons do not have any mass and can, therefore, only be measured by the interaction with matter, where the nature of the interaction with matter depends on the photon energy. A photon is characterized by its energy (E) which is related to the wavelength (λ) or the frequency (ν) of the EM wave by the Planck relation:

$$E = \hbar \nu = \hbar \frac{c}{\lambda} \quad (2.1)$$

where \hbar is the reduced Planck constant, and c is the speed of light in a vacuum. Based on the energy of the photons in the electromagnetic spectrum, the electromagnetic spectrum can be divided into different bands depending on the frequencies or energy of the EM, as displayed in Figure 2.1.

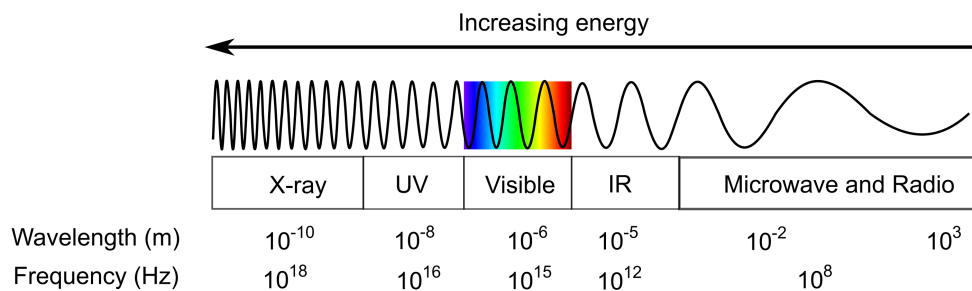


Figure 2.1 – The electromagnetic spectrum from high energy photons to low energy photons.

The division of the electromagnetic spectra is specifically useful in the context of the various interactions of EM waves with matter. The interaction mechanism between matter and EM waves depends on the interaction between the oscillating electric fields of the EM waves with the magnetic and charged particles like electrons in atoms, crystals, or molecules and is dependent

2.2. Interaction of Matter with Electromagnetic Irradiation for Structural, Optical and Electronic Characterization of Materials

on the frequency of the EM wave.^[151] In a simplified manner, two different interactions between EM waves and matter can be distinguished:

- **Absorption:** The EM wave is absorbed by the material causing electronic or structural changes in the material upon irradiation. The energy density of the irradiated EM wave becomes diminished. Measuring the intensity of EM waves after interaction with matter as a function of wavelength is referred to as spectroscopy.
- **Scattering:** The EM wave is completely or partially reflected or diffracted at the material and the energy density of the irradiated EM wave is conserved. In that case, it is referred to as elastic scattering, while scattering events where the energy density of the EM wave is reduced by partial absorption of the material is referred to as inelastic scattering.

High energy photons like X-rays strongly interact with the electron cloud of atoms and molecules, and it is, therefore, intriguing to use the absorption of X-rays to determine the bonding of electrons to materials. On the other hand, low-energy photons cannot interact with the electron in atoms, crystals, or molecules in the same way as X-rays. However, low-energy photons (e.g., EM in the IR region) can induce rotation and vibrations in molecules allowing them to probe vibrational and rotational states with electromagnetic waves in the range of infrared and microwaves.

2.2.1 Structural Characterization of Crystalline Phase by X-ray Diffraction

X-rays are photons with wavelengths ranging from 0.1 Ångstrom (Å) to around 10 nanometers (nm). Classical X-ray sources for structural determination like Cu-K α_1 ($\lambda = 1.54$ Å) have wavelengths that are around the inter-atomic distances in solid crystalline materials in the range of 1.5 and 4 Å.^[152–154] Similarly to visible light that can interfere at a double slit causing positive interference in a projected screen, X-rays interact at the geometric planes in a periodic crystal structure. By incident an X-ray source at an angle Θ , positive interference upon diffraction causes at the angle of reflection as illustrated in Figure 2.2. Based on Figure 2.2, Bragg's law for diffraction angles (Θ), in dependency of the inter-plane distance (d), the wavelength of the incident X-ray (λ) can be deduced:

$$n\lambda = 2d\sin(\Theta) \quad (2.2)$$

where $n = 1, 2, 3 \dots$ is the diffraction order.^[155] As X-rays are scattered at the crystal's electron cloud, the diffraction signal's intensity strongly depends on the atomic form factor of

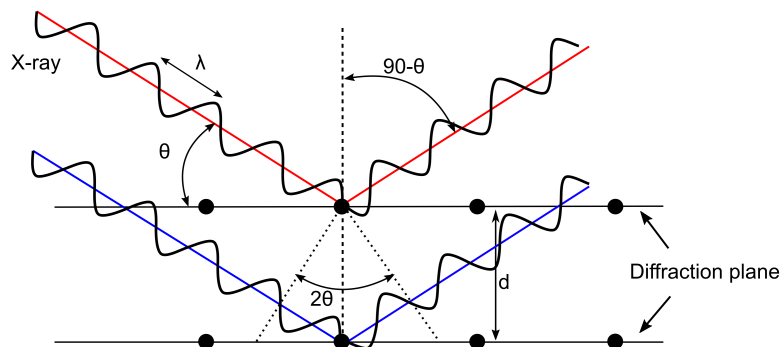


Figure 2.2 – Illustration of the X-ray diffraction principle with respective X-ray incident and reflection angle Θ .

the material.^[154] When probing every plane of a single crystal at different diffraction angles, measuring the diffraction patterns and diffraction intensities provides enough information to model and determine the crystal structure. Therefore, single-crystal XRD measurements are widely used in structural analysis. Moreover, assuming perfect mixing and random orientation of diffraction planes in a powder sample, X-ray diffraction can be extended for structural analysis on samples in powder form.

For crystalline films, however, as only diffraction planes perpendicular to the q_z scatter in XRD experiments, not all diffraction patterns are observable due to the preferential orientation of the crystallites on the substrate along a particular direction. Indeed, in layered perovskite materials, the inorganic slabs are usually oriented parallel to the substrate leading to intense scattering from the planes denoted as $00l$. The predominant presence of one specific scattering plane imposes a limitation to obtaining the exact crystal structure as the relative X-ray diffraction intensities, indispensable for structure determination, are compromised by the non-random orientation of the crystallites. Nonetheless, the shape of the diffraction peak on thin films can give information on the crystallinity of the polycrystalline thin film. Notably, the intensity of the diffraction peak is not a suitable measure for the crystallinity of a material. Estimates of the crystal domain size S along the q_z axis can be derived by the Scherrer equation:^[156]

$$S = \frac{0.9\lambda}{FWHM \cos(\Theta)} \quad (2.3)$$

where $FWHM$ corresponds to the full width at half maximum of a diffraction peak at diffraction angle Θ . The reduction of the domain size of the crystallites is expressed experimentally in a broadening of the diffraction peaks.

2.2.2 Grazing-Incidence Wide-Angle X-Ray Scattering (GIWAXS)

When using X-ray diffractometry in thin films on a reflection experiment (Bragg-Brentano geometry), only diffraction planes along the q_z direction can be detected. In thin films where the polycrystals are highly oriented on the substrate, not all diffraction planes are probed, and scattered X-rays in the off-plane direction (q_x or q_y) are not recorded. In order to assess diffraction planes in q_z direction, 2D-detectors can be employed in grazing-incidence wide-angle X-ray scattering (GIWAXS) experiments, as illustrated in Figure 2.3a. The 2D detector does not only measure along q_z axis but also along q_y resulting in 2D pictures, as displayed in Figure 2.3b-d.

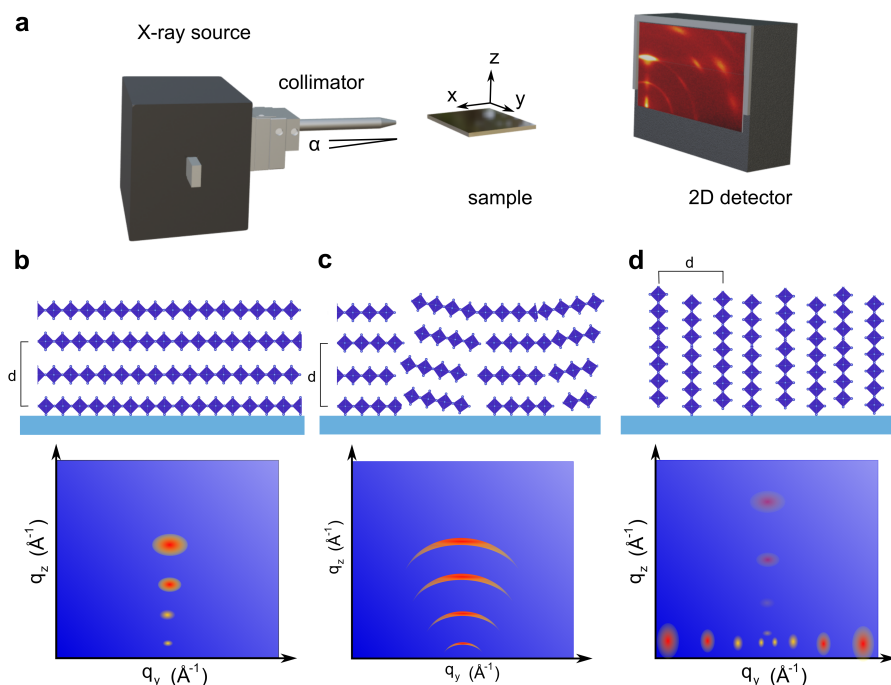


Figure 2.3 – **a)** Experimental setup of grazing-incidence wide-angle X-ray scattering measurements. Resulting GIWAXS image of **b)** perovskite layers oriented parallel to the substrate. **c)** With increasing anisotropy the spots become circular. **d)** GIWAXS image of perovskite layer orientated perpendicular to the substrate.

In contrast to the previously discussed Bragg-Brentano geometry, where the angle of the incident X-ray is the same as the angle of the detector, GIWAXS uses a circular shape X-ray spot on the sample at a low angle of incidence. Wide-angle scattering corresponds to scattering the diffraction on the molecular scale. GIWAXS is widely used to probe stacking in polymer blends. Using X-ray beams at a low angle of incidence has a few advantages. On the one hand, grazing incident techniques reduces the background scattering from the substrate and amplifies

the diffraction signal from thin films, making it interesting to characterize weakly scattering polymer films. Moreover GIWAXS is more surface sensitive and can be used to probe only the top layer of a crystalline thin film. Based on the incident beam wavelength, the critical angle below which total reflection occurs is given by the difference in refraction index (n) between the homogeneous material and the ambient air. Notably, equation 2.4 considers the refractive index of the X-ray photon (instead of the refractive index of the visible light) ^[153]

$$\alpha_c = \lambda \sqrt{\frac{r_e \rho}{\pi}} \quad (2.4)$$

where r_e is the classical electron radius ($2.814 \cdot 10^{-5} \text{Å}$). At incident beam angle below the critical angle ($\alpha_i < \alpha_c$), the incident X-ray beam does not penetrate the material, and a large quantity of X-ray photons are reflected at the interface. The loss of the X-rays due to absorbance can be considered negligible. Assuming the density of MAPbI₃ to be around the critical angle for Cu-K α_1 (1.54 Å) is around $\alpha = 0.3^\circ$. By probing the sample with an angle of incidence slightly above the critical angle α_c , only the top layer of the thin film can be analyzed, making GIWAXS a potent tool to investigate spatial phase distribution and crystal film formation in quasi-layered perovskite materials.

In layered perovskite films where the inorganic layer is perfectly oriented parallel to the substrate cause diffraction spots along q_z axis as displayed in Figure 2.3b. Perfectly un-oriented thin films have a diffraction pattern of circular shape with center at $q_z = q_y = 0$ in the GIWAXS image, while small deviations of perfectly orientation lead to smearing out of the spot into a ring-shaped pattern (Figure 2.3c). In preferential oriented layered perovskite films, the 001 diffraction of the layered perovskite is only visible along the q_y axis (Figure 2.3d).

At first glance, GIWAXS may render XRD data obsolete. However, GIWAXS only measures diffractions of q_x vs. q_z , the Ewald sphere is not probed as it is done in the Bragg-Brentano geometry. This leads to distortions of the expected semi-circles at higher q_x -values. This can be counteracted by transforming the 2D diffraction picture into the q_z vs. q_r presentation where $q_r = \sqrt{q_x^2 + q_y^2}$. This physically more accurate picture, however, leads to a missing wedge at high q_z . In this work, GIWAXS data are complemented by additional Bragg-Brentano XRD measurements.

Quantification of Thin Film Orientation by Herman's Orientation Parameter

Many optical and electronic properties of layered perovskite semiconductors and organic polymers on thin films are anisotropic, and the materials have a distinct preferential orientation. Samples of spin-coated layered perovskites on substrates are preferentially oriented where the layers tend to align along the q_z -vector, and the off-plane normals exhibit a cylindric orientation

2.2. Interaction of Matter with Electromagnetic Irradiation for Structural, Optical and Electronic Characterization of Materials

along that axis. In such a configuration, a phase distribution function can be relatively easily obtained by scanning ϕ at fixed Bragg angles (θ). However, it is desirable to quantify orientation by a single number. The simplest way is to represent the orientation by the average of $\cos^2(\phi)$ where the value is 1, 1/3, or 0 when the crystallites are perfectly in-plane (parallel to q_z), randomly or perpendicular to q_z respectively oriented. More often, the second-order Legendre function of $\cos\phi$ is used as proposed by Herman and Platzek,^[157] where the Herman orientation factor is determined by:

$$H = \frac{3 \langle \cos^2(\phi) \rangle - 1}{2} \quad (2.5)$$

The values 1, 0, or -0.5 corresponds to re perfectly in-plane (parallel to q_z), randomly or perpendicular to q_z , respectively.^[154]

2.2.3 Visible light Absorption and Emission Spectroscopy

While X-rays can interact with the electron clouds in the atoms by scattering, the photon energy of X-rays is above the ionization energy of most atoms and can also interact with a single electron by knocking it completely out of the atom. While X-rays are far too energetic to cause electronic transition between states, as briefly discussed in Chapter 1, photons in the range of ultraviolet (UV) and visible light can be absorbed by molecules or semiconductors by dipole oscillation of the same frequency resulting in vibronic transitions from a ground state into an electronic excited state, as shown in Figure 2.4. The fate of the excited states after a vibronic transition depends on the structure of the material. In general, these processes can be divided into radia-

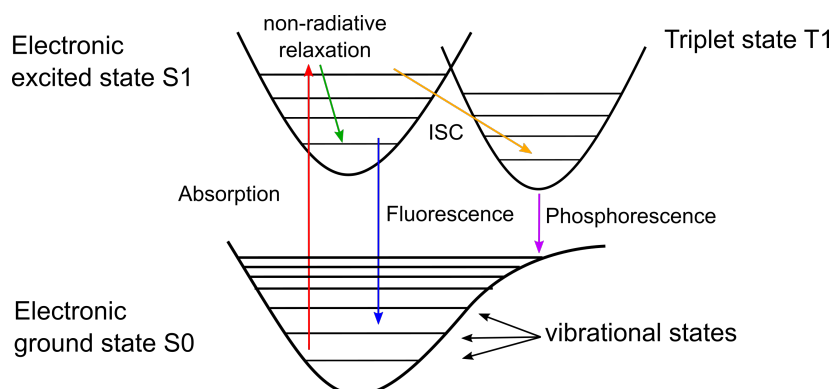


Figure 2.4 – Jablonski diagram of different electronic process upon absorption. ISC denotes the intersystem crossing process populating an excited triplet state causing long-lived phosphorescence due to spin-flip. Shorter-lived Fluorescence is due to S_1 to S_0 transitions.

tive and non-radiative processes. On a short time scale, non-radiative vibrational relaxation to a vibrational state with lower energy happens. Alternatively, the S_1 state can undergo a transition to a triplet state T_1 *via* non-radiative intersystem crossing. The excess energy in the higher vibrational states of the electronically excited states will be released to the neighboring molecules *via* non-radiative vibrational relaxation. Relaxation from the S_1 or T_1 to the electronic ground state S_0 *via* radiative relaxation leads to photoluminescence by fluorescence or phosphorescence, respectively. Time-dependent photoluminescence measurements allow us to obtain the lifetime and electronic nature of the excited state. As the radiative relaxation *via* phosphorescence involves a spin-flip, photoluminescence arising from phosphorescence is long-lived compared to the emission by fluorescence.

While phosphorescence only considers radiative transitions, a more powerful tool to investigate different electronic transfer and charge transfer processes is transient absorption spectroscopy based on a pulsed-probe setup.^[158] By exciting the sample with a femtosecond pulsed laser, the ground state is excited, leading to the formation of an excited state ($t = 0$ in Figure 2.5). The herein-described system is reported elsewhere and uses a pulsed 150 fs pump laser.^[159,160] A weak probe pulse with a delay time τ with respect to the pump pulse is sent through the sample, and at each delay time τ an absorption spectrum is determined.

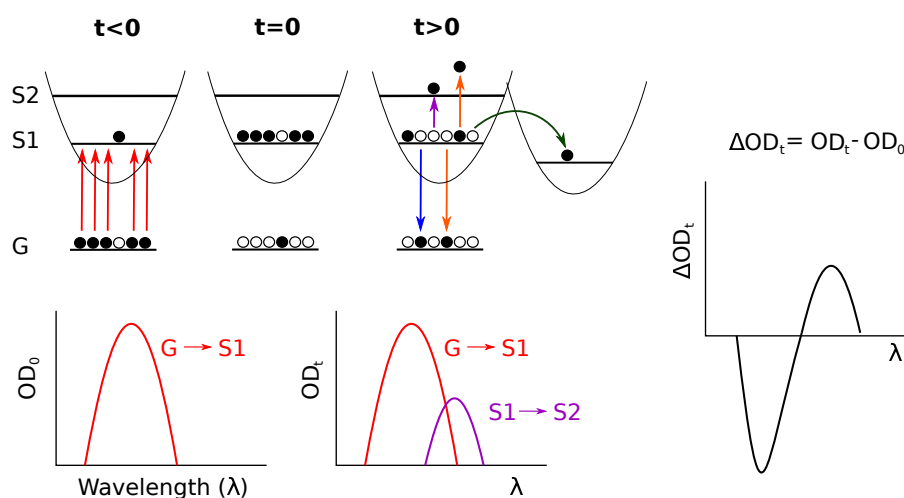


Figure 2.5 – Systematic presentation of transient absorption measurements including possible photo-physical process resulting in observable TA features. Figure was adapted from ref. 161.

The TA spectrum is usually reported as a differential spectra ($\Delta A(\tau, \lambda)$ spectrum) between the absorption spectrum of the excited sample at delay time τ and the absorption spectrum of the ground state, allowing to obtain information about various electronic processes. In general, three different contributions to the resulting ΔA spectra can be obtained:^[161]

- The excitation of the ground state by the pump leads to a reduction of electrons in the

2.2. Interaction of Matter with Electromagnetic Irradiation for Structural, Optical and Electronic Characterization of Materials

ground state. When the probe measures the absorbance, fewer electrons can be excited, leading to a negative signal in the ΔA spectrum known as the ground state bleach (GSB). In layered perovskite materials, the GSB overlaps with the position of the excitonic absorption band. After the initial pump, the GSB starts to regenerate mainly due to exciton recombination allowing the assessment of the GSB dynamics to obtain information about electron transfer and recombination processes. While in layered perovskites ($n = 1$), the GSB minimum is reached right after pump excitation ($t = 0$), in poly-dispersed quasi-layered perovskite thin films, an increase in the GSB after pump excitation ($t > 0$) can be observed which is attributed to electron funneling processes.

- While after the pump the ground state is regenerated by the recombination of the excitons, further excitation of the excited state to a higher excited state leads to a positive TA feature.
- Charge-transfer states and the formation of new optical active species in heterostructure systems can result in new positive features. Recent reports on CsPbBr₃ nanoparticles coated with PDI-based results in weak positive features arising from the PDI⁻.^[148] Moreover, the selective excitation of the PDI and subsequent injection of the holes into the nanoparticle results in a GSB from the perovskite growing over a time of a few picoseconds.

2.2.4 Sheet Conductivity *via* Time-Resolved Microwave Conductivity Measurement

Charge carriers generated by photoexcitation can be probed in a contactless manner using time-resolved microwave conductivity based on the absorbance of microwaves by free charge carriers. The experimental setup of TRMC is illustrated in Figure 2.6. The charge carriers are accelerated in-plane direction in an electric field by a standing microwave in a cavity resulting in partial absorption of the microwave power.

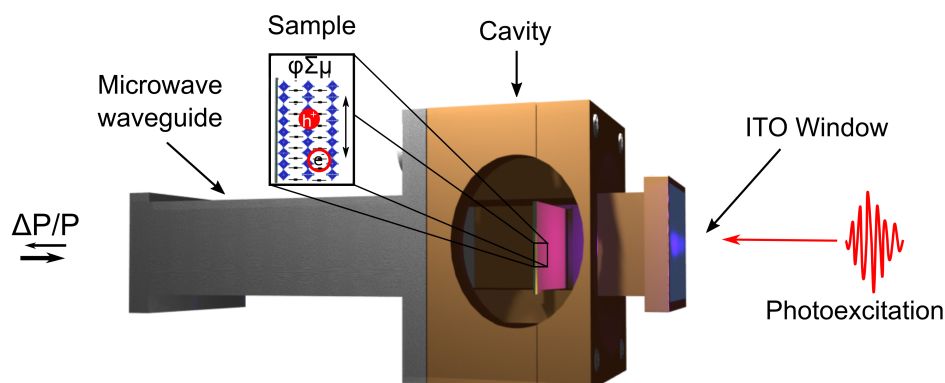


Figure 2.6 – Time-resolved microwave conductivity setup and microwave cavity.

The absorbed microwave power is proportional to the photoconductivity and ΔG expressed by:

$$\Delta G = \Delta \sigma_s \frac{a}{b} = -\frac{1}{K} \frac{\Delta P}{P} \quad (2.6)$$

where K is a sensitivity factor given by the experimental setup. The advantage of calculating the sensitivity factor is its relatively fixed value independent of the sample properties. K can be determined *via* a semi-analytical method elaborated in more detail elsewhere.^[162,163] Based on absorbed photons, the yield of free charges and their mobility $\sum \mu = \mu_e + \mu_h$ can be calculated from ΔG_{max} :

$$\phi \sum \mu = \frac{\Delta G_{max}}{I_0 q \beta F_a} \quad (2.7)$$

where I_0 is the unit of photons per unit area, q is the elementary charge, F_a is the fraction of light absorbed by the sample at the measurement wavelength. The coefficient β is based on the ratio of the inner dimension of the microwave cavity. The contact-free method and the probing of the photoconductivity in the in-plane direction make TRMC an interesting method to investigate layered perovskite materials, which are usually hard to probe by more conventional electrode-based measurements due to their anisotropic charge carrier properties.

In contrast to transient absorption measurements, where bound and free electrons and holes are detected, and PL measurements, where the radiative recombination from an exciton is observed, TRMC measurements are only sensitive to free charge carriers (electron and holes). The quality-factor Q of the microwave cavity thereby limits the time resolution of the measurement to around 10 ns. The study of shorter-lived charge carriers can be complemented by terahertz spectroscopy. Combining OPOT and TRMC measurements, therefore, allows to investigate free charge carrier mobilities over a range of several orders of magnitude.^[162,164]

2.3 Electronic Characterization *via* Space-Charge-Limited Current

While the spectroscopic methods can give hints about charge carrier properties under light illumination on a ultrafast timescale, the characterization of semiconducting materials with electrode-based methods remains essential, especially in view of the potential application of novel materials in electrode-based devices. If we consider a semiconductor with a given band gap, free charge carriers due to thermal excitation are close to randomly distributed in a homo-

2.3. Electronic Characterization *via* Space-Charge-Limited Current

geneous bulk material. However, at the boundary of the semiconductor, such as at electrode contacts, as the charge carrier density is not the same as in the contact and semiconductor charge carriers diffuse out into the contact. ^[165]

- **Diffusion:** Diffusion current occurs when charge carriers concentrations are unevenly distributed through the semiconductor by uneven doping or charge injection. Charge carriers diffuse from regions of high concentration to regions of low charge carrier concentration.

The inhomogeneity of charge distribution leads to the formation of an electric field which is denoted as a space-charge region. At the interface, the diffusion of charge carriers to the contact is counteracted by the drift current induced by the space-charge region's electric field. ^[165]

- **Drift:** Drift current appears due to an applied electric field. While holes move in the direction of the electric field, electrons move against the direction of an applied electric field.

The diffusion of the charge carriers at the interface is one of the main differences when compared with other electrode-free characterization methods such as TRMC.

The injecting single type charge carriers into the material, as well as drift and diffusion currents has to be considered which can be described by the charge equation:

$$j_n = e\mu_n nF + \mu_n kT \frac{dn}{dx} \quad (2.8)$$

where e is the fundamental charge, n is the electron density, μ is the mobility of the charge carrier, and $F(x)$ is the electric field in the semiconductor at position x . In the low voltage regime, the current density measured for single charge carrier type (electrons or holes) follows Ohm's law, and the number of thermally generated free charge carriers concentrations in the bulk is larger than the injected charge density. However, at a sufficient large bias, the charge carrier injection becomes dominant, and the charge carriers behave like electrons in a vacuum tube and is only limited by the space-charge at the injecting electrode. This current is denoted as space-charge-limited current. ^[166] In the space-charge-limited region, the current density is described by the drift current alone in good approximation:

$$j_n = e\mu n(x)F(x) \quad (2.9)$$

Replacing this expression by the Poisson equation and subsequent simplification following expression for the I - V characteristics at high voltage can be obtained.

$$J_n = \frac{9}{8} \mu \epsilon \epsilon_0 \frac{V^2}{L^3} \quad (2.10)$$

where ϵ_0 is the vacuum permittivity, ϵ is the relative permittivity of the material, V is the applied voltage, and L is the distance between the two electrodes.

In an experimental setup, space-charge-limited current can be measured by sandwiching the semiconducting material between two charge-selective electrodes to obtain electron or hole-only devices as illustrated in Figure 2.7a. By increasing the applied voltage at a steady scan rate, at low bias current, an ohmic behavior is indicated by a linear region where $I \propto V$, resulting in a linear regime with slope = 1 in a log-log plot. At high voltage, the current density is dominated by the Mott-Gurney law and $I \propto V^2$ resulting in a linear regime with slope = 2 in a log-log presentation, as illustrated in Figure 2.7b.

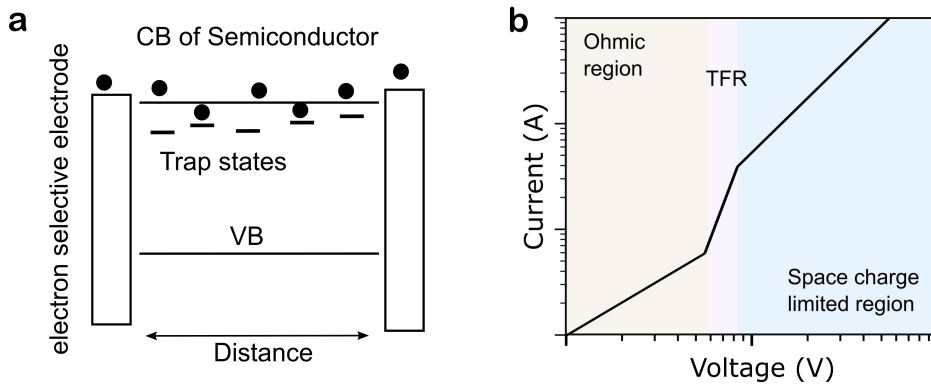


Figure 2.7 – **a)** Illustration of charge carrier transport through the semiconductor sandwiched between two electron-selective contacts. **b)** Current-Voltage log-log curve showing the ohmic region, trap filling region (TFR) and region dominated by space-charge-limited current.

In the presence of any traps which are $k_B T$ eV below the Fermi-level, injected charge carriers can be trapped, reducing the measured current during space-charge limited current measurements. The filling of the trap states can result in an trap-filling region (TRP) between the ohmic and SCLC regime with $I \propto V^m$ where $m > 3$.

2.3. Electronic Characterization *via* Space-Charge-Limited Current

Chapter 3

Tuning Naphthalene Diimide Spacer Cations for the Incorporation into a Layered RP Phase Perovskite Structure

3.1 Abstract

The large size of chromophore-based spacer cations imposes a challenge to their incorporation into a layered perovskite structure. Further insight into the layered perovskite phase-formation mechanism is required to determine crucial parameters for successful LHOIP formation. Herein we report the preparation and incorporation of asymmetric naphthalene diimide (NDI) spacer chromophore cations with different amine-bearing alkyl linker chain lengths into LHOIP thin film. Performing kinetic studies based on *in-situ* UV-Vis spectroscopy measurements during the LHOIP crystallization formation, we show that shorter linker chain lengths require higher annealing temperatures to form the LHOIP structure suggesting higher formation energy required for the incorporation of short alkyl chain bearing NDI cations. Further, it is shown that the increased formation energy hampers the formation of quasi-layered perovskite films with homogeneous phase distribution. Avrami-analysis of the layered perovskite formation shows a larger Avrami-coefficient ($n = 3.64$) for short linker chain-bearing cations compared to longer alkyl chain-bearing cations ($n = 2.43$), suggesting an evolution from three-dimensional to quasi-two-dimensional crystal growth mechanism with increasing linker chain length. Additionally, transient absorption and broadband fluorescent up-conversion spectroscopy indicate fast photoinduced charge transfer from the inorganic layer to the electron-accepting NDI-spacer cation. The presence of a type II heterostructure system has implications for the formation of free charge carriers and their mobilities. As electrons and holes are localized in different layers, the lifetime of the free charge carriers is enhanced by more than one order of magnitude, as indicated by time-resolved microwave conductivity measurements.

This chapter is based on published work: S. Nussbaum, E. Socie, L. Yao, J. Yum, J. Moser, and K. Sivula Chem. Mater. **2022**, 34, 3798–3805.

The herein presented transient absorption and broadband fluorescent emission spectra were recorded and fit by E. Socie. The synthesis of the spacer cations was assisted by L. Yao.

3.2 Introduction

LHOIPs are in the spotlight of researchers due to their widely tunable optoelectronic properties, facile solution processability, and increased stability over more conventional HOIPs. These features make LHOIP an attractive class of materials for low-cost and high-performance applications.^[49,68,167,168] In most cases, relatively simple spacer cations are employed, such as *n*-butylammonium (BA) or phenylethylammonium (PEA) with large HOMO-LUMO gaps that mismatch the inorganic perovskite's CB and VB energy levels. As these organic spacers are electrically isolating, LHOIPs have some decisive disadvantages over pure ABX₃ materials, such as anisotropic charge carrier properties and extremely high exciton binding energies of several hundred meV.^[78] More recently, researchers have focused on the incorporation of spacer cations based on semiconducting organic building blocks. As the HOMO-LUMO energy levels of the chromophore spacer cations match with the CB and VB of the inorganic layered perovskite, the semiconducting properties of the spacer cations can alter the electronic structure of the layered perovskite materials. This approach provides a possibility to overcome some of the disadvantages described above. Passarelli and co-workers, for example, showed enhanced out-of-plane conductivity when the HOMO and LUMO levels of the spacer cation chromophore are matched electronically with the CB and VB energy levels of the inorganic layer.^[46] By using electron-accepting spacer cations, type II heterostructures can be formed where the HOMO and LUMO energy levels of the chromophore are below the CB and VB of the perovskite, respectively, as displayed in Figure 3.1a. Such type II heterostructures were found to induce electron transfer to the spacer cation allowing to obtain long-lived charge-separated states.^[136,169] Despite the recent report about carbazole,^[100] naphthalene,^[131] and oligothiophenes^[139,170] based spacer cations incorporated into a layered perovskite structure, organic semiconducting spacer cations remain far less reported than systems based on simple aliphatic spacers.

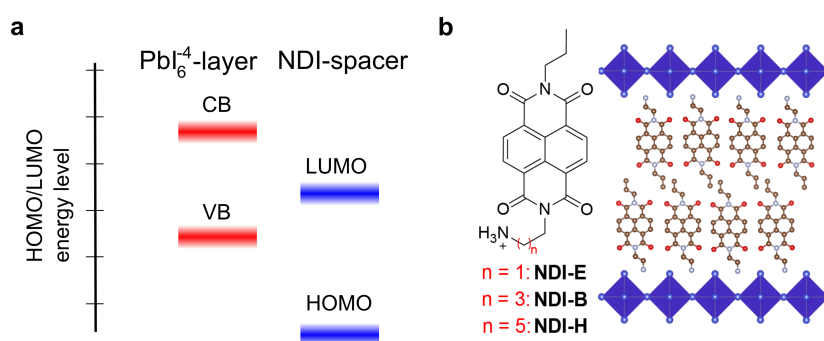


Figure 3.1 – **a)** Band alignment of the type II heterostructure structure indicated based on computational studies from ref. 171. **b)** Schematic description of the layered perovskite structure and chemical structure of the investigated NDI-based spacer cations.

A potentially interesting class of chromophore spacer cations is constituted by the rylene dyes, such as naphthalene diimide, illustrated in Figure 3.1b. Recent computational studies based on NDI-based chromophore dications suggest type II heterostructure features, where the electron-accepting chromophore contributes to the band structure of the perovskite layer resulting in the localization of the electrons in the organic layer while the holes remain in the inorganic slabs upon photoexcitation.^[171] Such a structure has been hypothesized to reduce the exciton binding energy by forming long-lived charge-separated states, as suggested by Gélvez-Rueda *et al.* based on their studies on perylene diimide coated CsPbBr₃ nanoparticles.^[148] However, the incorporation of rylene dye building block into a layered lead halide perovskite structure remains challenging potentially due to the various inter-molecular effects like van-der-Waals and $\pi - \pi$ -interactions that can interfere during the layered perovskite self-assembling synthesis and the size constraints of the cavity in the octahedral framework. Indeed, symmetric naphthalene diimide spacer dications with an amine-bearing ethyl linker (NDIC2) were investigated for the incorporation in a layered lead halide perovskite framework, but no layered perovskite structure but rather a 1D perovskitoid structure was obtained.^[172,173] While transient absorption and time-resolved microwave conductivity measurements suggest the formation of charge-separated states with enhanced free charge carrier lifetimes in such nanowires,^[148,174] forming an ordered layered structure is a prerequisite for the application in optoelectronic devices, such as solar cells to enable efficient charge transport through the layered perovskite film. Previous research conducted in our group showed that chromophore-cations with long amine-bearing linker chains were easier incorporated into a layered perovskite structure.^[175]

While the effect amine-bearing linker chain on the optoelectronic and structural properties has been studied in LHOIPs incorporating purely aliphatic and phenyl-based spacer cations^[176] the effect of the amine-bearing linker length remains to be systematically studied in OSiP materials. Understanding the kinetics governing the formation of layered perovskite materials incorporating large organic semiconducting chromophore spacer cations and investigating the effect of the linker chain length and its increase of molecular size on the crystal structure formation is a requirement to understand the determining parameters for the successful synthesis of these materials.

We hypothesized that by increasing the amine-bearing linker chain, the crystal growth mechanism would be potentially altered where with increasing spacer size, the formation of a 1D perovskitoid rather than a 2D layered perovskite phase is formed. In this work, we synthesized 3 NDI-based monovalent spacer cations, which differ only in the length of the amine-bearing alkyl chain, and investigated the formation of the layered RP phase. A schematic illustration of the desired RP structure and the chemical structure of the investigated cations are displayed in Figure 3.1b.

3.3 Experimental

Characterization and detailed synthetic procedures can be found in Appendix A.

Sample Preparation

Thin films of $(\text{NDI})_2\text{PbI}_4$ were formed using a 0.4 M NDI + 0.2 M PbI_2 in DMF solution. All films were spin-coated at 2500 rpm for 30 seconds and subsequently annealed at 180 °C for 30 minutes in an argon-filled glovebox.

Quasi-layered perovskite thin films were prepared by spin-coating a precursor solution of NDI, methylammonium iodide (MAI), and PbI_2 with molar ratios 2:4:5 (0.8 M PbI_2) in DMF on a glass substrate. The films were subsequently annealed at 180 °C for 10 minutes.

UV-vis Absorption and Photoluminescence Measurements

UV-Visible light absorption measurements were carried out with a UV-3600 Shimadzu spectrometer. For the Avrami-analysis, a home-built transparent heating window was used. The measurement was carried out under ambient conditions. The as-spin-coated samples were stored in an argon-filled glovebox until shortly before the measurement.

X-ray Diffraction and Grazing-Incidence Wide-Angle X-ray Scattering Measurements

Thin film X-ray diffraction (XRD) measurements were taken in Bragg-Brentano geometry using non-monochromatic $\text{Cu-K}\alpha_1$ radiation on a Bruker D8 Vario instrument equipped with a LynxEYE XE detector. Grazing-incidence wide-angle X-ray scattering experiments were carried out at the European Synchrotron Radiation Facility (in Grenoble, France) at beamline BM01. The samples were measured under ambient conditions with a 0.6506 Å (19.06 keV) X-ray source and a beam size of $0.5 \times 0.5 \text{ mm}^2$ onto the sample coming in at an incidence angle of $\alpha = 0.25^\circ$. GIWAXS images were processed using the Python packages pygix and pyFAI. ^[177,178]

Broadband Fluorescent Up-conversion Spectroscopy

Time-resolved PL measurements were carried out using a broadband up-conversion setup (FLUPS, LIOP-TEC). An extensive description of the setup can be found elsewhere. ^[179,180] Basically, after excitation by a pump pulse ($\lambda_{\text{pump}} = 400 \text{ nm}$) generated by a CPA Ti:sapphire laser (Libra-HE USP, Coherent), the fluorescence of the sample is collected and mixed with a gate pulse ($\lambda_{\text{probe}} = 1300 \text{ nm}$, type II sum frequency generation) in a 100 μm -thick BBO crystal (EKSMA Optics). The upconverted signal is dispersed in wavelength using UV gratings and recorded by a CCD camera (Newton 920, Andor). The time correction for the impulse response function (IRF) was calculated to be 240 fs using the cross-correlation between the un-absorbed pump and the probe.

Transient Absorption Spectroscopy

Ultrafast transient absorption (TA) measurements were conducted using a fs chirped-pulse amplified (CPA) Ti:sapphire laser (Clark-MXR, CPA-2001). A part of the laser output (778 nm, 1 kHz repetition rate) was frequency-doubled in a 0.5 mm-thick BBO crystal and chopped to generate the pump pulse ($\lambda_{pump} = 389$ nm, 500 Hz). The remaining part of the laser output was focused onto a CaF₂ crystal to produce a white-light continuum probe spanning from 400 to 780 nm. The white light is attenuated, and its beam cross-section is reduced to ensure homogeneity within the probe area. The probe beam was split before the sample; the signal and the reference were sent into two spectrographs (Spectra Pro 2150i, Princeton Instruments) and detected shot-to-shot using CCD cameras (Hamamatsu S07030-0906). The dynamics were obtained using a digitally controlled delay stage (PI) in the pump path. The time resolution of the experiment was calculated to be 300 fs using the cross-correlation of the pump and probe beam on a reference glass sample. Detailed information of the data-treatment on the FLUPS and TA results can be found in Appendix A.

Microwave Conductivity Measurements

TRMC measurements were performed by mounting the samples in a microwave cavity cell and placed in a setup similar to the one described elsewhere.^[162,181,182] A voltage-controlled oscillator (SiversIMA VO3262X) generated the microwaves (X-band region, 8.4-8.7 GHz). During the measurements, a change in the microwave power ($\frac{\Delta P}{P}$) reflected by the cavity upon sample excitation by 3 ns (full-width at half-maximum) pulses of a wavelength tunable optical parametric oscillator (OPO) coupled to a diode-pumped Q-switched Nd:YAG laser at a wavelength of 420 nm (50 Hz repetition rate) was monitored and correlated to the photoinduced change in the conductance of the sample, ΔG , given by eqn 2.6 and where K is the sensitivity factor derived from the frequency response of the resonant cavity using an analytical impedance model that considered both the cavity geometry and the substrate and thin film properties. The peak sum mobilities were obtained using eqn. 2.7.

3.4 Results and Discussion

NDI-based cations were synthesized in a straightforward one-pot reaction. Detailed synthetic procedures can be found in Figure A.1. The cations are labeled NDI-E, NDI-B, and NDI-H based on their corresponding amine-bearing alkyl linker lengths (ethyl, butyl, and hexyl), as displayed in Figure 3.1b. Asymmetric monocations were selected over symmetric dications due to the enhanced structural flexibility of the RP phase compared to the DJ phase perovskites, potentially easing the formation of a layered perovskite structure.^[47] We start the discussion with the NDI-E spacer cation. Precursor solutions were prepared by dissolving NDI-E cation and PbI_2 in a 2:1 molar ratio in *N,N*-dimethylformamide (DMF). The precursor solution was then spin-coated on a glass substrate, schematically illustrated in Figure 3.2a. The visible light absorption spectrum of the as-spin-coated thin film displayed in Figure 3.2b shows strong absorbance of the NDI chromophore at 400 nm and weak contribution of PbI_2 in the range between 440 and 500 nm. While the presented optical features in the as-spin-coated films do not imply the formation of a layered perovskite thin film, subsequent thermal annealing at 180 °C results in a phase with an absorption band at around 500 nm, as displayed in Figure 3.2c.

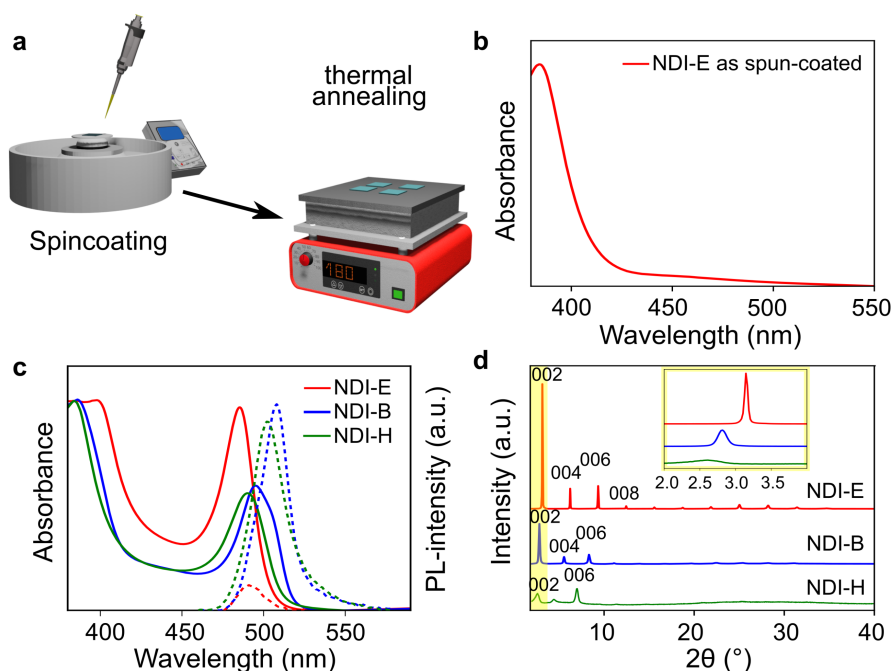


Figure 3.2 – **a)** Synthetic procedure for the thin film fabrication. The spin-coating of the precursor solution containing NDI-E and PbI_2 (2:1 molar ratio) results in a film with the absorption spectrum displayed in **b)**. The visible-light absorbance of the thin films after annealing **c)** and XRD **d)** show characteristic features for RP LHOIP.

The same procedure as described above with NDI-B and NDI-H cations results in the formation of smooth thin films with similarly shaped excitonic absorption bands at around 500 nm, comparable with the excitonic absorption band observed in (PEA)₂PbI₄ and (BA)₂PbI₄.^[183] In addition, photoluminescence (PL) emission with a small Stokes shift can be observed for all investigated films. The optical features observed in the NDI-based films are attributed to the formation of a quantum-confined structure, suggesting the formation of a layered perovskite phase. The formation of crystalline layered perovskite films is further indicated by the X-ray diffraction (XRD) patterns of the different films, displayed in Figure 3.2d. The XRD shows the characteristic equally-spaced diffraction peaks originating from the diffraction at the $[00l]$ -plane. While intense and narrow diffraction peaks for (NDI-E)₂PbI₄ suggest large and ordered domains, the domain size becomes smaller with increasing linker chain length, as indicated by the reduced intensity and broadening of the diffraction peaks highlighted in the inset of Figure 3.2d. Interplanar spacings (d_{00l}) in the range between 2.3 to 3.0 nm were found where d_{00l} becomes larger with increasing linker length following the trend of previously reported spacer cation systems.^[126]

We found that the annealing temperature was a crucial parameter for observing such an excitonic absorption band (*vide infra*). For all NDI-based layered perovskite films, an annealing temperature of at least 140 °C was required to form a crystalline phase. In comparison, *n*-butylammonium (BA) and phenylethylammonium (PEA) based LHOIPs are typically reported to form at annealing temperatures of only 100 °C. As-spin-coated films without any subsequent thermal annealing give amorphous films without any excitonic absorption band at around 500 nm (Figure A.2).

Notably, the absorption and emission band maxima (λ_{max}^{abs} and λ_{max}^{PL}) were blue-shifted compared to similarly-prepared (PEA)₂PbI₄ films (516 nm and 524 nm for λ_{max}^{abs} and λ_{max}^{PL} , respectively).^[183] The observed blue shift of the excitonic absorption band is reasonably due, in part, to the increased interplanar distance of the NDI-based layered perovskite compared to the smaller interplanar spacing of (PEA)₂PbI₄, which reduces the interaction between adjacent perovskite layers. However, the excitonic absorption band does not correlate with the interplanar spacing as the observed absorption band maxima position λ_{max}^{abs} for (NDI-H)₂PbI₄ (492 nm) is between the observed λ_{max}^{abs} of the (NDI-E)₂PbI₄ (485 nm) and (NDI-B)₂PbI₄ (498 nm) thin films. As distortions of the PbI₆⁴⁻ octahedra can also alter the absorption band position,^[47,106] different Pb-I-Pb bond angles in the investigated thin films could reasonably explain the observed differences in the absorption band positions. Unfortunately, obtaining single crystals to verify this was not possible despite significant efforts.

Surprisingly, the PL of (NDI-E)₂PbI₄ is strongly quenched compared to NDI-B and NDI-H-based films despite exhibiting the highest crystallinity among the investigated films. Given the electron-accepting properties of the NDI-chromophore core, which exhibits low-lying HOMO

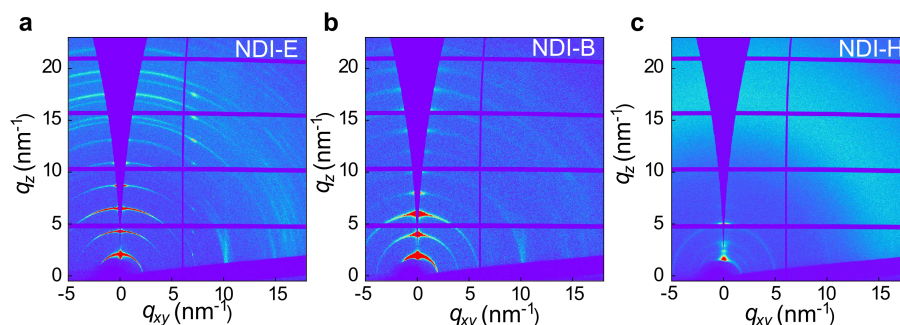


Figure 3.3 – Grazing-incidence wide-angle X-ray scattering for the (NDI-E)₂PbI₄ **a**), (NDI-b)₂PbI₄ **b**), and (NDI-H)₂PbI₄ **c**) thin film.

and LUMO energy levels as determined by cyclic voltammetry (Figure A.3 and Table A.1) and the optical band gap, the NDI-spacer cations form a type II band structure with the inorganic where the LUMO energy level of the NDI-chromophore core is located between the VB and CB of the inorganic PbI₆⁴⁻ octahedral layers.^[123] The substantial quenching of PL-intensity is consistent with previously-reported systems exhibiting a type II band alignment.^[123] The proximity of the NDI-E cation and the high crystallinity found in (NDI-E)₂PbI₄ perovskites may enhance charge transfer from the inorganic layer to the organic layer, as previously suggested and will be further discussed below.^[171]

Additional insights into the thin film formation of the NDI-based LHOIPs were obtained by GIWAXS, as displayed in Figure 3.3a-c. Highly in-plane oriented films where the inorganic slabs lay parallel to the substrate were obtained with all NDI-based cations, as indicated by the signals along the q_z -axis. Due to the high crystallinity in the (NDI-E)₂PbI₄, additional diffraction in the off-axis direction attributed to the $[11l]$ -planes can be observed. Herman's orientation parameters were found to be 0.73, 0.62, and 0.41 for (NDI-E)₂PbI₄, (NDI-B)₂PbI₄, and (NDI-H)₂PbI₄, respectively, suggesting a decline in crystal orientation with increasing linker chain length, as further shown in the azimuthal angle scans in Figure A.4. Herman's orientation parameters of 1 indicate near-perfect in-plane orientation, while a value of 0 indicates random oriented distribution. Our findings are consistent with previous work, where organic cations with shorter amine-bearing alkyl chains were found to form more favorably highly oriented perovskites.^[112]

Crystal Growth Mechanism

As the crystallinity and domain orientation are often attributed to the crystallization kinetics during the crystal phase formation,^[184,185] based on our observed trends in crystallinity and orientation, we hypothesized that the alkyl chain length affects the LHOIP phase formation rate during the thermal annealing process. Relatively rapid crystal phase formation, for ex-

ample, may result in increased randomness of crystallite orientation compared to kinetically slower crystallization. Additionally, as we previously suggested that the different linker lengths could induce changes in the Pb-I-Pb angles, it is reasonable to assume that deviations of the octahedral framework would impact the crystalline phase formation kinetics.^[186] While the phase formation mechanisms are relatively well studied for lead-based perovskite films and some quasi-layered perovskite films,^[187–189] a proper understanding of the linker length on the crystallization of pure layered perovskite remains scarce. Previous phase formation studies were conducted using mainly X-ray diffraction methods which are potentially less suitable for comparing thin films with varying degrees of crystallinity and orientation.^[187,189] For our system, tracking *in-situ* the evolution of the excitonic absorption band using UV-vis absorption spectroscopy, as illustrated in Figure 3.4a, was found to be a convenient way to investigate the formation of the crystalline perovskite quantum well structure during the thermal annealing process.^[190] For this, the as-spin-coated films were placed on a heated transparent FTO-coated glass window. Detailed descriptions of the setup and measurement can be found in Figure A.5. To find the crucial annealing temperature at which the layered perovskite quantum well starts to form, the absorbance at 485 nm ((NDI-E)₂PbI₄), 498 nm ((NDI-B)₂PbI₄) and 492 nm ((NDI-H)₂PbI₄), respectively, were measured while gradually increasing the temperature at a rate of 0.25 Ks⁻¹. The conversion coefficient, α , was determined by the following relationship:

$$\alpha = \frac{A(T) - A_{init}}{A_{fin}} \quad (3.1)$$

where $A(T)$ is the (quasi-steady-state) absorbance at a given temperature T , A_{init} and A_{fin} are the absorbance at the beginning and end of the measurement, assuming full phase conversion at the end of the annealing process.

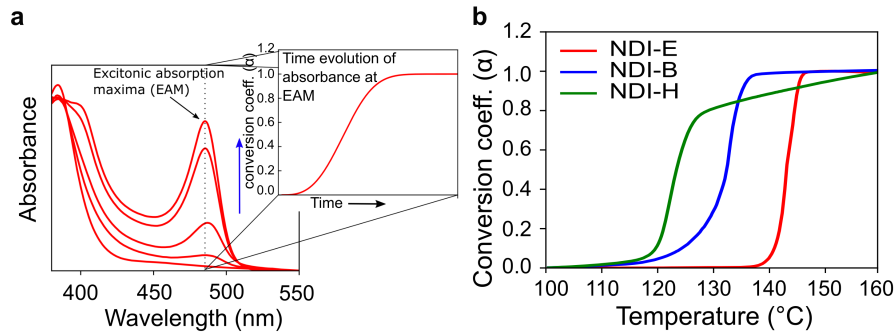


Figure 3.4 – **a)** Representative illustration of the *in-situ* absorption spectroscopy measurements to track the evolution of the thin film formation. **b)** Resulting curve when the temperature is gradually increased at a rate of 0.25 Ks⁻¹.

It is noted that the conversion coefficients were most likely independent of the wavelength around the excitonic absorption band (see Figure A.6), and no clear diffraction peaks were observed from the as-spin-coated films, as displayed in Figure A.2. The resulting phase formation curves are displayed in Figure 3.4b. For all investigated films, an increase in the annealing temperature triggers the formation of the perovskite phase, as indicated by the increasing conversion coefficient α . At temperatures greater than 160 °C, the plateau of the curves indicates maximum perovskite phase formation at that temperature. Considering the on-set temperature at which the excitonic absorbance band becomes optically detectable, a clear trend towards lower temperatures with increasing linker chain length can be observed.

Generally, the crystal growth mechanism consists of an initial nucleation step followed by interfacial crystal growth, the formation rate between 110 and 120 °C as found in (NDI-B)₂PbI₄ and more so in (NDI-H)₂PbI₄ can be potentially attributed to the formation of nuclei. After nuclei formation, the crystallites slowly start to grow, while at the same time, more and more nuclei are formed with increasing temperature. As the crystallites grow larger, neighboring crystallites start to impede each other resulting in low crystalline thin films. The observed slow phase formation at low temperatures for (NDI-H)₂PbI₄ and (NDI-B)₂PbI₄ stands in contrast to the phase formation observed for (NDI-E)₂PbI₄ films where the LHOIP phase starts to be formed rapidly after the temperature of 140 °C. We suggest that the reduced structural flexibility of the short alkyl chain-bearing NDI-E-cation hampers the formation of nuclei, as indicated by the higher annealing temperature required for the perovskite formation. As fewer growing sites do impede each other less, resulting in films of higher crystallinity compared to (NDI-B)₂PbI₄ and (NDI-H)₂PbI₄ films. Besides that, enhanced conformational flexibility may induce more defects and, reducing the crystallinity. The loss of kinetic control due to the easier perovskite formation when NDI-H is incorporated is indeed consistent with the reduced crystal orientation.

While the perovskite formation under non-isothermal conditions (as shown in Figure 3.4) gives good insights into the LHOIP formation temperature, no information about the crystal growth mode can be obtained. However, given the anisotropic character of the layered HOIPs, preferential crystal growth along a particular crystallographic direction is expected.^[191] In order to investigate the crystallization mode, Avrami analyses using *in-situ* absorption measurements during isothermal crystallization were performed. The temperature for the experiment was chosen based on the temperature where $\alpha \approx 0.5$ according to Figure 3.4b. For (NDI-E)₂PbI₄ and (NDI-B)₂PbI₄, sigmoid-shaped transition curves (α vs. time) were obtained, as illustrated in Figure 3.5a. Considering the amorphous phase before thin film annealing and the crystalline phase after annealing, such a phase transformation between an amorphous phase and a crystalline phase can be described by the Kohn-Mehl-Avrami model.^[192]

Fitting the obtained conversion coefficients to the Avrami equation:

$$\alpha(t) = 1 - e^{(-kt^n)} \quad (3.2)$$

where $\alpha(t)$ is the conversion coefficient as a function of time t , k a kinetic rate constant, and n the Avrami-coefficient, gives a more detailed insight into the crystallization mechanism.

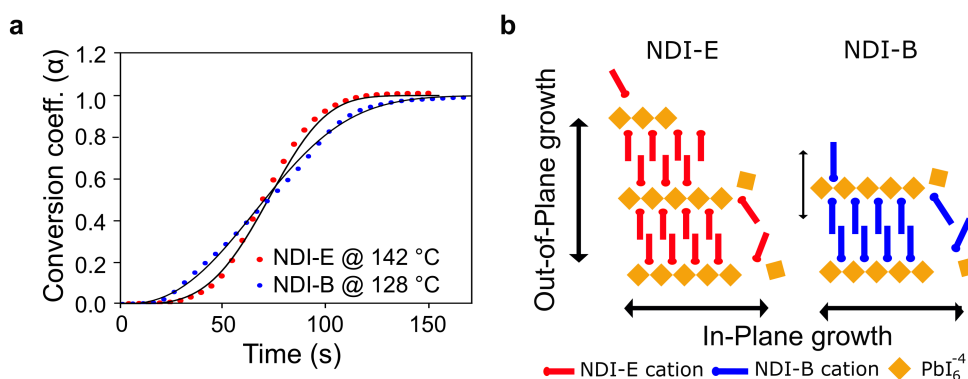


Figure 3.5 – **a)** Fit Avrami model to crystal phase formation under isothermal conditions. **b)** Proposed crystal growth mechanism based on the obtained Avrami-coefficients n .

Fitting the data in Figure 3.5a to the Avrami equation gives an Avrami-coefficient of $n = 3.69$ for NDI-E. As $n = 4$ is associated with three-dimensional crystal growth, a more isotropic crystal growth (proceeding along both the out-of-plane and the in-plane directions) is expected. This finding is in line with the observed high crystallinity for $(\text{NDI-E})_2\text{PbI}_4$ films. For the $(\text{NDI-B})_2\text{PbI}_4$ formation, an Avrami-coefficient of $n = 2.43$ at 128 °C was found, indicating a more two-dimensional crystal growth mode. Altogether, the crystal growth mechanism must be understood as a competing mechanism between in-plane and out-of-plane growth, as illustrated in Figure 3.5b. As XRD measured the crystallinity along the q_z vector, the loss of crystallinity observed in $(\text{NDI-B})_2\text{PbI}_4$ compared to $(\text{NDI-E})_2\text{PbI}_4$ films, and the reduced Avrami-coefficient n suggests a more predominant in-plane crystal growth mechanism in the case of $(\text{NDI-B})_2\text{PbI}_4$. The obtained results for NDI-E and NDI-B cations stand in strong contrast to layered perovskite formation when NDI-H was used as a spacer cation. In this case, isothermal kinetic measurements did not show a sigmoid-shaped transition curve following the Kohn-Mehl-Avrami model but rather a kinetically-limited behavior where the crystallization rate is affected by the conversion coefficient α , as shown in Figure A.7. Interestingly, this kinetically-limited growth behavior of $(\text{NDI-H})_2\text{PbI}_4$ can potentially be overcome by increasing the annealing temperature as higher crystallinity was found when annealed at 225 °C for 5 minutes, as shown in Figure A.8.

Investigation of Electron Transfer to the NDI by Transient Absorption Time-Resolved PL Spectroscopy

The formation of a defined layered structure with all herein investigated spacer cations gives the opportunity to study further electronic interactions between the inorganic slabs and the spacer cations. To investigate the potential ultrafast charge transfer process between the inorganic layer and the organic spacer cation causing quenching of the PL-intensity illustrated in Figure 3.6a, broadband fluorescent up-conversion spectroscopy (FLUPS) ^[179,193] was performed. Here, the sample emission is mixed with an ultrashort laser pulse in a nonlinear optical crystal to generate a signal at the sum frequency of the two incoming beams. The time resolution of the setup is only limited by the laser pulse duration (150 fs), which is ideal for studying initial and fast PL dynamics. The obtained PL dynamics for all investigated LHOIP films are displayed in Figure 3.6b. The temporal- and spectral-dependent PL-intensity of the films excited at 400 nm can be found in Figure A.9. The PL-decay was fit to a single exponential convoluted with the instrument response function (IRF) for NDI-E and NDI-B and PL lifetimes of 0.27 ps and 0.51 ps, respectively, were found.

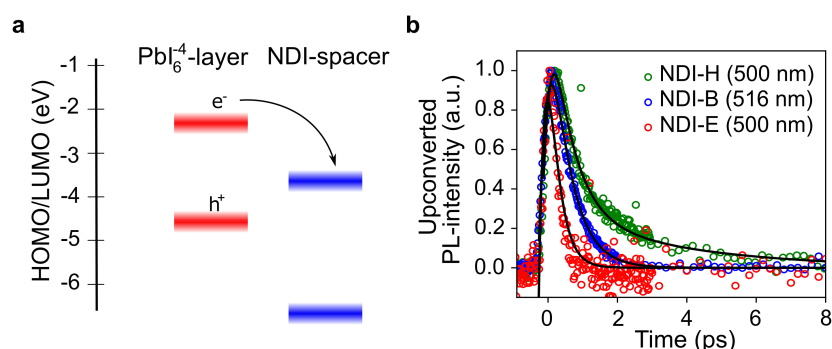


Figure 3.6 – **a)** Illustration of the electronic structure and electron transfer in the type II heterostructure. **b)** PL decay dynamics determined by FLUPS.

For the NDI-H film, a fit with a two-exponential decay (short lifetime of 0.62 ps and a longer time constant of 3.6 ps) matched better the experimental data. The fast decay times observed in the NDI-based layered perovskite films strongly contrast previously reported decay constants for (PEA)₂PbI₄ of several hundreds of picoseconds attributed to trapping processes. ^[194,195] Given the fast decay observed when employing electron-accepting perylene diimide (PDI) cations in proximity to HOIPs as previously reported, ^[148] we attribute the observation of short decay times herein to the charge transfer from the inorganic perovskite layer to the spacer cation. Indeed, the charge transfer becomes slower with increasing linker length and thus distance from the perovskite layer to the NDI core. Hence, the PL dynamics are determined by the depopulation of the confined excited state due to potential electron transfer from the inorganic layer

to the NDI-spacer cations resulting in a faster PL-decay than for similar systems incorporating aliphatic BA-based spacer cations.^[179] It is possible that the PL decay times may be affected by different defect densities in the thin films, which could form non-radiative trap-states. However, the defect density is expected to be inversely correlated with material crystallinity, which is inconsistent with the observations herein. As the FLUPS signal is proportional to the product of the electrons and holes, our conclusions regarding the charge transfer dynamics were further supported by TA spectroscopy.

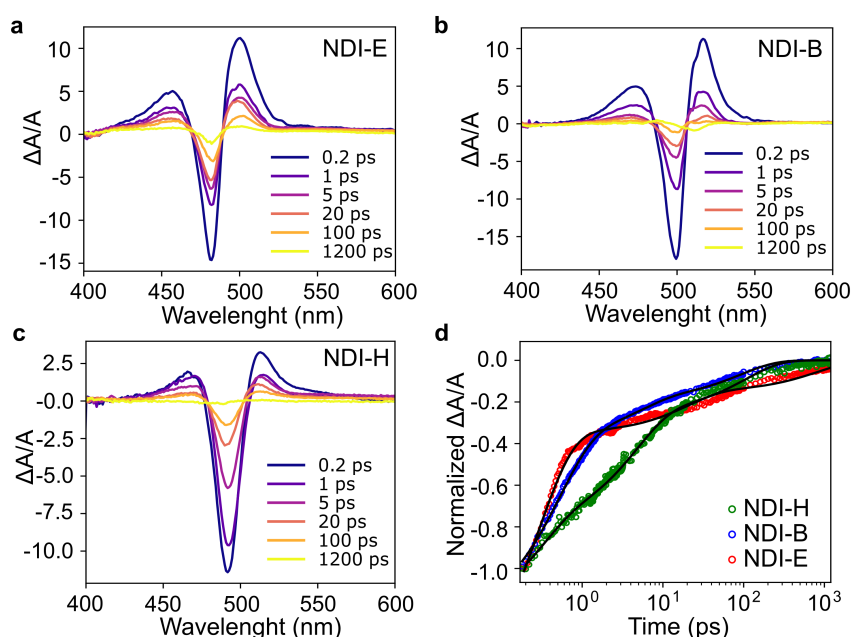


Figure 3.7 – Transient absorption spectra of **a)** NDI-E, **b)** NDI-B, and **c)** NDI-H. **d)** Corresponding GSB dynamics with tri-exponential fit.

TA spectra were obtained using a 400 nm pump laser and are shown in Figure 3.7a-c. For all investigated films, a ground state bleach (GSB) at around 490 to 500 nm can be observed attributed to the excitation of the perovskite layer ground state to the lower excited state. The absorption bleach decays without any observable shift of the bleach maxima, indicating the formation of a single exciton.^[148] The decay dynamics of the GSB are shown in Figure 3.7d, and Table 3.1 displays the calculated lifetimes using a global analysis of the TA data with three exponential decay components. The decay-associated spectra (DAS) are displayed in Figure A.10. The first dominant decay component (τ_1) can be attributed to the radiative recombination due to the similarity to the decay times obtained in the FLUPS measurement. Although previously reported electron transfer between $\text{Pb}(\text{Br}_{0.7}\text{I}_{0.3})_4$ to the naphthyl spacer cation *via* a Dexter electron transfer attributed a similarly short decay constant to an exciton-exciton annihilation process,^[196] the second decay process (τ_2) cannot be unequivocally assigned for

Chapter 3. Tuning Naphthalene Diimide Spacer Cations for the Incorporation into a Layered RP Phase Perovskite Structure

the herein investigated systems. Notably, DAS resulting from the global lifetime analysis of the GSB (Figure 3.7a-c) show maximum amplitudes matching the bleaching peak for all the three decay components for (NDI-E)₂PbI₄ and (NDI-B)₂PbI₄. These findings are contrasted by the mismatched maximum amplitudes for (NDI-H)₂PbI₄, where only the long decay component fits the bleaching peak maxima. The mismatch between the PL-decay in the (NDI-H)₂PbI₄ film is due to a more complex electron transfer kinetics consistent with the bi-exponential decay in the FLUPS. Considering the decay of the absorption bleach caused by the regeneration of the ground state, the prolonged decay time is strongly indicative of reduced exciton binding energy for (NDI-E)₂PbI₄ compared to the (NDI-B)₂PbI₄ film. ^[114]

Table 3.1 – Decay time constants of the absorption bleach for the investigated thin films derived from tri-exponential displayed in Figure 3.7d.

	(NDI-E) ₂ PbI ₄	(NDI-B) ₂ PbI ₄	(NDI-H) ₂ PbI ₄
τ_1 (ps)	0.27	0.51	0.81
τ_2 (ps)	18.1	5.9	4.8
τ_3 (ps)	498	94	119

Overall the FLUPS and TA results are consistent with the photoinduced electron transfer from the inorganic to the organic layer in the NDI-Based LHOIPs and show that increasing the alkyl linker has an effect on the charge transfer where electron transfer from the inorganic layer to the NDI is slower when the distance between the perovskite layer and the chromophore is larger. The localization of the electrons and holes in separate layers will potentially have a strong effect on the charge separation process upon photoexcitation.

While transient absorption and PL spectroscopy methods are not able to distinguish between bound excitons and free electrons and holes, conclusions on the effect of the type II heterostructure on the formation of free charge carriers remain elusive. In contrast to transient absorption spectroscopy, where the wavelength of the pump and probe sources are in the 400 — 1000 nm range, flash-photolysis time-resolved microwave conductivity measurement (fp-TRMC) measures the absorbance of a microwave probe after photoexcitation with a visible light pump. As the microwave probe is only sensitive to free charge carriers, fp-TRMC gives insight into the mobility and lifetime of free charge carriers. A detailed description of the method can be found in Chapter 2. As the sum of the fraction of free charge carriers (ϕ) and their charge carrier mobility is proportional to the absorbed microwave intensity $\frac{\Delta P}{P}$, the charge carrier mobility can be obtained based on equation 2.7.

Photoconductivities of the different NDI-based perovskite thin films and their respective TRMC transients are displayed in Figure 3.8a and Figure 3.8b. The TRMC transient of the free charge carriers was fit to a bi-exponential decay function where a short decay between 50–60 ns, and a long decay of 680 — 1400 ns was observed. Decay time constants are displayed in

Table A.2, and the transients over the whole measured range are displayed in Figure A.11. The mobility decay stands in contrast to the measured mobilities of phenylethylammonium PEA-based $(\text{PEA})_2\text{PbI}_4$, where only a mono-exponential decay was observed with a decay time of 35 ns. While the initial fast decay of free charge carriers in the range of around 30–60 ns can be attributed to the recombination in the inorganic layer, the prolonged charge carrier lifetime might be attributed to the type II heterostructure.

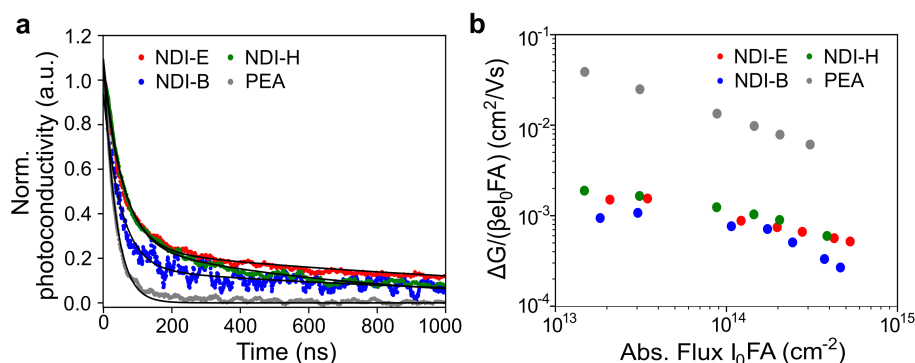


Figure 3.8 – **a)** TRMC transient for $(\text{NDI})_2\text{PbI}_4$ and $(\text{PEA})_2\text{PbI}_4$ based perovskite thin films, and **b)** extracted peak mobility at different excitation intensities assuming $\phi = 1$.

Assuming that every absorbed photon creates a free charge carrier ($\phi = 1$), the peak mobility was found to be in the range between 0.001 and 0.002 cm²·V⁻¹·s⁻¹ at $2 \cdot 10^{13}$ absorbed photons per cm² with only small differences between the different NDI-based spacer cations. The trend of decreasing mobilities due to non-linear effects (e.g., exciton-exciton annihilation) with increasing photon flux is consistent with the $(\text{PEA})_2\text{PbI}_4$ reference sample. At the same excitation wavelength and comparable absorbed photon flux, the found photoconductivity of the NDI-based RP phases are more than one order of magnitude higher than the previously reported photoconductivity of perovskite systems based on a NDIC2 dication.^[174] This increase can be attributed to an improved degree of orientation and structural ordering as we form a layered perovskite structure rather than a (1D) nanowire, as previously investigated. However, peak charge carrier mobilities are still lower than for PEA-based and BA-based layered perovskites. Despite the difference in crystallinity in our samples, no clear effect of the amine-bearing alkyl chain length on the photoconductivity determined by fp-TRMC was found. However, as XRD measures the crystallinity along q_z , while TRMC measures the sheet-mobility parallel to the substrate (q_{xy} -plane), the similar mobilities among all NDI-based RP phases further support our previously assessed crystal growth mechanism of the LHOIPs where crystallinity is preserved along the q_{xy} plane parallel to the substrate.

It has to be noted that the time resolution of fp-TRMC is limited by the cavity to a few nanoseconds. Given the ultrafast electron transfer from the perovskite to the inorganic spacer on the

sub-picosecond timescale, the effect of the linker chain on the electron transfer rate is too small to be observed in fp-TRMC. Moreover, the low photoconductivity determined for the NDI-based RP phase compared to simpler aliphatic species potentially arise due to the lower mobility of the electrons in the organic layer.

Formation of Quasi-Layered Perovskite Thin Films

It has been shown that $n = 1$ layered perovskite thin films based on NDI-spacer cations show considerable in-plane orientation when deposited on a glass substrate where the organic and inorganic layers are oriented parallel to the substrate. The organic spacer layer acts as an insulator hampering charge carrier mobility through the film. In order to tune the orientation of the LHOIP films, increasing the quantum well width by forming quasi-layered perovskite materials provides a simple strategy to obtain more isotropic perovskite films. Moreover, by mixing large spacer cations with small organic cations in the precursor solution and forming quasi-layered layered perovskite thin films, dielectric and quantum confinement effects are reduced. At the same time, the visible light absorbance is enhanced.

While quasi-layered perovskite films are widely investigated with simple aliphatic spacer cations, to the best of our knowledge, the formation of a quasi-layered perovskite incorporating an electron-accepting spacer chromophore and photoinduced electron transfer has not been reported yet. We hypothesized that the high annealing temperature to form the layered perovskite phase when NDI-based spacer cations are used might provide an opportunity to potentially control the crystallization of the quasi-layered perovskite films enabling to easier tune the orientation and distribution on quasi-layered thin films.^[197] We focus in the following on forming $n = 5$ thin films, where NDI cations are mixed together with methylammonium iodide (MAI) and PbI_2 in a 2:4:5 molar ratio, aiming for $(\text{NDI})_2(\text{MA})_4\text{Pb}_5\text{I}_{16}$ phase. The visible light absorption spectra of the quasi-layered films are displayed in Figure 3.9a. Similar to previously reported quasi-layered films based on aliphatic spacer cations, the formation of multiple phases with quantum well widths (n) of the general structure $(\text{NDI})_2(\text{MA})_{n-1}\text{Pb}_n\text{I}_{3n+1}$ can be determined in the absorption spectra.^[95] While using NDI-E as a spacer cation results in no excitonic absorption band that corresponds to the quasi-layered perovskite $(\text{NDI-E})_2(\text{MA})\text{Pb}_2\text{I}_7$ phase, the incorporation of NDI-B and NDI-H into a layered perovskite structure results in the formation of $(\text{NDI})_2(\text{MA})\text{Pb}_2\text{I}_7$ ($n = 2$) as well $(\text{NDI})_2(\text{MA})_2\text{Pb}_3\text{I}_{10}$ ($n = 3$) phase as clearly indicated by the excitonic absorption band at around 570 nm and 600 nm, respectively. Moreover, the $n = 4$ phase is observed when the NDI-H cation is incorporated. Notably, the $n = 2$ incorporating NDI-B and NDI-H can also be observed when methylammonium iodide and NDI-spacers were used in the precursor solution in a 1:2 molar ratio, as displayed in Figure A.12.

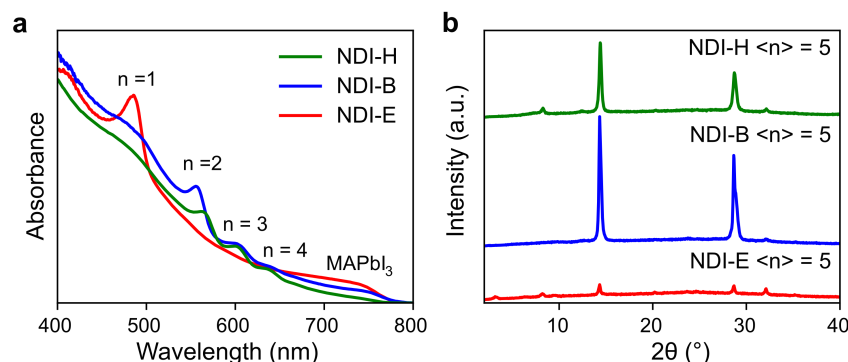


Figure 3.9 – **a**) Visible light absorption spectra of NDI-based quasi-layered films based ($\langle n \rangle = 5$), and **b**) XRD of the investigated films.

Considering the required annealing temperature for the formation of $(\text{NDI-E})_2\text{PbI}_4$ was found to be higher compared to the temperature required to form $(\text{NDI-B})_2\text{PbI}_4$ and $(\text{NDI-H})_2\text{PbI}_4$, we assume that during the annealing process of the $\langle n \rangle = 5$ films, the easy formation of MAPbI_3 growing from the liquid-surface interface towards the substrate leads to the complete consumption of MAI, as suggested by previous reports.^[97,198] This leads to the formation of $(\text{NDI-E})_2\text{PbI}_4$ closer to the substrate. Low-dimensional LHOIPs parallel to the substrate can be found in the XRD of NDI-E base quasi-layered thin film indicated by the diffraction peaks in the range below $2\theta = 5^\circ$ displayed in Figure 3.9b. Notably, the absorption spectrum of the NDI-E-based quasi-layered perovskite films displays the same features over a broad range of solvent-ratio and annealing conditions, as displayed in Figure A.13. On the other hand, as NDI-B and NDI-H require less thermal energy to be incorporated. The formation of these quasi-LHOIP phases competes with the formation of MAPbI_3 under the investigated condition. Indeed, considering the absorbance in the range between 700 and 760 nm due to the MAPbI_3 , a clear decrease in absorbance with increasing amine-bearing alkyl chain can be found, suggesting a lower contribution of the MAPbI_3 in the films incorporating NDI-H. In contrast to quasi-layered films incorporating NDI-E, XRD of NDI-B and NDI-H thin films displayed in Figure 3.9b show no diffraction peaks below $2\theta = 5^\circ$, indicating that the inorganic layers in the low dimensional layered perovskites crystallites are randomly oriented on the glass substrate reducing X-ray scattering at the $00l$ -plane of low dimensional perovskite phases.

3.5 Conclusion

In this work, three different spacer cations with various amine-bearing linker chain lengths attached to an electron-accepting naphthalene diimide core have been synthesized and success-

fully incorporated into a Ruddlesden-Popper type layered perovskite structure. By incorporating the NDI-chromophore with various linker chain lengths, the effect of this simple modification on the optoelectronic properties and crystal formation was investigated. While all investigated spacer cations formed a layered perovskite structure, studies on the thin film formation kinetics via *in-situ* absorption spectroscopy reveal that the alkyl linker chain length modifies the crystal phase formation kinetics and thermodynamics. By increasing the length of the amine-bearing linker chain, for example, lower annealing temperatures were required to form the crystalline layered perovskite phase. Furthermore, by comparing isothermal Avrami-analysis obtained by *in-situ* UV-vis absorption experiments, it was found that the short alkyl chain-bearing NDI-E has a more uniform crystal growth mechanism where crystal growth is equally fast among all crystal axis. This stands in contrast to layered perovskite materials incorporating longer alkyl chain-bearing NDI-B, where crystal growth is favored along the plane of the inorganic layer as suggested by an Avrami coefficient n closer to 3. The differences observed in the *in-situ* UV-vis measurements give a potential explanation for the observed trends in crystallinity and orientation where the loss of control of the crystallization in the formation of LHOIPs incorporating long amine-bearing alkyl chains result in lower crystallinity and more isotropically oriented films.

We hypothesized that the high annealing temperature required to form the layered perovskite structure incorporating the investigated NDI-based spacer cations might provide a path to modulate the phase distribution of the quasi-layered phases on thin films. The high annealing temperature required to incorporate NDI-E results in a quasi-layered film dominated by the 3D MAPbI₃ and (NDI-E)₂PbI₄ phases rather than a homogeneous distribution of multiple quantum wells of various well widths. More homogeneous films with clear indications of the $n = 2$ and $n = 3$ phases can be formed when NDI-based cations with longer amine-bearing linkers (NDI-B and NDI-H) were used, further suggesting that prolonging the linker chain length leads to easier incorporation of the spacer cation into a layered and quasi-layered perovskite phase. It remains unclear if these findings are also applicable to DJ phase perovskites, where the organic layer is formed by a single layer of divalent cations. Recent research suggests a 1D perovskitoid structure rather than a 2D layered perovskite structure when the incorporation of a short alkyl chain symmetric divalent spacer cation based on NDI was investigated.^[172,174] Increasing the alkyl chain might promote the formation of a (2D) layered perovskite structure. Notably, using NDI dications may further improve the solubility of the NDI-based cations beneficial to obtain thicker films required for the fabrication of optoelectronic devices.

The electron-accepting nature of NDI analyzed by cyclic voltammetry further suggests the formation of a layered perovskite, whose electronic structure can be described by a type II heterostructure where the HOMO and LUMO energy levels are below the VB and CB of the inorganic perovskite layer, respectively. Electron transfer from the inorganic layer to the organic

spacer cation upon photoexcitation was observed. FLUPS and TA spectra indicate ultrafast sub-picosecond electron transfer. Moreover, by increasing the distance from the NDI chromophore to the inorganic layer by prolonging the linker chain, electron transfer from the inorganic layer to the NDI chromophore is slower. Such behavior is expected as the probability of electron transfer becomes reduced with an increased NDI-perovskite distance determined by the amine-bearing alkyl chain. The spatial separation of the electron and holes in different layers was hypothesized to improve charge separation. The formation of free charge carriers was studied by TRMC. TRMC experiments indicate peak sum mobility one order of magnitude lower than for PEA-based perovskite materials. However, the obtained photoconductivities are greatly improved by almost one order of magnitude compared to TRMC photoconductivity found in 1D perovskite structure based on NDIC2. While it remains unclear whether the lower photoconductivity is due to reduced free carrier generation yield or due to reduced charge carrier mobility, the dynamics of the TRMC transient suggest that free charge carriers are longer present in the materials as the transient signal shows an additional slow decay with a decay time of several hundreds of nanoseconds. The prolonged lifetime of the free charge carriers might be beneficial for charge diffusion to the charge carrier-selective electrodes in solar cell devices. Notably, our findings are further supported by recent reports where a monocation based on NDI featuring an amine-bearing octyl chain is incorporated into a layered perovskite structure, enhancing the photocurrent by a factor of 40.^[199]

Chapter 4

Photogenerated Charge Transfer in Dion-Jacobson Type Layered Perovskite Based on Naphthalene Diimide

4.1 Abstract

Type II heterostructures based on electron-accepting spacer cations were reported to facilitate electron transfer to the spacer cation and allow the formation of long-lived charge transfer states. Based on our previous finding in Chapter 3, where the incorporation of electron-accepting naphthalene diimide cations with various amine-bearing linker chain lengths into a Ruddlesden-Popper phase was demonstrated, we investigate the incorporation of symmetric NDI-based cations into a DJ phase, where a monolayer of organic spacer cations forms the organic layer. While previous reports show the formation of a 1D perovskitoid nanowire when a symmetric NDI-based spacer cation (NDIC2) is attempted to be incorporated,^[172,174] we first show that a proper layered phase can be formed by prolonging the amine-bearing alkyl chain. We further investigate the charge transfer to the NDI-chromophore upon photoexcitation by transient absorption and broadband fluorescence up-conversion spectroscopy. Further, the formation of free charge carriers upon charge transfer excitons was investigated by time-resolved microwave conductivity and terahertz spectroscopy. While the obtained photoconductivity is comparable to the photoconductivity obtained for the RP phases based on NDI monovalent spacers investigated in Chapter 3, the successful formation of quasi-layered thin films allows further confirmation of electron transfer in phases with higher inorganic layer width (n). Moreover, we demonstrate that the ordered 2D structure allows for efficient electron mobility as electron-only space-charge limited current measurements suggested.

This chapter is based on an accepted manuscript: S. Nussbaum., E. Socie, G. C. Fish, N. J. Diercks, H. Hempel, D. Friedrich, J. Moser, J. Yum and K. Sivula Chem. Sci. **2023**, 14, 6052–6058
Herein presented transient absorption and broadband fluorescent absorption spectra were recorded and fit by E. Socie. Terahertz spectroscopy experiments were performed by H. Hempel. SEM pictures were obtained with the help of N. Diercks.

4.2 Introduction

Layered perovskite materials are under investigation for their application in optoelectronic devices due to their enhanced stability compared to conventional hybrid organic-inorganic materials.^[139,200] However, dielectric and quantum confinement effects increase the exciton binding energy and hamper the charge separation and free charge carrier generation upon photoexcitation.^[69] Moreover, the anisotropic charge carrier properties pose some challenges to the fabrication of high-efficient optoelectronic devices such as solar cells and light-emitting diodes (LEDs).^[201] Mitigating the quantum and dielectric confinement effects so far has been done by adjusting the width of the inorganic layer by tuning the stoichiometric ratio of the small A-site cations (A') and the bulky organic spacer cation (BOS) forming quasi-layered perovskite films of the general formula (BOS)₂A'_{*n*-1}Pb_{*n*}X_{3*n*+1} where X is a halide and *n* denotes the width of the inorganic slab. Moreover, with increasing well width, the crystallites become more randomly oriented on the substrate reducing the strong anisotropic charge carrier properties. Nonetheless, forming quasi-layered perovskite materials has to be considered a trade-off between efficiency and stability.^[201]

In Chapter 3, we introduced a monovalent spacer cation based on an electron-accepting naphthalene diimide chromophore core and demonstrated the successful incorporation into an LHOIP structure. Further, it has been shown that the amine-bearing alkyl linker, which connects the chromophore core to the inorganic perovskite framework, is a crucial variable determining the formation of the crystalline film. As such, it was found that increasing the amine-bearing linker results in precursor films which require lower annealing temperatures to form the crystalline layered perovskite phase. However, monovalent cations based on NDI show low solubility in solvents commonly used to fabricate LHOIP films. In the case of NDI-E specifically, the formation of a considerable amount of (NDI-E)₂PbI₄ oriented parallel to the substrate and the absence of any (NDI-E)₂(MA)_{*n*-1}PbI_{3*n*+1} phases where *n* > 2, limits the further investigation of these materials.

The incorporation of organic spacer dications generates what is commonly called DJ-type quasi-LHOIPs with a general formula of (BOS)(A')_{*n*-1}Pb_{*n*}I_{3*n*+1}. These materials have recently come forward as more promising due to enhanced stability and improved charge carrier transport through the organic layer. We hypothesize that the incorporation of a single layer of NDI-based dications might provide some benefits for the formation of higher *n*-value phases as the self-assembling process is determined by the covalent interactions of the dications with the inorganic slab rather than the van-der-Waals interactions governing the interactions between the NDI-monocations in the organic layer. Therefore, shifting from RP to DJ phases might modulate not only the phase distribution in quasi-layered perovskite films but also the stacking of the NDI-chromophore core in the organic layer. Furthermore, divalent spacer cations are

usually more soluble in the solvents commonly used for HOIPs and LHOIPs synthesis, such as DMSO and DMF. Hence, a lower concentration of the spacer cation is required in the precursor solution, and the DJ phases tend to be more stable than the RP phase.^[53,54,72] However, NDI-based dications based on an amine-bearing ethyl-alkane chain denoted as NDIC2 as illustrated in Figure 4.1a was found to facilitate the formation of NDI-PbI₂ nanowires, whose structure is illustrated in Figure 4.1b.

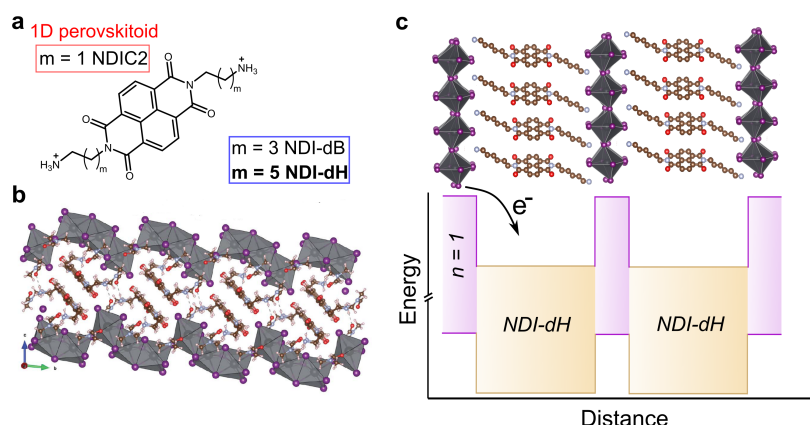


Figure 4.1 – **a)** Chemical structure of NDIC2 and the herein investigated NDI-dB and NDI-dH. **b)** Reported crystal structure of the lead-iodide nanowire obtained when NDIC2 is incorporation. Reproduced from ref. 174 with permission from The Royal Society of Chemistry. **c)** Schematic illustration of the desired (2D) layered perovskite structure.

Motivated by the observations in Chapter 3, where we found that prolonging the amine-bearing alkyl chain length reduces the heat of formation for the incorporation into a layered perovskite structure, we assumed that prolonging the amine-bearing alkyl chain length might be a promising approach for the incorporation of NDI-based dications in a structure schematically described in Figure 4.1c. By investigating thin films of quasi-layered perovskite materials of various MAI:NDI-dH ratios, we aim to explore the effect of the spacer cation on the charge separation at the NDI-perovskite interface in quasi-layered films. Moreover, in response to recent reports on 1D perovskite nanowires with NDIC2, we demonstrate that the ordered quasi-layered films allow comparable electron mobility through the film as found in the more conventional layered perovskite films incorporating *n*-butylammonium iodide.

4.3 Experimental

Sample Preparation

$\langle n \rangle = 1-5$ films were synthesized by spin-coating the precursor solution containing 0.2 M PbI₂ and a stoichiometric amount of NDI-dH and MAI in DMSO solution at 2000 rpm for 30 seconds on a glass substrate. The films were subsequently annealed at 180 °C for 10 minutes.

X-ray diffraction and Grazing-Incidence Wide-Angle X-ray Scattering Measurements

Thin film X-ray diffraction (XRD) measurements were taken in Bragg-Brentano geometry using non-monochromatic Cu-K α_1 radiation on a Bruker D8 Vario instrument equipped with a Lynx-EYE XE detector. Grazing-incidence wide-angle X-ray scattering experiments were carried out using a Bruker Vario TXS equipped with an Eiger 2D detector. A Cu-K α_1 X-ray source at an angle of incidence (α) of 2° was used. GIWAXS images were processed using the Python packages pygix and pyFAI.^[177,178]

Absorption Measurements, Transient Absorption, and Broadband Fluorescent Up-conversion Spectroscopy

Visible light absorption, TA spectra, and FLUPS were performed based on the same procedure described in Chapter 3. To extract the lifetimes displayed in Table 4.1, we performed a global analysis of the dynamic traces of the bleaching peak.^[202]

Optical-Pump Terahertz-Probe (OPTP) Spectroscopy

OPTP was used to measure photoconductivity transients and the initial sum of electron mobility and hole mobility with a time resolution of ~ 150 fs, as previously reported.^[195] To this end, terahertz pulses were generated by optical rectification of 800 nm laser pulses in a ZnTe crystal. After these terahertz pulses have been transmitted through the sample, their electric field E was measured by optoelectronic sampling in a second ZnTe crystal. Additional laser pulses with a length of ~ 150 fs, a wavelength of 400 nm, and a repetition rate of 150 kHz were used to photogenerate a sheet carrier concentration Δn_s of $2.2 \cdot 10^{13} \text{ cm}^{-2}$ per pulse in the sample. This photoexcitation reduced the transmitted THz field by ΔE , from which the sheet photoconductivity $\Delta \sigma_s$ can be obtained by the so-called thin film approximation:

$$\Delta \sigma_s = \epsilon_0 c (1 + n_{sub}) \frac{\frac{\Delta E}{E}}{1 + \frac{\Delta E}{E}} = e n_s \mu \Sigma \quad (4.1)$$

where c is the speed of light, ϵ_0 is the vacuum permittivity, n_{sub} is the reflective index of the quartz glass substrate at terahertz frequencies of ~ 2, and e is the elementary charge. The photo-

conductivity transient is measured by mechanically delaying the pump pulses with respect to the terahertz pulses. The sum mobility μ_{Σ} can be obtained from the peak value of the photoconductivity transient and the sheet carrier concentration Δns known from the excitation conditions.

Microwave Conductivity Measurements

TRMC measurements were performed according to the procedure described in Chapter 3. For $(\text{BA})_2\text{PbI}_4$ and $(\text{NDI-dH})\text{PbI}_4$ samples a K-factor of 45'000 was assumed.

SCLC

Samples were prepared according to previously reported architecture. Electron-only devices were fabricated based on a Glass/FTO/ TiO_2 /Perovskite/PCBM/silver architecture. The FTO substrates were cleaned for 30 minutes in the ultrasonic sonicator in acetone, soap-water (Hellmanex) solution, water, and isopropanol. The clean substrates were plasma cleaned for at least 10 minutes before sample deposition. TiO_2 layer was deposited by spin-coating a titanium isopropoxide solution in ethanol:HCl on the FTO-coated glass substrate according to the conditions reported elsewhere.^[203,204] The isopropoxide solution was spin-coated at 5000 rpm for 40 seconds. The films were then thermally annealed, following a ramped annealing step to 500 °C (dwell 45 min).

The perovskite films were coated using a precursor solution containing NDI-dH salt, MAI, and PbI_2 in 1:4:5 molar ratios. The perovskite film was coated at 2000 rpm for 30 seconds and subsequently annealed at 220 °C. PCBM solution (10 mg in 1 ml chlorobenzene) was coated at 3000 rpm for 30 seconds and subsequently dried at 100 °C for 10 minutes.

The thickness of the thin films was initially determined with a Bruker Dektak XT profilometer. Cross-section SEM on selected films was used to confirm the validity of the determined film thickness.

Electrochemical Impedance Spectroscopy (EIS)

The relative permittivity of the thin films was estimated based on the capacitance measured by impedance spectroscopy. The capacitance was determined using the impedance.py Python package.^[205] For this, a perovskite film was spin-coated on a FTO coated glass substrate and sandwiched with a gold electrode (0.16 cm²). Based on the determined geometric capacitance (C), assuming a plate capacitor geometry, ϵ is calculated using the device thickness (d), and area (A):^[113]

$$\epsilon = \frac{Cd}{A\epsilon_0} \quad (4.2)$$

4.4 Results and Discussion

We prepared NDI-based dications with different alkyl chain lengths of 4 or 6 carbons denoted as NDI-dB and NDI-dH, respectively. The chemical structures of the spacer cations are shown in Figure 4.1a. Detailed synthesis procedures and characterization of the spacer cations can be found in Appendix B. Starting with the (NDI-dH)PbI₄ composition ($n = 1$), the visible light absorption and PL spectra of the synthesized thin films are displayed in Figure 4.2a and show the typical excitonic absorption and emission bands similarly found in conventional (PEA)₂PbI₄ and (BA)₂PbI₄ layered perovskites.^[206] However, in contrast to (BA)₂PbI₄, the PL-intensity is quenched in the (NDI-dH)PbI₄ films, as displayed in Figure B.1. Figure 4.2b displays the XRD pattern of the thin film showing equally spaced diffraction peaks associated with the *00l*-planes suggesting the successful formation of a layered perovskite crystal phase where the inorganic slabs are oriented parallel to the substrate. Based on an assignment of the peak at $2\Theta = 3.84^\circ$, the interplanar spacing is 23.0 Å corresponding roughly to the size expected given the length of the NDI-dH cation of 22.7 Å. We note that the optoelectronic and structural properties of our (NDI-dH)PbI₄ thin films are distinct from the previously reported

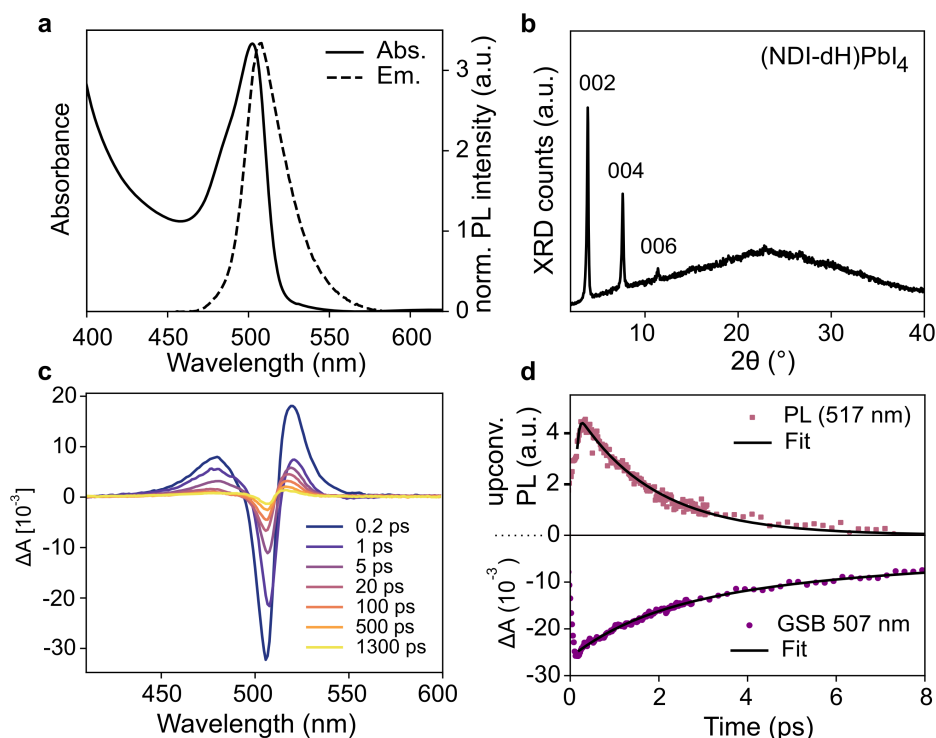


Figure 4.2 – **a**) Visible light absorption and PL steady-state spectra, and **b**) XRD of the (NDI-dH)PbI₄. XRD was recorded with a monochromated Cu-Kα₁ X-ray source. **c**) Transient absorption spectral slices, and **d**) Ultrafast PL and GSB dynamics of the (NDI-dH)PbI₄ films based on fluorescence up-conversion spectroscopy (FLUPS) and TA, respectively.

1D perovskitoid films based on a similar spacer cation with an ethyl-ammonium linker (NDIC2), illustrated in Figure 4.1a, where no excitonic absorption and emission bands were found.^[172–174] Notably, the desired DJ-type layered structure can also be obtained with the butylammonium linker (NDI-dB). Similar optoelectronic properties and XRD diffraction peaks associated with a smaller interplanar distance of 19.3 Å are observed, as shown in Figure B.2, which is comparable to the size of the cation (18.5 Å). The observed effects of the alkyl linker chain on structure and crystallinity are consistent with our previous finding in RP-based perovskite discussed in Chapter 3, indicating that the amine-bearing alkyl chain linker is an important parameter in the formation of layered perovskite materials. Despite the higher crystallinity found when NDI-dB is incorporated into a DJ-perovskite, the films with NDI-dH showed better morphology, as displayed in Figure B.3, likely due to a difference in cation solubility. Therefore, the following analysis focuses on the NDI-dH divalent spacer cation system.

To further investigate the effect of the NDI-spacer cation on the photogenerated charge carrier dynamics, ultrafast spectroscopic techniques were performed, namely transient absorption (TA) spectroscopy and ultrafast broadband fluorescence up-conversion spectroscopy (FLUPS).^[179,193] The TA spectra, ground state bleach (GSB), and PL-decay dynamics are shown in Figure 4.2c-d and Figure B.4 for (NDI-dH)PbI₄. The FLUPS dynamic shows an ultrashort PL lifetime with a decay time constant of around 1.65 ± 0.03 ps, which is comparable to the previously reported PL decay with RP-type analog materials discussed in Chapter 3 and can be attributed to electron transfer from the inorganic layer to the organic spacer as schematically illustrated in Figure 4.1c. The ultrafast PL decay stands in contrast to (PEA)₂PbI₄, where decay times of several hundreds of picoseconds are reported.^[195] The TA spectra show a GSB at 507 nm, corresponding to the position of the excitonic absorption band. The weak spectral signature of the expected NDI⁻ formation overlaps with the photoinduced absorption (PIA) at 450 – 500 nm.^[172,173] However, partial GSB decay and complete PL decay are characteristic of electron transfer processes.^[146] GSB dynamics were fit to a tri-exponential decay resulting in one fast decay constant ($\tau_1 = 1.66$ ps) followed by two slower decays with $\tau_2 = 6.11$ ps and $\tau_3 = 1510$ ps. Altering the pulsed laser fluence from 15 to 150 nJ showed no change in the TA spectra suggesting that Auger-type recombination processes do not contribute to the GSB dynamics, as displayed in Figure B.4. While τ_1 can be attributed to the electron transfer from the inorganic layer to the NDI spacer due to the similar time scale as the observed PL decay, the long decay components (τ_2 and τ_3) are attributed to potential electron back transfer from the NDI to the perovskite ground state and non-radiative recombination.

Generation of Free Charge Carriers in $n = 1$ DJ Phase Perovskite Materials

In order to investigate further the nature of the charge separation state at the organic-inorganic interface, flash-photolysis time-resolved microwave conductivity (fp-TRMC) measurements were performed. Probing the photogenerated charge carriers along the direction parallel to the substrate (displayed schematically in Figure 4.3a) by photoexciting the LHOIP thin film, the microwave probe is only absorbed by free charge carriers allowing to assess the photoconductivity as described in Chapter 2 and elsewhere.^[207] The fp-TRMC transient after photoexcitation at 420 nm of (NDI-dH)PbI₄ and (BA)₂PbI₄ as reference material are displayed in Figure 4.3b.

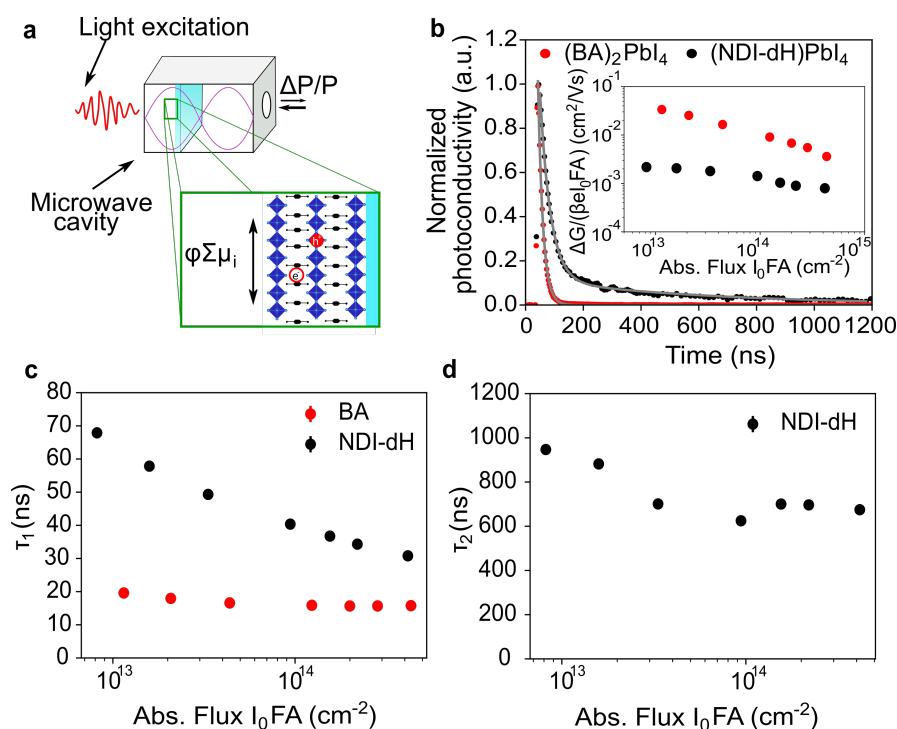


Figure 4.3 – **a)** Illustration of the fp-TRMC setup measuring the mobilities of free charge carriers along the axis parallel to the substrate and **b)** fp-TRMC transient of (NDI-dH)PbI₄ (closed black circles) and (BA)₂PbI₄ (closed red circles) with the obtained mobilities in the inset of the figure. Samples were excited at 420 nm. Decay time constants τ_1 **c)**, and τ_2 **d)** at different absorbed photon flux.

A prolonged transient decay for NDI-dH-based LHOIP can be observed where the free charge carrier decay can be fit to a bi-exponential decay with a short ($\tau_1 = 36$ ns) and a long ($\tau_2 = 597$ ns) decay constant. The observed free charge carrier dynamics stand in contrast to the dynamics in BA-based perovskite films, where the transient decays with a time constant of around 17 ns, as displayed in Figure 4.3c-d, suggesting that the prolonged lifetime of the free charge carriers is due to a type II heterostructure, which affords separate electrons and holes in different layers.

Moreover, the estimated mobility, as quantified by the sum mobility ($\phi \sum \mu$) in (NDI-dH)PbI₄ assuming $\phi = 1$, is around one order of magnitude higher than previously reported in NDIC2-based 1D perovskitoid materials.^[173,174] This increase in photoconductivity can be attributed to the 2D layered structure enhancing the mobility of the free charge carriers through the crystalline material. However, the measured photoconductivity is still more than one order of magnitude lower than the BA-based perovskite reference material. Notably, similar low photoconductivities were determined in Chapter 3 in (NDI)₂PbI₄, where the estimated mobilities were independent of the observed crystallinity along q_z , suggesting that the differences in crystallinity and interplanar distances not to be the sole reason for the observed low peak photoconductivity. Although it is possible that the free charge carrier generation yield (ϕ) is lower for (NDI-dH)PbI₄ resulting in decreased apparent mobilities from the fp-TRMC data, we suppose that the diminished sum mobility ($\phi \sum \mu$) observed for (NDI-dH)PbI₄ is due to the decreased mobility of the electrons located in the NDI.

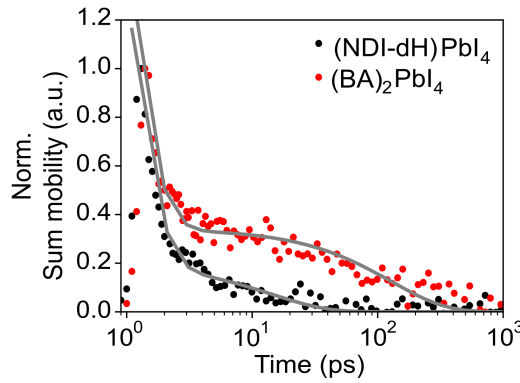


Figure 4.4 – Transient obtained from optical-pump terahertz-probe spectroscopy (OPTP). The sample was pumped at 400 nm.

As the time resolution of fp-TRMC (few ns) is larger than the time scale of electron transfer from the inorganic layer to the NDI chromophore, as determined by FLUPS and TA spectroscopy, optical-pump terahertz-probe (OPTP) spectroscopy was used to determine the sum mobilities a few picoseconds after photoexcitation at 400 nm. The transient intrinsic carrier mobility dynamics derived from the transient THz spectroscopy signal is displayed in Figure 4.4 and shows a bi-exponential decay with time constants of $\tau_1 \approx 0.55$ ps and $\tau_2 \approx 15$ ps. Given the similarities in time scale observed in FLUPS for the electron transfer, we assign the faster decay component to be the transfer of photoexcited electrons to the NDI-cation overlapping with contributions due to electron-phonon scattering. The obtained peak mobility determined by OPTP was found to be $0.35 \text{ cm}^2 \cdot \text{V}^{-1} \cdot \text{s}^{-1}$, which is in the same range as previously reported mobilities for BA-based and PEA-based perovskites, further suggesting that ϕ can be assumed to be comparable in (NDI-dH)PbI₄ and (BA)₂PbI₄.^[112,208,209]

Formation of quasi-layered films

Given the successful formation of the ordered and crystalline layered (NDI-dH)PbI₄ perovskite phase, we investigated whether a quasi-2D layered structure is preserved and electron transfer is observed when the energy sub-band width is increased. Thin films with phases of LHOIPs with larger well widths and higher n -number, as shown schematically in Figure 4.5a, were fabricated by mixing an appropriate amount of MAI into the precursor solution. In the following, the stoichiometric ratio in the precursor solution will be denoted by the indices $\langle n \rangle$ indicating the nominal quantum well width of (NDI-dH)MA _{$n-1$} Pb _{n} I_{3 $n+1$} expected to be formed. For films with $\langle n \rangle > 1$, a distribution of quantum wells of various well widths is usually formed.^[95,97,198] For the sake of clarity, the specific perovskite layer number phase will be denoted by the indices n .

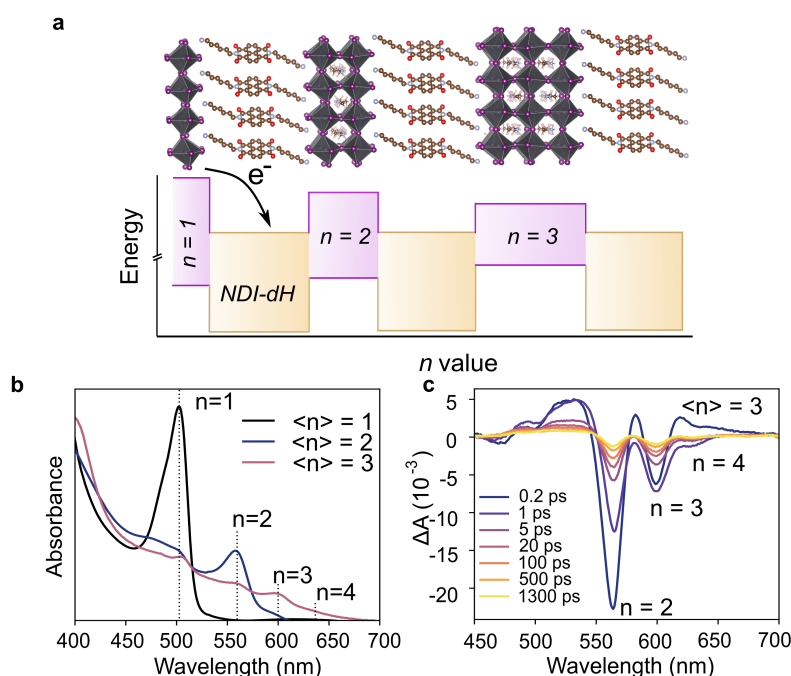


Figure 4.5 – **a)** Schematic illustration of the quasi-layered perovskite materials incorporating NDI-dH. The Energy levels of the inorganic layer as based on ref. 95. **b)** Visible light absorbance of $\langle n \rangle = 1$, $\langle n \rangle = 2$ and $\langle n \rangle = 3$ thin films and **c)** transient absorption slices of $\langle n \rangle = 3$ film.

The visible light absorbance spectra and XRD of thin films with $\langle n \rangle = 2$ or 3 are displayed in Figure 4.5b and Figure B.5, respectively. For $\langle n \rangle = 2$ thin film, the formation of $n = 2, 3$ phases is indicated by the characteristic excitonic absorption bands with an absorption maximum at 560 nm and 600 nm, respectively. Electron transfer kinetics were further investigated by analysis of the GSB-dynamics from TA spectroscopy displayed in Figure 4.5c and Figure B.6. A strong GSB for the $n = 2$ and $n = 3$ phases can be observed overlapping with the position of the excitonic absorption band displayed in 4.5b. The 0.25 ps growth component of the GSB in the $n = 3$ phase

Table 4.1 – Fit GSB decay dynamic for the investigated films.

Compound	$n = 1$	$n = 2$	$n = 3$	$\langle n \rangle = 4$	$\langle n \rangle = 5$
τ_1 (ps)	1.66	1.83	2.04	2.71	2.56
τ_2 (ps)	6.11	58.8	45.3	200	122
τ_3 (ps)	1510	2450	1690	2380	1540

is attributed to the electron funneling, as reported for similar systems.^[210,211] Notably, in the $\langle n \rangle = 3$ film, a weak feature in the range of 450 to 500 nm with a delay of around 1 ps is observed, potentially arising from the NDI^- anion. However, the signal was too weak to resolve further. The absence of any absorption beyond 680 nm in Figure 4.5b and the absence of any clear GSB associated with the 3D MAPbI_3 phase suggest that the formation of the MAPbI_3 is suppressed during the quasi-layered film fabrication.

The dynamics of the GSB decay were fit to a tri-exponential decay (Figure B.5). The decay components and fitting results displayed in Table 4.1 are consistent with an ultrafast decay component τ_1 attributed to the electron transfer from the inorganic layer to the NDI since a clear trend of increasing GSB decay time with an increase in the well width (n) is found. The ultrafast decay component τ_1 has not been previously described in aliphatic systems where GSB decay is often fit to a bi-exponential decay.^[114,212] Moreover, Proppe *et al.* assigned such a fast decay component to the NDI-chromophore in NDIC2 nanowires, while no fast decay component was observed in MAPbI_3 .^[172] The increase in the GSB decay time is plausibly ascribed to the decreased conduction band energy of the perovskite, reducing the driving force for electron transfer and mitigating quantum confinement as the quantum well width increases. A longer time for photogenerated carriers to diffuse to the NDI chromophore is required. For films with $\langle n \rangle > 3$, the visible light absorption displayed in Figure B.7 does not show any excitonic

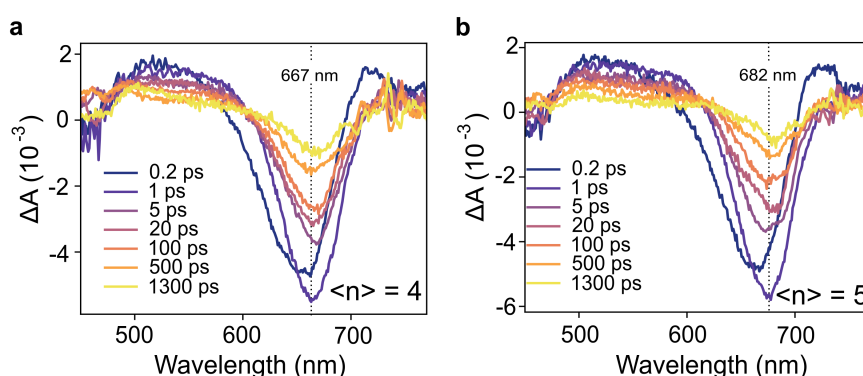


Figure 4.6 – Transient absorption slices of the **a)** $\langle n \rangle = 4$ and **b)** $\langle n \rangle = 5$ thin films. GSB minima shifts from 667 nm to 682 nm with increasing n . GSB for MAPbI_3 is reported above 700 nm.^[172]

absorption bands that can be assigned to the $n = 2, 3$ phases suggesting suppression of the formation of phases with lower n . The TA slices of the films $\langle n \rangle = 4-5$, displayed in Figure 4.6, further support these findings as only one single GSB can be observed. Under the investigated conditions, the NDI-dH appears to form a rather homogeneous distribution of quantum well and no signal from MAPbI₃ was obtained. Moreover, the GSB minima shift towards lower absorption energies with increasing $\langle n \rangle$ and can be associated with quasi-layered perovskite phases with large inorganic well-width. GSB decay dynamics are displayed in Figure B.8 and show comparable dynamics to phases with lower n where a fast initial decay (τ_1) is observed, as displayed in Table 4.1.

Optimization of Orientation in $\langle n \rangle = 5$ Thin Films

Given the spectroscopic results, which show that photons absorbed by the perovskite layers lead to electron transfer to the NDI layers even in quasi-layered perovskite systems, we next aimed to obtain device-based electronic characterization to demonstrate that the quasi-2D layered structure has suitable charge carrier transport properties for potential application in optoelectronic devices. High disorder and, therefore, low charge carrier transport through the film were hypothesized to be the limiting factor in NDIC2-based nanowires.^[173] We focused on $\langle n \rangle = 5$ films as similar perovskite structures based on butylammonium (BA) have been reported,^[95] allowing us to compare our new material with an established system. The crystallinity and orientation of the (NDI-dH)(MA)₄Pb₅I₁₆ thin films were optimized based on a solvent engineering method. In brief, we found that a solvent mixture of DMF:DMSO (2:3 v/v) in the precursor solution results in thin films where the inorganic layers are oriented perpendicular to the substrate, as shown by grazing-incidence wide-angle X-ray scattering (GIWAXS) in Figure 4.7a and XRD displayed in Figure 4.7b.

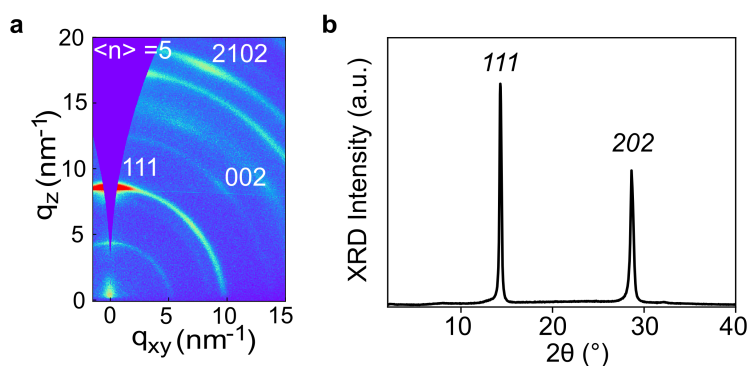


Figure 4.7 – **a)** GIWAXS with incident angle $\alpha = 2.0^\circ$ using a $K\alpha 1$ X-ray source and **b)** XRD of (NDI-dH)MA₄Pb₅I₁₆ spin-coated using the optimized conditions.

Notably, recent reports suggest improved orientation and crystallinity when NH_4SCN was mixed as an additive in the precursor solution.^[98,100] NH_4SCN supposedly retards the crystallization in the bulk forcing oriented crystal growth from the surface-air interface. Initial studies with different amounts of NH_4SCN displayed in the Appendix (Figure B.9), however, remained inconclusive as no clear trend towards improved orientation with increasing addition of NH_4SCN was observed. For further studies, NH_4SCN was not added.

Figure 4.8a shows the visible light absorbance of the films prepared under these conditions displaying excitonic absorption bands, which can be assigned to $n = 3$ and $n = 4$ phases. Comparing the absorption spectrum of the optimized $\langle n \rangle = 5$ films with the absorption spectrum of MAPbI_3 indicates no obvious formation of the 3D perovskite phase. We were unable to obtain any PL signal for the $\langle n \rangle = 5$ films, as shown in Figure 4.8b, likely due to electron transfer from the inorganic wells to the NDI spacer chromophore. Moreover, no PL at 750 nm arising from MAPbI_3 can be observed, suggesting the absence of any 3D perovskite phase supporting our previous findings in the TA spectra of the un-optimized $\langle n \rangle = 5$ thin films. This results is surprising as the presence of MAPbI_3 phase is relatively common in many quasi-layered perovskite films incorporating aliphatic and smaller aromatic spacer cations.^[97,198] The more homogeneous phase distribution towards phases with lower n -number may contribute to their improved stability compared to quasi-layered perovskite materials formed with BA spacer cations.

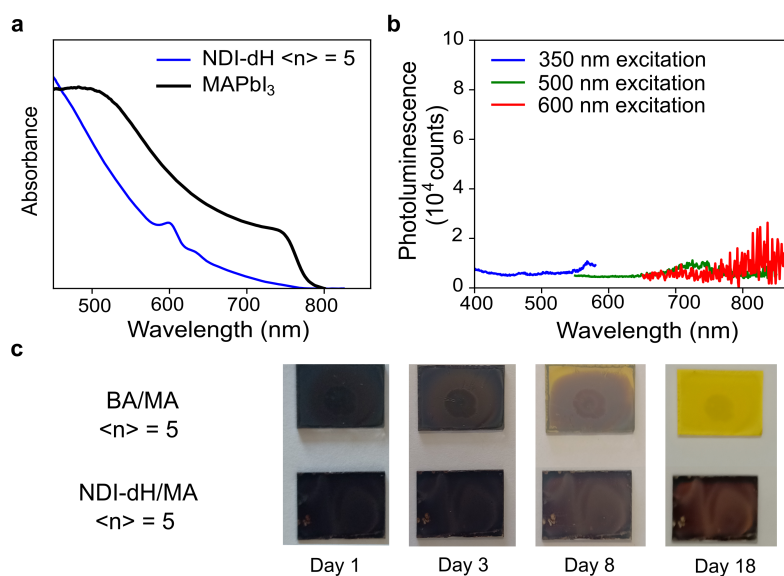


Figure 4.8 – **a)** Visible light absorption spectra of optimized NDI-dH ($\langle n \rangle = 5$) and 3D MAPbI_3 . **b)** PL spectra of NDI-dH ($\langle n \rangle = 5$, optimized) excited at 350, 500, and 600 nm. **c)** Stability of the NDI-dH and BA-based films ($\langle n \rangle = 5$) when stored under ambient conditions. The BA-based quasi-layered films were formed using the same conditions as for the space-charge limited current.

Figure 4.8c shows the degradation of BA-based ($\langle n \rangle = 5$) and NDI-dH-based ($\langle n \rangle = 5$) thin films when stored under ambient conditions. While clear signs of the yellow phase can be observed after a week for the BA-based films, the NDI-dH-based perovskites show minimal changes in color. It remains unclear whether the improved stability arises from the enhanced hydrophobicity of the NDI spacer or the potentially improved homogeneity of the quasi-layered phase, where the formation of less stable phases of quantum wells with larger well-widths is suppressed. Notably, layered perovskite films with a single layer of organic dications are reported to be more stable than layered perovskite with a bi-layer of monocations.^[53,54,72]

Based on the optimized thin film preparation conditions, electron-only devices were prepared based on a widely reported device architecture, where the perovskite layer is sandwiched between two electron-exclusive electrodes displayed in Figure 4.9a. Different perovskite layer thicknesses ranging from 600 nm to 1.2 μm , as displayed in the cross-section electron micrographs in Figure 4.9b, were fabricated. A typical current-voltage (I - V) curve of the electron-only space-charge-limited current (SCLC) is displayed in Figure 4.9c. At low voltage, a linear dependence between the current and voltage can be found, marking an ohmic region. A transition towards a region where $I \propto V^2$ is observed at higher voltages, indicating SCLC behavior.

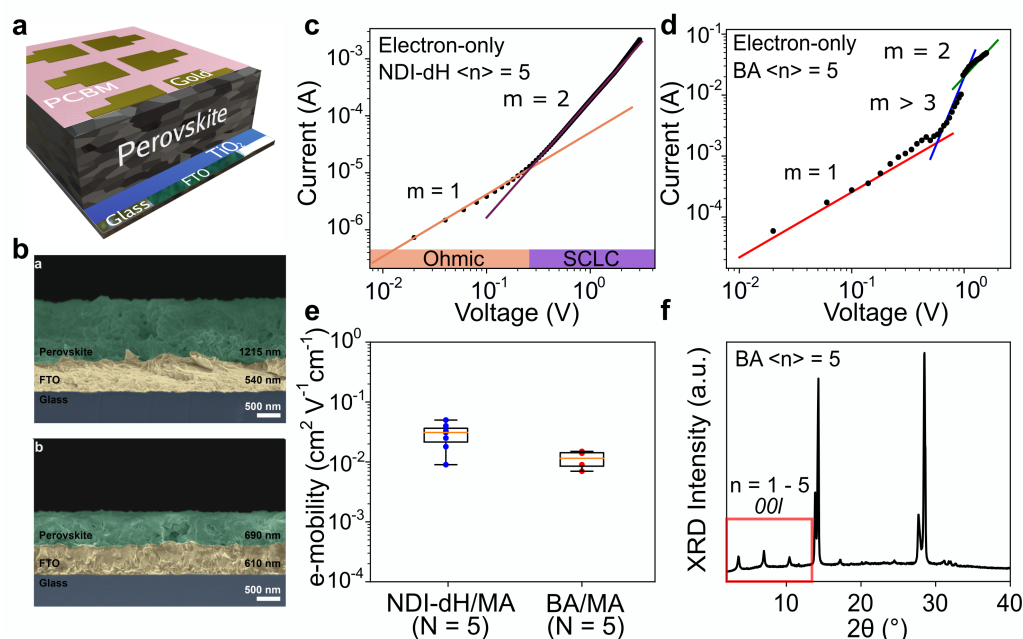


Figure 4.9 – **a)** Device architecture of the SCLC device setup for electron mobility. **b)** Cross-section electron micrographs for different thickness of NDI-dH $\langle n \rangle = 5$ films. Typical current-voltage (I - V) curve of the electron-only space-charge-limited current (SCLC) of **c)** NDI-dH ($\langle n \rangle = 5$) and **d)** BA ($\langle n \rangle = 5$) thin films. **e)** Obtained electron mobilities for BA and NDI based devices. **f)** XRD of the $\langle n \rangle = 5$ BA film. XRD were performed using a Cu- $K\alpha_1$ X-ray source.

The absence of any region with $I \propto V^m$ where $m > 3$, corresponding to a trap-filling region (TFR), is surprising as TFRs are routinely reported in BA-based perovskite films. Indeed, a comparable shape of the I - V -curve, as reported in the literature, was observed when $(\text{BA})_2(\text{MA})_4\text{Pb}_5\text{I}_{16}$ ($\langle n \rangle = 5$) films were investigated using the same device architecture. It is thus assumed that the trap density in the LHOIP films incorporating NDI-dH is below the minimal trap density ($nt_{\min} = 6 \cdot 10^{-14} \text{ cm}^{-3}$ at $T = 295 \text{ K}$ and $L = 1.2 \text{ }\mu\text{m}$) for the investigated thickness (L), as given by: ^[213]

$$n_{t,\min} = 4\pi^2 \frac{k_b T \epsilon}{q^2 L^2} \quad (4.3)$$

where ϵ is the dielectric constant of the material, T is the temperature, q is the elementary charge, and k_b is the Boltzmann constant. The low trap density provides further evidence that the observed PL quenching is due to electron transfer from the layered perovskite structure to the NDI spacer cation rather than non-radiative recombination *via* trap sites. Based on the SCLC behavior, the electron mobility, μ_e , was derived using Mott-Gurney-Law introduced in equation 2.10. The relative permittivity for the NDI $\langle n \rangle = 5$ was estimated to be $\epsilon_r = 16$ based on the capacitance determined by impedance spectroscopy displayed in Figure B.10. An electron mobility of $0.03 \text{ cm}^2 \cdot \text{V}^{-1} \cdot \text{s}^{-1}$ was found for the (NDI-dH)(MA)₄Pb₅I₁₆ thin films, which was slightly higher than the mobility obtained for our BA-reference sample ($0.01 \text{ cm}^2 \cdot \text{V}^{-1} \cdot \text{s}^{-1}$), as illustrated in Figure 4.9e. Given the spectroscopic results, which imply that photogenerated electrons in the inorganic layer are transferred to the organic layer, we assume that the measured μ corresponds to electron transport strongly influenced by the electronic structure of the organic layer.

We note that μ derived from the fp-TRMC measurements (on $n = 1$ films) can not be compared to the μ_e obtained with the $\langle n \rangle = 5$ SCLC devices. However, they are consistent with the established behavior that electrode-based measurements generally give lower μ than spectroscopic methods. ^[214] Regardless, the determined SCLC mobilities are in the same range as found in the literature. Our measured μ_e for the BA reference system is higher than previously reported for $\langle n \rangle = 2$ $(\text{BA})_2(\text{MA})_3\text{Pb}_4\text{I}_{13}$ films ^[95] but lower than the reported μ_e of pure MAPbI₃ single crystals ^[215] and the in-plane μ_e of single-crystal $(\text{PEA})_2(\text{MA})_2\text{Pb}_3\text{I}_{10}$ perovskites. ^[92]

We cannot completely discount crystalline orientation effects in the μ measurements. Indeed, in contrast to NDI-dH-based thin films, the XRD of our BA-based perovskite films show diffraction peaks below $2\Theta = 10^\circ$, as shown in Figure 4.9f. Such low-angle diffraction peaks are associated with layered or quasi-layered perovskite phases oriented parallel to the substrate acting as an insulating layer and reducing the mobility in the BA-based thin films.

Finally, we note that considering the strong ion migration observed in halide perovskite materials, it remains controversial whether SCLC measurements can accurately give information about μ and $n_{t,\min}$. However, the pulsed voltage sweep SCLC method allows the mitigation of

the ion migration effects.^[213,216,217] Using a voltage pulse of 50 ms duration and screening different dwell times ranging from 0.1 to 60 s, no difference in the I - V -curve was observed, indicating no impact of the ion migration on the obtained electron mobility for NDI-dH based $\langle n \rangle = 5$ films as displayed in Figure B.11, suggesting that the mobilities obtained with the continuous voltage scan provides electron mobilities not affected by potential ion migration.

4.5 Conclusion

While in Chapter 3, we assumed that prolonging the amine-bearing alkyl chain facilitates the incorporation of NDI-based spacer cations into a layered structure, we successfully demonstrated the application of this previously elaborated strategy on Dion-Jacobson-based divalent spacer cations and incorporated a novel NDI-based dication into a layered perovskite structure. Our findings contrast previous works on NDI-based dications with short alkyl chains (NDIC2), where the formation of a 1D perovskitoid structure was reported. In contrast to the 1D perovskitoid nanowires, the optical properties based on visible light absorption measurements are similar to the features observed in $(\text{BA})_2\text{PbI}_4$ suggesting the formation of a 2D layered perovskite structure.

The incorporation of the electron-accepting NDI-dH dication into a layered perovskite structure was found to form a type II heterostructure where photogenerated electrons transfer from the inorganic layer to the organic spacer resulting in PL quenching and ultrafast PL-decay as investigated by FLUPS.

Time-resolved microwave conductivity measurements on the (NDI-dH) PbI_4 films show a peak sum mobility almost one order of magnitude larger than determined in the previously reported 1D perovskitoid structure. However, similar to the photoconductivity determined in the NDI-based RP phases, the photoconductivity is still lower than in $(\text{BA})_2\text{PbI}_4$. We hypothesized that the mobility is limited by the charge carrier transport of the electrons located on the NDI. Ultrafast optical-pump terahertz-probe spectroscopy was used to investigate the formation of the free charge carriers a few ps after photoexcitation. Indeed, a fast decay upon photoexcitation is observed by the terahertz spectroscopy technique, potentially due to the electron transfer to the chromophore cation. Moreover, the peak mobility is similar to what was previously reported in $(\text{BA})_2\text{PbI}_4$ films.

Based on the successful formation of a layered perovskite phase, we investigated the electron transfer from the inorganic to the organic layer. We obtained thin films with clear features attributed to the $n = 2$ and $n = 3$ phases. For films where we aimed for the (NDI-dH) $\text{MA}_4\text{Pb}_5\text{I}_{16}$ ($\langle n \rangle = 5$) phase, the formation of MAPbI_3 was reduced while no excitonic absorption band for the (NDI-dH) $_2\text{PbI}_4$ was observed, suggesting a more homogeneous phase distribution. While $\langle n \rangle = 5$ films incorporating NDI-dH show higher stability compared to BA-based films ($\langle n \rangle = 5$), the

origin of the improved stability remains unknown. The homogeneous phase distribution, most of the phases being layered perovskite phases with relatively small ($n = 5$) widths of the inorganic slabs, may strongly contribute to the enhanced stability. Moreover, the large NDI-dH cation may be more hydrophobic than BA, efficiently protecting the LHOIP from moisture-induced degradation.

Further investigation allowed us to extract the dynamic of the electron transfer to the NDI by transient absorption spectroscopy, where an increase in the transfer rate to the NDI with increasing quantum well width was found. The hypothesized type II heterostructure and subsequent electron transfer from the inorganic to the organic layers are consistent with the observed quenching of the PL in these materials. To our surprise, electron tunneling from phases with low n to phases with higher n was observed, despite the relatively large interplanar distance induced by the NDI-cation.

Recent studies suggest that the formation of a 1D perovskitoid structure is a limitation for the application in optoelectronic devices. To confirm that the herein investigated quasi 2D perovskite structure allows efficient charge carrier transport through the thin film, electron-only devices were fabricated, and space-charge limited current (SCLC) was measured. The obtained I - V line shapes show a distinct ohmic and SCLC region but lack the presence of any trap-filling region, indicating an effective trap density lower than the minimum trap density. These findings are distinct from the BA-based reference materials, where a clear trap-filling region was observed.

The material herein presented is currently under investigation for solar cell device application. The improved stability and potential formation of more homogeneous phase distribution in quasi-layered perovskite with observed charge transfer from the inorganic layer to the organic layer upon photoexcitation may be a promising strategy to overcome the high exciton binding energy while maintaining high stability. However, the effects of different phase distributions and electronic interactions between the cation and the multiple quantum well perovskite phases on the photovoltaic performance still need to be explored. Moreover, further insights into potential electron transport through the organic layer are required.

Chapter 5

Free Charge Carrier Generation by Visible-light-absorbing Chromophore Spacer in Ruddlesden-Popper Type Perovskites

5.1 Abstract

Incorporating spacer cations based on semiconducting building blocks into a layered perovskite structure has shown to be a promising approach for tuning the optoelectronic properties of these materials. Based on the electronic interactions between the organic and inorganic layer, incorporating visible-light-absorbing spacer chromophores provides the possibility to enhance light absorption and free charge carrier generation in the resulting LHOP semiconductor. Moreover, being able to selectively photoexcite the spacer cation greatly enhances the spectroscopic tools suitable for studying these materials. However, suitable visible-light-absorbing spacer cations are rarely reported. In the herein presented work, we introduce a novel spacer cation based on a core-modified naphthalene diimide chromophore. By forming mixed I^-/Br^- halide composite layered perovskite structures, we tune the electronic structure of the inorganic layer and demonstrate the formation of type I and type II heterostructures depending on the halide mixture. Based on the various energy alignments, we investigate the formation of free charge carriers upon photoexcitation by TRMC and show that light absorption by the spacer cation can contribute to the formation of free charge carriers.

The presented results on PDI (synthesis and aggregation in solution) are based on data obtained during the master thesis by S. Nussbaum.^[218] PDI-H:PbI₂ Perovskite films were newly fabricated using adapted synthetic conditions based on the work elaborated in Chapter 3.

Herein presented transient absorption spectra were recorded by Aaron Terpstra. UPS measurements were performed by Dr. Mounir Mensi.

Results and data presented in this chapter are used for future publication under preparation.

5.2 Introduction

Engineering the properties of layered perovskite (LHOIP) and quasi-layered perovskite materials by modifying the spacer cations and understanding the structure-properties relationship has recently become the focus of researchers in order to adapt these materials for the application in optoelectronic devices.^[105,219] In this context, incorporating organic semiconducting building blocks into layered perovskite materials is an interesting approach to achieving new semiconductors where the organic spacer cation contributes electronically to the optoelectronic properties of these materials.^[121,122,134] By tuning the electronic properties of the organic spacer chromophore, the properties of the semiconductor can be shifted from a type I heterostructure (quantum well structure) to a type II heterostructure where the HOMO and LUMO energy levels of the spacer cation are offset to the CB and VB of the perovskite layer, as illustrated in Figure 5.1.

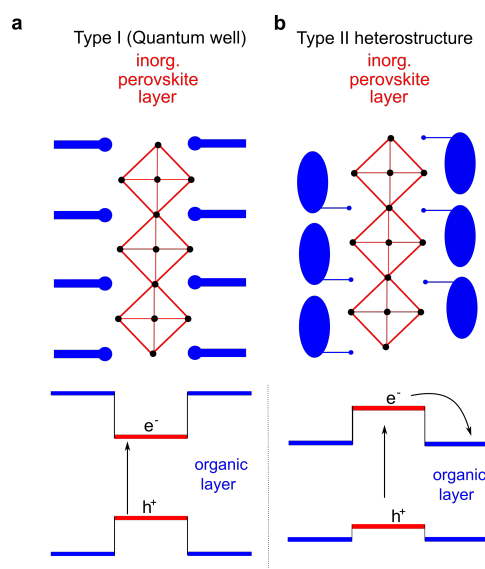


Figure 5.1 – Electronic structure of **a)** layered perovskite incorporating simple aliphatic spacer cations and **b)** incorporating organic semiconducting spacer cations.

Previously reported type II layered perovskite heterostructure systems have been shown to exhibit long-lived charge separation^[123,136] due to electron transfer from the inorganic layer to the organic layer upon photo-excitation. Localization of the electron and holes in the organic and inorganic layer, respectively, may increase the charge carrier separation efficiency, providing an strategy to overcome the high exciton binding energies often found in LHOIPs.^[148,199] The increased tunability makes type II heterostructure systems an interesting class of materials for various applications, such as LEDs or solar cell devices.

In Chapter 3 and Chapter 4, we demonstrated the incorporation of monovalent and divalent spacer cations based on a naphthalene diimide chromophore core forming RP and DJ LHOIP phases, respectively. Studies of the optoelectronic properties suggest rapid electron transfer to the organic spacer, as illustrated in Figure 5.1b, and the formation of long-lived free charge carriers as determined by flash photolysis time-resolved microwave conductivity measurements (fp-TRMC). We hypothesized that the observed lower photoconductivity determined by fp-TRMC in NDI-based LHOIPs compared to $(\text{BA})_2\text{PbI}_4$ is due to the reduced mobility of the charge carriers along the organic layer. This assessment was further supported by the fast transient observed in optical-pump terahertz-probe (OPTP) spectroscopy in Chapter 4.

While we sought to understand the charge carrier properties in oriented quasi-layered perovskite materials incorporating NDI-dH by SCLC, the formation of poly-dispersed quantum wells of various well widths and the resulting electron funneling overshadows the effect of the NDI spacer cations on the charge carrier transport in quasi-layered films. Focusing on phase-pure ($n = 1$) layered perovskite films and the formation of a single well quantum width eliminates the potential effects of electron funneling processes. However, the preferential orientation of the LHOIP on thin film where the inorganic slabs lay parallel to the substrate limits the toolbox for the characterization of the charge carrier properties. Moreover, investigation of potential hole injection from the spacer cation into the octahedral layer by spectroscopic techniques is limited, as the NDI chromophore can not be selectively photo-excited. A more comprehensive approach to further study the effect of such organic-inorganic type II heterostructure systems is by incorporating visible-light-absorbing spacer cations where the spacer cation is selectively excited by optical pump-probe setups (e.g., transient absorption spectroscopy or fp-TRMC). Incorporating an optical active spacer cation provides the opportunity to increase the optical contribution of the chromophore to the light-harvesting process. This might be an interesting approach to further increase the visible light absorbance in solar cell devices.

The family of rylene dyes, such as perylene and naphthalene diimide chromophores, constitutes an interesting class of visible-light-absorbing spacer cations. However, the incorporation of visible-light-absorbing perylene diimide spacer cation into a LHOIP has yet to be shown. Moreover, a better understanding of the mechanism governing the incorporation of the spacer cation into the layered perovskite structure is required to tune and design new spacer cations. Based on our previous research on NDI-based spacer cations, we modified the core of the NDI and synthesized a spacer cation with enhanced conjugated systems obtaining a visible-light-absorbing chromophore cation. Moreover, by tuning the electronic structure of the inorganic layer via halide mixing, we tune the alignment from a type II heterostructure to an inverted type I heterostructure and compare the free charge carrier dynamics by fp-TRMC in these materials by selectively exciting the spacer cation.

5.3 Experimental

Synthesis of the Spacer Cations

PDI-H cations are synthesized based on a two-step reaction from perylene-diimide. Detailed synthetic procedures can be found in Appendix C.

NDI-DAE cation was synthesized in a one-step reaction. Detailed synthesis and characterization of the products and intermediates can be found in Appendix C. In short, 1 molar equivalent of naphthalene dianhydride (NDI) was mixed with 1.05 molar equivalent of diamino ethyl and 1.05 molar equivalent of the corresponding NBoc-1,4-diamino butane. After dissolution in DMF (dry), the reaction was heated to 120 °C and stirred for 12 hours under an argon atmosphere. After purification by flash column chromatography in moderate yield. The material was further deprotected by trifluoro acetic acid (TFAA) and treated with HI and HBr, respectively, to obtain the desired NDI-DAE salt.

Sample Preparation

Thin films of (NDI-DAE)₂PbI(I_{1-x}Br_x)₄ were formed using a 0.4 M NDI-DAE + 0.2 M PbI₂ in DMSO solution. All films were spin-coated at 2000 rpm for 30 seconds and subsequently annealed at 200 °C for 10 minutes in a nitrogen-filled glovebox.

The *n*-butylammonium (BA) reference samples were formed by mixing the required ratios of a 0.4 M BA + 0.2 M PbI₂, and 0.4 M BA + 0.2 M PbBr₂ solution in DMSO, respectively. The precursor solution was spin-coated on quartz-substrate at 2000 rpm for 30 seconds. The films were annealed at 90 ° for 10 minutes.

UV-vis Absorption and Photoluminescence Measurements

UV-Visible light absorption measurements were carried out with a UV-3600 Shimadzu spectrometer. The unannealed samples were stored in an argon filled glovebox until shortly before the measurement. For the *in-situ* kinetics studies, NDI-DAE-based layered perovskite thin films were synthesized from a DMF precursor solution to ensure comparability with previous NDI-E, NDI-B, and NDI-H based perovskites. The same home-built transparent heating window was used as described in Chapter 3. The measurement was carried out under ambient conditions.

Transient Absorption Spectroscopy and Microwave Conductivity Measurement

Optical spectroscopy measurements and fp-TRMC measurements were performed as described in Chapter 3.

5.4 Results and Discussion

We start by investigating the incorporation of a perylene diimide (PDI) based spacer cation into a layered perovskite structure. Based on our previous findings on the importance of the amine-bearing linker chain length for the successful formation of LHOIP with NDI-based monocations, we synthesized a monovalent PDI chromophore which is connected to an amine-bearing hexyl chain that is linking the chromophore to the inorganic layer in the layered perovskite structure. The structure of the designed PDI-cation is displayed in Figure 5.2a and is denoted as PDI-H in the following. The second imide position was functionalized with a swallow-tail alkyl chain to make the salt more soluble in common solvents used in perovskite synthesis. Detailed synthetic conditions of the recently developed synthetic scheme are displayed in Figure C.1 (Appendix).^[218] The visible light absorption spectrum of the PDI-H cation spin-coated on glass displayed in Figure 5.2b shows the absorption of light in the range of 450 to 550 nm. To investigate whether PDI-H can form a layered perovskite phase, a precursor solution of PDI-H dissolved in a PbI_2 DMF solution to obtain a molar ratio PbI_2 : PDI-H of 1:2 was spin-coated on a glass substrate, and subsequently annealed at 200 °C. The resulting absorption spectrum of the thin film is displayed in Figure 5.2b and shows a strong contribution of the PDI chromophore to the absorption of the Pb_2 -chromophore film, while no excitonic absorption band as similarly found in NDI-based LHOIPs was observed. The XRD of the resulting film is displayed in Figure 5.2c and shows a completely amorphous film suggesting no formation of a crystalline LHOIP phase.

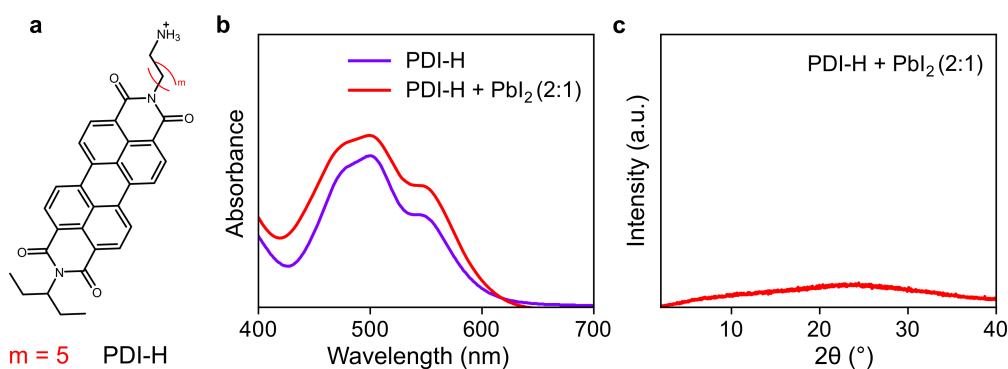


Figure 5.2 – **a)** Structure of PDI-H and **b)** visible light absorption spectra of the PDI-H cation as spin coated on a glass substrate and PbI_2 :PDI-H precursor solution spin-coated and annealed at 200 °C for 10 minutes. **c)** XRD of the PbI_2 :PDI-H thin film shows no indication for the formation of a layered perovskite structure.

As it is widely known that PDI molecules tend to aggregate in solution at high concentrations, it was hypothesized that the aggregation of the spacer cation in the precursor solution hinders the formation of a layered perovskite structure.^[220,221] Indeed, by investigating the visible

light absorption spectra at different PDI-H concentrations in DMF, displayed in Figure C.2, we observe signs of aggregation indicated by a shift of the absorption band intensities. Notably, the aggregation-induced changes in the absorption spectra are observed even at concentrations that are orders of magnitude lower than typically used for the film formation of layered perovskite materials. We hypothesized that the increased aromatic system results in stronger π - π and aggregation in the precursor solution hampering the incorporation of the spacer cation into a layered perovskite structure.

Design and Incorporation of NDI-DAE Spacers

In order to further investigate the size limitation of the rylene dye core, we moved to a bottom-up approach for rationally designing novel semiconducting chromophores. Using the successful incorporation of NDI-based spacer cations described in Chapter 3 as a template, we modified the chemical and electronic structure of the NDI chromophore by expanding the aromatic conjugated system. While the first imide position was functionalized with diamino ethyl, forming a fused imidazole system conjugated with the aromatic core of the NDI, the second imide position of the chromophore was attached to a butyl-ammonium linker chain. The chemical structure of the spacer cation is displayed in Figure 5.3a and is denoted as NDI-DAE.

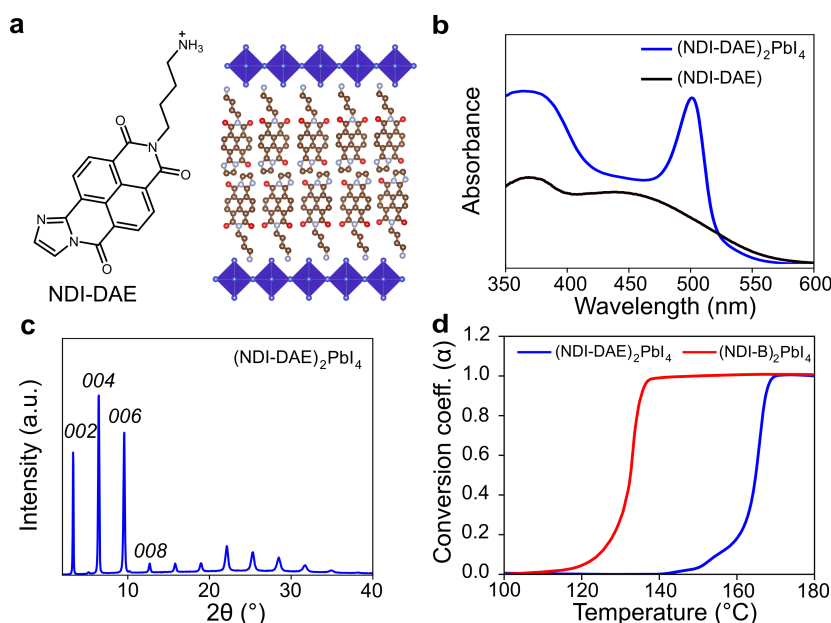


Figure 5.3 – **a**) Chemical structure of NDI-DAE and aimed crystal structure of the Layered perovskite material. **b**) Visible light absorption of the NDI-DAE cation and (NDI-DAE)₂PbI₄ LHOIP and PL of (NDI-DAE)₂PbI₄, and **c**) XRD of the (NDI-DAE)₂PbI₄. **d**) The required annealing temperature for the formation of (NDI-DAE)₂PbI₄ in comparison to (NDI-B)₂PbI₄.

Detailed synthetic procedures for the NDI-DAE-cation can be found in Appendix C. Compared to NDI, NDI-DAE has an enlarged aromatic system that strongly affects the electronic structure by reducing the HOMO-LUMO gap, while the chromophore core is smaller than the previously investigated PDI-H cation. The visible light absorption spectra of NDI-DAE spin-coated on glass show visible light absorption between 450 and 550 nm, as shown in Figure 5.3b. Following the procedure developed in Chapter 3 to form the layered perovskite structure, NDI-DAE was mixed in the precursor solution in DMSO and spin-coated on a glass slide, and subsequently thermally annealed at 200 °C. The visible absorption spectrum of the annealed film is displayed in Figure 5.3b, showing a strong excitonic absorbance band in the range of 500 nm suggesting the formation of a layered perovskite structure. Moreover, a weak PL emission band is observed at around 520 nm, as displayed in Figure C.3. The XRD is displayed in Figure 5.3c and shows equidistant diffraction peaks corresponding to the $00l$ diffraction plane of the in-plane oriented $(\text{NDI-DAE})_2\text{PbI}_4$ phase. Based on the first diffraction peak, an interplanar distance of 27 Å was determined, which is similar to the previously reported spacing for NDI-B (see Chapter 3).

Notably, the crystalline phase and the optical properties corresponding to a layered perovskite structure were only obtained when annealed at temperatures of more than 170 °C. To compare the annealing temperature required for the formation of the $(\text{NDI-DAE})_2\text{PbI}_4$ LHOIP, we investigated the evolution of the excitonic absorption band by *in-situ* absorbance measurement described in Chapter 3. Briefly, by increasing the temperature of the FTO window gradually at a rate of 0.25 K s^{-1} and measuring the absorbance at the wavelength of the excitonic absorption band, the evolution of the layered perovskite phase formation was tracked. Based on the absorbance at a given wavelength and at a given temperature T ($A(T)$), and the absorbance at the beginning (A_{init}) and end (A_{fin}) of the measurements, the conversion coefficient (α) was determined by the following relationship:

$$\alpha = \frac{A(T) - A_{init}}{A_{fin}} \quad (5.1)$$

The temperature increase triggers the formation of the perovskite phase, as indicated by the increasing conversion coefficient α , displayed in Figure 5.3d. Comparing the evolution of the absorbance band with increasing temperature with previously investigated $(\text{NDI-B})_2\text{PbI}_4$ phase formation, a clear difference can be observed where the $(\text{NDI-DAE})_2\text{PbI}_4$ requires a higher annealing temperature to form the LHOIP phase than $(\text{NDI-B})_2\text{PbI}_4$. We assume that this need for enhanced annealing temperature arises from increased aromatic interactions between the organic cations in the as-spin-coated NDI-DAE:PbI₂ films, requiring higher thermal energy to re-orientate the aggregates in order to form the crystalline structure.

Notably, a layered perovskite structure can also be formed when a NDI-DAE-chromophore with a longer amine-bearing hexyl chain is used as a linker. Similarly to the observed trends in Chapter 3 and Chapter 4, lower crystallinity is obtained, as shown in Figure C.4. Moreover, no indication of a layered perovskite structure was found when NDI-DAE with an amine-bearing ethyl linker chain was investigated, as displayed in Figure C.5. These findings further underline the importance of the length of the amine-bearing alkane chain for the successful incorporation into a layered perovskite structure.

While XRD and absorption spectra suggest the formation of a layered perovskite structure, the PL-intensity of the $(\text{NDI-DAE})_2\text{PbI}_4$ is quenched when compared to $(\text{BA})_2\text{PbI}_4$, as illustrated in Figure C.3. PL quenching can be attributed to the electron transfer from the inorganic layer to the NDI-DAE chromophore due to a type II heterostructure. The electronic structure of NDI-DAE was determined by ultraviolet photoelectron spectroscopy (UPS), confirming the formation of a type II heterostructure, as shown in Figure C.6 and Figure C.7.

To investigate whether the formation of a type II heterostructure can enhance charge separation and creates long-lived free charge carriers, as similarly seen in NDI-based RP perovskite, we turned to flash-photolysis time-resolved microwave conductivity (fp-TRMC) measurements. The obtained transient and calculated photoconductivities for different photon flux is displayed in Figure 5.4, where sum mobilities of $2 \cdot 10^{-4} \text{ cm}^2 \cdot \text{V}^{-1} \cdot \text{s}^{-1}$ at $3 \cdot 10^{13}$ absorbed photon flux per cm^2 assuming ϕ to be 1. The determined mobilities show the characteristic dependency on the absorbed photon flux where with increasing excitons generation, exciton-exciton interactions cause a reduction of the determined photoconductivity. We note that the determined photoconductivities are lower than for the more conventional $(\text{BA})_2\text{PbI}_4$ at the same photon flux and lower than recently investigated $(\text{NDI-B})_2\text{PbI}_4$ thin films. We assume that the reduced mobility of the electrons in the organic layer results in the observed lower photoconductivity, similarly as previously elaborated in Chapter 3 and 4 in NDI-based LHOIP thin films.

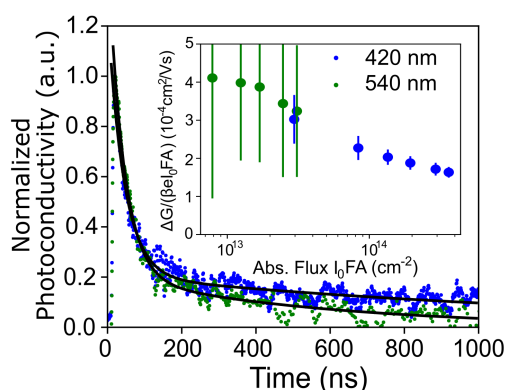


Figure 5.4 – TRMC transient of $(\text{NDI-DAE})_2\text{PbI}_4$ when excited at 420 nm and 540 nm.

The formation of spatially separated electrons and holes in the inorganic and organic layers of the LHOIP, respectively, may further cause the prolonged transient decay in (NDI-DAE)₂PbI₄ where the free charge carrier decay can be fit to a bi-exponential decay with a short ($\tau_1 = 28$ and 30 ns, respectively) and a long ($\tau_2 = 400 - 900$ ns) decay constant. This contrasts the free charge carrier dynamics in (BA)₂PbI₄, where the transient decays with a single time constant of around 17 ns. Notably, comparable photoconductivities and decay dynamics were obtained when the samples were photoexcited at 540 nm at an absorbed photon flux of $3 \cdot 10^{13} \text{ cm}^{-2}$, as shown in the inset of Figure 5.4. While a measurable TRMC signal up to 540 nm may suggest a contribution of the spacer cation to the light-harvesting process, the overlap between the excitonic absorption band and the absorption of the spacer cation is limiting further studies, and systems with fewer spectral overlap are required.

While there are only a few examples of chromophores spacer cations based on 5 aromatic rings reported, and based on our observations with PDI-H-based cations, we empathize that with NDI-DAE we reached the potential size limitation of the rylene dye-based spacer cation. Further expanding the conjugated aromatic system in such a planar aromatic system will likely hamper the incorporation of such cations into a layered perovskite structure. This said, tuning the absorbance range of the spacer cation by reducing the HOMO-LUMO gap and potentially forming inverted type I heterostructures where the HOMO and LUMO energy levels of the cations lay between CB and VB of the inorganic perovskite layer is a challenging approach. Therefore we turned to possibilities to tune the electronic structure of the inorganic perovskite layer.

Tuning the CB and VB Energy Levels of the Perovskite by Halide Composition Engineering

As the band structure is determined by the p-orbitals of the halide (VB) and the overlap of 6p orbitals of lead and p orbitals of the halide (CB), the simplest way to tune the electronic structure of the inorganic layer is by the engineering of the halide composition as already demonstrated in 3D and quasi-layered perovskites.^[222] However, mixed halide systems are considered pseudo-binary alloys where the halides are not distributed homogeneously through the inorganic layer.^[53,223–225] As Seitz *et al.* previously suggested, local fluctuation of the halide concentration and site-to-site disorder alters the band gap locally, and the diffusion of excitons and free charge carriers through the material is strongly affected.^[226]

To investigate the effect of halide mixture on the optoelectronic and charge carrier properties in BA-based (BA)₂Pb(I_{1-x}Br_x)₄ with various Br⁻ and I⁻ content (with $x = 1, 0.75, 0.50, 0.25$, and 0) were investigated. BA is optically and electronically inactive, so the charge carrier dynamics solely arise from the inorganic perovskite layer. The UV-vis absorption of (BA)₂Pb(I_{1-x}Br_x)₄

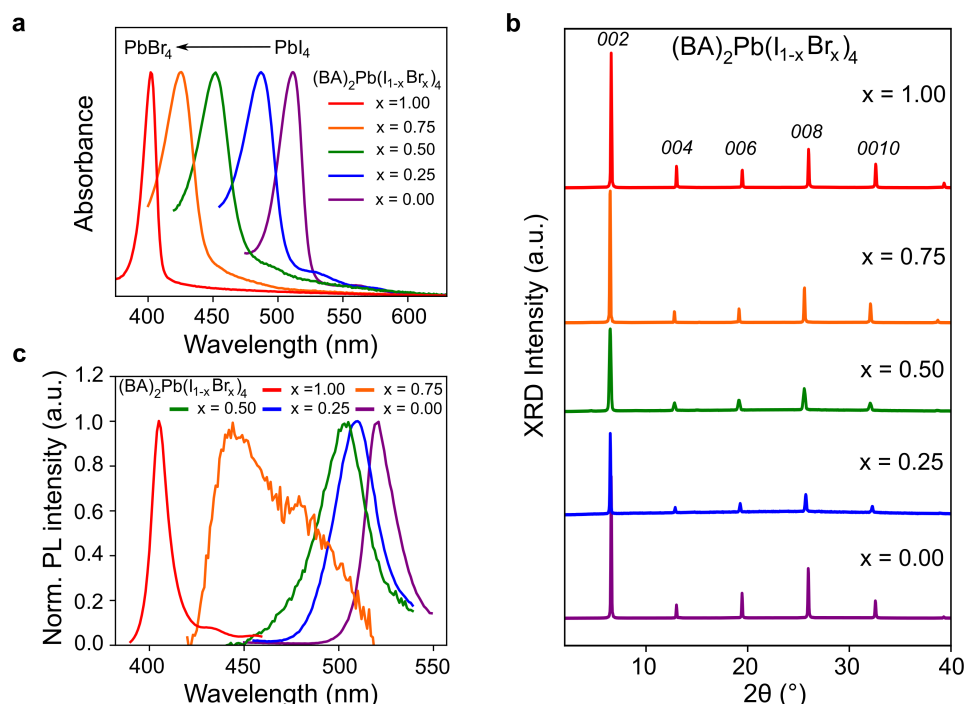


Figure 5.5 – **a)** Visible light absorption, **b)** XRD and **c)** PL emission spectrum of mixed halide LHOIPs of the general formula $(\text{BA})_2\text{Pb}(\text{I}_{1-x}\text{Br}_x)_4$.

thin films are displayed in Figure 5.5a, showing a shift of the excitonic absorption band from 520 nm for pure $(\text{BA})_2\text{PbI}_4$ to around 400 nm for $(\text{BA})_2\text{PbBr}_4$ suggesting an increase in the band gap energy. The interplanar spacing determined for d_{002} for the different compounds is not affected by the halide mixture, as no shift in the XRD diffraction peaks displayed in Figure 5.5b was observed.

Based on the various thin films, the VB energy levels of the different materials were estimated by UP spectroscopy. UPS measurements of the $(\text{BA})_2\text{PbI}_4$ and $(\text{BA})_2\text{PbBr}_4$ films are displayed in Figure C.7 and Figure C.8, showing the stabilization of the VB and the destabilization of the CB. Previous reports further support the assessment of the VB energy levels.^[227] Similarly to the visible light absorption spectra, PL spectra displayed in Figure 5.5c show a shift of the characteristic excitonic emission band towards higher energies with increasing bromide content. However, in contrast to the observed continuous shift in the visible light absorption spectra, the Stokes shift becomes larger when the inorganic layer is composed of a halide mix. The increase in the Stokes shift may indicate exciton transfer from iodide-poor regions with a large band gap to the iodide-rich regions with smaller band gaps.

The photoconductivity all halide mixture thin films obtained by fp-TRMC are displayed in Figure 5.6a. With increasing bromide content, the photoconductivity decreases, reaching a minimum for the $(\text{BA})_2\text{Pb}(\text{I}_{0.5}\text{Br}_{0.5})_4$ and $(\text{BA})_2\text{Pb}(\text{I}_{0.25}\text{Br}_{0.75})_4$ film. For the mixed halide films,

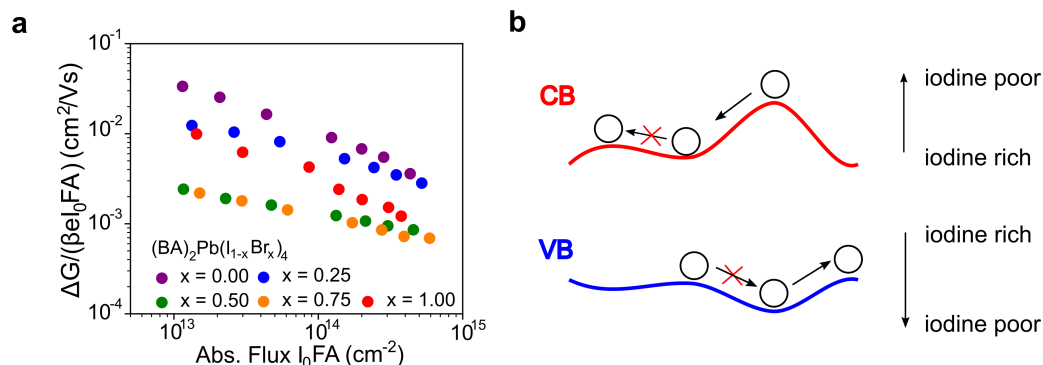


Figure 5.6 – **a**) Sum mobilities of $(\text{BA})_2\text{Pb}(\text{I}_{1-x}\text{Br}_x)_4$ thin films determined by fp-TRMC assuming $\phi = 1$. **b**) The trend in TRMC sum mobilities can be rationalized by previously reported inhomogeneity hampering the charge carrier mobility through the inorganic layer.

the photoconductivity was found to be more than one order of magnitude lower than observed on the $(\text{BA})_2\text{PbI}_4$ films. Although the decrease in photoconductivity with increasing bromide content can be explained by an increase in the exciton binding energy limiting the formation of free charge carriers, we emphasize that the mobility is limited by the formation of the pseudo-binary alloy depicted in Figure 5.6b. Notably, the trend in photoconductivity is consistent with recently reported lower exciton diffusion in mixed halide systems due to the trapping of the electrons and holes in iodide-rich and iodide-poor regions, respectively.^[226] Moreover, the pure $(\text{BA})_2\text{PbBr}_4$ film shows higher mobility than the mixed halide systems. The differences in determined photoconductivity between $(\text{BA})_2\text{PbI}_4$ and $(\text{BA})_2\text{PbBr}_4$ by a factor of 2 is attributed to the lower dielectric constant of the bromide-based octahedral perovskite structure compared to the iodide-based perovskite reducing the quantum yield of the absorbed photons generating free charge carriers.

Investigation of Mixed Halide NDI-DAE-Based LHOIP

Given the successful formation of $(\text{NDI-DAE})_2\text{PbI}_4$ and the possibility of tuning the electronic structure by composition engineering of the halide distribution in the inorganic layers, we aim to investigate different energy alignments between the NDI-DAE chromophore and the perovskite layer by tuning the halide mixture in the inorganic layer. Consistently, as observed in $(\text{BA})_2\text{Pb}(\text{I}_{1-x}\text{Br}_x)_4$ films, the characteristic excitonic absorption band shifts towards higher band gap energy upon increased bromide content, as illustrated in Figure 5.7a where for the $(\text{NDI-DAE})_2\text{PbBr}_4$ only the NDI-DAE chromophore absorbs in the range between 420 and 560 nm. The interplanar distances remain unchanged for all investigated halide mixtures, as shown

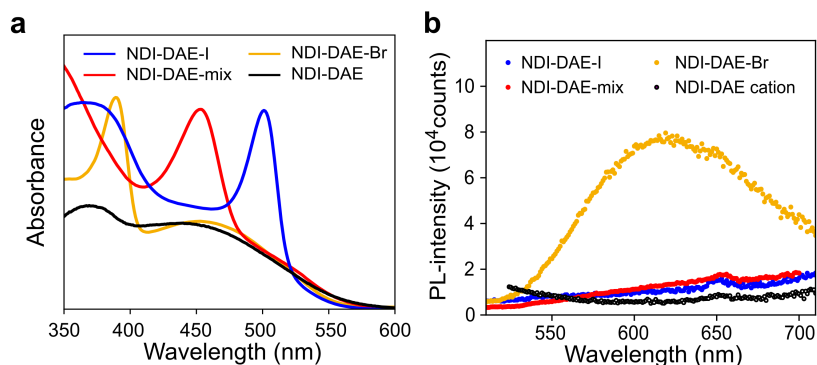


Figure 5.7 – **a)** Visible light absorbance of NDI-DAE-I, NDI-DAE-mix and NDI-DAE-Br thin films as well the visible light absorbance of the spacer chromophore. **b)** PL emission of the corresponding thin films excited at 400 nm. The PL quenching of the NDI-DAE-mix and NDI-DAE-I films is potentially due to the type II heterostructure arrangement where the PL is quenched due to hole transfer to the organic chromophore to the NDI-DAE chromophore to the inorganic layer.

in the XRD in Figure C.9. We focus in the following on three cases of different halide mixtures in the inorganic layer. For the sake of clarity, the different compositions are referred to as NDI-DAE-Br, NDI-DAE-I, and NDI-DAE-mix for the pure bromide-based ((NDI-DAE)₂PbBr₄) LHOIP, the pure iodide-based ((NDI-DAE)₂PbI₄) LHOIP, and for the LHOIP containing a 1:1 halide mix ((NDI-DAE)₂Pb(I_{0.5}Br_{0.5})₄), respectively.

The PL spectra of the three films are displayed in Figure 5.7b showing a broad emission band with an emission maximum at 600 nm for NDI-DAE-Br films. Selectively exciting the spacer cation at around 500 nm and performing emission spectra at the emission band at 600 nm shows the origin of the PL emission to be the spacer cation, as illustrated in Figure C.10. Indeed, the PL emission is characteristic of the NDI-DAE chromophore as previously reported in solution.^[228] Surprisingly, no such emission is observed for the NDI-DAE-mix and NDI-DAE-I thin films. Spin-coating the pure spacer cation on a quartz substrate results in no observable PL emission, suggesting aggregation-induced quenching when the spacer is not incorporated into a layered perovskite structure. We hypothesized that the PL quenching from the chromophore is due to different energy alignments between the chromophore and the inorganic layers, where in the case of the NDI-DAE-I and NDI-DAE-mix films, hole injection from the inorganic layer quenches the PL from the organic chromophore, as displayed in Figures 5.8a.^[229] On the other hand, NDI-DAE-Br forms an inverted type I heterostructure, where hole injection from the NDI-DAE chromophore to the perovskite layers is inhibited, and PL emission from the chromophore is facilitated, as displayed in Figure 5.8b. This hypothesis is supported by the energy alignment found by UPS measurements, suggesting the HOMO energy level of the cation above the VB energy level of the PbBr₆⁴⁻ perovskite framework, as displayed in Figure 5.8c. In (NDI-DAE)₂PbI₄,

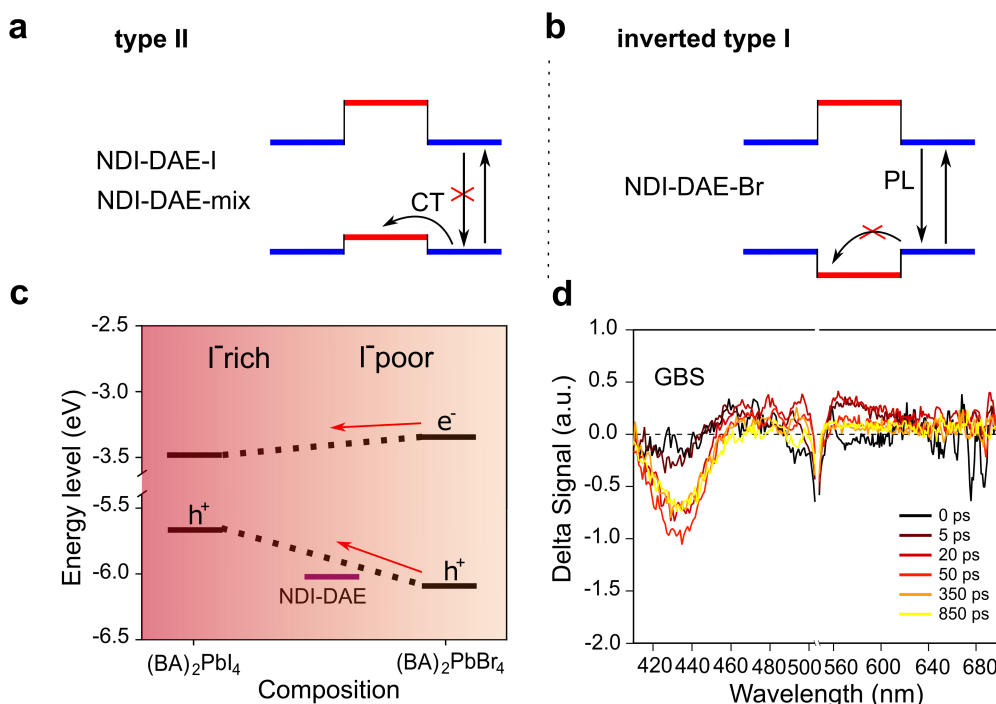


Figure 5.8 – Schematic presentation of the energetic structure of **a)** a type II heterostructure, and **b).** inverted type I heterostructure. **c)** Illustration of conduction and valence band energy levels of NDI-DAE relative to (BA)₂PbI₄ and (BA)₂PbBr₄ determined by Ultraviolet photoelectron spectroscopy (UPS). **d)** TA slices of NDI-DAE-mix after photoexcitation at 525 nm.

the HOMO energy level of the NDI-DAE is found to be below the VB energy level of the PbI₆⁴⁻ perovskite layer. Moreover, the hole injection is supported by preliminary TA spectroscopy results where the NDI-DAE cation in the NDI-DAE-mix was selectively excited at 525 nm. The resulting TA slices are displayed in Figure 5.8d. By only exciting the spacer cation, a weak ground state bleach with a delay of around 20–50 ps at 440 nm. We contribute the presence of a GSB to the hole injection from the chromophore to the perovskite. The position of the ground state bleach corresponds to the absorption band for the mixed halide perovskite layer. Given the inhomogeneity in the halide distribution of the perovskite, we note that exciton diffusion may cause such a GSB in specific cases. However, given the electronic structure of the pure bromide-based and pure iodide-based layered perovskite displayed in Figure 5.8c, hole and electron transfer from the iodide-rich to the iodide-poor region is thermodynamically not favored. On the other hand, electron and hole transfer from the bromide-rich to the iodide-rich phases is thermodynamically possible and is manifested in an increased Stokes shift, as described in the previous section.

Formation of Free Charge Carriers in Mixed Halide Layered Perovskites

To further investigate the potential formation of free charge carriers by the absorption of the chromophore spacer cations, NDI-DAE-mix was excited at different wavelengths, and the fp-TRMC transient was recorded. Based on the wavelength-dependent TRMC peak photoconductivities, an action-spectrum proportional to the photogenerated free charge carrier concentration can be derived as previously reported.^[230] This allows to assess the contributions of the spacer chromophore to the free charge carrier generation. Figure 5.9a shows the intensity normalized maximum photoconductance $\Delta G_{\text{max}}/(\beta I_0 q)$ as a function of wavelength after photoexcitation. Thereby, the y-axis in Figure 5.9a represents the peak photoconductivity normalized by incident light intensity but not by the absorbance of the sample. By doing so, the absorbance spectrum of the mixed halide thin film can be reproduced in good approximation, showing a clear contribution to the formation of free charge carrier upon excitation in the range from 500 nm to 550 nm. As in this range only the NDI-DAE chromophore absorbs, the results suggest that the hole transfer from the organic spacer to the inorganic layer in the NDI-DAE-mix thin film after photoexcitation of the NDI-DAE chromophore can contribute to the free charge carrier generation in the LHOIP. Arguably, the shape of this action-spectrum does not completely overlap with the absorption spectra because the photoconductivity is dependent on the absorbed photon flux.

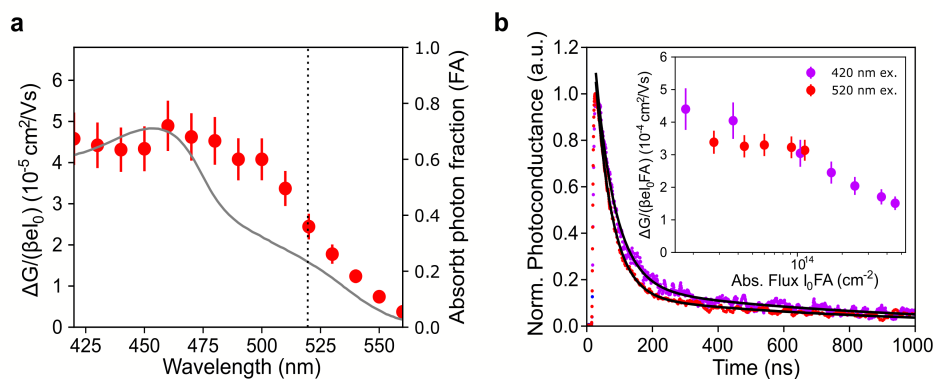


Figure 5.9 – **a)** Peak photoconductivity at various wavelength for NDI-DAE-mix normalized by incident light intensity but not absorbance. **b)** Transient of the free charge carrier dynamics when excited at 420 and 520 nm at $3 \cdot 10^{13}$ absorbed photons per cm^2 . The inset shows the photoconductivity at different absorbed photon flux. The error bars are calculated based on uncertainties given by the photon fluence.

We therefore excited the same film at 420 nm with different photon densities. At 420 nm, the perovskite as well as the organic chromophore are excited. Additionally, the same film was excited at 520 nm, where only the chromophore absorbs. The obtained transients are displayed in Figure 5.9b. At 420 nm excitation, at an absorbed photon flux of $3 \cdot 10^{13}$ photoconductivity

of $4 \cdot 10^{-4} \text{ cm}^2 \cdot \text{V}^{-1} \cdot \text{s}^{-1}$ was obtained in the NDI-DAE-mix thin film. Notably, the obtained photoconductivity is higher than the photoconductivity obtained for the $(\text{NDI-DAE})_2\text{PbI}_4$. These findings are surprising, as a reduced mobility in mixed halide systems incorporating aliphatic BA spacer cations due to local disorder in the pseudo-alloy was shown to decrease the photoconductivity. Moreover, similar to the $(\text{NDI-DAE})_2\text{PbI}_4$, the decay dynamics of the free charge carriers, as displayed in Figure 5.9b, can be fit to a bi-exponential decay function with a fast decay with a short time constant τ_1 and a longer lifetime τ_2 suggesting similar decay processes in the NDI-DAE-mix. Comparable photoconductivities and free charge carrier dynamics were obtained when the thin film was excited at 520 nm suggesting electronic interactions between the organic and inorganic components during the free charge carrier formation. The electronic coupling of the organic and inorganic layer in a type II heterostructure and the localization of the photoexcited electrons on the inorganic layer is assumed to reduce the effect of the inhomogeneous distribution of the halides in the inorganic layer resulting in comparable mobilities for NDI-DAE-mix and NDI-DAE-I.

While the NDI-DAE cation in the pure iodide and mixed halide form a type II heterostructure, we elucidated the free charge carrier generation in the $(\text{NDI-DAE})_2\text{PbBr}_4$, which was found to form a type I heterostructure. Different mobilities and decay dynamics are expected because the organic layer does not inject photogenerated holes into the inorganic layer. Furthermore, exciting just the chromophore allows us to probe the photoconductivity of the cation in the layered perovskite structure without affecting the electronic structure by contributions of the perovskite layers. The transient and the obtained peak photoconductivity are displayed in Figure 5.10a and Figure 5.10b, showing peak photoconductivities up to 3x lower when excited at 500 nm compared to the NDI-DAE-I and NDI-DAE-mix shown in Figure C.11.

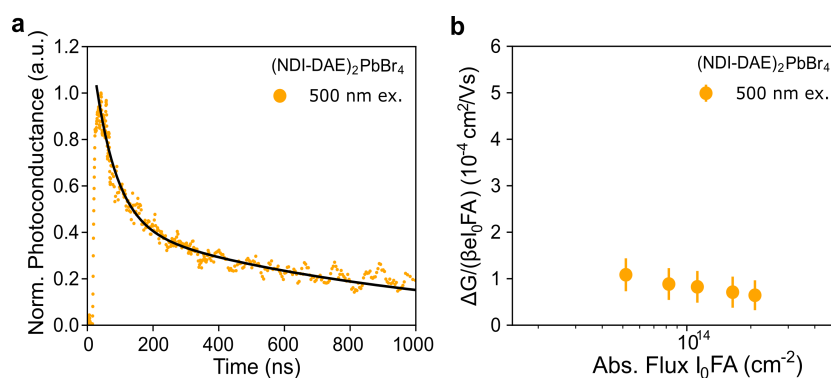


Figure 5.10 – **a)** Transient of $(\text{NDI-DAE})_2\text{PbBr}_4$ when excited at 500 nm, and **b)** resulting mobilities. The error bars are calculated based on uncertainties given by the photon fluence.

Moreover, the free charge carrier dynamic of NDI-DAE-Br when only the cation is excited shows comparable dynamics as the photoconductivity in the pure chromophore film when

only the cation salt is spin-coated on the quartz substrate, as shown in Figure C.12. While further studies on single crystals are required further to elucidate the charge carrier mobilities in the organic layer, our results suggest that the chromophore cation can contribute to the light-harvesting process in LHOIP materials.

5.5 Conclusion

Based on the elaborated strategies to incorporate large chromophore spacer cations into a LHOIP structure, we designed and synthesized a novel chromophore based on a core-modified NDI system denoted as NDI-DAE. The increased aromatic system of the novel cations reduces the chromophore's HOMO-LUMO gap, enhancing light absorption in the range between 400 and 560 nm. While LHOIP-formation with chromophores connected to a butyl and hexyl amine-bearing chain are demonstrated by visible light absorption spectroscopy and XRD, no indication for the formation of a LHOIP was found when a NDI-DAE-based cation with an ethyl amine-bearing linker was used. These findings suggest that the amine-bearing linker chain length is an important parameter for the successful incorporation of large chromophore-based spacer cations into a LHOIP structure. Moreover, increasing the aromatic system of the NDI-core requires higher annealing temperatures to form a crystalline LHOIP phase when compared to other NDI-based monocations. It is assumed that this increase in annealing temperature required to form the LHOIP phase is due to stronger π - π interactions requiring higher energies for structural reconfiguration in the as-spin-coated films. While we suggest that these inter-molecular interactions may be a limiting factor for the incorporation into a layered perovskite structure, further studies and quantification of aggregation are required by temperature-dependent NMR in order to correlate the required energy to form the LHOIP with the Gibbs energy of aggregation.

While further enhancing the visible light absorbance of the spacer chromophore is limited by the size constraint for the incorporation into a RP phase, we focused on tuning the CB and VB of the inorganic perovskite layer by halide composition engineering. A series of $(\text{NDI-DAE})_2\text{Pb}(\text{I}_{1-x}\text{Br}_x)$ films with $x = 0.0, 0.5$, and 1.0 were fabricated, and their optoelectronic properties were investigated. While $(\text{NDI-DAE})_2\text{PbI}_4$ and $(\text{NDI-DAE})_2\text{Pb}(\text{I}_{0.5}\text{Br}_{0.5})_4$ were found to form a type II heterostructure, $(\text{NDI-DAE})_2\text{PbBr}_4$ forms a type I heterostructure where the HOMO and LUMO energy of NDI-DAE are between the CB and VB of the perovskite layer. The formation of an inverted type I heterostructure leads to pronounced PL emission from the spacer cation. In contrast, the PL emission from the organic chromophore is quenched in the type II heterostructure, potentially due to hole injection from the organic chromophore to the perovskite layer, as suggested by TA experiments. We note that the electron and hole transfer dynamics are currently investigated in more detail by transient absorption spectroscopy.

Given the different energy alignments, we explored the formation of free charge carriers upon selective excitation of the spacer cations in type I and type II heterostructure systems. The formation of free charge carriers upon photoexcitation was studied using fp-TRMC measurements. For (NDI-DAE)₂Pb(I_{0.5}Br_{0.5})₄ and (NDI-DAE)₂PbI₄ similar photoconductivities of around $2 \cdot 10^{-4} \text{ cm}^2 \cdot \text{V}^{-1} \cdot \text{s}^{-1}$ were obtained after photoexcitation at 420 nm. These findings contrast the observed trend in investigated (BA)₂Pb(I_{1-x}Br_x)₄ films, where strongly reduced photoconductivities were found in the mixed halide system. While the energetic disorder due to energetic inhomogeneities in BA-based mixed halide pseudo-alloys hamper charge carrier mobilities along the inorganic layer, the type II heterostructure in (NDI-DAE)₂Pb(I_{0.5}Br_{0.5})₄ and (NDI-DAE)₂PbI₄ and the resulting electron transfer from the perovskite layer to the NDI-DAE reduces the effect of imperfect halide mixing in the inorganic layer.

Finally, selective excitation of the chromophore in mixed halide system reveals that the visible light absorption of the spacer chromophore can contribute to the free charge carrier generation providing a strategy to enhance light harvesting in LHOIP-based solar cells.

Chapter 6

Conclusion and Outlook

Layered perovskite materials have been previously shown to be a versatile and highly tunable subclass of hybrid organic-inorganic semiconductors suitable for a wide range of applications. Incorporating spacer cations based on organic semiconducting building blocks provides an interesting approach to engineering materials combining the properties of organic and inorganic semiconductors, opening the door for a whole batch of novel semiconducting materials. Incorporating large semiconducting chromophores into LHOIPs and understanding the electronic interactions between the organic and inorganic layers remains crucial for further developing novel semiconducting materials. In this work, we focused on synthesizing novel OSiPs and aimed to elaborate guidelines for the incorporation of such semiconducting building blocks into the perovskite structure. We further investigated the various interactions between the perovskite and organic semiconductor layer. Based on the novel cations described in this work, the following conclusions can be made:

- In Chapter 3, using naphthalene diimide as a chromophore core, we initially studied the incorporation of bulky spacer cations into a Ruddlesden-Popper layered perovskite phase. We synthesized three novel spacer cations and elaborated on the effect of the amine-bearing linker chain on the crystalline perovskite phase formation. An intriguing relationship between the amine-bearing linker chain length and the crystallinity of the layered perovskite film was found. With increased alkyl linker chain length, a decrease in crystallinity and out-of-plane ordering was observed. To investigate the reason for this trend, the critical annealing temperature at which the layered perovskite thin films start to form were determined using *in-situ* UV-vis spectroscopy. We found that for all thin films, annealing temperatures of more than 140 °C are required in order for the LHOIP to be formed. Notably, the required annealing temperatures are higher than for the conventional BA-based LHOIPs. Notably, higher annealing temperatures are required for NDI-based spacer cations with only a 2-carbon linker chain. We hypothesized that the decrease in alkyl chain length reduces the structural flexibility and hinders the nucleation and subsequent crystal growth. In contrast, nucleation and crystal growth of LHOIPs incorporating long alkyl chain-bearing NDI-based spacer cations start at lower temperatures. Losing control over the nucleation is considered to be the reason for the observed lower crystallinity in (NDI-H)₂PbI₄. Our results suggest that the amine-bearing

alkyl chain length is critical for successfully synthesizing layered perovskite materials incorporating large semiconducting spacer cations. The relationship between the amine-bearing alkyl chain length and the observed crystallinity was further confirmed in Chapter 4, where divalent cations based on NDI were incorporated into a layered perovskite (DJ) phase. Only cations with an amine-bearing butyl chain and hexyl chain formed layered perovskite materials under the investigated synthetic conditions. Moreover, in Chapter 5, only cations with an amine-bearing butyl and hexyl chains were found to form a layered perovskite structure. We stress that tuning the kinetics and thermodynamics of the LHOIP crystallization process by engineering the spacer cation provides a suitable route to alter the phase distribution in quasi-layered perovskite films.

- Photoluminescence and transient absorption spectroscopy confirmed the formation of a type II heterostructure by incorporating NDI-based spacer cations into the layered perovskite framework. The optical properties of these materials show characteristic intense excitonic absorption bands at around 500 nm. However, in contrast to LHOIPs based on aliphatic spacer cations, the PL emission is strongly quenched. Moreover, time-resolved photoluminescence spectroscopy shows ultrafast PL decay. In Chapter 3, a slower PL decay dynamic was found when the distance between the NDI and the inorganic layer was increased by the amine-bearing alkyl linker chain indicating that the quenching is due to the sub-picosecond electron transfer from the inorganic layer to the NDI-chromophore. The electron transfer is further observed in the transient absorption spectra where the ground state bleach dynamics show a tri-exponential decay. Thereby, a sub-picosecond decay can be attributed to the radiative recombination limited by the electron transfer to the NDI-chromophore. Moreover, similar features in the TA and TRPL can be found in RP as well as in DJ phases of NDI-based spacer chromophores investigated in Chapter 3 and Chapter 4.
- While PL and TA results suggest spatial separation of electrons and holes in the NDI and perovskite layer, fp-TRMC measurements were conducted to investigate the effect of this spatial separation on the free charge carrier generation. The obtained photoconductivities for the $(\text{NDI})_2\text{PbI}_4$ and $(\text{NDI})\text{PbI}_4$ were found to be one order of magnitude lower than the photoconductivity of $(\text{BA})_2\text{PbI}_4$ and $(\text{PEA})_2\text{PbI}_4$ phases. However, the transient of the excitons showed a prolonged decay component suggesting an increased lifetime of the free charge carriers. By further investigations of the free charge carrier formation with OPTP, it is suggested that the reduced photoconductivity results from the electrons' limited mobility in the organic layer. The possibility of obtaining a spatial separation of the electrons and holes in the organic and inorganic layer, respectively, provides a powerful strategy to overcome the effect of notoriously high exciton binding energies in LHOIPs.

-
- As the inorganic and organic layers of the NDI-based LHOIPs were found to be oriented parallel to the substrate, we aimed to improve the morphology and orientation by forming quasi-layered perovskite thin films in Chapter 4. Quasi-layered perovskite films with different quantum well sizes incorporating NDI-based dications and methylammonium iodide were investigated by absorption spectroscopy. Notably, the NDI dication show improved solubility in DMSO and DMF over monovalent NDI-based cations, enabling the fabrication of thicker films. With increasing methylammonium iodide concentration, clear signs for the formation of $n = 1, 2, 3$, and 4 were found in the absorption spectra. Moreover, in all investigated quasi-layered films incorporating NDI-dH, the formation of MAPbI_3 was suppressed, suggesting a more homogeneous energy landscape. The suppression of less stable MaPbI_3 and the increased hydrophobicity of the NDI-dH cation makes NDI-dH quasi-layered perovskite films more stable than films based on BA. Moreover, electron transfer from the quasi-perovskite layers to the NDI-chromophore were further studied by transient absorption spectroscopy suggesting the formation of possible charge-transfer excitons even in quasi-layered perovskite thin films.
 - Addressing recent reports on the 1D perovskite formation with NDIC2, we aimed to optimize the crystal orientation in NDI-dH based $\langle n \rangle = 5$ films by solvent engineering. We obtained thin films where the inorganic layers are oriented perpendicular to the substrate. As the inorganic and organic layer act as charge carrier channels, space-charge limited current based on electron-only devices were measured. The investigated quasi-layered perovskite thin films based on NDI-dH show similar mobilities as those obtained for BA-based perovskite materials. However, in contrast to the investigated BA-based reference material, no trap-filling region (TFR) was observed. The shape of the IV-curve suggests reduced trap density when NDI-dH is incorporated into quasi LHOIP films. Nonetheless, it remains unclear whether the reduced trap density arises from differences in the distribution of the poly-dispersed quantum wells or due to electronic interactions between the organic and inorganic domains.
 - While electron funneling processes limit the comparison between various spacer cations in quasi-layered perovskite films, we focused on further understanding electronic interactions between organic semiconducting spacer cations and the inorganic perovskite layer in $n = 1$ LHOIPs. By expanding our investigation and including perylene diimide-based spacer cations, we elaborate on the size limitation of the chromophore core for the successful incorporation into a layered perovskite structure. Initial studies of perylene diimide-based spacer cations show strong aggregation of the PDI cations in the precursor solution, as indicated by the aggregation-induced shifts in the absorbance spectrum with increasing PDI concentration. We assumed that the strong π - π interactions be-

tween PDI in the precursor solution hampers the formation of the LHOIP phase. Directly modifying the NDI-chromophore and expanding the aromatic system of NDI, a visible light-absorbing spacer cation labeled NDI-DAE was obtained. While NDI-DAE-based cations may tend to aggregate less in the precursor compared to PDI-based cations, increased $\pi - \pi$ interactions between the NDI-DAE chromophore cores were hypothesized to be the reason for substantially increased annealing temperatures required to form the LHOIP.

- The incorporation of a novel visible light absorbing spacer cation was demonstrated in Chapter 5. By tuning the CB and VB of the inorganic layer by halide mixing, we investigated different energy alignments between the organic and inorganic layer. While $(\text{NDI-DAE})_2\text{PbI}_4$ and $(\text{NDI-DAE})_2\text{Pb}(\text{I}_{0.5}\text{Br}_{0.5})_4$ form a type II heterostructure where the HOMO and LUMO energy levels of the NDI-DAE are located below the VB and CB, respectively, $(\text{NDI-DAE})_2\text{PbBr}_4$ has shown to form an inverted type I heterostructure where the HOMO and LUMO energy levels of the NDI-DAE chromophore are between the CB and VB of the lead-bromide perovskite. While in the type II heterostructure, no PL from the organic chromophore can be observed, PL emission from the NDI-DAE chromophore can be observed in the type I heterostructure. The quenching of the PL in the type II heterostructures is reasonably explained by hole injection from the chromophore to the perovskite layer upon photoexcitation.
- Based on the different energy alignments observed in Chapter 5, we addressed whether light absorption from the chromophore spacer can contribute to the light-harvesting process in layered perovskite semiconductors. Selective excitation of the spacer cation in TRMC experiments shows that photogenerated free charge carriers can be obtained via excitation of the spacer chromophore. Moreover, comparable mobilities and free charge carrier decay dynamics were obtained for $(\text{NDI-DAE})_2\text{PbI}_4$ and $(\text{NDI-DAE})_2\text{Pb}(\text{I}_{0.5}\text{Br}_{0.5})_4$. This finding is surprising considering the pseudo-binary alloy found in $(\text{BA})_2\text{Pb}(\text{I}_{0.5}\text{Br}_{0.5})_4$ strongly hampers charge carrier mobility in the inorganic layers.

While the synthesis of novel spacer cations and subsequent incorporation into a layered perovskite structure enhanced the understanding of the formation of OSiP and potential electronic interactions at the organic-inorganic interface, the exact nature of the charge carrier transport in the organic layer remains unknown. Moreover, our investigations were limited to layered perovskite thin film. The structure-property relationship in these materials remains to be further investigated. Based on the shortcomings of this work, we further aim to highlight the importance of new strategies and approaches to study these new semiconductors.

Future Work

Considering the disadvantages of current HOIP and LHOIP-based solar cells, the high stability of the NDI-based quasi-layered perovskite materials provides an advantage over the current state-of-the-art materials. Moreover, the contribution of the NDI chromophore to the electronic structure may assist the charge separation and charge carrier transport in optoelectronic devices. However, given the different phase distributions of multiple quantum wells in quasi-layered perovskite films, questions concerning the electronic interactions between different phases and their effect on exciton trapping and funneling processes remain unanswered. While current quasi-layered perovskite materials in highly efficient solar cell devices consist of mainly MAPbI₃ with an LHOIP passivation layer, the effect of the phase distribution on the photovoltaic efficiency and charge transport has come forward as an important aspect currently under investigation in the field. While in systems based on BA and PEA, the cations are electronically inactive and charge carrier funneling processes occur only between the different LHOIP phases, NDI-based cations are electronically active. The charge carrier transport and charge separation process are more complex due to different interactions of the NDI chromophore with different LHOIP phases. Designing an efficient solar cell architecture can be challenging despite the possibility of tuning the phase distribution in the quasi-layered perovskite films by modifying the amine-bearing linker length. In order to simplify the electronic interaction imposed by the presence of NDI-based cation it is suggested to initially investigate perovskite-based solar cells based on a 3D/2D architecture where the NDI-based LHOIP layer acts as a passivation and electron extracting layer.

Focusing on simple LHOIP ($n = 1$), further investigations are required to understand the nature of charge carrier transport in the type II heterostructure LHOIP. While SCLC measurements provide a powerful tool for determining hole and electron mobility, the crystal growth of the LHOIPs with the organic and inorganic layer oriented parallel to the substrate limits the application of electrode-based SCLC measurements for the determination of the charge carrier along the organic and inorganic layer, respectively. Nonetheless, SCLC measurements directly on single crystals provide further insight into the nature of the charge carrier transport in these highly anisotropic materials. Moreover, the synthesis of LHOIP single crystals is necessary to obtain further structural information via single-crystal XRD and clarify the structure-properties relationship further. Recent studies on NDI-C8-based RP phases provide single crystal XRD results, where single-crystals were obtained by a vapor diffusion method.^[199] While the vapor diffusion method has shown to be suitable for the synthesis of LHOIP single crystal incorporating various spacer cations, as further elaborated in Appendix D, it remains unclear whether the reported procedure is applicable to NDI-based dications.

In order to systematically study the effect of the spacer cation on the crystal and electronic structure of the LHOIP deposited as a thin film on a substrate, TRMC has been previously shown to be a powerful tool for investigating the thin film photoconductivity. Initial studies show that even simple spacers based on phenylethylammonium and *n*-butylammonium derivatives can strongly impact the charge carrier mobility (Appendix D), where differences in charge carrier mobilities of more than one order of magnitude were determined. Systematically studying the structure-properties relationship in simpler systems might help to further modify organic semiconducting spacer cations by, e.g., dipole engineering of the molecule.

As the aggregations of large planar aromatic spacer cations are assumed to limit the incorporation of large bulky spacer cations into a layered perovskite structure, we focus on developing semiconducting spacer cations based on iso-indigo chromophores. The electron-accepting properties combined with the good visible light absorbance and structural flexibility containing heteroatoms results in improved solubility and reduced aggregation. The easy synthesis of monovalent and divalent cations outlined in Appendix D and the large library of commercially available precursors with various substitutions at the phenyl core makes this class of organic semiconductor intriguing for further studies. Moreover, initial results suggest the potential formation of low-dimensional layered 2D or 1D perovskitoid structures (Further details are displayed in Appendix E).

Alternatively, tuning the electronic structure by co-incorporating aromatic spacer cations with electron-donating or electron-accepting dopants forming organic-charge transfer complexes in the organic layers has been proposed recently as an approach to reduce the exciton binding energy. Indeed, the electron-accepting nature of NDI forms such charge-transfer complexes with electron-donating small molecules like pyrene in solution, as shown in Appendix F. However, initial studies with an established model system using TRMC suggest reduced photoconductivity upon co-incorporation of such an organic charge-transfer complex, assumably due to local electronic distortion preventing efficient charge transport along the inorganic layer.

Bibliography

- [1] W. F. Brinkman, D. E. Haggan, and W. W. Troutman, A history of the invention of the transistor and where it will lead us, *IEEE Journal of Solid-State Circuits*, **1997**, 32, 1858–1865.
- [2] L. Łukasiak and J. Andrzej, History of Semiconductors, *Journal of Telecommunications and Information Technology*, **2010**, 1, 3–9.
- [3] I. M. Ross, The foundation of the silicon age, *Bell Labs Technical Journal*, **1997**, 2, 3–14.
- [4] P. Y. Yu and M. Cardona, Fundamentals of Semiconductors: Physics and Materials Properties, 4th ed., Berlin: Springer, 2010, chap. 1, 1–15.
- [5] A. Köhler and H. Bässler, Electronic Processes in Organic Semiconductors: An Introduction, Weinheim: Wiley, 2022, 1–22.
- [6] B. G. Yacobi, Semiconductor Materials: An Introduction to Basic Principles, New York: Kluwer Academic, 2003, chap. 4, 59–105.
- [7] M. Kodan, OLED Displays and Lighting, Chichester: Wiley, 2017, chap. 1, 12–16.
- [8] A. Smets, K. Jäger, I. Olindo, R. Van Swaaij, and M. Zeman, Solar Energy: The Physics and Engineering of Photovoltaic Conversion Technologies and Systems, Cambridge: UIT Cambridge Ltd, 2016, chap. 5, 35–46.
- [9] European-Commission, *A European Green Deal*, 2023, URL: http://commission.europa.eu/strategy-and-policy/priorities-2019-2024/european-green-deal_en (visited on 04/30/2023).
- [10] P. Würfel and U. Würfel, Physics of Solar Cells: From Basic Principles to Advanced Concepts, 3rd ed., Weinheim: Wiley, 2016, chap. 3–5, 42–120.
- [11] N. Zhou and A. Facchetti, Charge Transport and Recombination in Organic Solar Cells (OSCs), in: *Organic and Hybrid Solar Cells*, ed. by H. Huang and J. Huang, Cham: Springer, 2014, chap. 2, 19–52.
- [12] M. Schleuning, I. Y. Ahmet, R. van de Krol, and M. M. May, The role of selective contacts and built-in field for charge separation and transport in photoelectrochemical devices, *Sustainable Energy Fuels*, **2022**, 6, 3701–3716.

Bibliography

- [13] D. Sica, O. Malandrino, S. Supino, M. Testa, and M. C. Lucchetti, Management of end-of-life photovoltaic panels as a step towards a circular economy, *Renewable and Sustainable Energy Reviews*, **2018**, 82, 2934–2945.
- [14] A. Louwen, W. Van Sark, R. Schropp, and A. Faaij, A cost roadmap for silicon heterojunction solar cells, *Solar Energy Materials and Solar Cells*, **2016**, 147, 295–314.
- [15] K. J. Yu, Z. Yan, M. Han, and J. A. Rogers, Inorganic semiconducting materials for flexible and stretchable electronics, *NPJ Flexible Electronics*, **2017**, 1, 4.
- [16] C. Battaglia, A. Cuevas, and S. De Wolf, High-efficiency crystalline silicon solar cells: status and perspectives, *Energy & Environmental Science*, **2016**, 9, 1552–1576.
- [17] P. C. Sarker, M. R. Islam, A. K. Paul, and S. K. Gosh, Solar Photovoltaic Power Plants: Necessity and Techno-Economical Development, in: *Renewable Energy and the Environment*, ed. by M. R. Islam, N. K. Roy, and S. Rahman, Singapore: Springer, 2018, chap. 2, 41–69.
- [18] L. A. Zafoschnig, S. Nold, and J. C. Goldschmidt, The Race for Lowest Costs of Electricity Production : Techno-Economic Analysis of Silicon , Perovskite and Tandem Solar Cells, *IEEE Journal of Photovoltaics*, **2020**, 10, 1632–1641.
- [19] X. Huang, C. Liu, and P. Zhou, 2D semiconductors for specific electronic applications : from device to system, *NPJ 2D Materials and Applications*, **2022**, 6, 51.
- [20] S. Wang, X. Liu, and P. Zhou, The Road for 2D Semiconductors in the Silicon Age, *Advanced Materials*, **2022**, 34, 2106886.
- [21] H. Huang and W. Deng, Charge Transport and Recombination in Organic Solar Cells (OSCs), in: *Organic and Hybrid Solar Cells*, ed. by H. Huang and J. Huang, Cham: Springer, 2014, chap. 2, 19–52.
- [22] V. Coropceanu, A. Demetrio, S. Filho, Y. Olivier, R. Silbey, and J.-L. Bre, Charge Transport in Organic Semiconductors, *Chemical Reviews*, **2007**, 107, 926–952.
- [23] S. Giannini and J. Blumberger, Charge Transport in Organic Semiconductors: The Perspective from Nonadiabatic Molecular Dynamics, *Accounts of Chemical Research*, **2022**, 55, 819–830.
- [24] J. Frenkel, On the Transformation of Light into Heat in Solids. I, *Physical Review*, **1931**, 37, 17–44.
- [25] S. Giannini, W.-T. Peng, L. Cupellini, D. Padula, A. Carof, and J. Blumberger, Exciton transport in molecular organic semiconductors boosted by transient quantum delocalization, *Nature Communications*, **2022**, 13, 27553.
- [26] O. V. Mikhnenko, P. W. M. Blom, and T.-Q. Nguyen, Exciton diffusion in organic semiconductors, *Energy Environmental Science*, **2015**, 8, 1867–1888.

- [27] Y. Firdaus et al., Long-range exciton diffusion in molecular non-fullerene acceptors, *Nature Communications*, **2020**, 11, 5220.
- [28] J. Wang, Z. Zheng, Y. Zu, Y. Wang, X. Liu, S. Zhang, M. Zhang, and J. Hou, A Tandem Organic Photovoltaic Cell with 19.6 % Efficiency Enabled by Light Distribution Control, *Advanced Materials*, **2021**, 33, 2102787.
- [29] V. M. Goldschmidt, Die Gesetze der Krystallochemie, *Die Naturwissenschaften*, **1926**, 14, 477–485.
- [30] C. J. Bartel, C. Sutton, B. R. Goldsmith, R. Ouyang, C. B. Musgrave, L. M. Ghiringhelli, and M. Scheffler, New tolerance factor to predict the stability of perovskite oxides and halides, *Science Advances*, **2019**, 5, 1–10.
- [31] A. Kojima, K. Teshima, Y. Shirai, and T. Miyasaka, Organometal Halide Perovskites as Visible-light Sensitizers for Photovoltaic Cells, *Journal of the American Chemical Society*, **2009**, 131, 6050–6051.
- [32] T. M. Brenner, D. A. Egger, L. Kronik, G. Hodes, and D. Cahen, Hybrid organic—inorganic perovskites: low-cost semiconductors with intriguing charge transport properties, *Nature Reviews Materials*, **2016**, 1, 15007.
- [33] N. J. Jeon, J. H. Noh, W. S. Yang, Y. C. Kim, S. Ryu, J. Seo, and S. I. Seok, Compositional engineering of perovskite materials for high-performance solar cells, *Nature*, **2015**, 517, 476–480.
- [34] Y. Wang, X. Zhang, D. Wang, X. Li, J. Meng, J. You, Z. Yin, and J. Wu, Compositional Engineering of Mixed-Cation Lead Mixed-Halide Perovskites for High-Performance Photodetectors, *ACS Applied Materials and Interfaces*, **2019**, 11, 28005–28012.
- [35] C. Motta, F. El-Mellouhi, S. Kais, N. Tabet, F. Alharbi, and S. Sanvito, Revealing the role of organic cations in hybrid halide perovskite $\text{CH}_3\text{NH}_3\text{PbI}_3$, *Nature Communications*, **2015**, 6, 7026.
- [36] J. Berry et al., Hybrid Organic-Inorganic Perovskites (HOIPs): Opportunities and Challenges, *Advanced Materials*, **2015**, 27, 5102–5112.
- [37] J. H. Lee, N. C. Bristowe, J. H. Lee, S. H. Lee, P. D. Bristowe, A. K. Cheetham, and H. M. Jang, Resolving the Physical Origin of Octahedral Tilting in Halide Perovskites, *Chemistry of Materials*, **2016**, 28, 4259–4266.
- [38] A. Amat, E. Mosconi, E. Ronca, C. Quarti, P. Umari, K. Nazeeruddin, M. Grätzel, and F. D. Angelis, Cation-Induced Band-Gap Tuning in Organohalide Perovskites: Interplay of Spin-Orbit Coupling and Octahedra Tilting, *Nano Letters*, **2014**, 14, 3608–3616.

Bibliography

- [39] Y. Chen et al., Extended carrier lifetimes and diffusion in hybrid perovskites revealed by hall effect and photoconductivity Measurements, *Nature Communications*, **2016**, 7, 12253.
- [40] National-Renewable-Research-Laboratory, *Best Research-Cell Efficiency Chart*, 2023, URL: <https://www.nrel.gov/pv/cell-efficiency.html> (visited on 03/30/2023).
- [41] J. Y. Kim, J. W. Lee, H. S. Jung, H. Shin, and N. G. Park, High-Efficiency Perovskite Solar Cells, *Chemical Reviews*, **2020**, 120, 7867–7918.
- [42] S. A. Kulkarni, S. G. Mhaisalkar, N. Mathews, and P. P. Boix, Perovskite Nanoparticles: Synthesis, Properties, and Novel Applications in Photovoltaics and LEDs, *Applied Physics Letters*, **2018**, 3, 1800231.
- [43] G. Abdelmageed, L. Jewell, K. Hellier, L. Seymour, B. Luo, F. Bridges, J. Z. Zhang, and S. Carter, Mechanisms for light induced degradation in MAPbI₃ perovskite thin films and solar cells, *Applied Physics Letters*, **2016**, 109, 233905.
- [44] C. Zheng and O. Rubel, Unraveling the Water Degradation Mechanism of CH₃NH₃PbI₃, *Journal of Physical Chemistry C*, **2019**, 123, 19385–19394.
- [45] M. Salado, D. Payno, and S. Ahmad, Enhancing operational stability in perovskite solar cells by solvent-free encapsulation method, *Sustainable Energy Fuels*, **2022**, 6, 2264–2275.
- [46] J. V. Passarelli, D. J. Fairfield, N. A. Sather, M. P. Hendricks, H. Sai, C. L. Stern, and S. I. Stupp, Enhanced Out-of-Plane Conductivity and Photovoltaic Performance in n = 1 Layered Perovskites through Organic Cation Design, *Journal of the American Chemical Society*, **2018**, 140, 7313–7323.
- [47] L. Mao et al., Hybrid Dion-Jacobson 2D Lead Iodide Perovskites, *Journal of the American Chemical Society*, **2018**, 140, 3775–3783.
- [48] G. Wu, R. Liang, Z. Zhang, M. Ge, G. Xing, and G. Sun, 2D Hybrid Halide Perovskites: Structure, Properties, and Applications in Solar Cells, *Small*, **2021**, 17, 1–24.
- [49] C. C. Stoumpos, D. H. Cao, D. J. Clark, J. Young, J. M. Rondinelli, J. I. Jang, J. T. Hupp, and M. G. Kanatzidis, Ruddlesden-Popper Hybrid Lead Iodide Perovskite 2D Homologous Semiconductors, **2016**, 28, 2852–2867.
- [50] C. C. Stoumpos, C. D. Malliakas, and M. G. Kanatzidis, Semiconducting Tin and Lead Iodide Perovskites with Organic Cations: Phase Transitions, High Mobilities, and Near-Infrared Photoluminescent Properties, *Inorganic Chemistry*, **2013**, 52, 9019–9038.
- [51] H. Nagasaka, M. Yoshizawa-Fujita, Y. Takeoka, and M. Rikukawa, Tuning the Structures and Optical Properties of Perovskites by Varying the Alkylamine Type and Chain Length, *ACS Omega*, **2018**, 3, 18925–18929.

- [52] T. Yu, L. Zhang, J. Shen, Y. Fu, and Y. Fu, Hydrogen bonds and steric effects induced structural modulation of three layered iodoplumbate hybrids from nonperovskite to perovskite structure, *Dalton Transactions*, **2014**, 43, 13115–13121.
- [53] T. L. Leung, I. Ahmad, A. A. Syed, A. M. C. Ng, J. Popović, and A. B. Djurišić, Stability of 2D and quasi-2D perovskite materials and devices, *Communications Materials*, **2022**, 3, 63.
- [54] S. Ahmad et al., Dion-Jacobson Phase 2D Layered Perovskites for Solar Cells with Ultra-high Stability, *Joule*, **2019**, 3, 794–806.
- [55] N. Mercier, Hybrid Halide Perovskites : Discussions on Terminology and Materials, *Angewandte Chemie International Edition*, **2019**, 32, 1858–1865.
- [56] M. G. La-Placa, D. Guo, L. Gil-Escrig, F. Palazon, M. Sessolo, and H. J. Bolink, Dual-source vacuum deposition of pure and mixed halide 2D perovskites: thin film characterization and processing guidelines, *Journal of Materials Chemistry C*, **2020**, 8, 1902–1908.
- [57] I. C. Smith, E. T. Hoke, D. Solis-Ibarra, M. D. McGehee, and H. I. Karunadasa, A Layered Hybrid Perovskite Solar-Cell Absorber with Enhanced Moisture Stability, *Angewandte Chemie International Edition*, **2014**, 53, 11414–11417.
- [58] M. Shao et al., Over 21 % Efficiency Stable 2D Perovskite Solar Cells, *Advanced Materials*, **2022**, 34, 2107211.
- [59] A. Caiazzo and R. A. J. Janssen, High Efficiency Quasi-2D Ruddlesden – Popper Perovskite Solar Cells, *Advanced Energy Materials*, **2022**, 12, 2202830.
- [60] H. Tsai et al., High-efficiency two-dimensional Ruddlesden–Popper perovskite solar cells, *Nature*, **2016**, 536, 312–317.
- [61] Y. Huang, Y. Li, E. L. Lim, T. Kong, Y. Zhang, J. Song, A. Hagfeldt, and D. Bi, Stable Layered 2D Perovskite Solar Cells with an Efficiency of over 19% via Multifunctional Interfacial Engineering, *Journal of the American Chemical Society*, **2021**, 143, 3911–3917.
- [62] Y. Zhang and N.-G. Park, Quasi-Two-Dimensional Perovskite Solar Cells with Efficiency Exceeding 22%, *ACS Energy letters*, **2022**, 7, 757–765.
- [63] B. Zhao et al., High-efficiency perovskite–polymer bulk heterostructure light-emitting diodes, *Nature Photonics*, **2018**, 12, 783–789.
- [64] Z. Tan et al., Two-Dimensional (C₄H₉NH₃)₂PbBr₄ Perovskite Crystals for High-Performance Photodetector, *Journal of the American Chemical Society*, **2016**, 138, 16612–16615.
- [65] T. Matsushima, S. Hwang, A. S. Sandanayaka, C. Qin, S. Terakawa, T. Fujihara, M. Yahiro, and C. Adachi, Solution-Processed Organic–Inorganic Perovskite Field-Effect Transistors with High Hole Mobilities, *Advanced Materials*, **2016**, 28, 10275–10281.

Bibliography

- [66] F. Zhang, Q. Zhang, X. Liu, Y. Hu, Z. Lou, Y. Hou, and F. Teng, Property Modulation of Two-Dimensional Lead-Free Perovskite Thin Films by Aromatic Polymer Additives for Performance Enhancement of Field-Effect Transistors, *ACS Applied Materials and Interfaces*, **2021**, 13, 24272–24284.
- [67] C. R. Kagan, D. B. Mitzi, and C. D. Dimitrakopoulos, Organic-inorganic Hybrid Materials as Semiconducting Channels in Thin-film Field-effect Transistors, *Science*, **1999**, 286, 945–947.
- [68] G. Grancini et al., One-Year stable perovskite solar cells by 2D/3D interface Engineering, *Nature Communications*, **2017**, 8, 15684.
- [69] M. Dyksik, S. Wang, W. Paritmongkol, D. K. Maude, W. A. Tisdale, M. Baranowski, and P. Plochocka, Tuning the Excitonic Properties of the 2D $(\text{PEA})_2(\text{MA})_{n-1}\text{Pb}_n\text{I}_{3n+1}$ Perovskite Family via Quantum Confinement, *Journal of Physical Chemistry Letters*, **2021**, 12, 1638–1643.
- [70] M. Kober-Czerny, S. G. Motti, P. Holzhey, B. Wenger, J. Lim, L. M. Herz, and H. J. Snaith, Excellent Long-Range Charge-Carrier Mobility in 2D Perovskites, *Advanced Functional Materials*, **2022**, 32, 2203064.
- [71] J. Gong, M. Hao, Y. Zhang, M. Liu, and Y. Zhou, Layered 2D Halide Perovskites beyond the Ruddlesden-Popper Phase : Tailored Interlayer Chemistries for High-Performance Solar Cells, *Angewandte Chemie International Edition*, **2022**, 61, e202112022.
- [72] C. Ma, D. Shen, T. W. Ng, M. F. Lo, and C. S. Lee, 2D Perovskites with Short Interlayer Distance for High-Performance Solar Cell Application, *Advanced Materials*, **2018**, 30, 1800710.
- [73] K. Tanaka, F. Sano, T. Takahashi, T. Kondo, R. Ito, and K. Ema, Two-dimensional Wannier excitons in a layered-perovskite-type crystal $(\text{C}_6\text{H}_{13}\text{NH}_3)_2\text{PbI}_4$, *Solid State Communications*, **2002**, 122, 249–252.
- [74] M. Shinada and S. Sugano, Interband Optical Transitions in Extremely Anisotropic Semiconductors. I. Bound and Unbound Exciton Absorption, *Journal of the Physical Society of Japan*, **1966**, 21, 1936–1946.
- [75] R. Chakraborty and A. Nag, Correlation of Dielectric Confinement and Excitonic Binding Energy in 2D Layered Hybrid Perovskites Using Temperature Dependent Photoluminescence, *Journal of Physical Chemistry C*, **2020**, 124, 16177–16185.
- [76] R. Chakraborty and A. Nag, Dielectric confinement for designing compositions and optoelectronic properties of 2D layered hybrid perovskites, *Physical Chemistry Chemical Physics*, **2021**, 23, 82–93.

-
- [77] M. Shimizu, J.-I. Fujisawa, and J. Ishi-Hayase, Influence of dielectric confinement on excitonic nonlinearity in inorganic-organic layered semiconductors, *Physical Review B*, **2005**, 71, 205306.
- [78] J. C. Blancon et al., Extremely efficient internal exciton dissociation through edge states in layered 2D perovskites, *Science*, **2017**, 355, 1288–1292.
- [79] K. Tanaka, T. Takahashi, T. Kondo, and K. Ema, Image charge effect on two-dimensional excitons in an inorganic-organic quantum-well crystal, *Physical Review B*, **2005**, 71, 045312.
- [80] C. M. Mauck and W. A. Tisdale, Excitons in 2D Organic–Inorganic Halide Perovskites, *Trends in Chemistry*, **2019**, 1, 380–393.
- [81] T. Ishihara, Optical properties of PbI-based perovskite structures, *Journal of Luminescence*, **1994**, 60-61, 269–274.
- [82] D. H. Cao, C. C. Stoumpos, O. K. Farha, J. T. Hupp, and M. G. Kanatzidis, 2D Homologous Perovskites as Light-Absorbing Materials for Solar Cell Applications, **2015**, 137, 7843–7850.
- [83] C. Sun et al., High-performance large-area quasi-2D perovskite light-emitting diodes, *Nature Communications*, **2021**, 12, 2207.
- [84] A. Z. Chen et al., Origin of vertical orientation in two-dimensional metal halide perovskites and its effect on photovoltaic performance, *Nature Communications*, **2018**, 9, 1336.
- [85] C. McDonald, C. Ni, P. Maguire, P. Connor, J. T. Irvine, D. Mariotti, and V. Svrcek, Nanostructured Perovskite Solar Cells, *Nanomaterials*, **2019**, 9, 1481.
- [86] A. Z. Chen et al., Understanding the Formation of Vertical Orientation in Two-Dimensional Metal Halide Perovskite Thin Films, *Chemistry of Materials*, **2019**, 31, 1336–1343.
- [87] C. M. M. Myae Soe et al., Understanding Film Formation Morphology and Orientation in High Member 2D Ruddlesden–Popper Perovskites for High-Efficiency Solar Cells, *Advanced Energy Materials*, **2018**, 8, 1700979.
- [88] J. Xing et al., Color-stable highly luminescent sky-blue perovskite light-emitting diodes, *Nature Communications*, **2018**, 9, 3541.
- [89] A. Jana, Q. Ba, and K. S. Kim, Formation of a photoactive quasi-2D formamidinium lead iodide perovskite in water, *Journal of Materials Chemistry A*, **2019**, 7, 25785–25790.
- [90] L. Kong et al., Smoothing the energy transfer pathway in quasi-2D perovskite films using methanesulfonate leads to highly efficient light-emitting devices, *Nature Communications*, **2021**, 12, 1246.

Bibliography

- [91] L. N. Quan et al., Perovskites, Ligand-Stabilized Reduced-Dimensionality Perovskites, *Journal of the American Chemical Society*, **2016**, 138, 2649–2655.
- [92] Y. Lin et al., Unveiling the operation mechanism of layered perovskite solar cells, *Nature Communications*, **2019**, 10, 1008.
- [93] N. Liu et al., Probing Phase Distribution in 2D Perovskites for Efficient Device Design, *ACS Applied Materials and Interfaces*, **2020**, 12, 3127–3133.
- [94] Y. Jiang, J. Wei, and M. Yuan, Energy-Funneling Process in Quasi-2D Perovskite Light-Emitting Diodes, *Journal of Physical Chemistry Letters*, **2021**, 12, 2593–2606.
- [95] T. He et al., Reduced-dimensional perovskite photovoltaics with homogeneous energy landscape, *Nature Communications*, **2020**, 11, 1672.
- [96] C.-H. Chen, C.-H. Hsu, I.-C. Ni, B.-H. Lin, C.-I. Wu, C.-C. Kuo, and C.-C. Chueh, Regulating the phase distribution of quasi-2D perovskites using a three-dimensional cyclic molecule toward improved light-emitting performance, *Nanoscale*, **2022**, 14, 17409–17417.
- [97] J. Wang et al., Templated growth of oriented layered hybrid perovskites on 3D-like perovskites, *Nature Communications*, **2020**, 11, 582.
- [98] F. Zhang et al., Enhanced Charge Transport in 2D Perovskites via Fluorination of Organic Cation, *Journal of the American Chemical Society*, **2019**, 141, 5972–5979.
- [99] C. Liang et al., Two-dimensional Ruddlesden–Popper layered perovskite solar cells based on phase-pure thin films, *Nature Energy*, **2021**, 6, 38–45.
- [100] J. Yang et al., π -Conjugated Carbazole Cations Enable Wet-Stable Quasi-2D Perovskite Photovoltaics, *ACS Energy Letters*, **2022**, 4451–4458.
- [101] K. Wang, C. Wu, D. Yang, Y. Jiang, and S. Priya, Quasi-Two-Dimensional Halide Perovskite Single Crystal Photodetector, *ACS Nano*, **2018**, 12, 4919–4929.
- [102] Y. Zhang, M. Sun, N. Zhou, B. Huang, and H. Zhou, Electronic Tunability and Mobility Anisotropy of Quasi-2D Perovskite Single Crystals with Varied Spacer Cations, *Journal of Physical Chemistry Letters*, **2020**, 11, 7610–7616.
- [103] R. Quintero-Bermudez et al., Compositional and orientational control in metal halide perovskites of reduced dimensionality, *Nature Materials*, **2018**, 17, 900–907.
- [104] M. P. Arciniegas and L. Manna, Designing Ruddlesden–Popper Layered Perovskites through Their Organic Cations, *ACS Energy Letters*, **2022**, 7, 2944–2953.
- [105] E. Mahal, S. C. Mandal, and B. Pathak, Understanding the role of spacer cation in 2D layered halide perovskites to achieve stable perovskite solar cells, *Materials Advances*, **2022**, 3, 2464–2474.

- [106] K.-Z. Du, Q. Tu, X. Zhang, Q. Han, J. Liu, S. Zauscher, and D. B. Mitzi, Two-Dimensional Lead(II) Halide-Based Hybrid Perovskites Templated by Acene Alkylamines: Crystal Structures, Optical Properties, and Piezoelectricity, *Inorganic Chemistry*, **2017**, 56, 9291–9302.
- [107] E. R. Dohner, A. Jaffe, L. R. Bradshaw, and H. I. Karunadasa, Intrinsic White-light Emission from Layered Hybrid Perovskites, *Journal of the American Chemical Society*, **2014**, 136, 13154–13157.
- [108] B. Saparov and D. B. Mitzi, Organic-Inorganic Perovskites: Structural Versatility for Functional Materials Design, *Chemical Reviews*, **2016**, 116, 4558–4596.
- [109] D. B. Mitzi, S. Wang, C. A. Feild, C. A. Chess, and A. M. Guloy, Conducting Layered Organic-Inorganic Halides Containing <110>-Oriented Perovskite Sheets, *Science*, **1995**, 267, 1473–1476.
- [110] T. Ishihara, J. Takahashi, and T. Goto, Optical properties due to electronic transitions in two-dimensional semiconductors $(C_nH_{2n+1}NH_3)_2PbI_4$, *Physical Review B*, **1990**, 42, 11099–11107.
- [111] M. E. Kamminga, H. H. Fang, M. R. Filip, F. Giustino, J. Baas, G. R. Blake, M. A. Loi, and T. T. Palstra, Confinement Effects in Low-Dimensional Lead Iodide Perovskite Hybrids, *Chemistry of Materials*, **2016**, 28, 4554–4562.
- [112] C. Li, J. Yang, F. Su, J. Tan, Y. Luo, and S. Ye, Conformational disorder of organic cations tunes the charge carrier mobility in two-dimensional organic-inorganic perovskites, *Nature Communications*, **2020**, 11, 5481.
- [113] M. P. Hughes, K. D. Rosenthal, N. A. Ran, M. Seifrid, G. C. Bazan, and T. Q. Nguyen, Determining the Dielectric Constants of Organic Photovoltaic Materials Using Impedance Spectroscopy, *Advanced Functional Materials*, **2018**, 28, 1801542.
- [114] B. Cheng et al., Extremely reduced dielectric confinement in two-dimensional hybrid perovskites with large polar organics, *Communication Physics*, **2018**, 1, 80.
- [115] S. Tan et al., Effect of High Dipole Moment Cation on Layered 2D Organic-Inorganic Halide Perovskite Solar Cells, *Advanced Energy Materials*, **2019**, 9, 1803024.
- [116] G. Yan, G. Sui, W. Chen, K. Su, Y. Feng, and B. Zang, Selectively Fluorinated Benzylammonium-Based Spacer Cation Enables Graded Quasi-2D Perovskites for Efficient and Stable Solar Cells, *Chemistry of Materials*, **2022**, 34, 3346–3356.
- [117] J. Shi, Y. Gao, X. Gao, Y. Zhang, J. Zhang, X. Jing, and M. Shao, Fluorinated Low-Dimensional Ruddlesden-Popper Perovskite Solar Cells with over 17% Power Conversion Efficiency and Improved Stability, *Advanced Materials*, **2019**, 31, 1901673.

Bibliography

- [118] H. Xu et al., High-performance and moisture-stable perovskite solar cells with a 2D modified layer *via* introducing a high dipole moment cation, *Journal of Materials Chemistry C*, **2019**, 7, 15276–15284.
- [119] V. I. E. Queloz et al., Spatial Charge Separation as the Origin of Anomalous Stark Effect in Fluorous 2D Hybrid Perovskites, *Advanced Functional Materials*, **2020**, 30, 2000228.
- [120] J. Leveillee et al., Tuning Electronic Structure in Layered Hybrid Perovskites with Organic Spacer Substitution, *Nano Letters*, **2019**, 19, 8732–8740.
- [121] W. A. Dunlap-Shohl et al., Tunable internal quantum well alignment in rationally designed oligomer-based perovskite films deposited by resonant infrared matrix-assisted pulsed laser evaporation, *Materials Horizons*, **2019**, 6, 1707–1716.
- [122] W. Zhao, S.-N. Hsu, B. W. Boudouris, and L. Dou, Two-Dimensional Organic Semiconductor-Incorporated Perovskite (OSiP) Electronics, *ACS Applied Electronic Materials*, **2021**, 3, 5155–5164.
- [123] Y. Gao et al., Molecular engineering of organic–inorganic hybrid perovskites quantum wells, *Nature Chemistry*, **2019**, 11, 1151–1157.
- [124] X. Xu and X. Wang, Perovskite Nano-Heterojunctions: Synthesis, Structures, Properties, Challenges, and Prospects, *Small Structures*, **2020**, 1, 2000009.
- [125] E. Shi, Y. Gao, B. P. Finkenauer, Akriti, A. Coffei, and L. Dou, Two-dimensional halide perovskite nanomaterials and heterostructures, *Chemical Society Reviews*, **2018**, 47, 6046–6072.
- [126] M. Era, K. Maeda, and T. Tsutsui, Enhanced phosphorescence from naphthalene-chromophore incorporated into lead bromide-based layered perovskite having organic–inorganic superlattice structure, *Journal of Physical Chemistry Letters*, **1998**, 296, 417–420.
- [127] K. Ema, M. Inomata, Y. Kato, H. Kunugita, and M. Era, Nearly Perfect Triplet-Triplet Energy Transfer from Wannier Excitons to Naphthalene in Organic-Inorganic Hybrid Quantum-Well Materials, *Physical Review Letters*, **2008**, 100, 257401.
- [128] F. Lédée et al., Tetrazine molecules as an efficient electronic diversion channel in 2D organic–inorganic perovskites, *Materials Horizons*, **2021**, 8, 1547–1560.
- [129] Y. L. Lin and J. C. Johnson, Interlayer Triplet Energy Transfer in Dion-Jacobson Two-Dimensional Lead Halide Perovskites Containing Naphthalene Diammonium Cations, *Journal of Physical Chemistry Letters*, **2021**, 12, 4793–4798.
- [130] Y. Tian et al., Sensitized Molecular Triplet and Triplet Excimer Emission in Two-Dimensional Hybrid Perovskites, *Journal of Physical Chemistry Letters*, **2020**, 11, 2247–2255.

- [131] M. Braun, W. Tuffentsammer, H. Wachtel, and H. C. Wolf, Tailoring of energy levels in lead chloride based layered perovskites and energy transfer between the organic and inorganic planes, *Chemical Physics Letters*, **1999**, 303, 157–164.
- [132] L. Ge et al., Stimulating Efficient and Stable Ultralong Phosphorescence of 2D Perovskites by Dual-Mode Triplet Exciton Stabilization, *Chemistry of Materials*, **2022**, 34, 8917–8924.
- [133] H. Hu et al., Harvesting Triplet Excitons in Lead-Halide Perovskites for Roomtemperature Phosphorescence, *Chemistry of Materials*, **2019**, 31, 2597–2602.
- [134] W. Shao, S. Yang, K. Wang, and L. Dou, Light-Emitting Organic Semiconductor-Incorporated Perovskites: Fundamental Properties and Device Applications, *Journal of Physical Chemistry Letters*, **2023**, 14, 2034–2046.
- [135] C. Qin et al., Triplet management for efficient perovskite light-emitting diodes, *Nature Photonics*, **2020**, 14, 70–75.
- [136] S. Deng, J. M. Snaider, Y. Gao, E. Shi, L. Jin, R. D. Schaller, L. Dou, and L. Huang, Long-lived charge separation in two-dimensional ligand-perovskite heterostructures, *Journal of Chemical Physics*, **2020**, 152, 044711.
- [137] R. Herckens et al., Multi-layered hybrid perovskites templated with carbazole derivatives: optical properties, enhanced moisture stability and solar cell characteristics, *Journal of Material Chemistry A*, **2018**, 6, 22899–22908.
- [138] M. Van Landeghem, W. Van Gompel, R. Herckens, L. Lutsen, D. Vanderzande, S. Van Doorslaer, and E. Goovaerts, Light-Induced Charge Transfer in Two-Dimensional Hybrid Lead Halide Perovskites, *Journal of Physical Chemistry C*, **2021**, 125, 18317–18327.
- [139] D. B. Mitzi, K. Chondroudis, and C. R. Kagan, Design, Structure, and Optical Properties of Organic-Inorganic Perovskites Containing an Oligothiophene Chromophore, *Inorganic Chemistry*, **1999**, 38, 6246–6256.
- [140] L. Etgar, The merit of perovskite's dimensionality; can this replace the 3D halide perovskite?, *Energy and Environmental Science*, **2018**, 11, 234–242.
- [141] Y. Dong et al., Orbital Interactions between Organic Semiconductor Spacer and Inorganic Layer in Dion-Jacobson Perovskite Enable Efficient Solar Cells, *Advanced Materials*, **2022**, 35, 2205258.
- [142] Z. Xu, D. Lu, X. Dong, M. Chen, Q. Fu, and Y. Liu, Highly Efficient and Stable Dion-Jacobson Perovskite Solar Cells Enabled by Extended π -Conjugation of Organic Spacer, *Advanced Materials*, **2021**, 33, 2105083.
- [143] W. T. Van Gompel et al., 2D layered perovskite containing functionalised benzothienobenzothiophene molecules: formation, degradation, optical properties and photoconductivity, *Journal of Materials Chemistry C*, **2020**, 8, 7181–7188.

Bibliography

- [144] K. Chondroudis and D. B. Mitzi, Electroluminescence from an Organic-Inorganic Perovskite Incorporating a Quaterthiophene Dye within Lead Halide Perovskite Layers, *Chemistry of Materials*, **1999**, 11, 3028–3030.
- [145] K. Mase, K. Okumura, N. Yanai, and N. Kimizuka, Triplet sensitization by perovskite nanocrystals for photon upconversion, *Chemical Communications*, **2017**, 53, 8261–8264.
- [146] X. Luo et al., Mechanisms of triplet energy transfer across the inorganic nanocrystal/organic molecule interface, *Nature Communications*, **2020**, 11, 28.
- [147] A. C. Véron, A. Linden, N. A. Leclaire, E. Roedern, S. Hu, W. Ren, D. Rentsch, and F. A. Nüesch, One-Dimensional Organic-Inorganic Hybrid Perovskite Incorporating Near-Infrared-Absorbing Cyanine Cations, *Journal of Physical Chemistry Letters*, **2018**, 9, 2438–2442.
- [148] M. C. Gélvez-Rueda, M. B. Fridriksson, R. K. Dubey, W. F. Jager, W. van der Stam, and F. C. Grozema, Overcoming the exciton binding energy in two-dimensional perovskite nanoplatelets by attachment of conjugated organic chromophores, *Nature Communications*, **2020**, 11, 1901.
- [149] J. V. Passarelli et al., Tunable exciton binding energy in 2D hybrid layered perovskites through donor-acceptor interactions within the organic layer, *Nature Chemistry*, **2020**, 12, 672–682.
- [150] M. C. Gélvez-Rueda, W. T. M. Van Gompel, R. Herckens, L. Lutsen, D. Vanderzande, and F. C. Grozema, Inducing Charge Separation in Solid-State Two-Dimensional Hybrid Perovskites through the Incorporation of Organic Charge-Transfer Complexes, *Journal of Physical Chemistry Letters*, **2020**, 11, 824–830.
- [151] I. Perez-Juste and O. Nieto Faza, Interaction of Radiation with Matter, in: *Structure Elucidation in Organic Chemistry: The Search for the Right Tools*, ed. by M.-M. Cid and J. Bravo, Weinheim: John Wiley & Sons, 2015, chap. 1.
- [152] Y. Waseda, E. Matsubara, and K. Shinoda, X-Ray Diffraction Crystallography: Introduction, Examples and Solved Problems, Berlin: Springer, 2011, chap. 1, 1–20.
- [153] L. Tolan, X-Ray Scattering from Soft-Matter Thin Films: Materials Science and Basic Research, Berlin: Springer, 1999, chap. 2, 5–31.
- [154] R.-J. Roe, Methods of X-ray and Neutron Scattering in Polymer Science, New York: Oxford University Press, 2000, chap. 1–3, 1–132.
- [155] W. H. Bragg and W. L. Bragg, The reflection of X-rays by crystals, *Proceedings of the Royal Society of London. Series A*, **1913**, 88, 428–38.

-
- [156] P. Scherrer, Bestimmung der Größe und der inneren Struktur von Kolloidteilchen mittels Röntgenstrahlen, *Nachrichten von der Gesellschaft der Wissenschaften zu Göttingen, Mathematisch-Physikalische Klasse*, **1918**, 1918, 98–100.
- [157] P. H. Herman and P. Platzek, *Kolloid Z*, **1939**, 87, 246.
- [158] K. E. Knowles, M. D. Koch, and J. L. Shelton, Three applications of ultrafast transient absorption spectroscopy of semiconductor thin films: spectroelectrochemistry, microscopy, and identification of thermal contributions, *Journal of Materials Chemistry C*, **2018**, 6, 11853–11867.
- [159] G. C. Fish, Unravelling the mechanism of ultrafast photoinduced charge generation in organic and hybrid photovoltaic systems, PhD thesis, EPFL, 2023.
- [160] E. Socie, Ultrafast carrier and quasiparticle dynamics in strongly confined perovskite nanoplatelets, PhD thesis, EPFL, 2022.
- [161] R. Berera, R. van Grondelle, and J. T. Kennis, Ultrafast transient absorption spectroscopy: principles and application to photosynthetic systems, *Photosynthesis Research*, **2009**, 101, 105–118.
- [162] T. J. Savenije, A. J. Ferguson, N. Kopidakis, and G. Rumbles, Revealing the Dynamics of Charge Carriers in Polymer:Fullerene Blends Using Photoinduced Time-Resolved Microwave Conductivity, *Journal of Physical Chemistry C*, **2013**, 117, 24085–24103.
- [163] M. Schleuning et al., Generalized Method to Extract Carrier Diffusion Length from Photoconductivity Transients: Cases of BiVO₄, Halide Perovskites, and Amorphous and Crystalline Silicon, *PRX Energy*, **2022**, 1, 023008.
- [164] H. Hempel et al., Predicting Solar Cell Performance from Terahertz and Microwave Spectroscopy, *Advanced Energy Materials*, **2022**, 12, 2102776.
- [165] K. W. Böer, Creation of Space-Charge Regions in Solids, Berlin: Springer, 2010, chap. 2, 15–39.
- [166] N. F. Mott and R. W. Gurney, Electronic Processes in Ionic Crystals, New York: Oxford University Press, 1940.
- [167] M. A. Mahmud et al., Origin of Efficiency and Stability Enhancement in High-Performing Mixed Dimensional 2D-3D Perovskite Solar Cells: A Review, *Advanced Functional Materials*, **2022**, 32, 2009164.
- [168] C. Chen, Y. Sun, J. Peng, J. Tang, K. Zheng, and Z. Liang, 2D Ruddlesden-Popper Perovskites for Optoelectronics, *Advanced Materials*, **2018**, 30, 1703487.

Bibliography

- [169] J. K. Pious et al., Self-Assembled Organic Cations-Assisted Band-Edge Tailoring in Bismuth-Based Perovskites for Enhanced Visible Light Absorption and Photoconductivity, *Journal of Physical Chemistry Letters*, **2021**, 12, 5758–5764.
- [170] W. Deng, H. Fang, X. Jin, X. Zhang, X. Zhang, and J. Jie, Organic–inorganic hybrid perovskite quantum dots for light-emitting diodes, *Journal of Materials Chemistry C*, **2018**, 6, 4831–4841.
- [171] S. Maheshwari, T. J. Savenije, N. Renaud, and F. C. Grozema, Computational Design of Two-Dimensional Perovskites with Functional Organic Cations, *Journal of Physical Chemistry C*, **2018**, 122, 17118–17122.
- [172] A. H. Proppe et al., Naphthalenediimide Cations Inhibit 2D Perovskite Formation and Facilitate Subpicosecond Electron Transfer, *Journal of Physical Chemistry C*, **2020**, 124, 24379–24390.
- [173] A. Mishra et al., Naphthalenediimide/Formamidinium-Based Low-Dimensional Perovskites, *Chemistry of Materials*, **2021**, 33, 6412–6420.
- [174] E. Amerling et al., Charge transfer states and carrier generation in 1D organolead iodide semiconductors, *Journal of Materials Chemistry A*, **2021**, 9, 14977–14990.
- [175] B. Primera Darwich et al., Benzodithiophene-Based Spacers for Layered and Quasi-Layered Lead Halide Perovskite Solar Cells, *ChemSusChem*, **2021**, 14, 3001–3009.
- [176] F. Li et al., Effects of Alkyl Chain Length on Crystal Growth and Oxidation Process of Two-Dimensional Tin Halide Perovskites, *ACS Energy Letters*, **2020**, 5, 1422–1429.
- [177] G. Ashiotis, A. Deschildre, Z. Nawaz, J. P. Wright, D. Karkoulis, F. E. Picca, and J. Kieffer, The fast azimuthal integration Python library: pyFAI, *Journal of Applied Crystallography*, **2015**, 48, 510–519.
- [178] N. Striebeck and U. Nöchel, Direct mapping of fiber diffraction patterns into reciprocal space, *Journal of Applied Crystallography*, **2009**, 42, 295–301.
- [179] M. Gerecke, G. Bierhance, M. Gutmann, N. P. Ernsting, and A. Rosspeintner, Femtosecond broadband fluorescence upconversion spectroscopy: Spectral coverage versus efficiency, *Review of Scientific Instruments*, **2016**, 87, 1–6.
- [180] E. Socie, B. R. Vale, A. Burgos-Caminal, and J. E. Moser, Direct Observation of Shallow Trap States in Thermal Equilibrium with Band-Edge Excitons in Strongly Confined CsPbBr₃ Perovskite Nanoplatelets, *Advanced Optical Materials*, **2021**, 9, 2001308.
- [181] R. R. Prabhakar et al., Sulfur Treatment Passivates Bulk Defects in Sb₂Se₃ Photocathodes for Water Splitting, *Advanced Functional Materials*, **2022**, 32, 2112184.

- [182] J. E. Kroeze, T. J. Savenije, and J. M. Warman, Electrodeless Determination of the Trap Density, Decay Kinetics, and Charge Separation Efficiency of Dye-Sensitized Nanocrystalline TiO_2 , *Journal of the American Chemical Society*, **2004**, 126, 7608–7618.
- [183] V. S. Chirvony et al., Inhomogeneous Broadening of Photoluminescence Spectra and Kinetics of Nanometer-Thick (Phenethylammonium) $_2\text{PbI}_4$ Perovskite Thin Films: Implications for Optoelectronics, *ACS Applied Nano Materials*, **2021**, 4, 6170–6177.
- [184] Y. Xu, M. Wang, Y. Lei, Z. Ci, and Z. Jin, Crystallization Kinetics in 2D Perovskite Solar Cells, *Advanced Energy Materials*, **2020**, 10, 2002558.
- [185] N. Zhou, Y. Shen, L. Li, S. Tan, N. Liu, G. Zheng, Q. Chen, and H. Zhou, Exploration of Crystallization Kinetics in Quasi Two-Dimensional Perovskite and High Performance Solar Cells, *Journal of the American Chemical Society*, **2018**, 140, 459–465.
- [186] H. C. Chia et al., Critical Intermediate Structure That Directs the Crystalline Texture and Surface Morphology of Organo-Lead Trihalide Perovskite, *ACS Applied Materials and Interfaces*, **2017**, 9, 36897–36906.
- [187] J. Dong, S. Shao, S. Kahmann, A. J. Rommens, D. Hermida-Merino, G. H. ten Brink, M. A. Loi, and G. Portale, Mechanism of Crystal Formation in Ruddlesden–Popper Sn-Based Perovskites, *Advanced Functional Materials*, **2020**, 30, 2001294.
- [188] A. Ummadisingu and M. Grätzel, Revealing the detailed path of sequential deposition for metal halide perovskite formation, *Science Advances*, **2018**, 4, e170140.
- [189] Q. Hu et al., *In situ* dynamic observations of perovskite crystallisation and microstructure evolution intermediated from $[\text{PbI}_6]^{4-}$ cage nanoparticles, *Nature Communications*, **2017**, 8, 15688.
- [190] K. Suchan, J. Just, P. Becker, E. L. Unger, and T. Unold, Optical *in situ* monitoring during the synthesis of halide perovskite solar cells reveals formation kinetics and evolution of optoelectronic properties, *Journal of Materials Chemistry A*, **2020**, 8, 10439–10449.
- [191] Z. Yao et al., Role of alkyl chain length in diaminoalkane linked 2D Ruddlesden–Popper halide perovskites, *CrystEngComm*, **2018**, 20, 6704–6712.
- [192] S. J. Park, A. R. Kim, J. T. Hong, J. Y. Park, S. Lee, and Y. H. Ahn, Crystallization Kinetics of Lead Halide Perovskite Film Monitored by *In Situ* Terahertz Spectroscopy, *Journal of Physical Chemistry Letters*, **2017**, 8, 401–406.
- [193] L. Zhao, J. L. Lustres, V. Farztdinov, N. P. Ernstring, L. Zhao, and J. L. Pe, Femtosecond fluorescence spectroscopy by upconversion with tilted gate pulses, *Physical Chemistry Chemical Physics*, **2005**, 7, 1716–1725.

Bibliography

- [194] H. Duim, S. Adjokatse, S. Kahmann, G. H. ten Brink, and M. A. Loi, The Impact of Stoichiometry on the Photophysical Properties of Ruddlesden–Popper Perovskites, *Advanced Functional Materials*, **2020**, 30, 1907505.
- [195] A. Burgos-Caminal, E. Socie, M. E. Bouduban, and J. E. Moser, Exciton and Carrier Dynamics in Two-Dimensional Perovskites, *Journal of Physical Chemistry Letters*, **2020**, 11, 7692–7701.
- [196] M. M. Elshanawany, A. G. Ricciardulli, M. Saliba, J. Wachtveitl, and M. Braun, Mechanism of ultrafast energy transfer between the organic–inorganic layers in multiple-ring aromatic spacers for 2D perovskites, *Nanoscale*, **2021**, 13, 15668–15676.
- [197] C. M. M. Soe et al., Structural and thermodynamic limits of layer thickness in 2D halide perovskites, *Proceedings of the National Academy of Sciences of the United States of America*, **2019**, 116, 58–66.
- [198] J. Liu, J. Leng, K. Wu, J. Zhang, and S. Jin, Observation of Internal Photoinduced Electron and Hole Separation in Hybrid Two-Dimensional Perovskite Films, *Journal of the American Chemical Society*, **2017**, 139, 1432–1435.
- [199] Z. Feng et al., Artificial p-n-Like Junction Based on Pure 2D Organic – Inorganic Halide Perovskite Structure Having Naphthalene Diimide Acceptor Moieties, *Advanced Optical Materials*, **2023**, 11, 2202734.
- [200] J. V. Milić, Multifunctional layered hybrid perovskites, *Journal of Materials Chemistry C*, **2021**, 9, 11428–11443.
- [201] X. Zhao, T. Liu, and Y.-l. Loo, Advancing 2D Perovskites for Efficient and Stable Solar Cells : Challenges and Opportunities, *Advanced Materials*, **2022**, 34, 2105849.
- [202] G. C. Fisch, J. M. Moreno-Naranjo, A. Billion, D. Kratzert, E. Hack, I. Krossing, F. Nüesch, and J.-E. Moser, Critical role of H-aggregation for high-efficiency photoinduced charge generation in pristine pentamethine cyanine salts, *Physical Chemistry Chemical Physics*, **2021**, 23, 23886–23895.
- [203] M. Saliba, J.-P. Correa-Baena, C. M. Wolff, M. Stollerfoht, N. Phung, S. Albrecht, D. Neher, and A. Abate, How to Make over 20% Efficient Perovskite Solar Cells in Regular (n–i–p) and Inverted (p–i–n) Architectures, *Chemistry of Materials*, **2018**, 30, 4193–4201.
- [204] K. Yan, M. Long, T. Zhang, Z. Wei, H. Chen, S. Yang, and J. Xu, Hybrid Halide Perovskite Solar Cell Precursors: Colloidal Chemistry and Coordination Engineering behind Device Processing for High Efficiency, *Journal of the American Chemical Society*, **2015**, 137, 4460–4468.

-
- [205] M. D. Murbach, B. Gerwe, N. Dawson-Elli, and L.-k. Tsui, impedance.py: A Python package for electrochemical impedance analysis, *The Journal of Open Source Software*, **2020**, 5, 2349.
- [206] J. Zhang, X. Zhu, M. Wang, and B. Hu, Establishing charge-transfer excitons in 2D perovskite heterostructures, *Nature Communications*, **2020**, 11, 2618.
- [207] M. C. Gélvez-Rueda et al., Interconversion between Free Charges and Bound Excitons in 2D Hybrid Lead Halide Perovskites, *Journal of Physical Chemistry C*, **2017**, 121, 26566–26574.
- [208] R. L. Milot et al., Charge-Carrier Dynamics in 2D Hybrid Metal–Halide Perovskites, *Nano Letters*, **2016**, 16, 7001–7007.
- [209] Z. Qin, C. Zhang, L. Chen, X. Wang, and M. Xiao, Charge Carrier Dynamics in Sn-Doped Two-Dimensional Lead Halide Perovskites Studied by Terahertz Spectroscopy, *Frontiers in Energy Research*, **2021**, 9, 658270.
- [210] M. Yuan et al., Perovskite energy funnels for efficient light-emitting diodes, *Nature Nanotechnology*, **2016**, 11, 872–877.
- [211] N. Wang et al., Perovskite light-emitting diodes based on solution-processed self-organized multiple quantum wells, *Nature Photonics*, **2016**, 10, 699–704.
- [212] Q. Shang et al., Unveiling Structurally Engineered Carrier Dynamics in Hybrid Quasi-Two-Dimensional Perovskite Thin Films toward Controllable Emission, *Journal of Physical Chemistry Letters*, **2017**, 8, 4431–4438.
- [213] V. M. Le Corre, E. A. Duijnste, O. El Tambouli, J. M. Ball, H. J. Snaith, J. Lim, and L. J. A. Koster, Revealing Charge Carrier Mobility and Defect Densities in Metal Halide Perovskites via Space-Charge-Limited Current Measurements, *ACS Energy Letters*, **2021**, 6, 1087–1094.
- [214] J. Peng, Y. Chen, K. Zheng, T. Pullerits, and Z. Liang, Insights into charge carrier dynamics in organo-metal halide perovskites: from neat films to solar cells, *Chemical Society Reviews*, **2017**, 46, 5714–5729.
- [215] L. M. Herz, Charge-Carrier Mobilities in Metal Halide Perovskites: Fundamental Mechanisms and Limits, *ACS Energy Letters*, **2017**, 2, 1539–1548.
- [216] K. Sivula, Improving Charge Carrier Mobility Estimations When Using Space-Charge-Limited Current Measurements, *ACS Energy Letters*, **2022**, 7, 2102–2104.
- [217] E. A. Duijnste, J. M. Ball, V. M. Le Corre, L. J. A. Koster, H. J. Snaith, and J. Lim, Toward Understanding Space-Charge Limited Current Measurements on Metal Halide Perovskites, *ACS Energy Letters*, **2020**, 5, 376–384.

Bibliography

- [218] S. Nussbaum, *Synthesis and Characterisation of Novel Hybrid 2D Semiconducting Materials (Master Thesis)*, 2019.
- [219] W. Fu, H. Liu, X. Shi, L. Zuo, X. Li, and A. K. Jen, Tailoring the Functionality of Organic Spacer Cations for Efficient and Stable Quasi-2D Perovskite Solar Cells, *Advanced Functional Materials*, **2019**, 29, 1900221.
- [220] K. Dirian et al., A water-soluble, bay-functionalized perylenediimide derivative — correlating aggregation and excited state dynamic, *Nanoscale*, **2018**, 10, 2317–2326.
- [221] J. Schill, L.-G. Milroy, J. A. M. Lugger, A. P. H. Schenning, and L. Brunsveld, Relationship between Side-Chain Polarity and the Self-Assembly Characteristics of Perylene Diimide Derivatives in Aqueous Solution, *Chemistry A European Journal*, **2017**, 6, 266–272.
- [222] G. Lanty, K. Jemly, Y. Wei, J. Laymarie, J. Even, J. Lauret, and E. Deleporte, Room-Temperature Optical Tunability and Inhomogeneous Broadening in 2D-Layered Organic-Inorganic Perovskite Pseudobinary Alloys, *Journal of Physical Chemistry Letters*, **2014**, 5, 3958–3963.
- [223] Y. Nah et al., Spectral Instability of Layered Mixed Halide Perovskites Results from Anion Phase Redistribution and Selective Hole Injection, *ACS Nano*, **2021**, 15, 1486–1496.
- [224] Y.-R. Wang et al., Photo De-Mixing in Dion-Jacobson 2D Mixed Halide Perovskites, *Advanced Energy Materials*, **2022**, 12, 2200768.
- [225] S. Toso, I. Gushchina, A. G. Oliver, L. Manna, and M. Kuno, Are Mixed-Halide Ruddlesden–Popper Perovskites Really Mixed?, *ACS Energy Letters*, **2022**, 4242–4247.
- [226] M. Seitz et al., Halide Mixing Inhibits Exciton Transport in Two-dimensional Perovskites Despite Phase Purity, *ACS Energy Letters*, **2022**, 7, 358–365.
- [227] E. Shi et al., Two-dimensional halide perovskite lateral epitaxial heterostructures, *Nature*, **2020**, 580, 614–620.
- [228] H. Langhals and H. Jaschke, Naphthalene Amidine Imide Dyes by Transamination of Naphthalene Bisimides, *Chemistry A European Journal*, **2006**, 12, 2815–2824.
- [229] S. Guo et al., Reconfiguring band-edge states and charge distribution of organic semiconductor-incorporated 2D perovskites via pressure gating, *Science Advanced*, **2022**, 8, eadd1984.
- [230] D. A. Grave et al., Extraction of mobile charge carrier photogeneration yield spectrum of ultrathin-film metal oxide photoanodes for solar water splitting, *Nature Materials*, **2021**, 20, 833–840.

- [231] G. Shao, Work Function and Electron Affinity of Semiconductors: Doping Effect and Complication due to Fermi Level Pinning, *Energy and Environmental Materials*, **2021**, 4, 273–276.

Appendix A

Appendix: Tuning Naphthalene Diimide Spacer Cations for the Incorporation into a Layered RP Phase Perovskite Structure

Materials and Experimental

Lead iodide (PbI_2 , 99.99%, CAS: 10101-63-0) and 1,4,5,8-Naphthalenetetracarboxylic dianhydride (97%, CAS: 81-30-1) were obtained from TCI and was used without any further purification. Propylamine (99% CAS: 107-10-8) and HI-solution (57% wt.%, no stabilizer CAS:10034-85-2) were purchased from Sigma-Aldrich. NBoc-1,2-diaminoethyl (98%, CAS: 57260-73-8) and N-Boc-1,6-hexanediamine (95%, CAS: 51857-17-1) were purchased from Fluorochem. N-Boc-1,4-butanediamine (95%, CAS: 68076-36-8) was obtained from ABCR.

Synthesis of NDI

NDI-based cations were synthesized following the synthetic scheme displayed in Figure A.1.

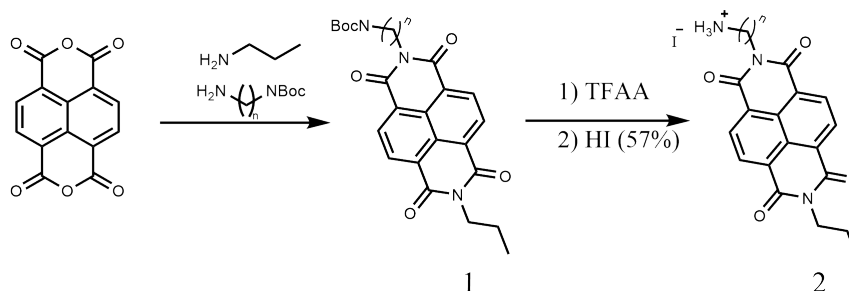


Figure A.1 – Synthetic scheme of NDI-based spacer cations

Appendix A. Appendix: Tuning Naphthalene Diimide Spacer Cations for the Incorporation into a Layered RP Phase Perovskite Structure

Synthesis of NDI-E-Boc

2 g (mmol, 1 eqv.) of Naphthalene-dianhydride (NDA) and 1.25 g (mmol, 1.05 eqv.) were transferred in a dry 2-neck-flask and dissolved in 20 ml of dry DMF under argon atmosphere. After injection of 0.65 ml of propylamine, the reaction mixture was heated to 140 °C. After 12 hours of constant stirring, the solvent was evaporated and the desired product was obtained after purification over a silica gel column using DCM/Ethylacetate 95:5 mixture as eluent. The product was recrystallized from DCM/Iso-propanol mixture to obtain the pure product as a white solid. Yield: 0.875 g (1.94 mmol, 26%)

^1H NMR (400 MHz, CDCl_3 -d) δ 8.75 (s, 4H), 7.38 (t, J = 5.7 Hz, 2H), 4.24 – 4.04 (m, 2H), 1.78 (h, J = 7.5Hz, 2H), 1.22 (s, 8H), 9.03 (t, J = 7.4 Hz, 3H).

^{13}C NMR (100 MHz, CDCl_3 -d) δ 163.21, 162.83, 131.6, 130.91, 126.78, 126.68, 126.64, 126.47, 79.29, 42.45, 40.65, 39.20, 28.38, 28.15, 11.49

Synthesis of NDI-B-Boc

NDI-B-Boc was synthesized following the same procedure as described above. Yield: 25%

^1H NMR (400 MHz, CDCl_3 -d) δ 8.76 (s, 4H), 4.60 (br, 1H), 4.19 (m, 4H), 3.20 (q, J = 7.5 Hz, 2H), 1.43 (t, J = 7.4 Hz, 3H).

^{13}C NMR (100 MHz, CDCl_3 -d) δ 162.99, 162.98, 156.08, 131.13, 131.08, 126.85, 126.67, 79.33, 42.58, 40.57, 40.30, 28.55, 27.77, 25.53, 21.52, 11.62.

Synthesis of NDI-H-Boc

NDI-H-Boc was synthesized following the same procedure as described above.

^1H NMR (400 MHz, CDCl_3 -d) δ 8.78 (s, 4H), 4.54 (br, 1H), 4.28 – 4.15 (m, 4H), 3.13 (t, J = 6.6 Hz, 2H), 1.86 – 1.69 (m, 4H), 1.46 (m, 15H), 1.06 (t, J = 7.4 Hz, 3H)

^{13}C NMR (100 MHz, CDCl_3 -d) δ 163.01, 131.11, 131.09, 126.82, 126.75, 77.36 42.58, 40.92, 28.58, 28.11, 26.82 25.53, 11.63

NDI-E

Free NDI-E amine was obtained by stirring the protected NDI-E in 20 ml of 10 % Trifluoroacetic acid DCM solution. After 2 h the solvent was concentrated and the dry solid was redissolved in Methanol. After cooling the mixture in an ice-bath to 0 °C around 3 eqv. of 57 % HI-solution was added. After stirring the mixture for 2 hours, solid NDI-amine iodide precipitated as a yellowish solid. The precipitant was collected by centrifugation and washed 3x with diethyl ether. After recrystallization from isopropanol-methanol-mixture the product was dried under high-vacuum for 6 hours. NDI-B and NDI-H salts were synthesized accordingly.

¹H-NMR (400 MHz, DMSO-d₆) δ 8.67 (s, 4H), 7.79 (br, 3), 4.33 (t, J = 5.9 Hz, 2H), 4.02 (m, 2H), 3.18 (t, J = 5.9 Hz, 2H), 1.84-1.62 (m, 2H), 0.95 (t, J = 7.4 Hz, 3H)

¹³C-NMR (100 MHz, DMSO-d₆) δ 163.22, 162.61, 130.42, 126.43, 126.33, 126.18, 12.08, 41.73, 40.15, 39.94, 39.78, 39.73, 39.52, 39.31, 39.10, 38.89, 37.83, 37.52, 20.78, 11.42

HR-MS (ESI-QTOF): C₁₉H₁₈N₃O₄⁺: expected: 352.1292; found: 352.1292

NDI-B

¹H-NMR (400 MHz, DMSO-d₆) δ 8.62 (s, 4H), 7.62 (br, 3), 4.07 (t, J = 6.8 Hz, 2H), 4.04 – 3.95 (m, 2H), 2.84 (t, J = 7.4 Hz, 2H), 1.68 – 1.63 (m, 6H), 0.95 (t, J = 7.4 Hz, 3H)

¹³C-NMR (400 MHz, DMSO-d₆) δ 162.68, 162.58, 130.52, 130.50, 126.28, 126.11, 126.07, 126.06, 41.73, 38.74, 24.76, 24.63, 20.82, 11.44

HR-MS (ESI-QTOF): C₂₁H₂₂N₃O₄⁺: expected: 380.1605; found: 380.1612

NDI-H

¹H-NMR (400 MHz, DMSO-d₆) : 8.62 (s, 4H), 7.58 (br, 3), 4.09 – 3.94 (m, 4H), 2.79 (q, J = 7.5 Hz, 2H), 1.68 (m, 4H), 1.54 (m, 2H), 1.38 (m, 4H), 0.9 (t, J = 7.4 Hz, 3H)

¹³C-NMR (100 MHz, DMSO-d₆) : 162.60, 130.47, 130.44, 126.22, 126.21, 126.09, 41.70, 38.83, 27.28, 26.95, 26.07, 25.53, 20.82, 11.43

HR-MS (ESI-QTOF): C₂₃H₂₆N₃O₄⁺: expected: 408.1918; found: 408.1915

Appendix A. Appendix: Tuning Naphthalene Diimide Spacer Cations for the Incorporation into a Layered RP Phase Perovskite Structure

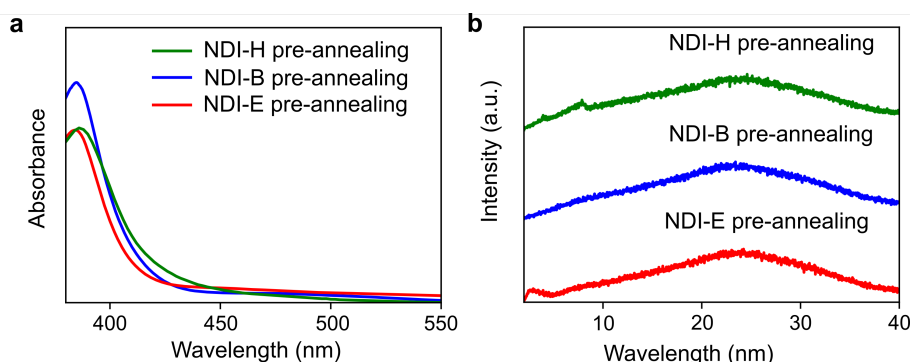


Figure A.2 – Visible light absorption spectra **a)** and XRD **b)** of the as-spun coated (NDI-E)₂PbI₄, (NDI-B)₂PbI₄, and (NDI-H)₂PbI₄ films.

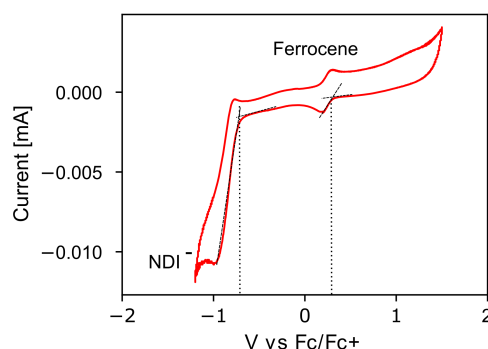


Figure A.3 – Cyclic voltammogram of NDI-E in DCM using Ferrocene as internal standard to measure oxidation potential of the spacer cation. Measurement was performed on Boc-protected NDI-E to prevent reduction of the I⁻ ion.

Cyclic voltammograms were obtained using a three-electrode cell setup with platinum foil as working electrode, Pt-wire as counter electrode and Ag⁺/AgCl as a reference electrode. To eliminate the oxidation of the iodide, NBoc-protected NDI-E in chloroform with tetrabutylammonium hexafluorophosphate (Bu₄NPF₆, 0.1 mol/L) as the supporting electrolyte was used. LUMO energy level was calculated based on the onset potential of the reduction process and the potential of the ferrocene reference (ferrocene vs. vacuum: - 4.8 V).

Table A.1 – Determined LUMO level of NDI-E-Boc based on CV. HOMO was derived from the optical band gap.

HOMO (eV)	LUMO (eV)	Optical Bandgap
-6.77	-3.67	3.1 eV

Analysis of GIWAXS data

The orientation of the layered perovskite films was determined by the Herman's orientation factor (H) defined by following equation:

$$\cos^2 \phi = \frac{\sum_{\phi=0}^{\pi} I(\phi) \cos^2(\phi) \sin(\phi)}{\sum_{\phi=0}^{\pi} I(\phi) \sin(\phi)} \quad (\text{A.1})$$

and

$$H = \frac{3 \cos^2(\phi) - 1}{2} \quad (\text{A.2})$$

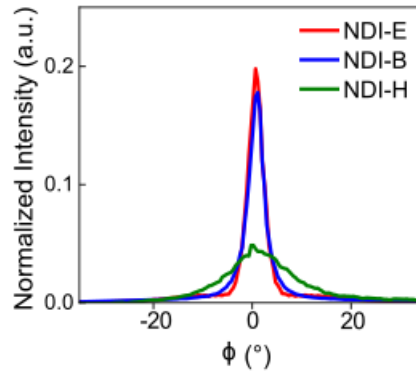


Figure A.4 – Integrated and normalized azimuthal angle (ϕ) derived from grazing-incidence small-angle X-ray scattering measurements.

Appendix A. Appendix: Tuning Naphthalene Diimide Spacer Cations for the Incorporation into a Layered RP Phase Perovskite Structure

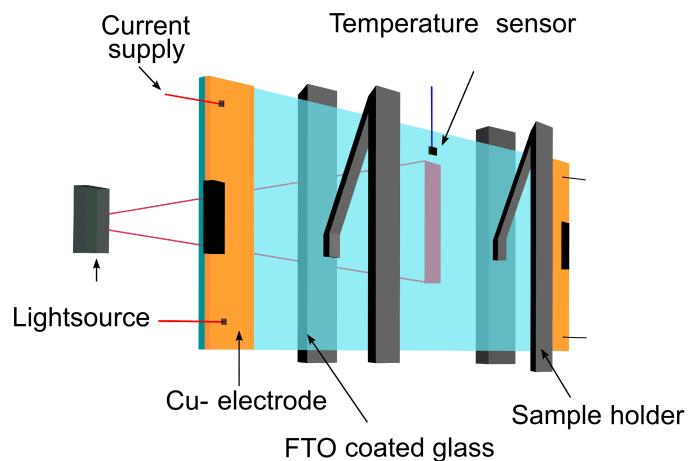


Figure A.5 – Setup of the FTO-coated window for *in-situ* UV-vis absorption measurements. The temperature of the window was controlled *via* a feedback loop with a temperature sensor directly on the window.

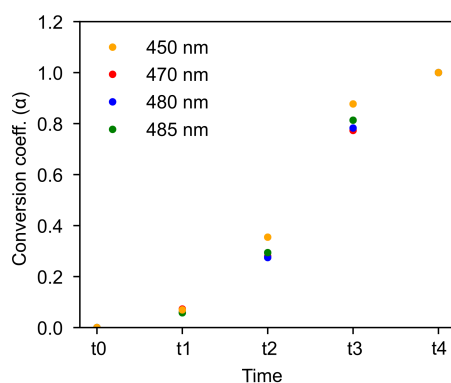


Figure A.6 – Evolution of the conversion coefficient at different absorption wavelength. The data was obtained by annealing NDI-E based films on a hot plate and measure full spectra after certain periods of time.

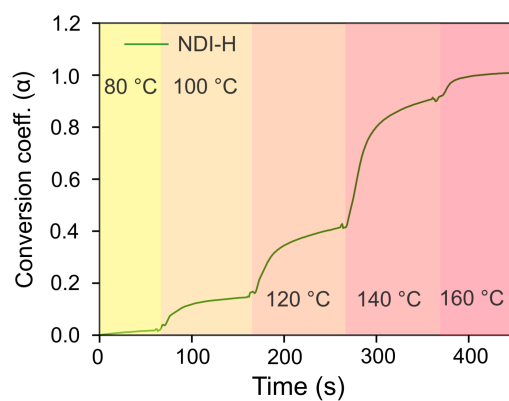


Figure A.7 – Evolution of conversion coefficient (α) over annealing of $(\text{NDI-H})_2\text{PbI}_4$.

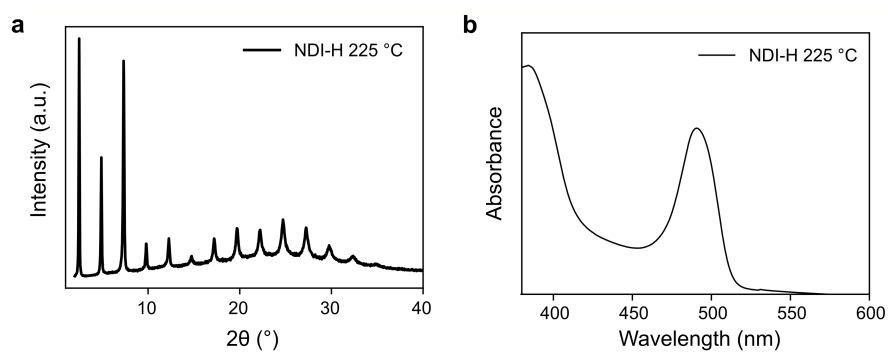


Figure A.8 – **a)** XRD and **b)** visible light absorption spectra of NDI-H annealed at 220 °C.

Appendix A. Appendix: Tuning Naphthalene Diimide Spacer Cations for the Incorporation into a Layered RP Phase Perovskite Structure

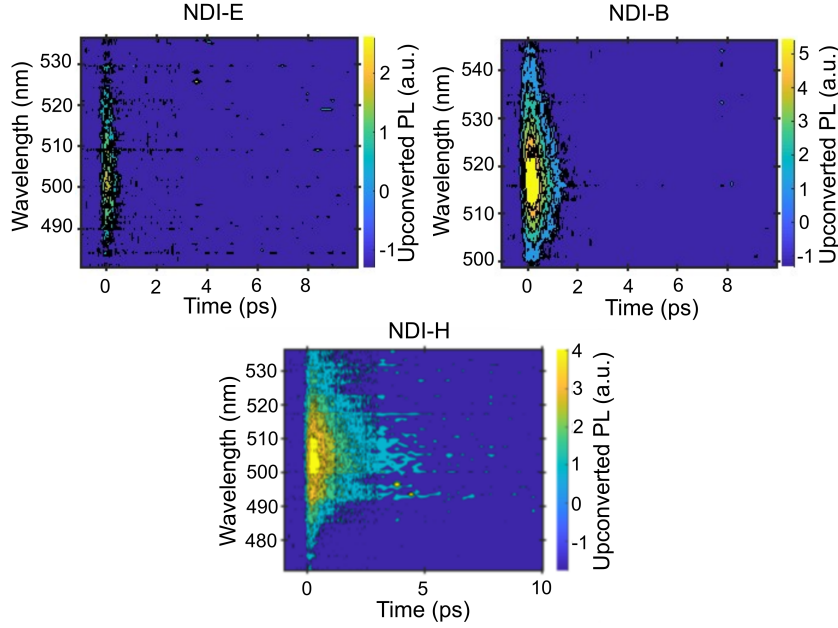


Figure A.9 – Temporal- and spectral dependent PL-intensity of (NDI-E)₂PbI₄, (NDI-B)₂PbI₄, and (NDI-H)₂PbI₄ excited at 400 nm.

Data Analysis and Fitting

We fitted the PL decays using a global analysis. For each sample, we applied a mono-exponential (NDI-E and NDI-B) or bi-exponential (NDI-H) decay function convoluted with a Gaussian function to fit every dynamic trace. The amplitudes and lifetimes were left free, while the Gaussian width and time-zero were fixed. These values were extracted from a 2D Gaussian fit using the cross-correlation between the un-absorbed pump beam and the gate beam around time-zero.

To extract the lifetimes displayed in Table 1, we performed a global analysis of the dynamic traces of the bleaching peak. A tri-exponential decay function was used to fit the data from 0.20 ps to 1200 ps leaving the amplitudes and lifetimes free and setting y_0 to 0. The decay-associated spectra (DAS, Figure A.10) display the extracted amplitude coefficients A_1 , A_2 , A_3 for each time constant (τ_1 , τ_2 , τ_3) versus the wavelength.

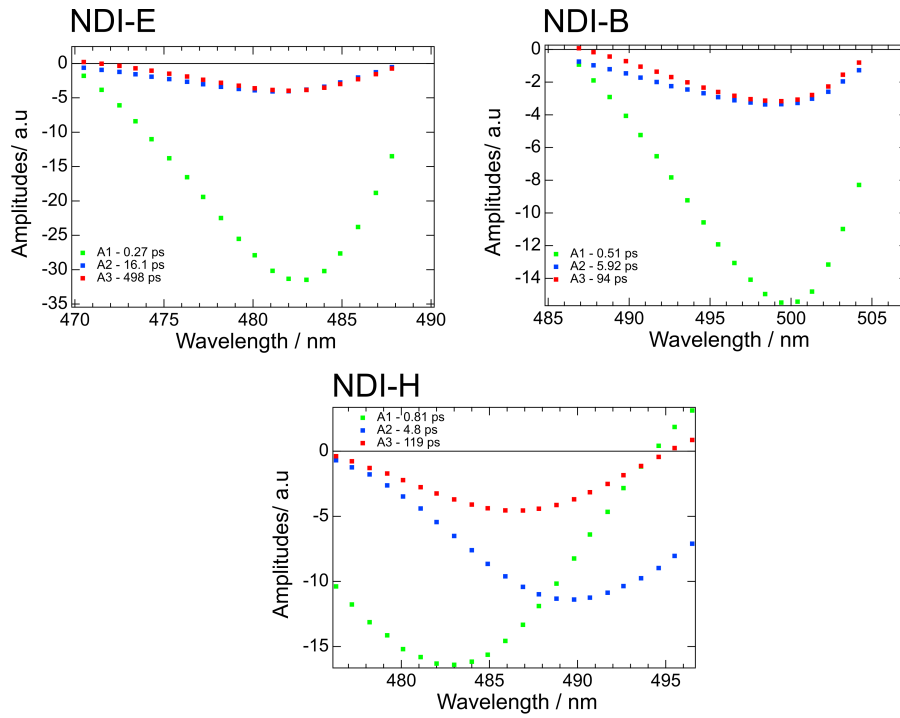


Figure A.10 – Decay associated spectra resulting from the global analysis of the ground state bleach.

Table A.2 – Decay dynamics of free charge carrier decay. NDI-based perovskites where excited at 420 nm with $2 \cdot 10^{13}$ photons per cm^2 .

	(NDI-E) ₂ PbI ₄	(NDI-B) ₂ PbI ₄	(NDI-H) ₂ PbI ₄	(PEA) ₂ PbI ₄
τ_1 (ns)	58	50	54	35
τ_2 (ns)	1442	1209	686	—

Appendix A. Appendix: Tuning Naphthalene Diimide Spacer Cations for the Incorporation into a Layered RP Phase Perovskite Structure

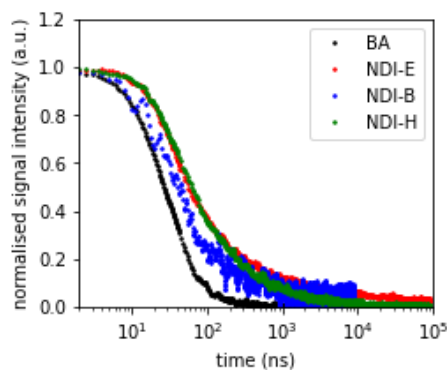


Figure A.11 – fp-TRMC transient of $(\text{NDI})_2\text{PbI}_4$ on logarithmic scale excited at 420 nm. NDI-based perovskites were excited with $2 \cdot 10^{13}$ photons per cm^2 .

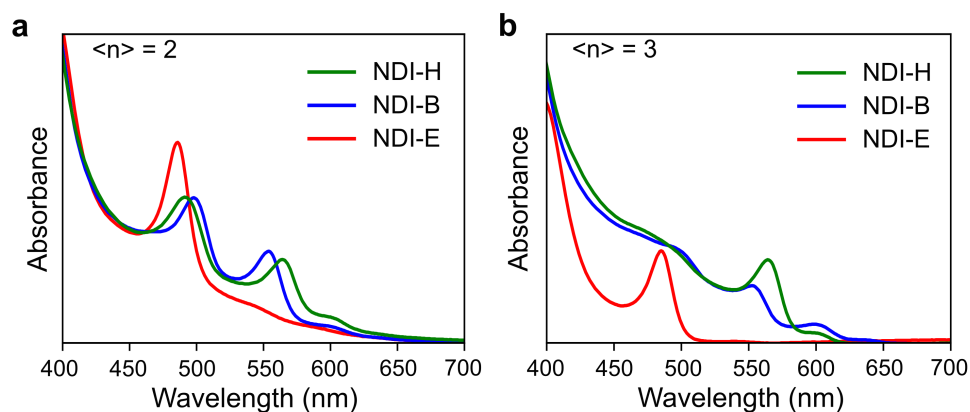


Figure A.12 – Visible light absorption of quasi-layered films with **a)** $\langle n \rangle = 2$ and **b)** $\langle n \rangle = 3$.

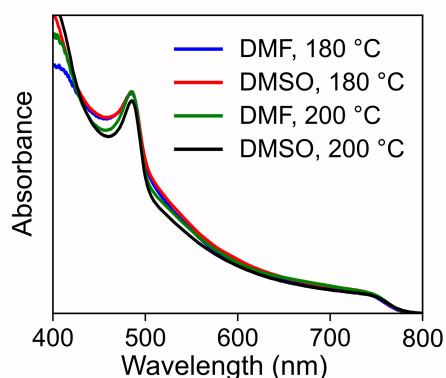


Figure A.13 – Absorption spectra of thin film of quasi-layered perovskite aimed for the phase $(\text{NDI-E})_2\text{MA}_4\text{Pb}_5\text{I}_{16}$ at various solvent (DMSO and DMF) and annealing temperatures.

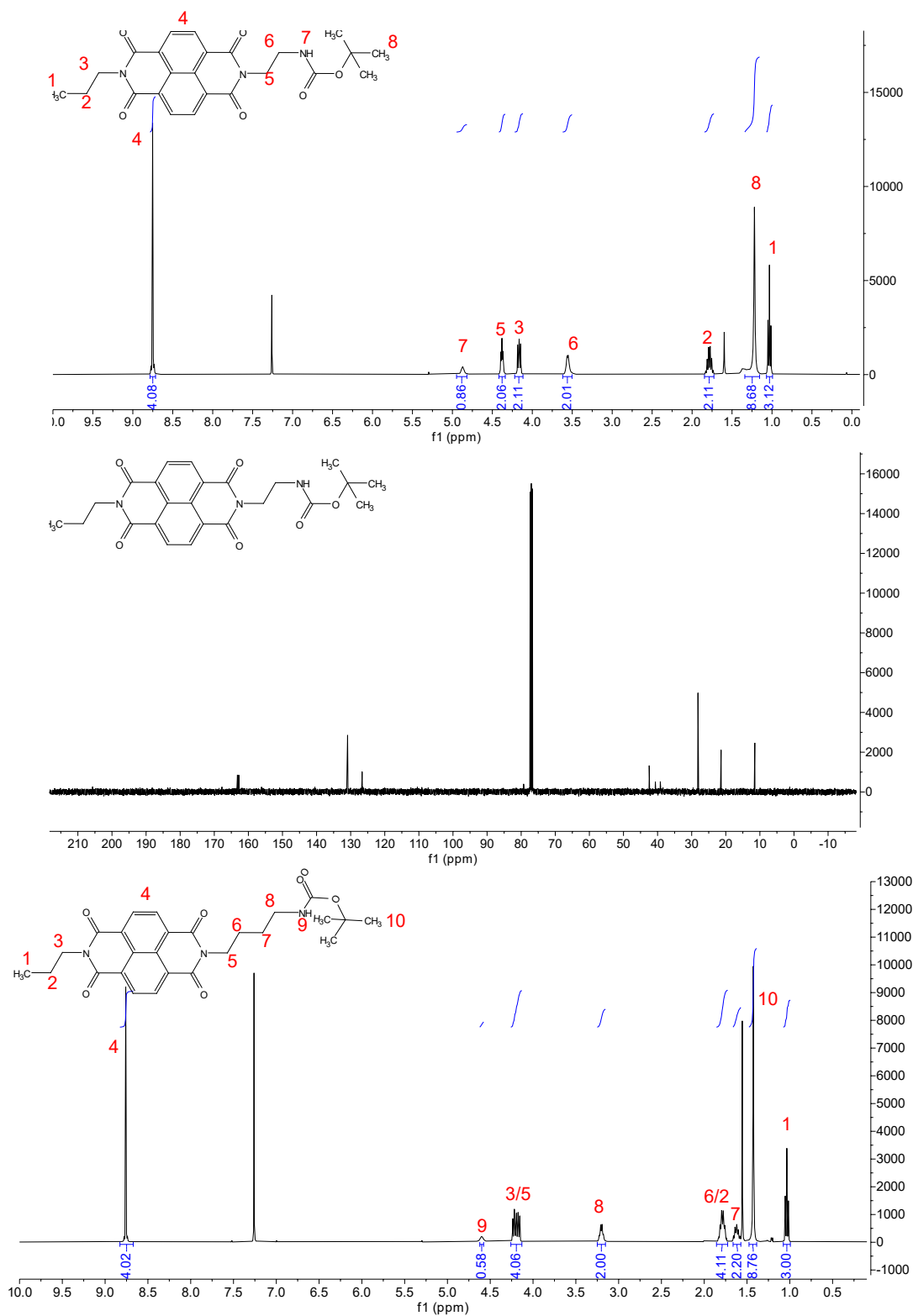


Figure A.14 – ^1H -NMR of NDI-E-Boc (top), ^{13}C -NMR of NDI-E-Boc (center), and ^1H -NMR of NDI-B-Boc (bottom) recorded in chloroform- d .

Appendix A. Appendix: Tuning Naphthalene Diimide Spacer Cations for the Incorporation into a Layered RP Phase Perovskite Structure

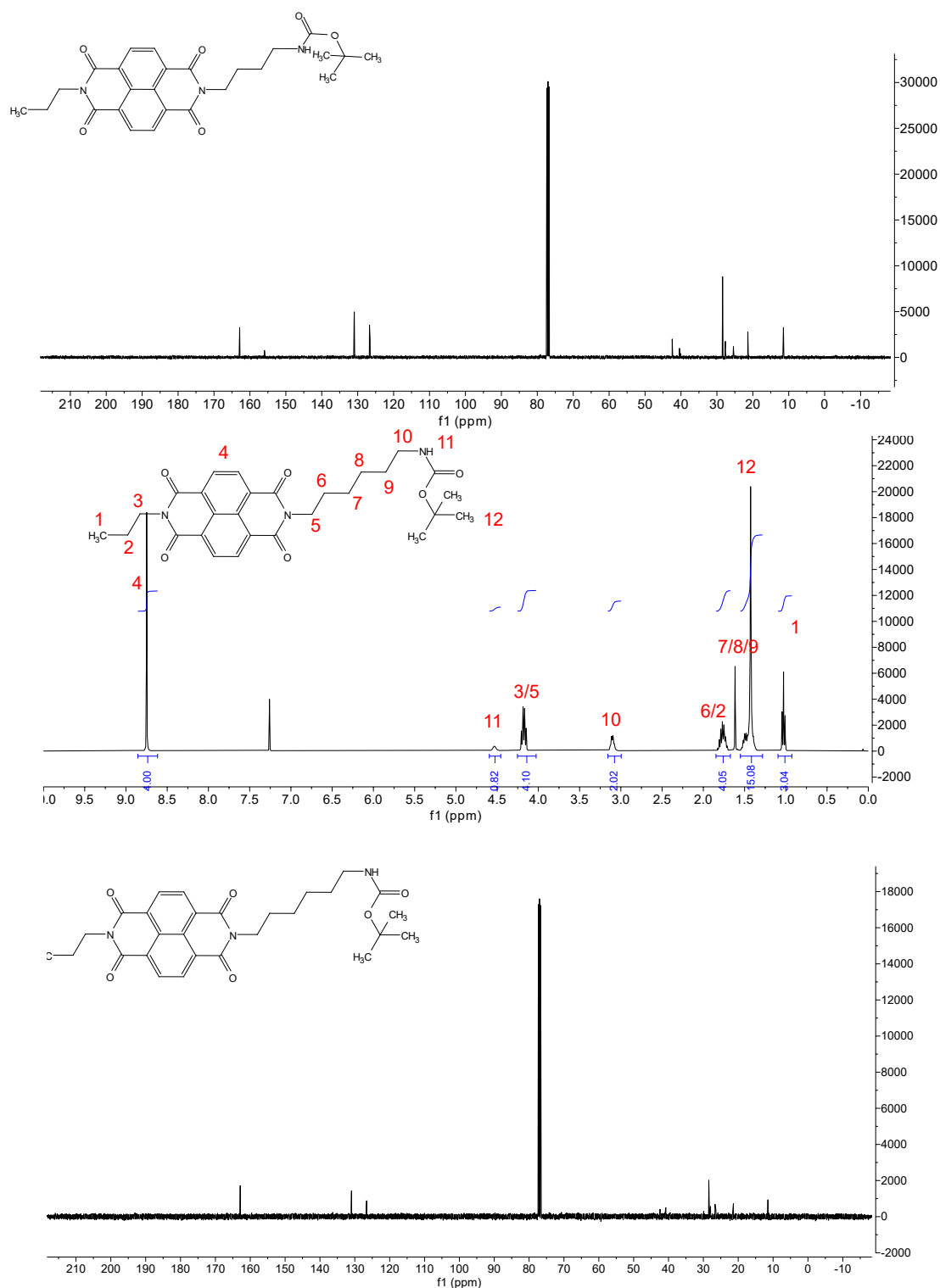


Figure A.15 – ^{13}C -NMR of NDI-B-Boc (top), ^1H -NMR of NDI-H-Boc (center), and ^{13}C -NMR of NDI-H-Boc (bottom) recorded in chloroform-d.

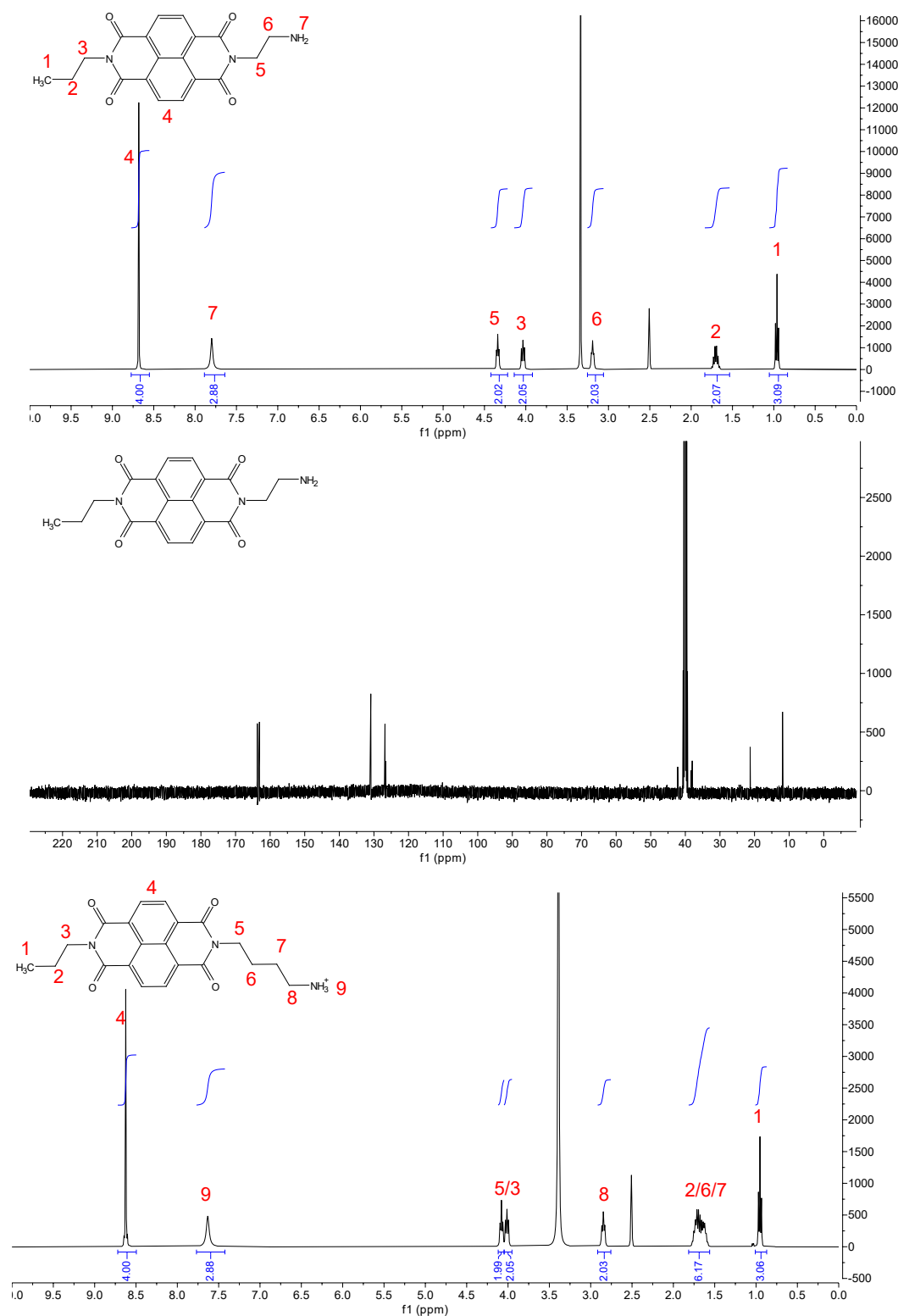


Figure A.16 – ¹H-NMR of NDI-E (top), ¹³C-NMR of NDI-E (center), and ¹H-NMR of NDI-B (bottom) recorded in DMSO-d₆.

Appendix A. Appendix: Tuning Naphthalene Diimide Spacer Cations for the Incorporation into a Layered RP Phase Perovskite Structure

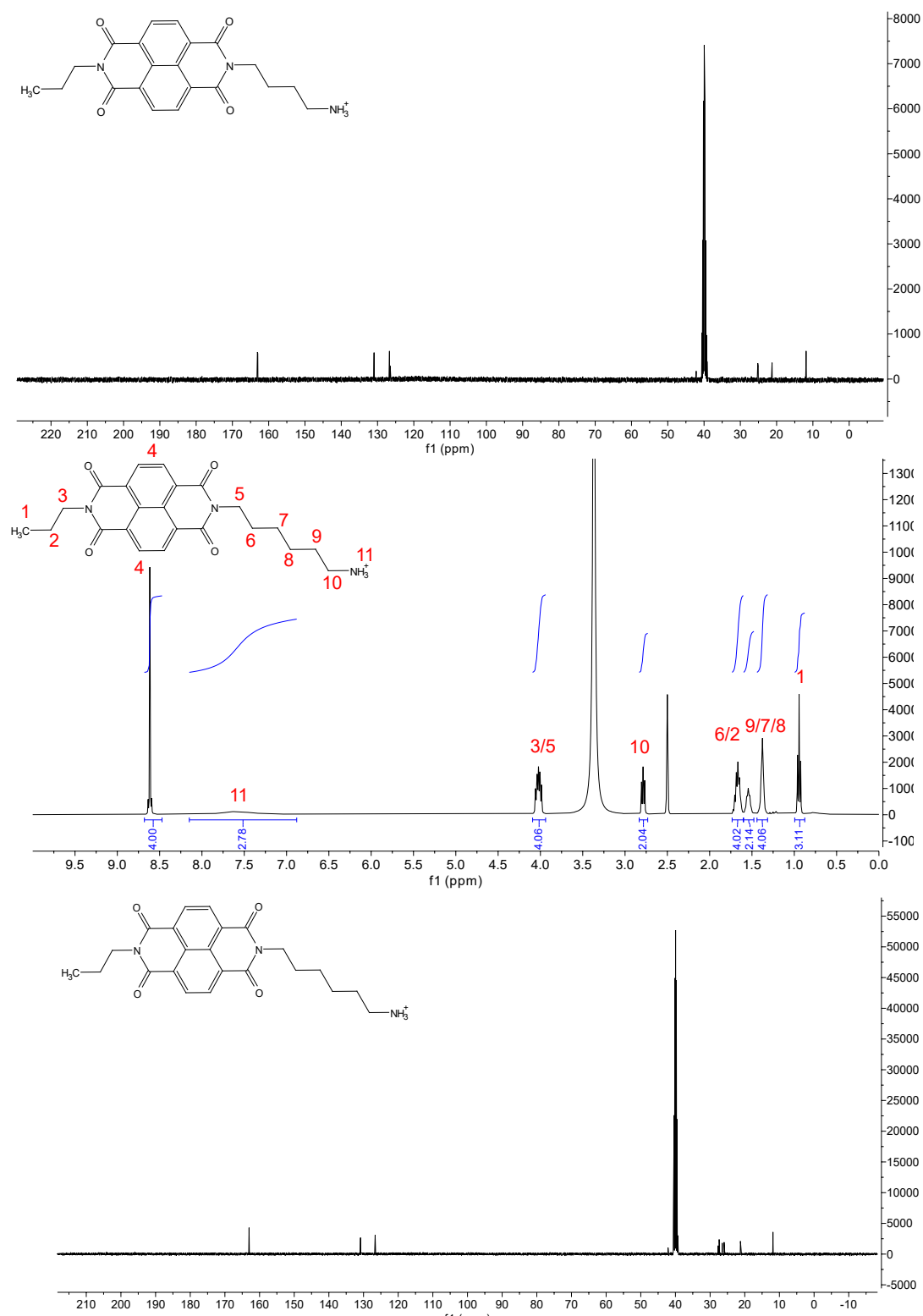


Figure A.17 – ¹³C-NMR of NDI-B (top), ¹H-NMR of NDI-H (center), and ¹³C-NMR of NDI-H (bottom) recorded in DMSO-d₆.

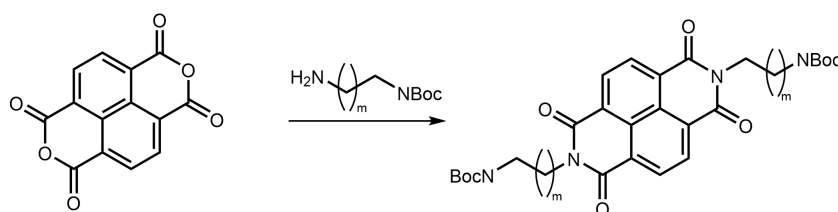
Appendix B

Appendix: Photogenerated Charge Transfer in Dion-Jacobson Type Layered Perovskite Based on Naphthalene Diimide

Materials and Experimental

Naphthalenedianhydride and N-Boc-1,6-hexanediamine (95%, CAS: 51857-17-1) were obtained from Fluorochem, N-Boc-1,4-butanediamine (95%, CAS: 68076-36-8) was purchased from ABCR. Perovskite precursor solutions were prepared with lead (II) iodide (99.99%, CAS: 10101-63-0) from TCI. Methylammonium iodide (>99.99%, CAS: 14965-49-2) and n-butylammonium iodide (>99%, CAS: 36945-08-1) were purchased from GreatCell.

Synthesis and Characterization of NDI-dH



NDI-dH-Boc was synthesized according to previously reported procedure: 5g of naphthalene dianhydride was mixed with NBoc-1,6-diaminohexane in a two-neck flask. After establishing an Argon atmosphere, The reaction mixture was dissolved in 80 ml of N,N-dimethylformamide (DMF) and heated up to 90 °C under continuous stirring. After 12 hours, the reaction mixture was concentrated and redissolved in (dichloromethane) DCM. Residue DMF was removed by 3x extraction with Water. The organic phase was collected and the pure product was obtained in 91 % yield after silica gel chromatography using DCM:ethylacetate as evolving eluent. The product

Appendix B. Appendix: Photogenerated Charge Transfer in Dion-Jacobson Type Layered Perovskite Based on Naphthalene Diimide

was further purified by recrystallisation from isopropanol:DCM mixture.

^1H NMR (400 MHz, CDCl_3 -d) δ 8.75 (s, 4H), 4.53 (s, 2H), 4.23 – 4.14 (m, 4H), 3.10 (q, J = 6.5 Hz, 4H), 1.74 (q, J = 7.6 Hz, 4H), 1.55 – 1.37 (m, 4H), 1.43 (m, 26H).

^{13}C NMR (101 MHz, CDCl_3 -d) δ 162.98, 156.13, 121.10, 126.80, 40.90, 30.06, 28.56, 28.08, 26.79, 26.54

HRMS (ESI-QTOF) m/z : $[\text{M} + \text{Na}^+]$: Calcd for $\text{C}_{36}\text{H}_{48}\text{N}_4\text{NaO}_8^+$ 687.3364; Found 687.3380.

Elemental analysis

	C	H	N
Calculated	65.04	7.28	8.43
Found average	65.07	7.31	8.44

NDI-dB

NDI-dB -Boc was synthesized according the same procedure as NDI-dH-Boc.

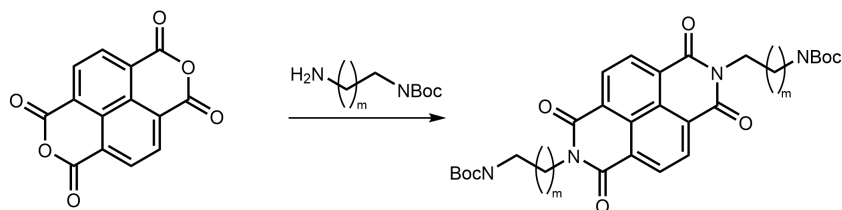
^1H NMR (400 MHz, CDCl_3 -d) δ 8.75 (s, 4H), 4.61 (s, 2H), 4.21 (t, J = 7.4 Hz, 4H), 3.20 (q, J = 6.7 Hz, 4H), 1.85-1.73 (m, 4H), 1.63 (d, J = 8.0 Hz, 4H), 1.42 (s, 18 H).

^{13}C NMR (101 MHz, CDCl_3 -d) δ 162.96, 156.09, 131.14, 126.84, 126.74, 116.78, 40.58, 28.55, 27.77, 25.52

Elemental analysis

	C	H	N
Calculated	63.14	6.62	9.20
Found average	62.93	6.57	9.07
Standard deviation	0.01	0.03	0.01

NDI-dH-Iodide Salt Formation



The NBoc protected NDI-dH was deprotected by dissolving NDI-dH-Boc in 15 % TFA:DCM solution. After evaporation the solvent and the excess of TFA, the crude solid was redissolved in methanol. After cooling the solution to 0 °C, 3 eqv. of hydroiodic acid was added. The mixture was stirred for 1 hours. The precipitate was collected by centrifugation and washed with diethyl ether until no yellow liquid could be removed.

^1H NMR (400 MHz, DMSO- d_6) δ 8.67 (s, 4H), 7.61 (br, 6H), 4.11 – 4.02 (m, 4H), 2.80 (t, J = 7.5 Hz, 4H), 1.67 (t, J = 7.4 Hz, 4H), 1.55 (d, J = 7.5 Hz, 4H), 1.38 (td, J = 8.7, 8.0, 4.2 Hz, 8H).

^{13}C NMR (101 MHz, DMSO- d_6) δ 162.61, 130.42, 126.28, 126.28, 38.77, 27.26, 26.90, 26.04, 25.49

HRMS (ESI/QTOF) m/z : $[\text{M}]^+$ Calcd for $\text{C}_{26}\text{H}_{34}\text{N}_4\text{O}_4^{+2}$ 233.1285; Found 233.1296.

NDI-dB-Iodide Salt

^1H NMR (400 MHz, DMSO- d_6) δ 8.70 (s, 4H), 7.61 (br, 6H), 4.10 (t, J = 6.9 Hz, 4H), 2.85 (d, J = 7.8 Hz, 4H), 1.73 (q, J = 7.4 Hz, 4H), 1.62 (q, J = 7.3, 6.7 Hz, 4H)

^{13}C NMR (101 MHz, DMSO- d_6) δ 163.23, 131.01, 126.81, 126.67, 39.16, 25.22, 25.09.

HRMS (ESI/QTOF) m/z : $[\text{M}]^+$ Calcd for $\text{C}_{22}\text{H}_{26}\text{N}_4\text{O}_4^{+2}$ 205.0972; Found 205.0977.

Appendix B. Appendix: Photogenerated Charge Transfer in Dion-Jacobson Type Layered Perovskite Based on Naphthalene Diimide

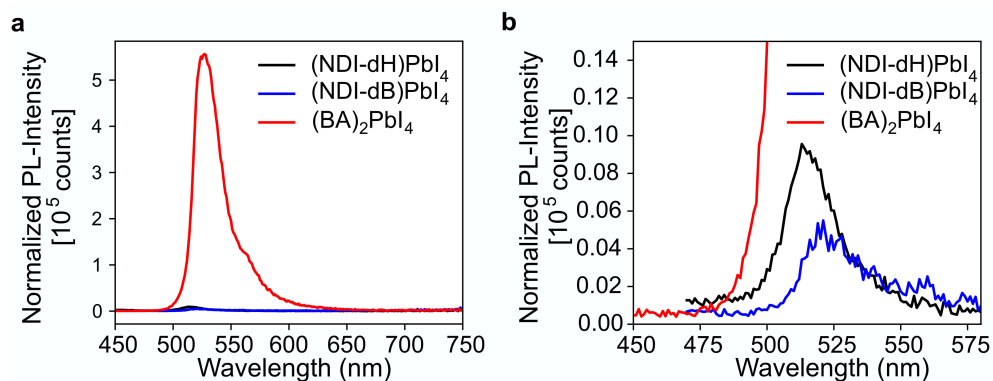


Figure B.1 – **a**) PL-intensity of (NDI-dB)PbI₄, (NDI-dH)PbI₄, and (BA)₂PbI₄ excited at 400 nm (3 nm slit). The PL-intensity is normalized to the absorbed photons at 400 nm, **b**) Zoom of Figure a.

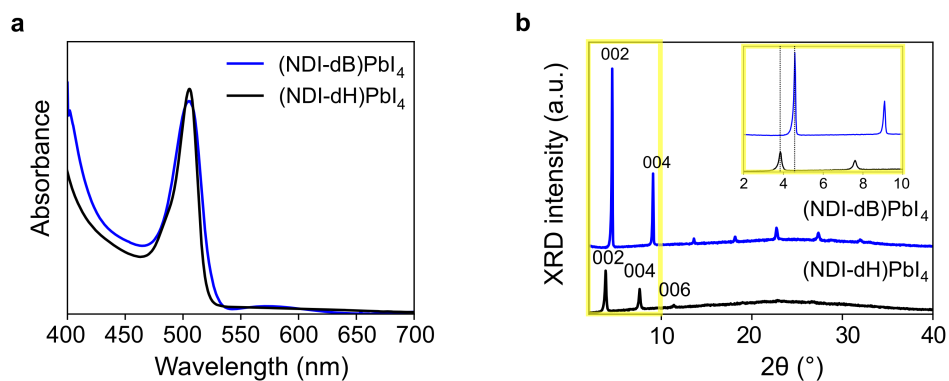


Figure B.2 – **a**) UV-vis absorbance and **b**) XRD of NDI-dH and NDI-dB based ($n = 1$) layered perovskite thin films.

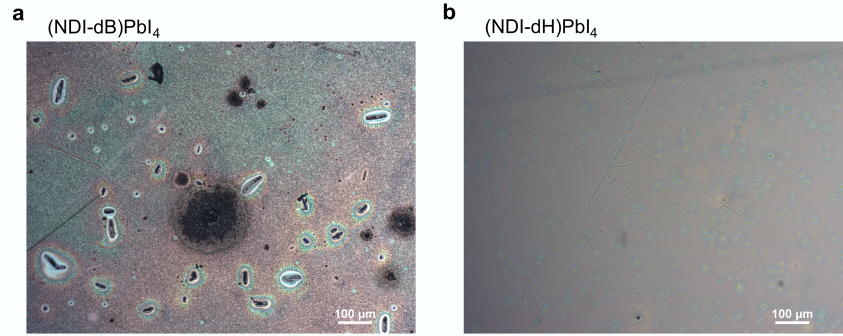


Figure B.3 – **a)** Image from optical microscope of (NDI-dB)PbI₄, and **b)** (NDI-dH)PbI₄.

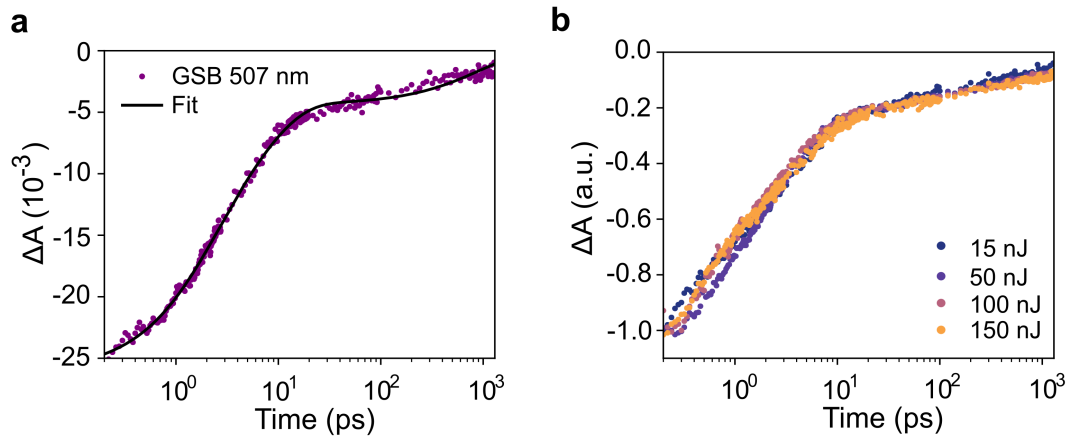


Figure B.4 – **a)** Ground state bleach (GSB) dynamics at 507 nm for (NDI-dH)PbI₄ films and **b)** GSB at 507 nm at different photon flux.

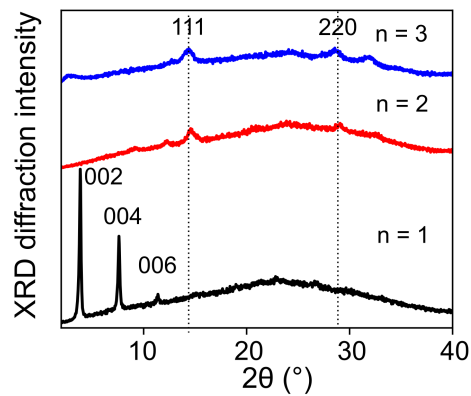


Figure B.5 – XRD of NDI-dH based perovskites $n = 1-3$ thin films.

Appendix B. Appendix: Photogenerated Charge Transfer in Dion-Jacobson Type Layered Perovskite Based on Naphthalene Diimide

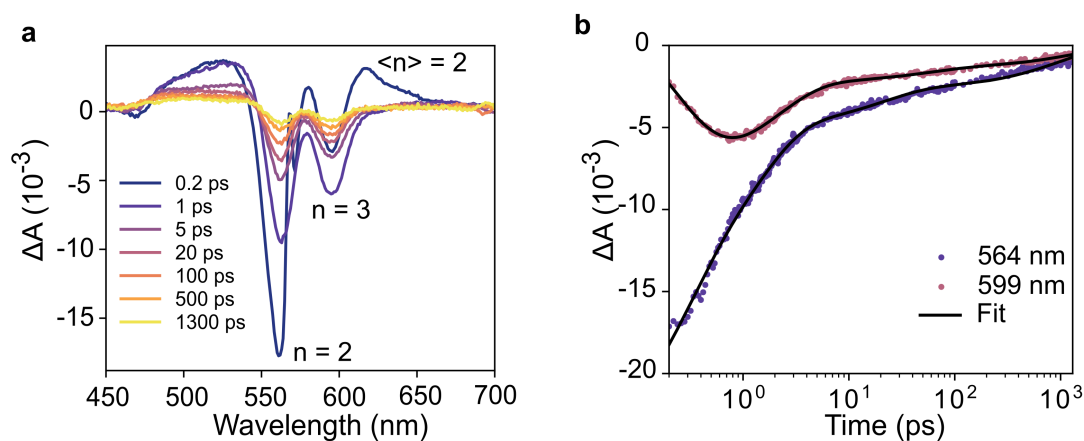


Figure B.6 – **a)** TA slices of $\langle n \rangle = 2$ film and **b)** GSB decay and fit of the $n = 2$ and $n = 3$ phase.

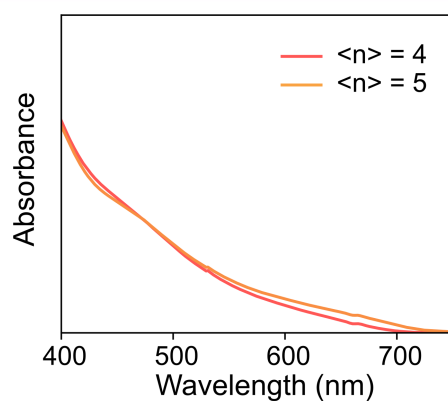


Figure B.7 – UV-vis absorbance of un-optimized $\langle n \rangle = 4$ and $\langle n \rangle = 5$ films.

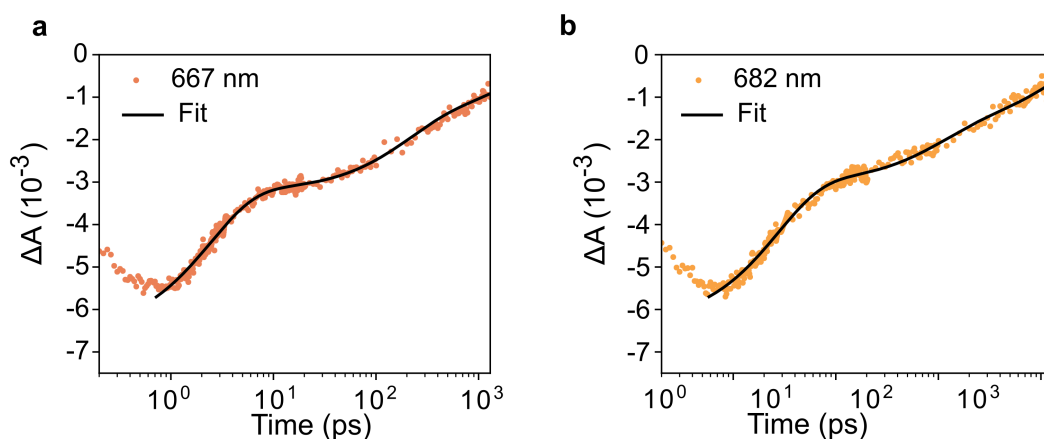


Figure B.8 – Ground state decay fit for **a)** $n = 4$ and **b)** $n = 5$ films.

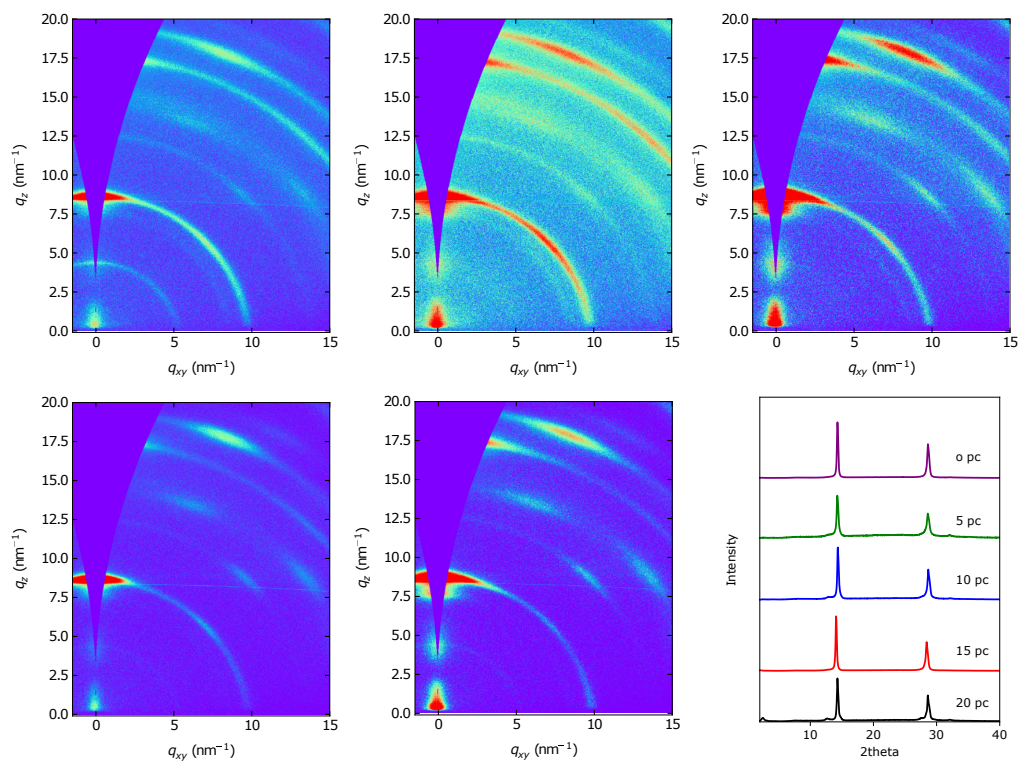


Figure B.9 – GIWAXS of thin film using various amounts of NH_4SCN in the precursor solution. The percentage are referred to as molar percentage of the PbI_2 .

Appendix B. Appendix: Photogenerated Charge Transfer in Dion-Jacobson Type Layered Perovskite Based on Naphthalene Diimide

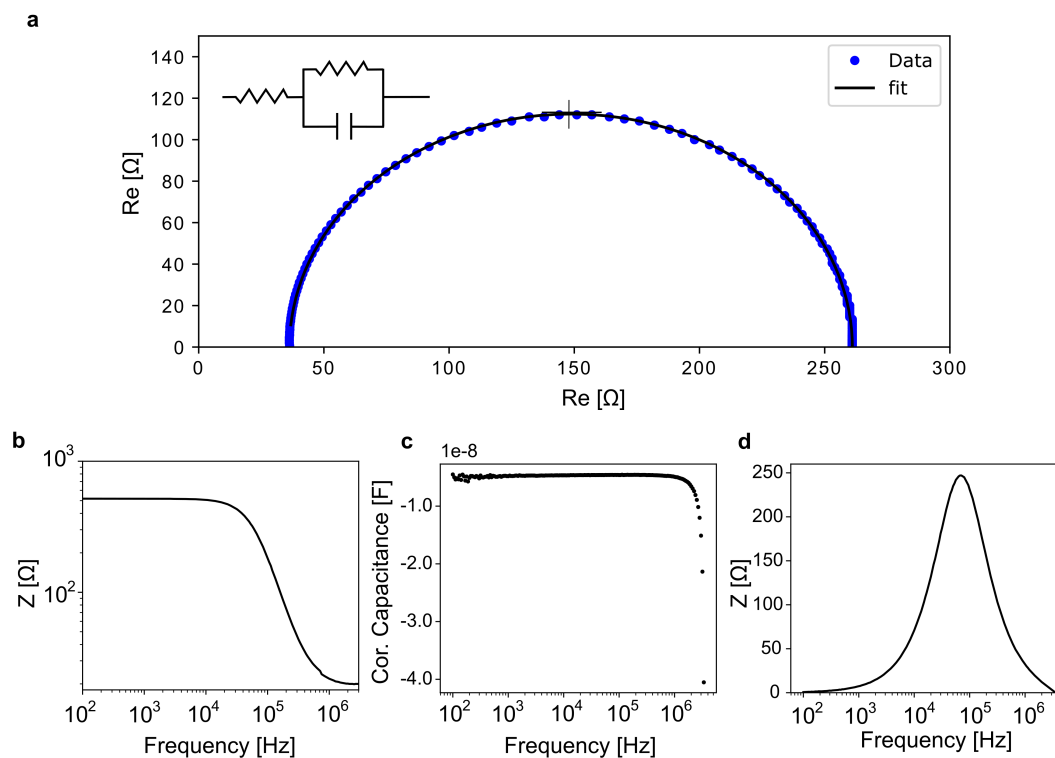


Figure B.10 – Obtained Impedance spectrum of NDI-dH based perovskite ($n = 5$). For the measurement the NDI-dH film was spin-coated on FTO and gold electrodes (0.16 cm^2) were evaporated on top.

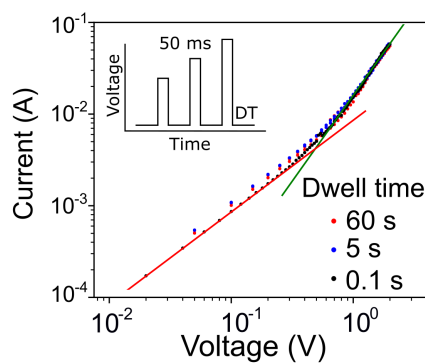


Figure B.11 – I-V curve for NDI-dH $n = 5$ using pulsed SCLC measurements for different dwell times.

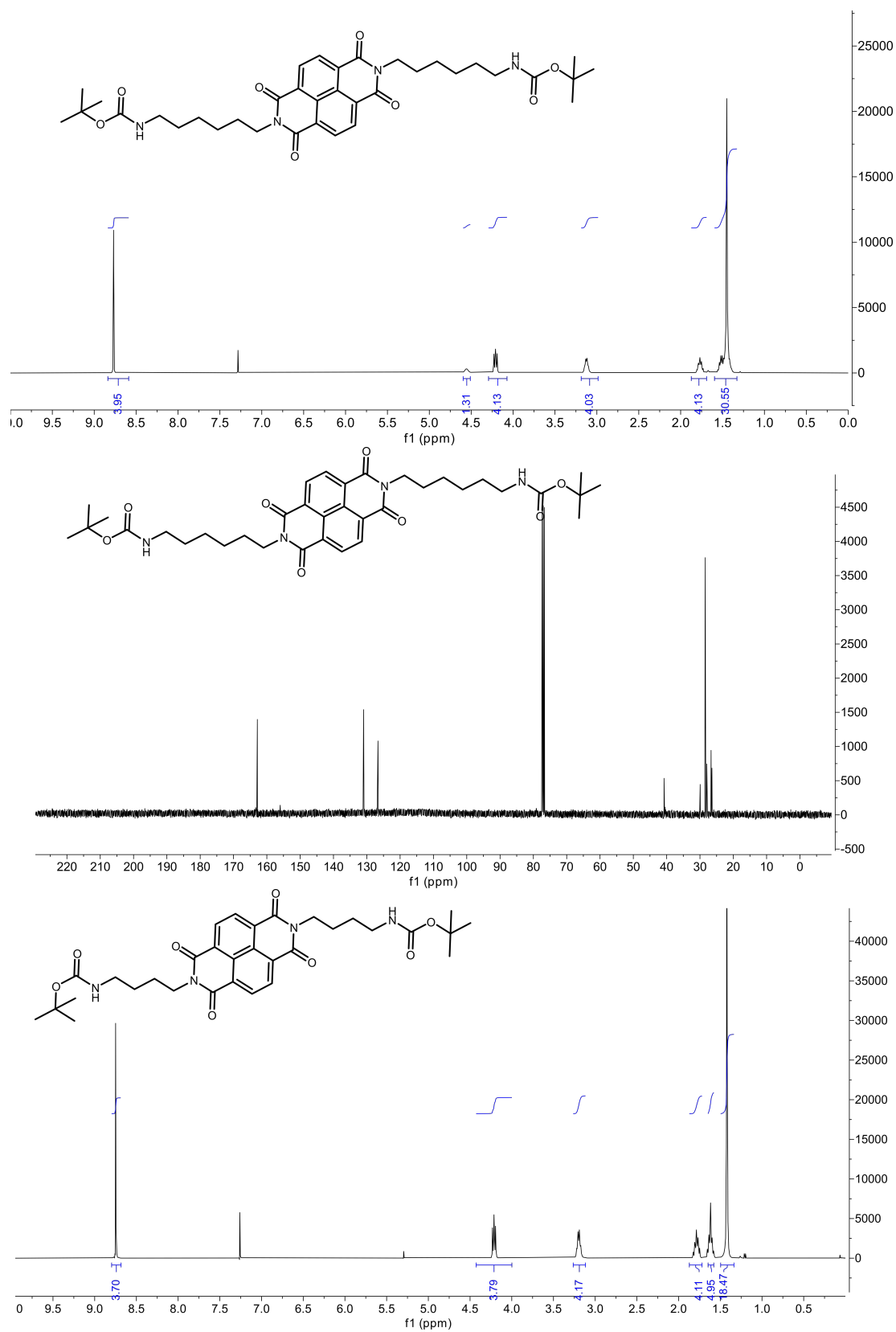
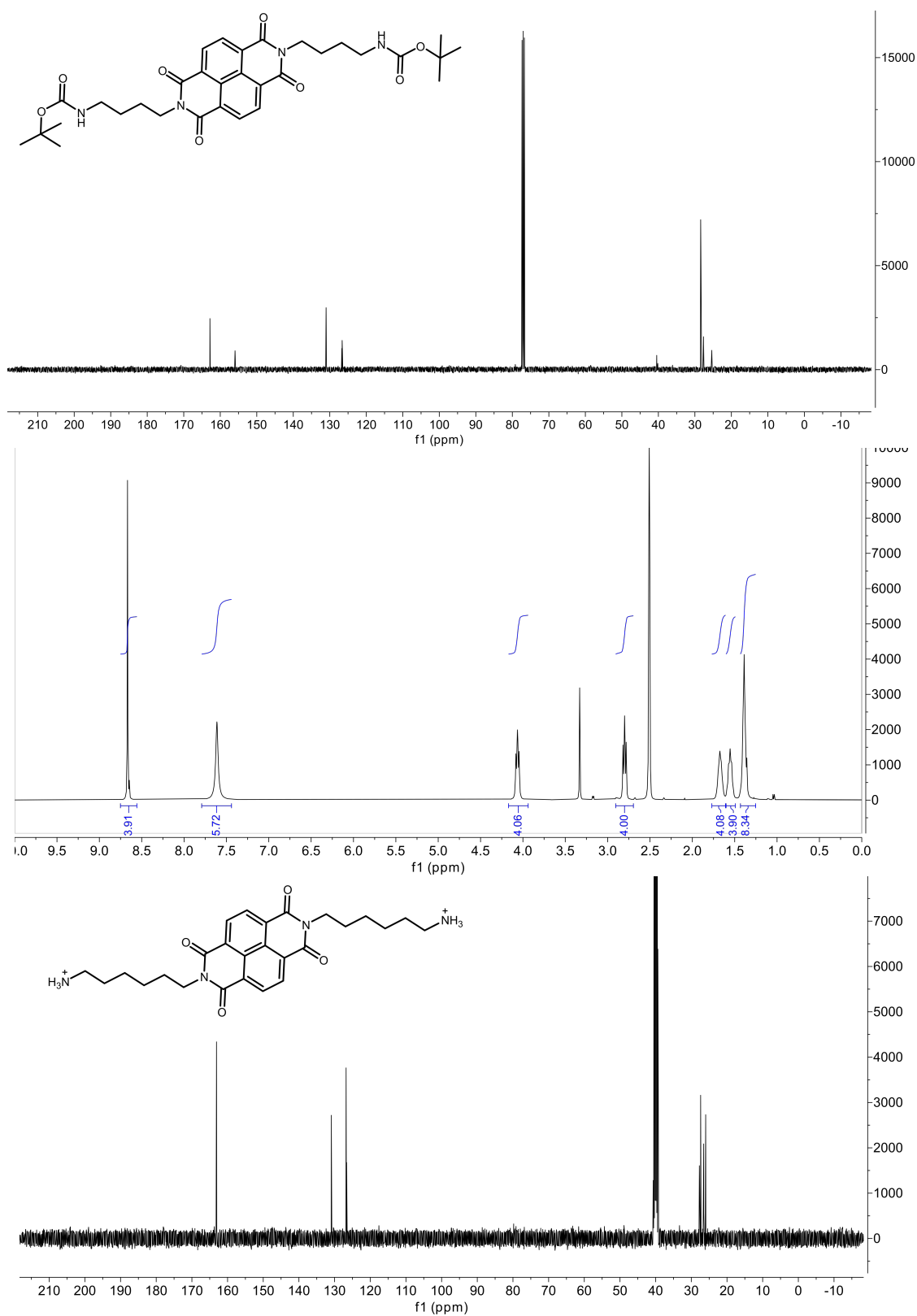


Figure B.12 – ^1H -NMR of NDI-dH-Boc (top), ^{13}C -NMR of NDI-dH-Boc (center), and ^1H -NMR of NDI-dB-Boc (bottom) in CDCl_3 .

Appendix B. Appendix: Photogenerated Charge Transfer in Dion-Jacobson Type Layered Perovskite Based on Naphthalene Diimide



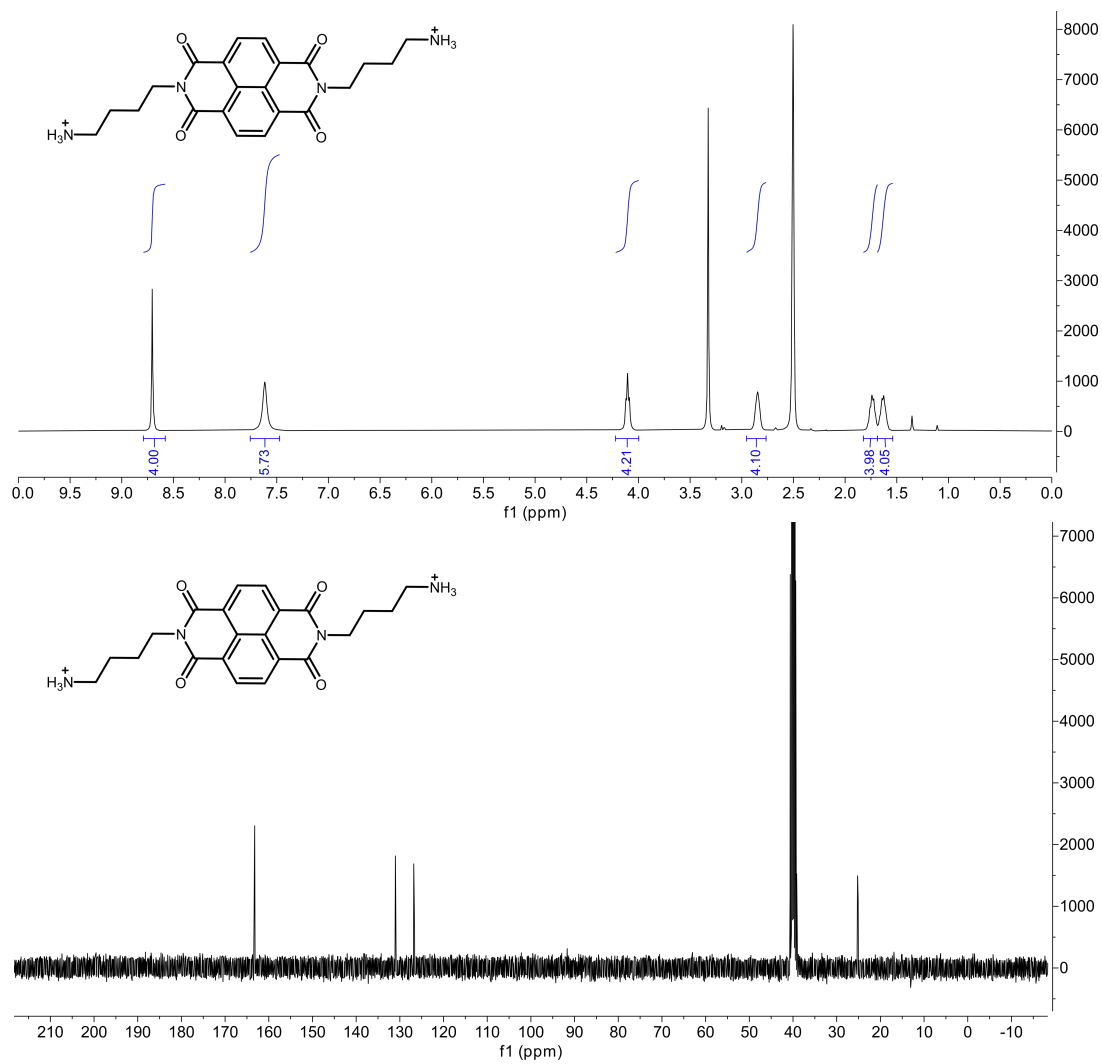


Figure B.14 – ^1H -NMR of NDI-dB (top), and ^{13}C -NMR of NDI-dB in DMSO- d_6 (bottom).

Appendix C

Appendix: Free Charge Carrier Generation by Visible Light Absorbing Chromophore Spacer in Ruddlesden-Popper Type Perovskites

Materials and Experimental

Boc-1,2-diaminoethyl (98%, CAS: 57260-73-8) and N-Boc-1,6-hexanediamine (95%, CAS: 51857-17-1) were purchased from Fluorochem, N-Boc-1,4-butanediamine (95%, CAS: 68076-36-8) and perylene dianhydride (95%, CAS: 128-69-8) and Naphthalene-1,4,5,8-tetracarboxylic dianhydride (95%, CAS: 81-30-1) was purchased from ABCR. Perovskite precursor solutions were prepared with lead (II) iodide (99.99%, CAS: 10101-63-0) and lead(II) bromide (>98 %, CAS: 10031-22-8) from TCI.

Synthesis of PDI-based Spacer Cation

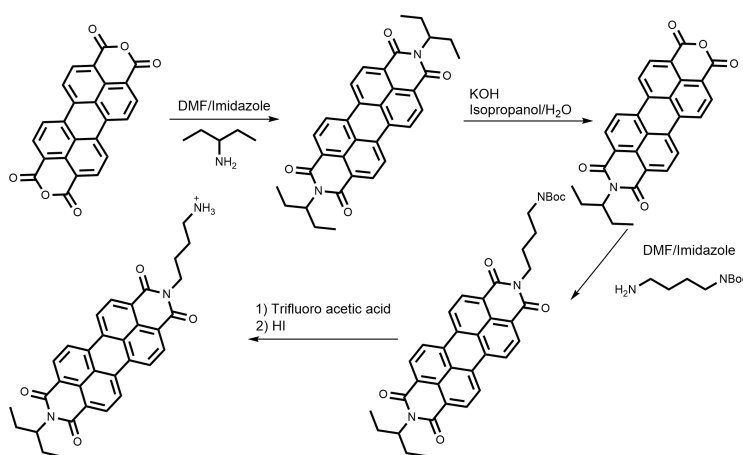
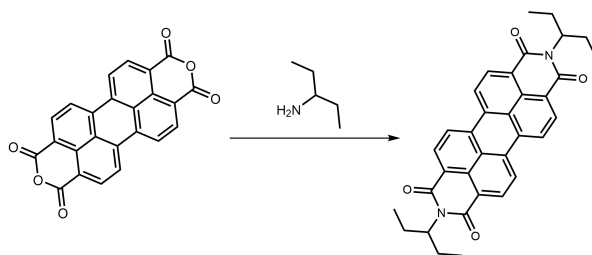


Figure C.1 – Schematic procedure for the synthesis of PDI-H.

Appendix C. Appendix: Free Charge Carrier Generation by Visible Light Absorbing Chromophore Spacer in Ruddlesden-Popper Type Perovskites

The desired product PDI-H was obtained by a multi-step synthesis forming firstly the Bis (ethylpropyl) perylene -3,4,9,10-tetracarboxylic diimide as previously described in our group.^[218] Using KOH in isopropanol, N-(ethylpropyl) perylene -3,4,9,10-tetracarboxylic monoimide monoanhydride was and was further reacted as described in the following scheme.

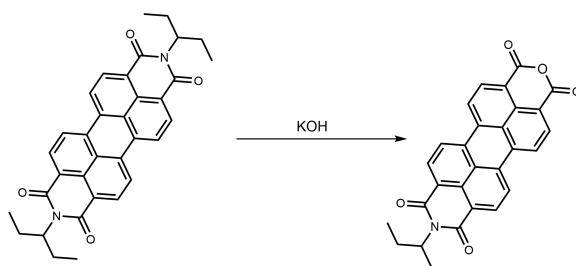
N,N'-Bis(ethylpropyl)perylen-3,4,9,10-tetracarboxylic Diimide



Perylene-3,4,9,10-tetracarboxylic dianhydride (2.004 g, 5.1 mmol, 1 eqv.) and 3-amino pentane (1.8 mmol, 15.5 mmol, 3 eqv.) mixed with imidazole (11 g) and 7 ml DMF and transferred to a round-bottomed flask. The reaction mixture was heated up to 140 °C and stirred for 8 h. Then the reaction mixture was diluted in 200 ml of water, and the solid was filtered off and washed with water. The solid was redissolved in DCM and washed 3x with deionized water. After concentrating the organic phase crude product was purified by column chromatography using DCM as eluent obtaining the desired product as a red water-insoluble solid in good yields 2.556 g (4.82 mmol, 94%)

¹H-NMR (400 MHz, CDCl₃-d) δ 8.69 – 8.57 (m, 8H), 5.06 (td, J = 9.5, 4.9 Hz, 2H), 2.27 (ddd, J = 13.7, 9.3, 7.1 Hz, 4H), 1.95 (dp, J = 14.0, 7.2 Hz, 4H), 0.93 (t, J = 7.4 Hz, 12H).

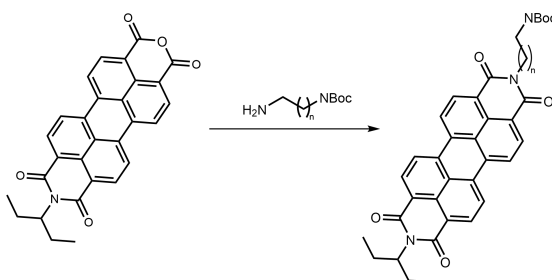
N-(ethylpropyl)perylen-3,4,9,10-tetracarboxylic Monoimide Monoanhydride



A suspension of N,N'-di(1-ethylpropyl)perylen-3,4,9,10-tetracarboxylic diimide (2a), and KOH (35 g, 0.54 mol) in isopropanol (350 mL) and water (50 mL) was refluxed for 1.5 h and monitored

by TLC. Then 100 ml of acetic acid was added and the reaction mixture was stirred for 1h. In addition, 60 ml of 2M HCl solution was added and stirred for 12 h. The crude product was obtained after filtration, redissolved in DCM and washed with water. The organic layer was concentrated and the resulting solid was used without further purification in the next step.

Synthesis of PDI-H-Boc



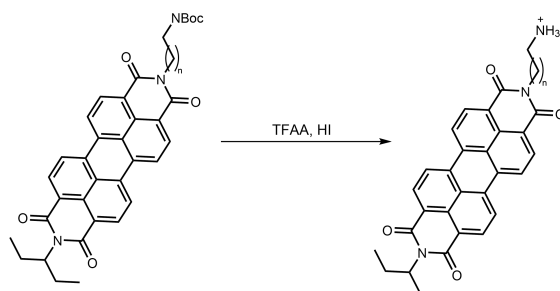
1.05 g (2.28 mmol, 1 eqv.) of the monoanhydride were transferred in a two-neck flask and mixed together with 6 g of imidazole and 351.5 mg (1.92 mmol, 84%) of Zn(OAc)₂. After establishing an argon atmosphere, 6 ml of DMF was added and the reaction mixture was heated to 120 °C. Then 0.8 ml (3.56 mmol, 1.56 eqv.) of NBoc-1,6-diaminohexane was added. The reaction mixture was heated up to 140°C and stirred overnight. After 12 h 100 ml of H₂O was added and the solid was filtered off. The crude product was purified by silica column using DCM/MeOH (0.5%) as eluent to yield 621 mg (0.94 mmol, 37% 2 steps) of the product as a red solid. The product was subsequently recrystallized from a isopropanol/THF mixture.

¹H-NMR (400 MHz, CDCl₃): δ 8.52 (d, J = 7.8 Hz, 2H), 8.34 (dd, J = 16.7, 7.9 Hz, 4H), 8.23 (d, J = 8.0 Hz, 2H), 5.06 (tt, J = 9.5, 5.9 Hz, 1H), 4.59 (br, 1H), 4.10 (t, J = 7.6 Hz, 2H), 3.12 (t, J = 6.9 Hz, 2H), 2.28 (dp, J = 21.5, 7.7 Hz, 2H), 1.98 (dp, J = 14.1, 7.2 Hz, 2H), 1.72 (m, 2H), 1.52 (t, J = 6.9 Hz, 2H), 1.43 (m, 13H), 0.98 (t, J = 7.4 Hz, 6H).

¹³C-NMR (101 MHz, CDCl₃): δ 163.27, 77.36, 57.95, 40.57, 30.07, 28.59, 26.87, 26.58, 25.19, 11.56

MS (MALDI-TOF) (negative mode): m/z calcd. for C₄₀H₄₂N₃O₆ [M⁻] : 659.30 found: 659.2

Deprotection of PDI-H-Boc and Salt Formation



Boc-protected PDI-H was deprotected by stirring PDI-H-Boc in a 10:1 %v/v DCM:trifluoro acetic acid for 2 h.

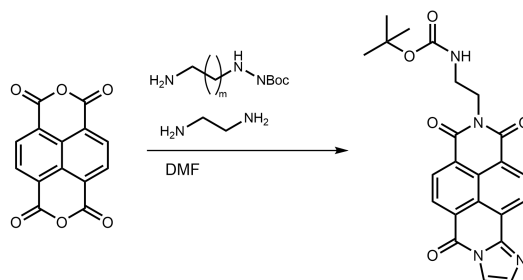
To obtain the corresponding salt, 323.32 mg of the amine was dissolved in about 20 ml of MeOH and cooled down to 0 °C in the ice bath. HI (90 μ l) was added dropwise and the reaction mixture was stirred at 0 °C for 2.5 h. The final product was precipitated by adding 25 ml of diethyl ether and obtained by centrifugation for 5 minutes at 7800 rpm. After disposing of the supernatant, the solid was redispersed in diethyl ether and again centrifuged for 5 minutes at 7800 rpm. This was repeated 3 times until the supernatant was colorless. Finally, the solid was dried at a high-vacuum for 3 h.

¹H-NMR (400 MHz, DMSO-d₆) δ 8.53 (d, J = 8.1 Hz, 2H), 8.40 (t, J = 8.8 Hz, 4H), 8.10 (d, J = 8.2 Hz, 2H), 7.62 (br, 3H), 4.97 (dd, J = 9.8, 4.3 Hz, 1H), 3.91 (d, J = 7.6 Hz, 2H), 2.80 (t, J = 7.6 Hz, 2H), 2.25 – 2.15 (m, 2H), 1.93 (dt, J = 13.9, 6.6 Hz, 2H), 1.58 (dd, J = 16.9, 9.7 Hz, 4H), 1.38 (m, 4H), 0.94 (t, J = 7.4 Hz, 6H).

ESI-MS (negative mode): m/z calcd. for C₃₅H₃₄N₃O₄ [M⁻] : 560.25; found: 560.42

Due to the limited solubility of the PDI salt no C-NMR could be recorded.

NDI-DAE-Boc (NDI-DAE-B-Boc)



NDI-DAE-Boc was synthesized following an adapted procedure previously reported.^[228] 5.0 g (18.74 mmol, 1 eqv.) of 1,4,5,8-Naphthalenetetracarboxylic dianhydride were dissolved in 80 ml of dry DMF under an argon atmosphere. Then 1.5 ml (1.08 g, 18.74 mmol, 1 eqv.) ethylenediamine and 3.53 g (18.76 mmol, 1 eqv.) of N-Boc-1,4-diaminobutane were added. The reaction mixture was stirred for 24 h at 120 °C. The crude product was precipitated by adding 100 ml water to the reaction and obtained after subsequent filtration of the precipitant. Additionally, the precipitant was redissolved in DCM and washed with H₂O (5x 50 ml) to remove remaining DMF. The desired product was obtained by silica gel column purification using DCM:methanol (99.5:0.5) as eluent. Yield: 2.031 g (2.24 mmol, 12%).

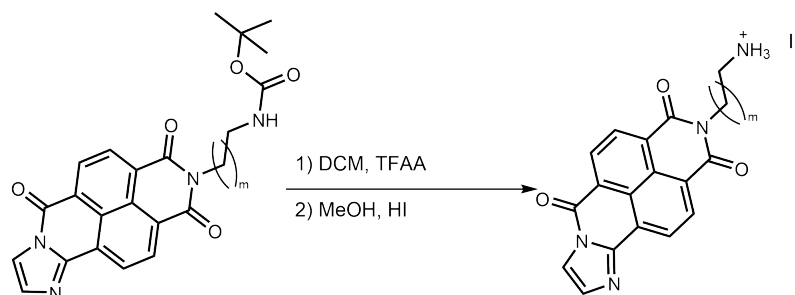
¹H-NMR (400 MHz, CDCl₃) δ 8.89 (d, J = 7.6 Hz, 1H), 8.81 – 8.72 (m, 3H), 7.94 (d, J = 1.6 Hz, 1H), 7.45 (d, J = 1.6 Hz, 1H), 4.63 (br, 1H), 4.26 – 4.18 (m, 2H), 3.21 (q, J = 6.5 Hz, 2H), 1.86 – 1.74 (m, 2H), 1.66-1.63 (m, 4H), 1.43 (s, 9H).

¹³C-NMR (101 MHz, CDCl₃) δ 163.05, 162.91, 158.34, 156.09, 144.58, 133.20, 132.22, 130.74, 128.37, 127.61, 126.68, 125.78, 125.47, 124.79, 123.79, 116.49, 66.31, 53.57, 40.52, 28.56, 27.78, 25.58.

HRMS (ESI/QTOF) m/z: [M + Na]⁺ Calcd for C₂₅H₂₄N₄NaO₅⁺ 483.1639; Found 483.1638.

	C	H	N
Calculated	65.21	5.25	12.17
Found average	64.97	5.20	12.05
Standard deviation	0.05	0.01	0.04

NDI-DAE-Iodide Salt



^1H NMR (400 MHz, DMSO) δ 8.60 (d, J = 7.6 Hz, 1H), 8.50 (d, J = 7.6 Hz, 1H), 8.42 (d, J = 7.7 Hz, 1H), 8.36 (d, J = 7.6 Hz, 1H), 7.99 (d, J = 1.6 Hz, 1H), 7.63 (s, 3H), 7.42 (d, J = 1.6 Hz, 1H), 4.03 (t, J = 6.8 Hz, 2H), 2.86 (h, J = 5.9 Hz, 2H), 1.79 – 1.68 (m, 2H), 1.68 – 1.56 (m, 2H).

^{13}C -NMR (101 MHz, DMSO- d_6) δ 162.41, 162.28, 157.69, 143.70, 132.72, 131.47, 131.21, 130.13, 127.08, 126.36, 126.14, 124.87, 124.39, 123.60, 122.68, 116.64, 38.71, 24.76, 24.63.

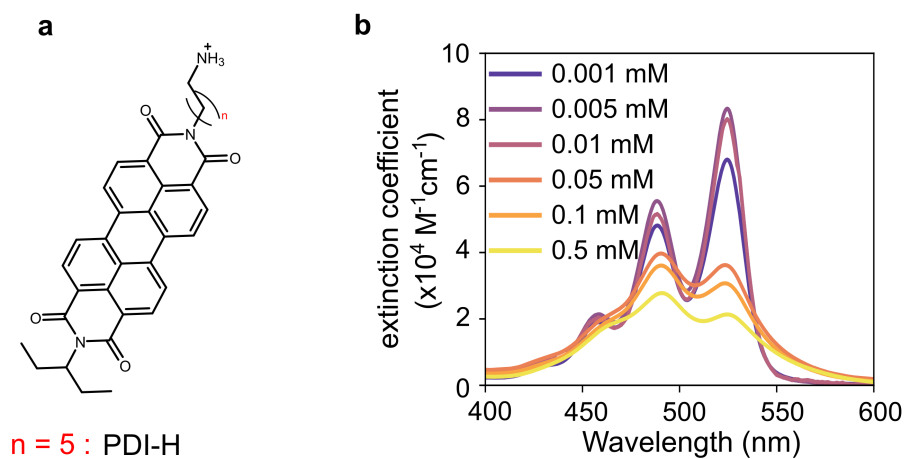


Figure C.2 – UV-vis of PDI-H in DMF at different concentration showing aggregation in the precursor solution.

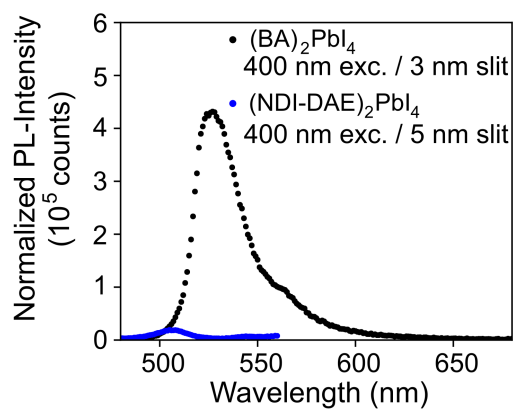


Figure C.3 – PL-intensity of the $(\text{NDI-DAE})_2\text{PbI}_4$.

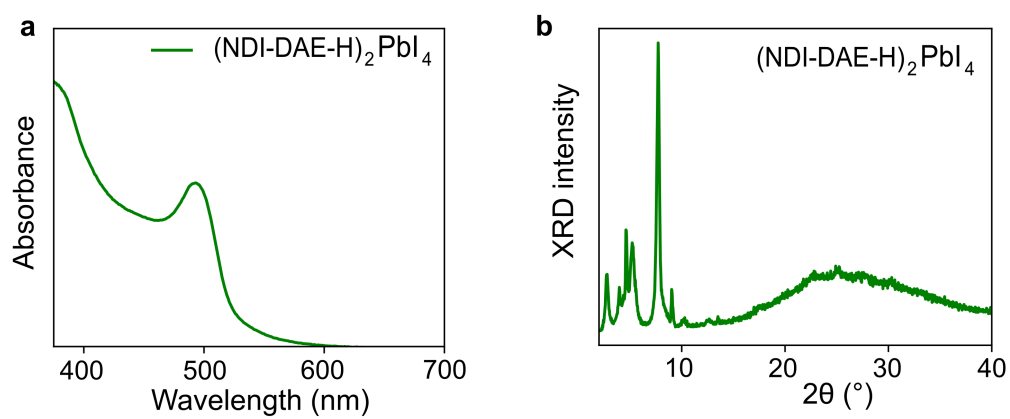


Figure C.4 – UV-vis **a)** and XRD **b)** of NDI-DAE with a hexyl based alkane chain incorporated into a layered perovskite structure.

Appendix C. Appendix: Free Charge Carrier Generation by Visible Light Absorbing Chromophore Spacer in Ruddlesden-Popper Type Perovskites

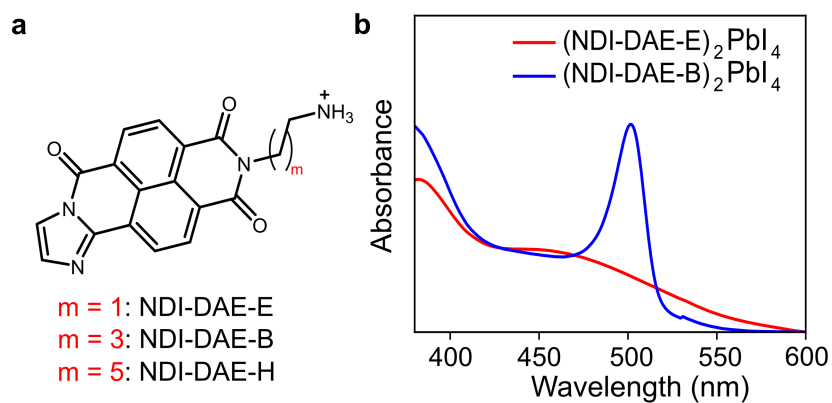


Figure C.5 – UV-vis of NDI-DAE with a ethyl based alkane chain.

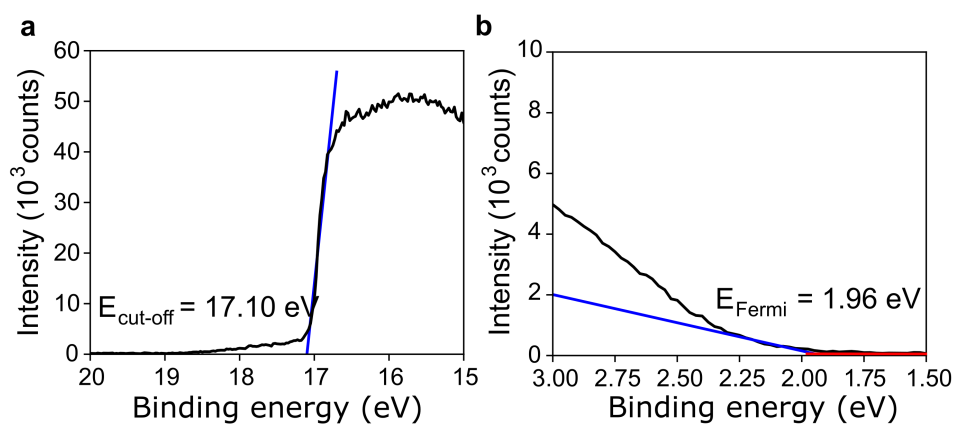


Figure C.6 – UPS spectra of NDI-DAE chromophore spin-coated on FTO coated glass substrate. $E_{\text{HOMO}} = -6.08 \text{ eV}$.

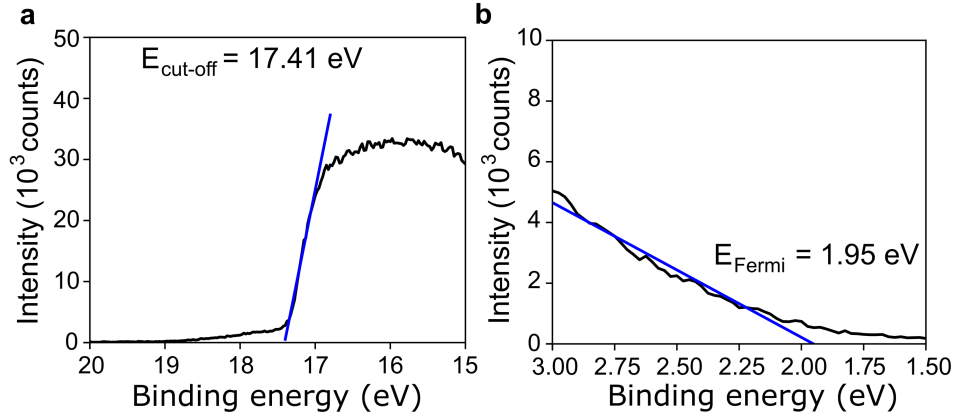


Figure C.7 – UPS spectra of $(\text{BA})_2\text{PbI}_4$ chromophore spin-coated on FTO coated glass substrate $E_{\text{VB}} = -5.76$ eV.

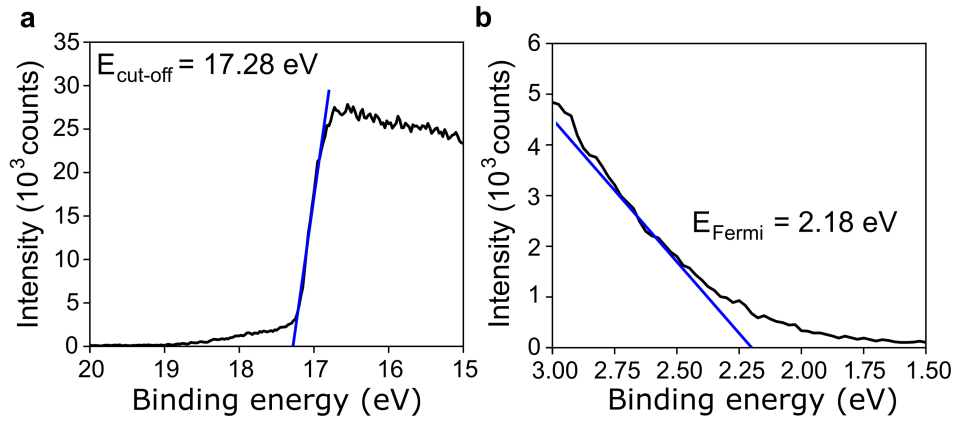


Figure C.8 – UPS spectra of $(\text{BA})_2\text{PbBr}_4$ chromophore spin-coated on FTO coated glass substrate $E_{\text{VB}} = -6.14$ eV.

UPS Spectroscopy

HOMO and VB energy levels were determined based on $E_{\text{cut-off}}$ and E_{Fermi} :^[231]

$$E_{\text{HOMO}} = 21.22 - E_{\text{cut-off}} + E_{\text{Fermi}} \quad (\text{C.1})$$

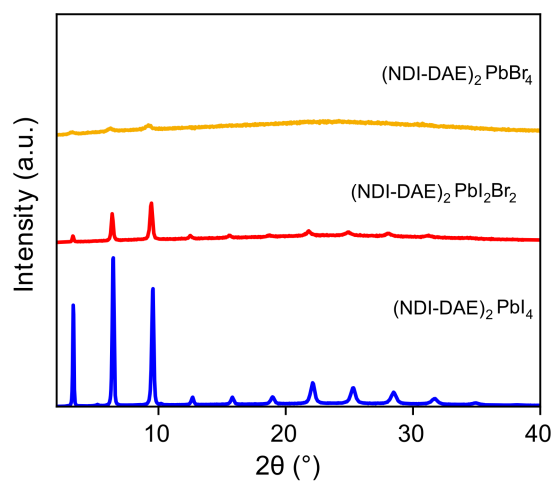


Figure C.9 – XRD of NDI-DAE-I, NDI-DAE-mix and NDI-DAE-Br.

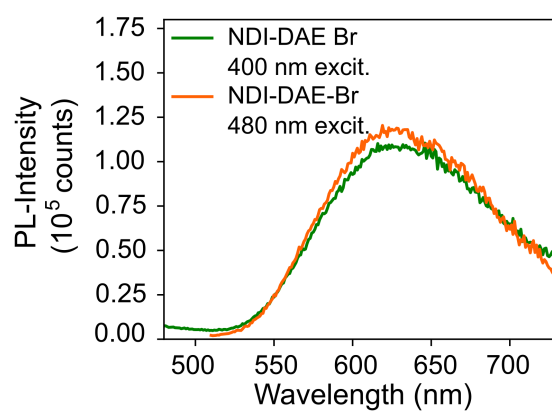


Figure C.10 – PL emission of $(\text{NDI-DAE})_2\text{PbI}_4$ when excited at 480 nm.

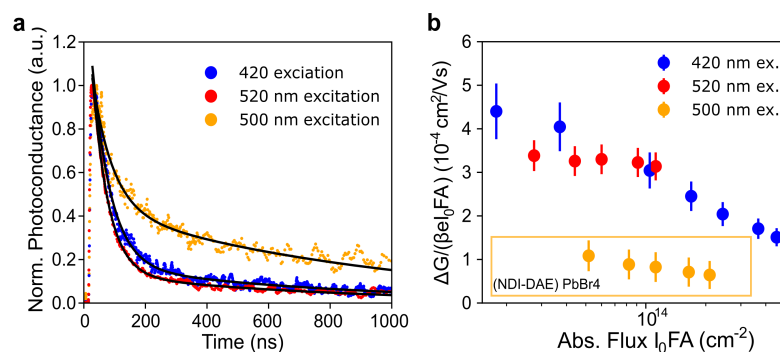


Figure C.11 – **a)** TRMC transient of (NDI-DAE)₂Pb(I_{0.5}Br_{0.5})₄ excited at 420 nm and 520 nm and the Transient of (NDI-DAE)₂PbBr₄ (yellow dots). **b)** Obtained peak mobility assuming $\phi = 1$.

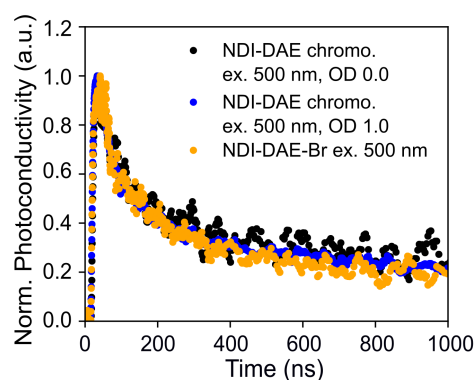


Figure C.12 – Overlap of the TRMC transient of the NDI-DAE chromophore cation spin-coated on quartz substrate (NDI-DAE-chromophore) and (NDI-DAE)₂PbBr₄ excited at 500 nm.

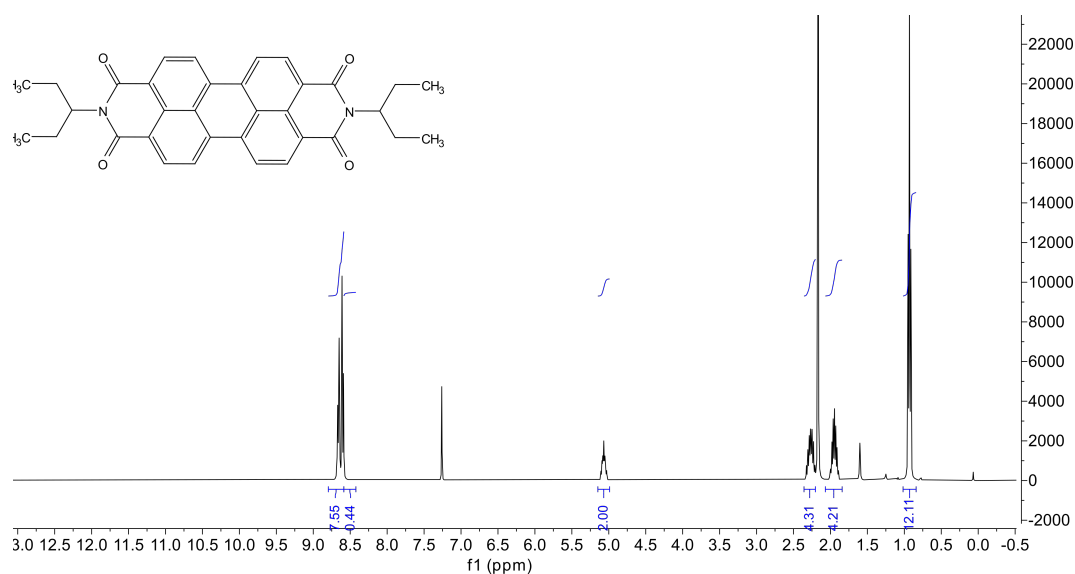


Figure C.13 – ¹H-NMR of PDI-C5-sym in Chloroform-d.

Appendix C. Appendix: Free Charge Carrier Generation by Visible Light Absorbing Chromophore Spacer in Ruddlesden-Popper Type Perovskites

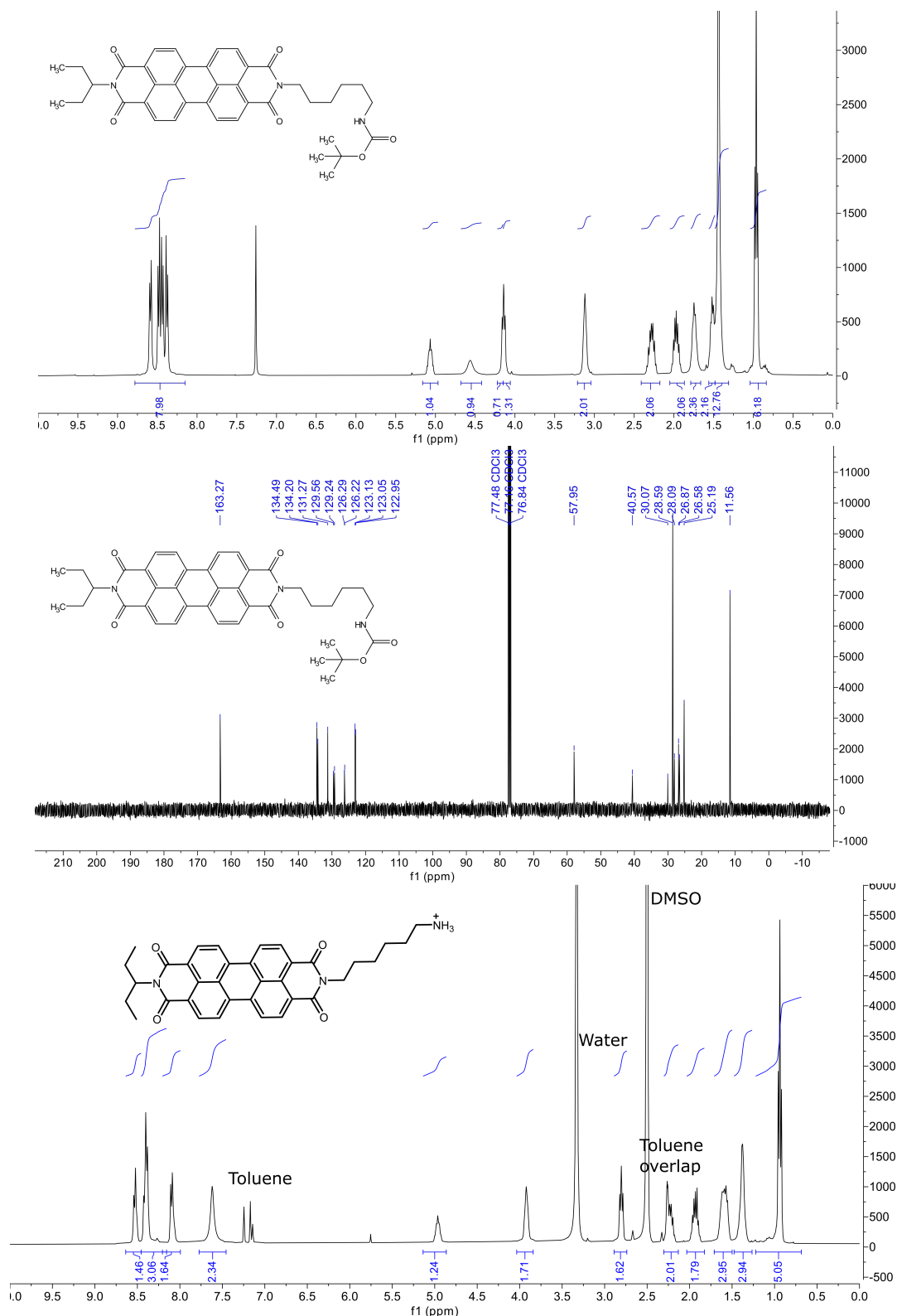


Figure C.14 – ^1H -NMR of PDI-H-Boc (top), ^{13}C -NMR of PDI-H-Boc in CDCl_3 (center), and ^1H -NMR of PDI-H in DMSO-d_6 (bottom). Around 5 %v/v of Toluene- d_8 was added to the DMSO to obtain better NMR coupling.

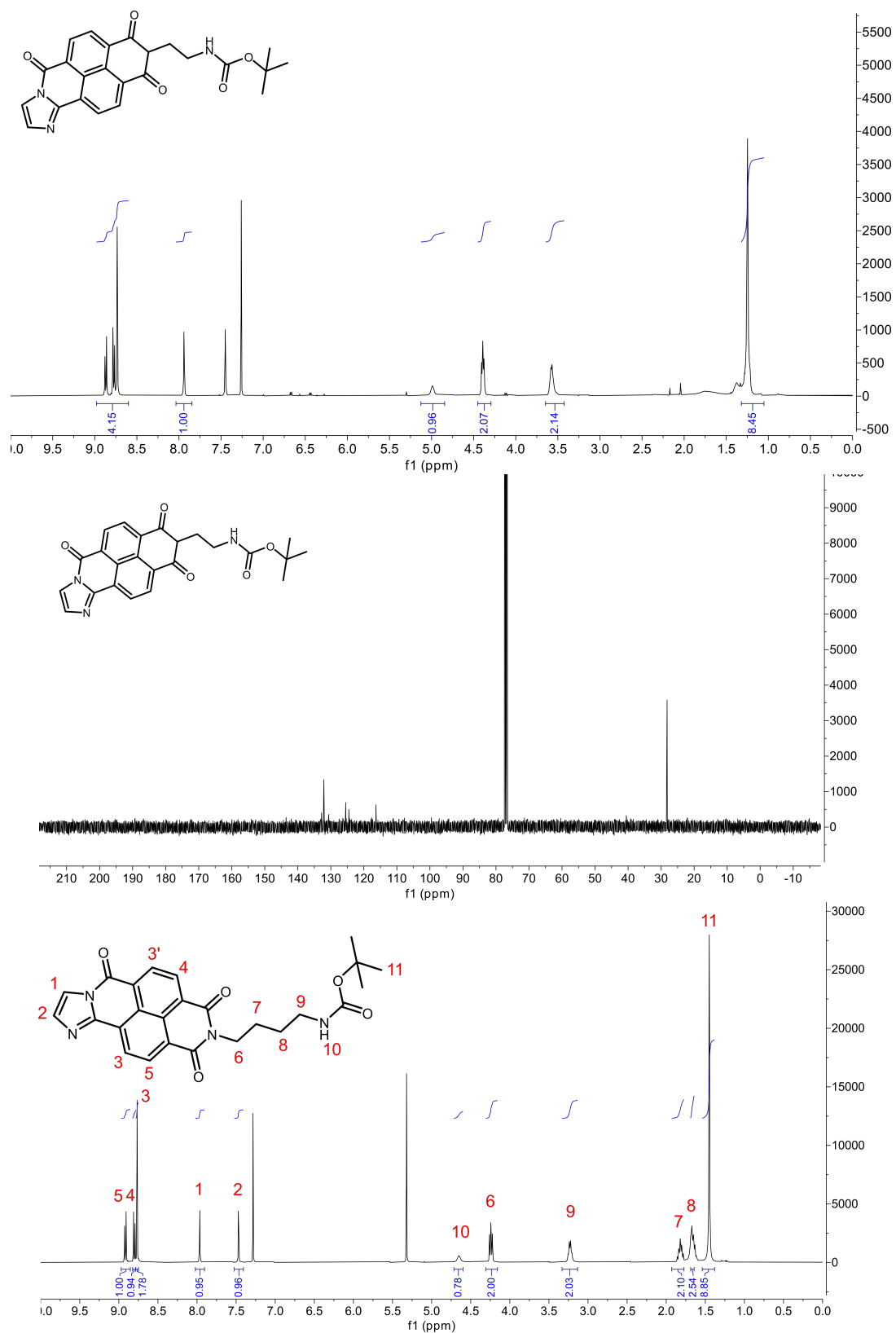


Figure C.15 – ^1H -NMR of NDI-DAE-E-Boc in CDCl_3 (top), ^{13}C -NMR of NDI-DAE-E-Boc in CDCl_3 (center), and ^1H -NMR of NDI-DAE-Boc in CDCl_3 (bottom).

Appendix C. Appendix: Free Charge Carrier Generation by Visible Light Absorbing Chromophore Spacer in Ruddlesden-Popper Type Perovskites

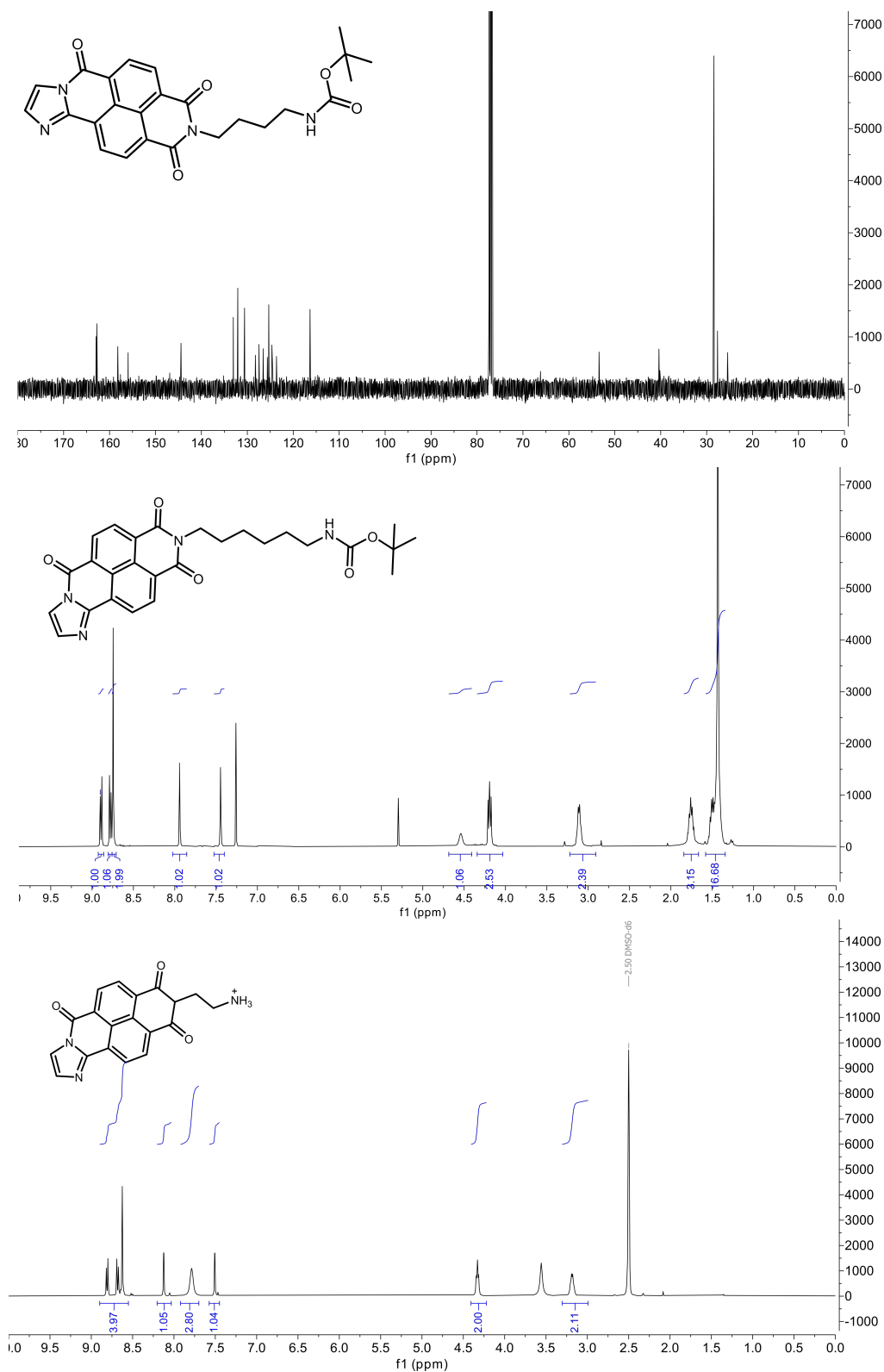


Figure C.16 – ^{13}C -NMR of NDI-DAE-Boc in CDCl_3 (top), and ^1H -NMR of NDI-DAE-H-Boc in CDCl_3 (center), ^1H -NMR of NDI-DAE-E in $\text{DMSO}-d_6$ (bottom).

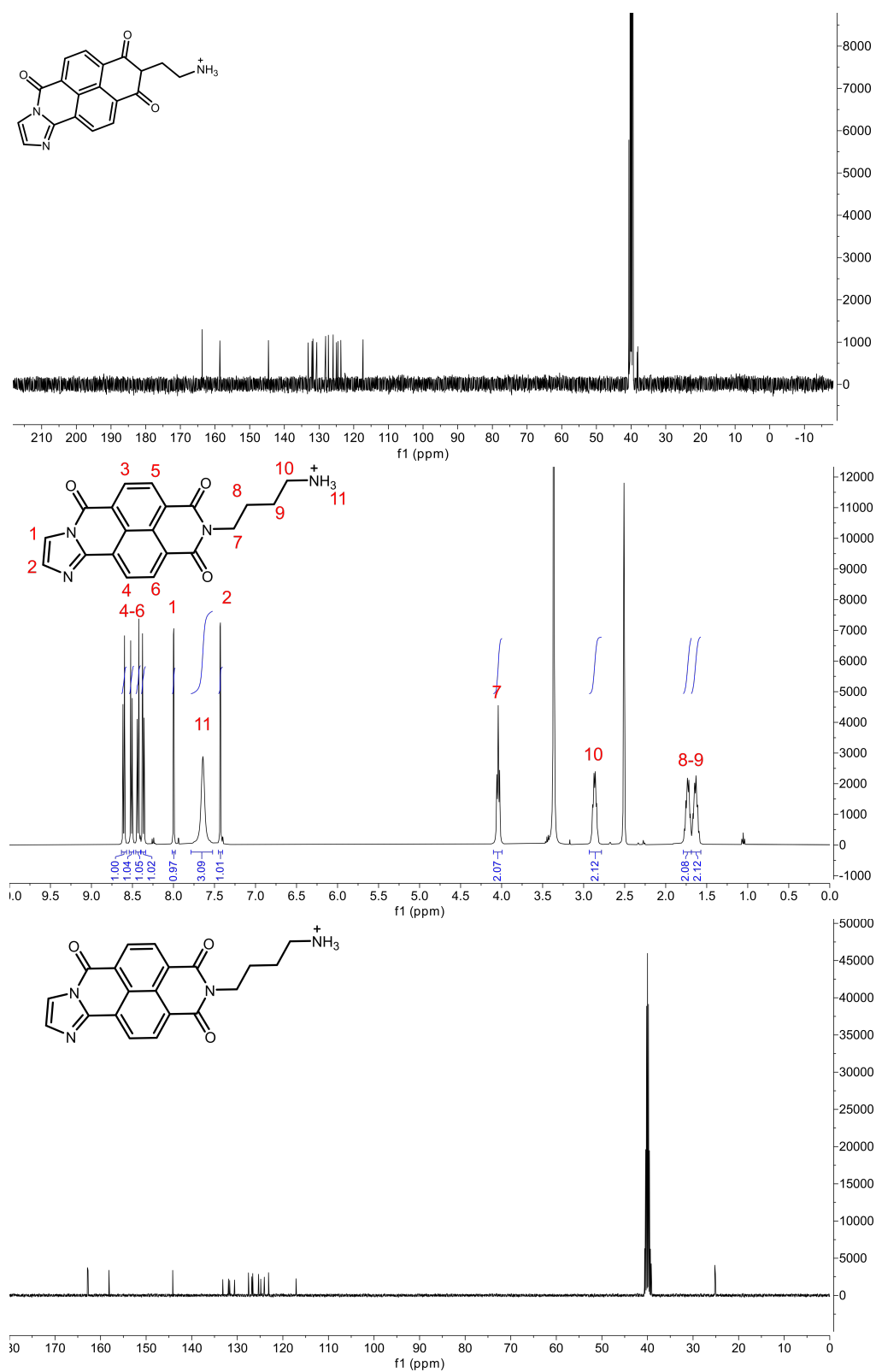


Figure C.17 – ^{13}C -NMR of NDI-DAE-E in DMSO- d_6 (top), ^1H -NMR of NDI-DAE in DMSO- d_6 (center), ^{13}C -NMR of NDI-DAE in DMSO- d_6 (bottom).

Appendix C. Appendix: Free Charge Carrier Generation by Visible Light Absorbing Chromophore Spacer in Ruddlesden-Popper Type Perovskites

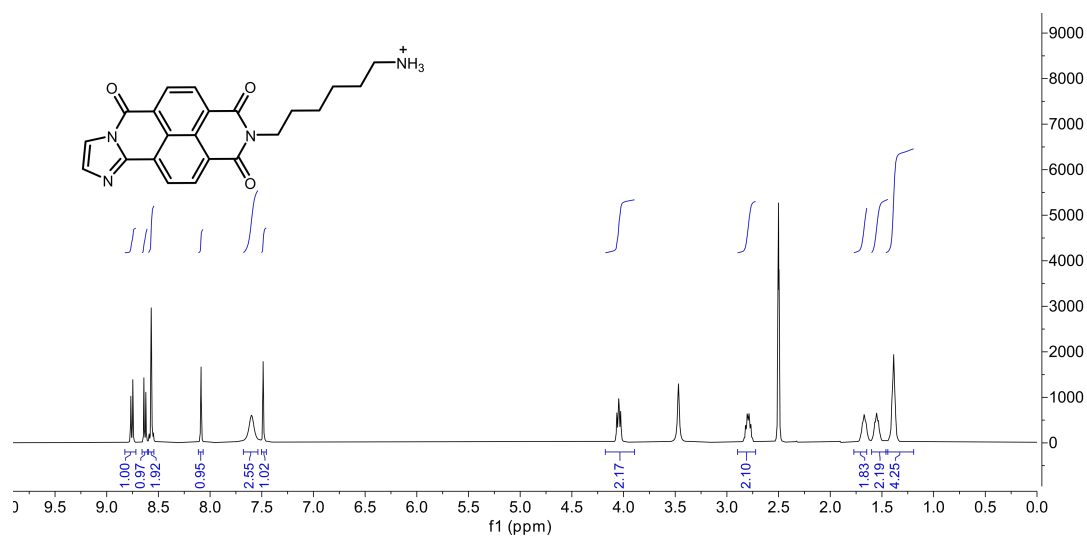


Figure C.18 – ¹H-NMR of NDI-DAE-H in DMSO-d₆.

Appendix D

Appendix: Conclusion and Outlook — Synthesis of a High-Dipole Spacer Cation

Introduction

The application of layered perovskite materials is hampered by the quantum and dielectric confinement effect, resulting in strong exciton binding energies and anisotropic charge carrier properties. Recent reports suggest that high-dipole spacer cations can help charge separation in quasi-layered perovskites. For example, Queloz *et al.* suggested the formation of a charge-separated state in the inorganic layer indicated by a strong photoinduced stark effect. ^[119]

The effect of the spacer cations dipole moment on the exciton binding energy and free charge-carriers remains unknown. In order to investigate the effect of the spacer cation's dipole moment, we focus on simple single-quantum well $n = 1$ layered perovskite systems on thin films and incorporated a novel phenylammonium-based spacer cation into the layered perovskite structure. The structure of the spacer cation is displayed in Figure D.1. The attached malononitrile group induces a strong dipole moment of 7.8 D.

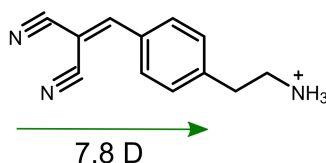


Figure D.1 – Chemical structure of the investigated MN-PEA spacer cation and calculated dipole moment of the MN-PEA core.

As LHOIP materials show strong orientation where the inorganic layer lies parallel to the substrate, lateral photoinduced conductivity is measured by fp-TRMC so study the charge carrier separation efficiency. Thereby the time decay of the transient signal and the peak signal intensity can be taken as a measure for the charge carrier separation process.

Results and data presented in this section are used for future publication under preparation.

Synthesis and Characterization of MN-PEA

640 mg (1.eqv.) and 170 mg Malononitrile (1.2 eqv) were transferred in a two-neck flask and dissolved in approx. 10 ml of Ethanol. After addition of catalytic amounts of triethylamine (5 drops), the reaction mixture was refluxed at 70 °C. After 30 minutes the reaction was led cooled down until crystal growth of needle-like crystals started. The reaction mixture was cooled at 4 °C overnight. Then, the subtenant was removed. The white crystals where twice recrystallized from ethanol to obtain 260 mg of the desired product as white needle shaped crystals. Notably, purification of the product by silica gel column lead to decomposition of the material on the silica.

¹H-NMR: (400 MHz, CDCl₃) δ 7.96 – 7.79 (m, 2H), 7.74 (s, 1H), 7.44 – 7.30 (m, 2H), 4.56 (s, 1H), 3.41 (q, J = 6.8 Hz, 2H), 2.90 (t, J = 7.0 Hz, 2H), 1.43 (s, 9H).

¹³C-NMR: (101 MHz, CDCl₃) δ 159.69, 155.83, 147.27, 131.11, 130.19, 129.31, 113.93, 112.80, 81.85, 79.54, 41.30, 36.65, 28.41.

HRMS (ESI/QTOF) m/z: [M + Na]⁺ Calcd for C₁₇H₁₉N₃NaO²⁺: 320.1369; Found 320.1362. Elemental Analysis

	C	H	N
Calculated	68.671	6.44	14.13
Found average	68.64	6.45	13.95
Standard deviation	0.01	0.02	0.02

MN-PEA Salt Formation

To form the MN-PEA iodide salt, Boc-protected MN-PEA was dissolved in methanol, and an excess of HI was added. After stirring the reaction at room temperature for 2h, diethyl ether was used to precipitate the desired ammonium iodide. The product was washed multiple times with diethyl ether and recrystallized from ethanol.

¹H NMR (400 MHz, DMSO) δ 8.54 (s, 1H), 7.93 (d, J = 8.0 Hz, 2H), 7.78 (s, 3H), 7.53 (d, J = 8.0 Hz, 2H), 3.11 (dq, J = 11.0, 5.9 Hz, 2H), 2.96 (t, J = 7.7 Hz, 2H).

¹³C NMR (101 MHz, DMSO) δ 161.63, 144.95, 131.29, 130.41, 114.74, 113.79, 81.51, 33.55.

HRMS (ESI/QTOF) m/z: [M + I-1]⁺ Calcd for C₁₂H₁₂N₃⁺ 198.1026; Found 198.1032

Preliminary Results

MN-PEI was used as a spacer cation. Thin films of $(\text{MN-PEA})_2\text{PbI}_4$ were formed by mixing MN-PEAI with PbI_2 in a 2:1 ratio in DMF. The solution was spin-coated on a glass slide and annealed at 100 °C for 10 minutes. The visible light absorption spectrum shows a characteristic excitonic absorption band at 490 nm comparable to the optical features found in $(\text{PEA})_2\text{PbI}_4$ as shown in Figure D.2 a. Thin film XRD displayed in Figure D.2 b show equidistant diffraction peaks corresponding to the 002 plane. Based on the first diffraction peak, the distance between neighboring inorganic slabs were found to be 23 Å compared to 16 Å for $(\text{PEA})_2\text{PbI}_4$ and 16 Å for $(\text{F-PEA})_2\text{PbI}_4$. Further structural information was obtained by single crystal XRD (sc-XRD). Single crystals were obtained by vapor diffusion using dichloromethane as an anti-solvent. In contrast to $(\text{PEA})_2\text{PbI}_4$ and $(\text{F-PEA})_2\text{PbI}_4$, where the aromatic core of the cation are oriented face-to-face with respect to each other, the MN-PEA cations are face-to-edge oriented in the organic layer as shown in Figure D.2. The diffraction peaks on thin films are consistent with the diffraction peaks as found in the single crystals indicating that the same phase is formed on the thin film as the structure indicated by the sc-XRD.

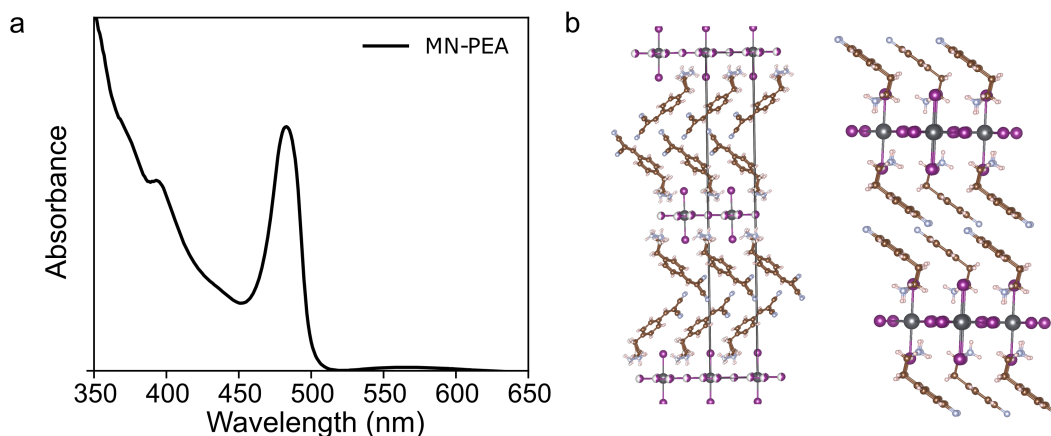


Figure D.2 – **a)** Visible-light absorption spectrum of $(\text{MN-PEA})_2\text{PbI}_4$. **b)** Orientation of the aromatic spacer cation and $(\text{F-PEA})_2\text{PbI}_4$ based on sc-XRD.

Comparing the position of the excitonic absorption band of $(\text{MN-PEA})_2\text{PbI}_4$ with the excitonic absorption band of $(\text{PEA})_2\text{PbI}_4$ and $(\text{F-PEA})_2\text{PbI}_4$, a clear shift towards higher energies is observed. Although such a shift can arise from difference in the octahedral distortions, we assume that the differences arises from a reduction of the exciton binding energy as the Pb-I-Pb angle for $(\text{F-PEA})_2\text{PbI}_4$ (152.4 °) and $(\text{MN-PEA})_2\text{PbI}_4$ (152.6 °) are comparable.

Stability of the MN-PEA Spacer Cation upon Incorporation

During the synthesis of the MN-PEA it was found that purification with silica gel lead to impure MN-PEA product as shown in Figure D.3a. We were able to identify the side-product as the reduced MN-PEA as displayed in Figure D.3b. This degradation product was not obtained when the MN-PEA was purified by re-crystallization and was not found in the crude reaction mixture suggesting that the side-product arise from the silica gel purification. To confirm that the MN-PEA cation is not reduced in the annealing step during the thin film formation, thin films formed were re-dissolved in DMSO-d6 and NMR was performed. The NMR does not show any signal associated to the side-product. Moreover, thermogravimetric analysis shows no thermal decomposition of the spacer cation up to 200 °C suggesting that the degradation only occurs during the silica gel purification. We were not able to determine the degradation mechanism.

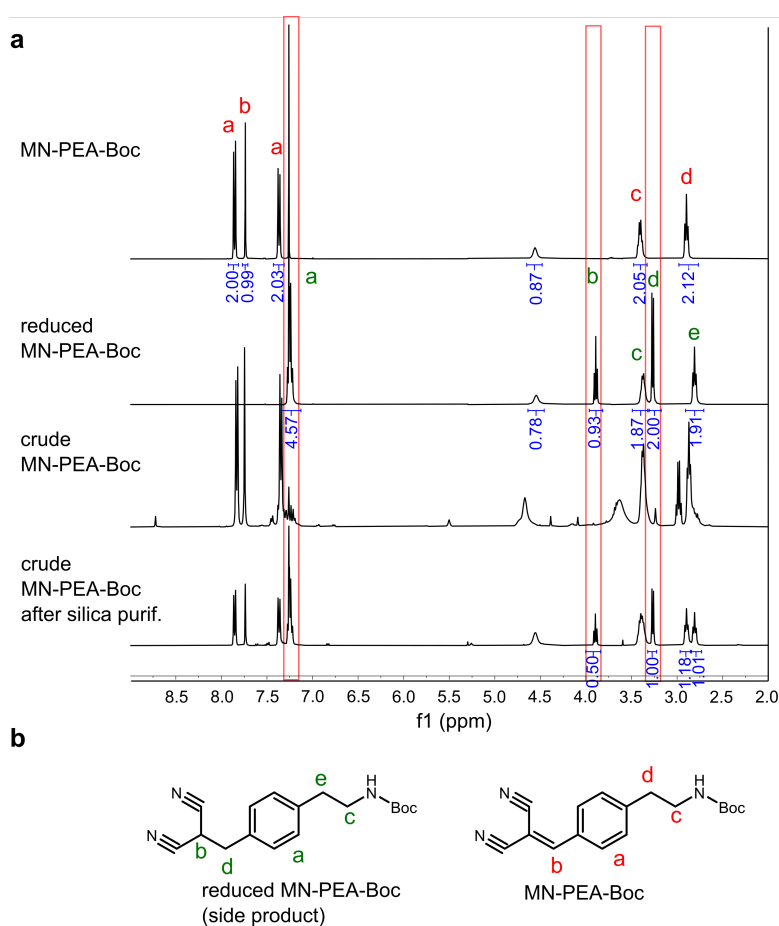


Figure D.3 – NMR of the MN-PEAI cation in DMSO and NMR of the redissolved (MN-PEA)₂PbI₄ in DMSO.

Effect of the Spacer Cation on the Photoconductivity

Thin film sample of various spacer cations were fabricated on quartz substrate and fp-TRMC of the samples were measured. The resulting transients and mobilities are displayed in Figure D.4.

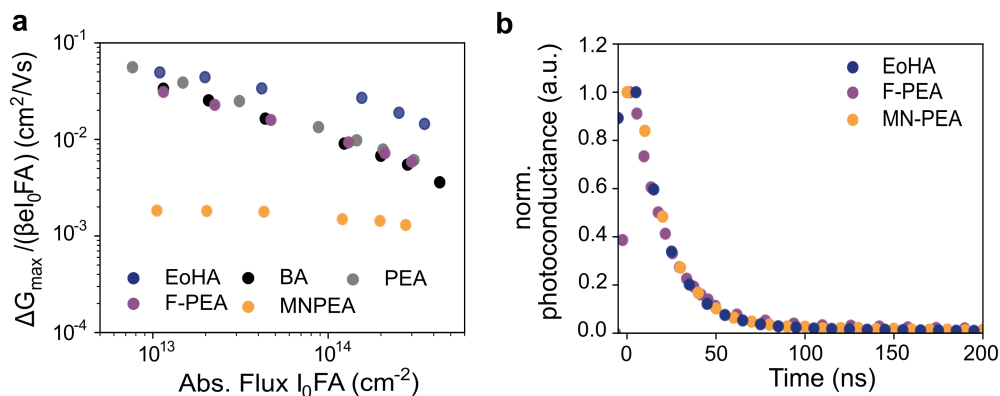


Figure D.4 – **a)** TRMC mobilities at various absorbed photon flux after photoexcitation at 420 nm, and **b)** corresponding TRMC transient.

Despite similar crystal structure, TRMC shows a reduction of the photoconductivity of more than one order of magnitude upon incorporation of MN-PEA compared to PEA and BA based spacer cations. The TRMC decay shows a free charge carrier decay that can be fit to a mono-exponential decay. Decay time constants are consistent with all investigated spacer cations. Although the reduced photoconductivity observed in $(\text{MN-PEA})_2\text{PbI}_4$ may arise from a reduction in the mobility, the comparable structure of the inorganic layer as well as the similar free charge carrier recombination dynamic suggest that less free charge carriers are formed upon photoexcitation.

Conclusion

While a novel high-dipole moment spacer cation was synthesized and incorporated into a LHOIP structure we aimed to investigate the effect of the dipole moment on the optoelectronic properties. Although the observed absorption features suggest reduced exciton binding energies, fp-TRMC measurements indicate reduced photoconductivity of $(\text{MN-PEA})_2\text{PbI}_4$ compared to similar spacer cations. While further investigations of the film quality and orientation are required to exclude potential differences in the thin film quality, further experiments are required. As such sheet conductivity measurements may further provide insight into the film quality and film mobility. Moreover, temperature dependent PL measurements may provide a more suitable approach to determine the exciton binding energy.

Appendix E

Appendix: Conclusion and Outlook – Synthesis of Isoindigo-based Spacer Cations

Introduction

Isoindigo-based chromophore is a tunable and widely studied building block in organic electronics. For example indigo-based materials are investigated for electron-acceptors in organic photovoltaics and are under investigation for the application in OFETs. In contrast to indigo, isoindigo molecules have two free amine positions, that lay opposite to each other enabling easy functionalization with an anchoring group, while the isoindigo core still absorbs visible lights. Moreover, as well monocations as well as dications can be easily formed. In this project, the synthesis and characterization of isoindigo-based spacer cations are demonstrated.

Isoindigo-based Quantum Well Structure

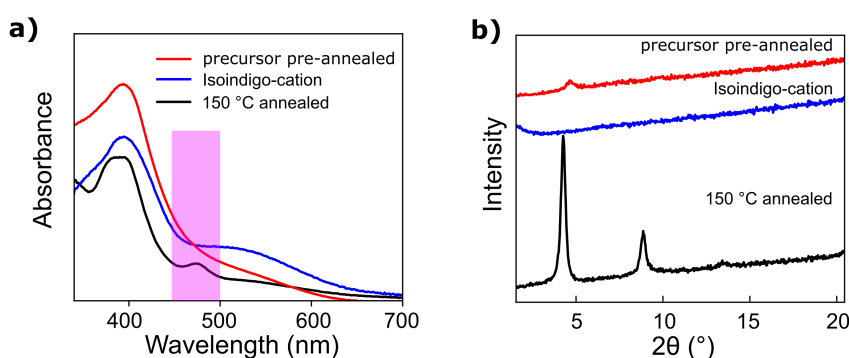


Figure E.1 – **a)** UV-Vis absorption spectra and **b)** XRD spectra of Isoindigo-based quantum well structure.

Visible light absorption of monovalent isoindigo-based cation are displayed in Figure E.1. While the cation absorbs light beyond 600 nm, no crystal phase formation was observed for the as-

Appendix E. Appendix: Conclusion and Outlook – Synthesis of Isoindigo-based Spacer Cations

spin-coated cation. When mixing PbI_2 and the spacer cation in a DMSO precursor solution, a crystalline phase upon annealing at 150°C is observed. In the visible light absorption spectra a weak excitonic absorption band at 480 nm was observed. Compared to $(\text{PEA})_2\text{PbI}_4$ the excitonic absorption band is shifted towards higher energies as observed in NDI-based and MN-PEA based cations. Notably, annealing the as spin-coated films is required to form the crystalline phase as without the annealing step an amorphous film is formed. Further research focus on the optimization of the thin film formation to increase crystallinity.

Synthesis and Characterization of Isoindigo based cations

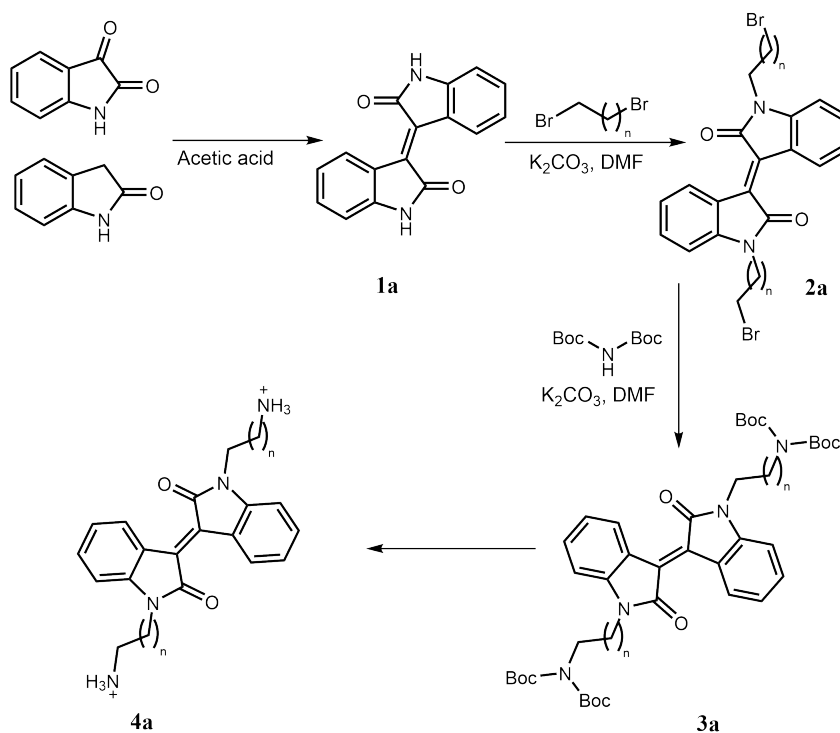


Figure E.2 – Synthetic scheme for the synthesis of Isoindigo-based dications.

A schematic description of the synthetic route is displayed in Figure E.2. The isoindigo core is formed by a condensation reaction with isatin and oxindole. Functionalization of the free amine can be done by attaching a dibromoalkane chain and subsequent Gabriel synthesis in mild conditions.

Isoindigo-dia-C4-Br (2a, n = 3)

2 g of the crude Isoindigo was mixed with 1 g of K₂CO₃ and dissolved in dry DMF. After addition of 3 ml of 1,4-dibromobutane the reaction mixture was stirred at r.t. After 12 h the reaction mixture was filtered to remove K₂CO₃. After concentration of the solvent the desired product was obtained after purification by silica gel column chromatography. The product was recrystallized from DCM:Hexane mixture to obtain the desired product needle-shaped crystals. Yield: 34%

¹H-NMR (400 MHz, CDCl₃) δ 9.16 (dd, J = 8.0, 1.2 Hz, 2H), 7.37 (td, J = 7.7, 1.2 Hz, 2H), 7.07 (td, J = 7.8, 1.1 Hz, 2H), 6.81 (dd, J = 7.9, 1.1 Hz, 2H), 3.84 (t, J = 6.7 Hz, 4H), 3.47 (t, J = 6.2 Hz, 4H), 2.02 – 1.84 (m, 8H).

¹³C-NMR (101 MHz, CDCl₃) δ 167.93, 144.39, 133.46, 132.54, 129.99, 122.41, 121.68, 107.87, 38.98, 33.06, 29.82, 26.05.

HRMS (ESI/QTOF) m/z: [M + Na]⁺ Calcd for C₂₄H₂₄Br₂N₂NaO²⁺ 553.0097; Found 553.0091.

EA: Anal. Calcd for C₂₄H₂₄Br₂N₂O₂: C, 54.16; H, 4.54; N, 5.26. Found: C, 54.10; H, 4.51; N, 5.20

Isoindigo-dia-C6-Br (2a, n=5)

Isoindigo-dia-C6-Br was synthesized following the same procedure as for Isoindigo-dia-C4-Br. Yield 1.020 g ()

¹H NMR (400 MHz, CDCl₃) δ 9.17 (dd, J = 8.1, 1.2 Hz, 2H), 7.36 (td, J = 7.7, 1.2 Hz, 2H), 7.05 (td, J = 7.8, 1.1 Hz, 2H), 6.79 (dd, J = 7.9, 1.1 Hz, 2H), 3.79 (t, J = 7.3 Hz, 4H), 3.39 (t, J = 6.7 Hz, 4H), 1.91 – 1.80 (m, 4H), 1.73 (p, J = 7.4 Hz, 4H), 1.56 – 1.36 (m, 8H).

¹³C NMR (101 MHz, CDCl₃) δ 168.04, 144.77, 133.68, 132.55, 130.10, 122.40, 121.84, 108.00, 40.02, 33.87, 32.75, 28.01, 27.49, 26.36.

HRMS (ESI/QTOF) m/z: [M + Na]⁺ Calcd for C₂₈H₃₂Br₂N₂NaO²⁺ 609.0723; Found 609.0710

EA: Anal. Calcd for C₂₈H₃₂Br₂N₂O₂: C, 57.16; H, 5.48; N, 4.76. Found: C, 57.12; H, 5.45; N, 4.70.

Isoindigo-dia-C6-NBoc (3a, n = 5)

¹H-NMR (400 MHz, CDCl₃) δ 9.18 (dd, J = 8.0, 1.2 Hz, 2H), 7.35 (td, J = 7.7, 1.2 Hz, 2H), 7.04 (td, J = 7.8, 1.1 Hz, 2H), 6.78 (d, J = 7.8 Hz, 2H), 3.77 (t, J = 7.4 Hz, 4H), 3.63 – 3.47 (m, 4H), 1.81 – 1.64 (m, 4H), 1.61 – 1.54 (m, 4H), 1.49 (s, 36H), 1.37 (ddd, J = 25.9, 11.2, 3.8 Hz, 8H).

¹³C-NMR (101 MHz, CDCl₃) δ 167.99, 152.84, 144.82, 133.68, 132.49, 130.12, 122.32, 121.85, 107.98, 82.19, 46.46, 40.12, 29.07, 28.24, 27.61, 26.92, 26.70.

HRMS (ESI/QTOF) m/z: [M + Na]⁺ Calcd for C₄₈H₆₈N₄NaO₁₀⁺ 883.4828; Found 883.4836.

EA: Anal. Calcd for C₄₈H₆₈N₄O₁₀: C, 66.95; H, 7.96; N, 6.51. Found: C, 66.97; H, 7.92; N, 6.44

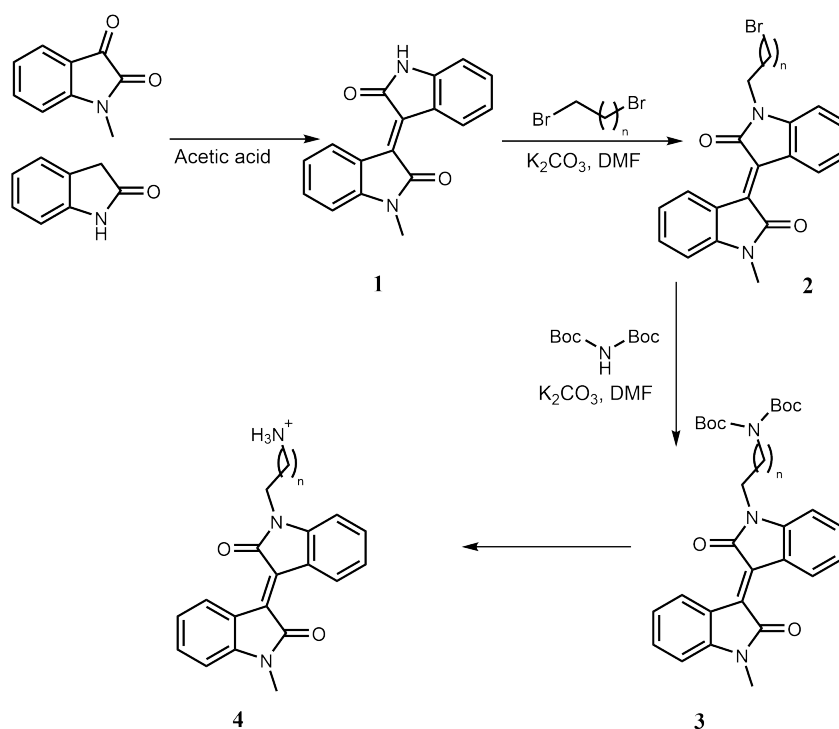


Figure E.3 – Synthetic scheme for the synthesis of Isoindigo-based monocations.

Synthesis of N-Methyl Isatin

5 g of isatin was weighted in in a two-neck flask and mixed together in 5 g of K₂CO₃. After establishing an argon-atmosphere, 50 ml of DMF (dry) was added. The reaction was started upon addition of Iodomethane and stirred at room temperature. After 12 hours, undissolved K₂CO₃ was decanted and the reaction mixture was concentrated. After redissolving the solid in DCM, remaining K₂CO₃ was removed by extraction with water. The organic phase was concentrated and the pure product was obtained after flash column chromatography. Yield: 80%

¹H-NMR (400 MHz, CDCl₃) δ 7.60 (t, J = 7.7 Hz, 2H), 7.12 (td, J = 7.5, 0.9 Hz, 1H), 6.93 - 6.86 (m, 1H), 3.25 (s, 3H).

¹³C-NMR (101 MHz, CDCl₃) δ 183.47, 158.37, 151.60, 138.53, 125.41, 123.97, 117.59, 110.05, 77.48, 77.16, 76.84, 26.35

HRMS (LTQ-Orbitrap) m/z: [M + H]⁺ Calcd for C₉H₈NO₂⁺ 162.0550; Found 162.0547.

Synthesis of N-Methyl-Isoindigo (1)

2 g N-Methylisatin and 2 g of was refluxed at acetic acid for 2 h. Then the reaction mixture was quenched by Addition of water. The precipitate was filtrated and dried. The obtained 3.5 g of purple solid was used without any further purification.

Isoindigo-mono-C4-Br (2a, n = 3)

3 g of Isoindigo precursor (1) and 5 g of K₂CO₃ were weighted into a two-neck flask and dissolved in 40 ml of DMF (dry). An excess (4 ml) of 1,4- dibromobutane was added and the reaction was stirred at room temperature for 12 h. After filtration of the excess K₂CO₃ and concentration of the reaction mixture, the crude was redissolved in DCM and extracted 3x with water. The organic phase was collected and the pure compound was obtained by flash column chromatography using DCM:Hexane as evolving eluent. (Yield: 49 %) ¹H-NMR (400 MHz, CDCl₃) δ 9.19 (ddd, J = 17.3, 8.1, 1.2 Hz, 2H), 7.37 (tdd, J = 7.7, 3.3, 1.2 Hz, 2H), 7.07 (td, J = 7.8, 1.1 Hz, 2H), 6.84 – 6.75 (m, 2H), 3.83 (t, J = 6.7 Hz, 2H), 3.47 (t, J = 6.1 Hz, 2H), 3.29 (s, 3H), 2.02 – 1.84 (m, 4H).

¹³C-NMR (101 MHz, CDCl₃) δ 168.11, 145.43, 144.47, 133.78, 133.39, 132.64, 132.55, 130.16, 129.97, 122.57, 122.53, 121.86, 121.71, 107.94, 107.85, 39.11, 33.20, 29.98, 26.29, 26.19.

Isoindigo-mono-C6-Br (2b, n = 5)

Isoindigo-mono-C6-Br was synthesized according to the same procedure as Isoindigo-mono-C4-Br

¹H-NMR (400 MHz, CDCl₃) δ 9.24 – 9.15 (m, 2H), 7.37 (tdd, J = 7.6, 6.2, 1.2 Hz, 2H), 7.06 (tdd, J = 7.8, 4.5, 1.1 Hz, 2H), 6.79 (d, J = 7.8 Hz, 2H), 3.79 (t, J = 7.3 Hz, 2H), 3.39 (t, J = 6.7 Hz, 2H), 3.29 (s, 3H), 1.86 (p, J = 6.9 Hz, 2H), 1.74 (p, J = 7.5 Hz, 2H), 1.55 – 1.44 (m, 2H), 1.42 (dd, J = 10.6, 5.1 Hz, 2H).

¹³C-NMR (101 MHz, CDCl₃) δ 168.02, 167.90, 145.25, 144.61, 133.50, 132.43, 132.36, 129.98, 129.85, 122.43, 122.26, 121.71, 121.61, 107.83, 107.68, 39.88, 33.73, 32.61, 27.87, 27.35, 26.22, 26.15.

HRMS (ESI/QTOF) m/z: [M + H]⁺ Calcd for C₂₃H₂₄BrN₂O²⁺ 439.1016; Found 439.1017.

Isoindigo-mono-C4-NBoc (3a, n = 3)

2 g of 2a, 3 g of Gabriel-reagent and 5 g of K₂CO₃ were dissolved in 40 ml of Dimethylformamide The reaction as stirred at room temperature for 12 hours. After filtration of the excess of

Appendix E. Appendix: Conclusion and Outlook – Synthesis of Isoindigo-based Spacer Cations

K₂CO₃, the reaction mixture was concentrated and purified by column chromatography using DCM/Ethyl acetate as evolving eluent (Yield: 82%) ¹H NMR (400 MHz, CDCl₃) δ 9.19 (ddd, J = 7.6, 6.1, 1.2 Hz, 2H), 7.36 (dtd, J = 10.5, 7.7, 1.2 Hz, 2H), 7.11 – 7.00 (m, 2H), 6.80 (dd, J = 11.2, 7.8 Hz, 2H), 3.81 (s, 2H), 3.62 (s, 2H), 3.29 (s, 3H), 1.70 (s, 4H), 1.48 (s, J = 3.5 Hz, 18H). HRMS (nanochip-ESI/LTQ-Orbitrap) m/z: [M + Na]⁺ Calcd for C₃₁H₃₇N₃NaO₆⁺ 570.2575; Found 570.2559.

EA: Anal. Calcd for C₃₁H₃₇N₃O₆: C, 67.99; H, 6.81; N, 7.67. Found: C, 68.03; H, 6.71; N, 7.65.

Isoindigo-mono-C6-NBoc (3b, n = 5)

¹H-NMR (400 MHz, CDCl₃) δ 9.20 (ddd, J = 8.0, 2.7, 1.2 Hz, 2H), 7.36 (qd, J = 7.6, 1.2 Hz, 2H), 7.06 (tdd, J = 7.8, 5.2, 1.1 Hz, 2H), 6.87 – 6.70 (m, 2H), 3.77 (t, J = 7.4 Hz, 2H), 3.64 – 3.48 (m, 2H), 3.29 (s, 3H), 1.71 (p, J = 7.7 Hz, 2H), 1.63 – 1.55 (m, 2H), 1.49 (s, 18H), 1.44 – 1.29 (m, 4H).

¹³C-NMR (101 MHz, CDCl₃) δ 168.18, 152.85, 145.36, 144.84, 133.72, 132.51, 130.10, 130.03, 122.55, 122.33, 121.84, 121.77, 107.99, 107.79, 82.20, 46.46, 40.12, 29.07, 28.24, 27.60, 26.93, 26.70, 26.28.

HRMS (APPI/LTQ-Orbitrap) m/z: [M]⁺ Calcd for C₃₃H₄₁N₃O₆⁺ 575.2990; Found 575.3000.

EA: C₃₁H₃₇N₃O₆: C, 67.99; H, 6.81; N, 7.67. Found: C, 68.03; H, 6.71; N, 7.65.

Appendix F

Appendix: Conclusion and Outlook -Incorporation of Organic-Charge Transfer Complexes in the Organic Layer

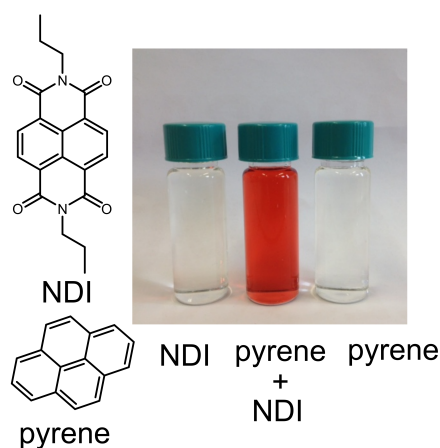


Figure F.1 – Formation of organic charge-transfer complex in solution formed by naphthalene diimide and pyrene and naphthalene diimide:pyrene (1:1 molar ratio, center) in DCM.

Synthesis of TCBQ-Naphthalene organic charge-transfer complex layered perovskites

TCBQ-naphthalene organic charge-transfer complexes in the organic slab of a LHOIP were reported by Passarelli *et al.*^[149] naphthalene-C3-I, and PbI_2 were dissolved in 1:1 DMF/DMSO to obtain a solution containing 1.0 M naphthalene-C3-I and 0.5 M PbI_2 . This solution was used to dissolve ,4,5,6-tetrachlorocyclohexa-3,5-diene-1,2-dione (TCBQ), resulting in a second solution with the stoichiometric formula $(\text{naphthalene-C3-I})_2\text{PbI}_4 + x(\text{C}_6\text{Cl}_4\text{O}_2)$ where $x = 1$. Solutions 1 and 2 were used to prepare the precursor solutions of the general formula (naphthalene-C3-

Appendix F. Appendix: Conclusion and Outlook -Incorporation of Organic-Charge Transfer Complexes in the Organic Layer

$\text{I}_2\text{PbI}_{4+x}(\text{C}_6\text{Cl}_4\text{O}_2)$ with $x = 1, 0.8, 0.6, 0.4, 0.2$, and 0.0 . The film were formed by spin-coating the solutions on freshly cleaned quartz slides at 2000 rpm for 30 seconds and subsequently annealed at 100°C for 10 minutes.

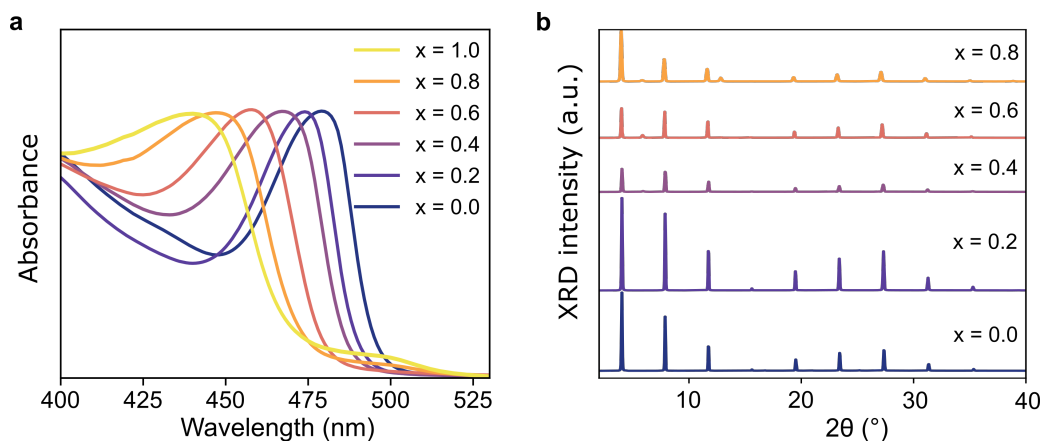


Figure E2 – **a)** UV-vis absorption spectra and **b)** XRD TCBQ-Naphthalene organic charge-transfer perovskites following the same synthetic conditions as ref. 149.

Synthesis of Naphthalene-C3-Boc and formation of organic charge-transfer complexes

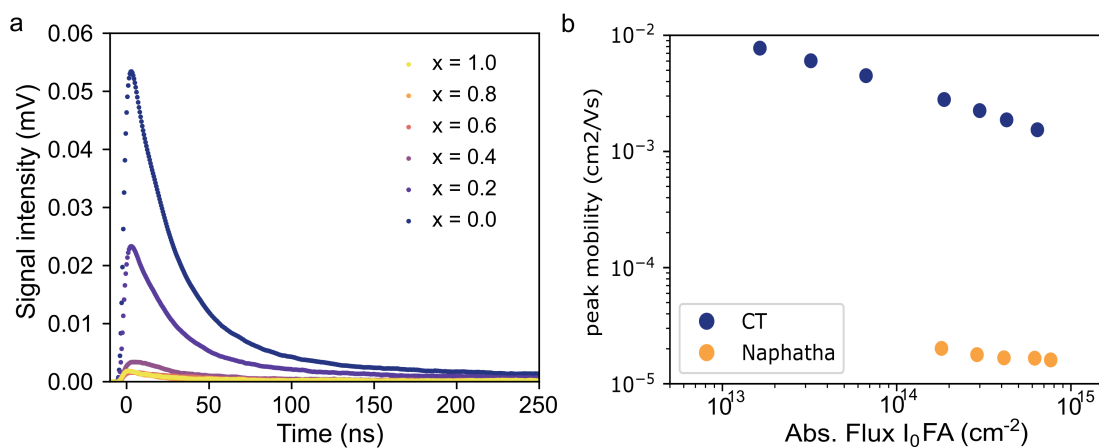


Figure E3 – **a)** TRMC transient of TCBQ charge transfer after photoexcitation at 420 nm, and **b)** mobilities for $x = 1.0$ under assumption $\phi = 1$.

Synthesis of Naphthalene-C3-Boc

Naphthalene-C3-Boc was synthesized based on an adapted procedure reported by Passarelli *et al.*:^[46]

1 g (6.9 mmol, 1 eqv.) of 1-naphtol was mixed with around 5 g of potassium carbonate, and 3 g of 3-(Boc-amino)-propyl bromid and dissolved in a round bottom flask in DMF (dry). After establishing an argon atmosphere, the reaction mixture was heated to 100 ° and stirred overnight. After 12 h, the organic solvent was evaporated, and the crude was redissolved in DCM and washed 3x with water. The desired product was obtained after purification by silica gel column using DCM:Hexane (7:3 v/v) as evolving eluent in good yields (60 %).

The Desired iodide salt was obtained by dissolving naphthalene-C3-Boc in a minimal amount of methanol and subsequently adding a HI (57% in water). After stirring the solution for 1 hour, diethyl ether was added, and the precipitate was obtained after centrifugation. The solid product was washed multiple times with diethyl ether and subsequently dried on a high-vacuum for 10 hours.

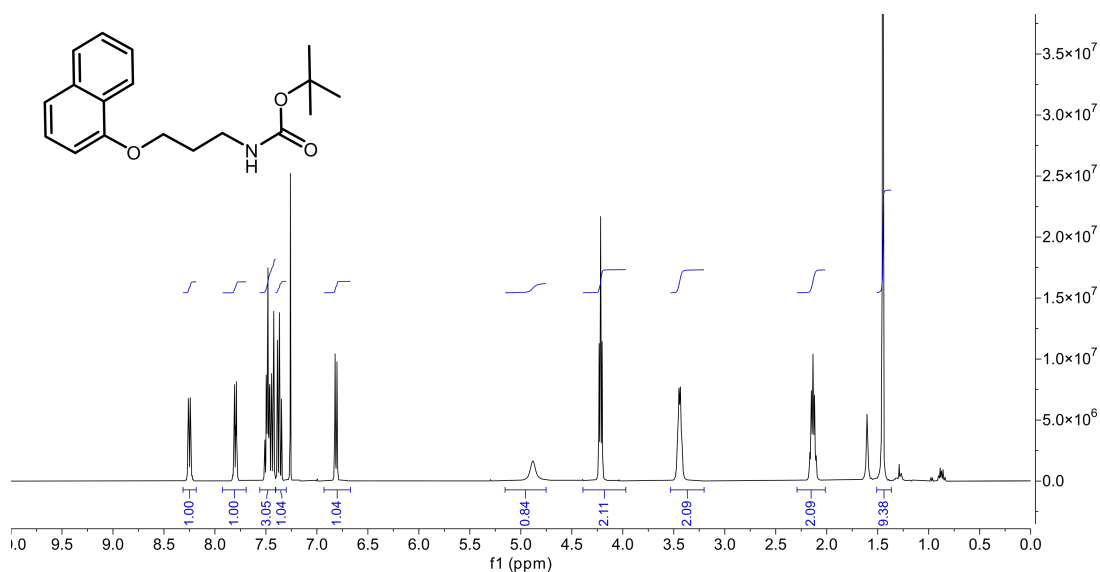


Figure F4 – ¹H-NMR of Naphthalene-C3-Boc in CDCl₃.

Appendix F. Appendix: Conclusion and Outlook -Incorporation of Organic-Charge Transfer Complexes in the Organic Layer

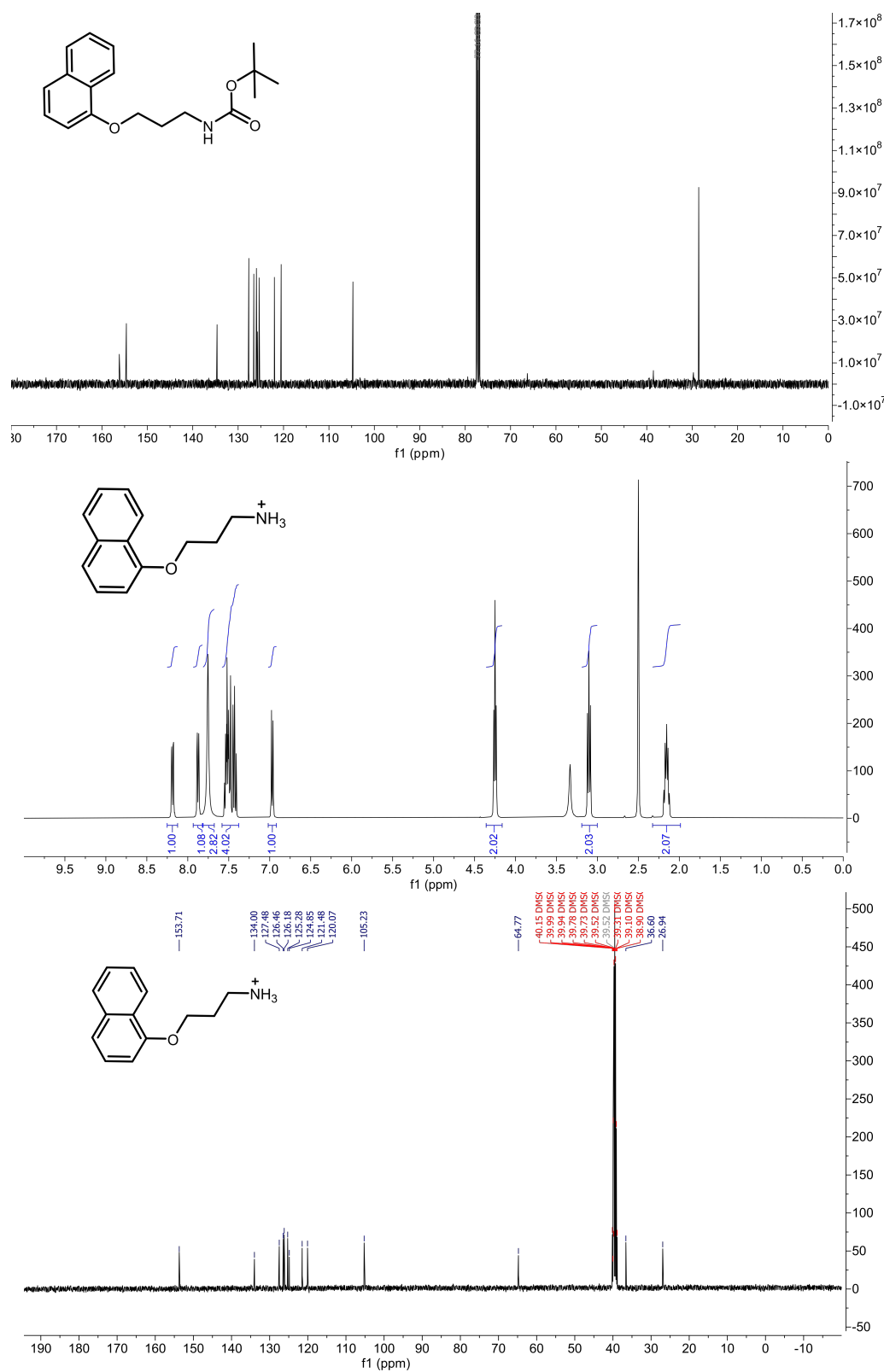


Figure E5 – ^{13}C -NMR of Naphthalene-C3-Boc in CDCl_3 (top), and ^1H -NMR of Naphthalene-C3-salt in DMSO-d_6 (center), and ^{13}C -NMR of Naphthalene-C3-salt in DMSO-d_6 (bottom).

Simon Nussbaum

Curriculum Vitae

Personal Details

<i>Birth</i>	May 22, 1994	<i>Phone</i>	+41 79 583 84 06
<i>Citizenship</i>	Swiss	<i>Mail</i>	Simon.Nussbaum@epfl.ch
<i>Address</i>	Route de Cossonay 11 1008 Prilly, Switzerland		

Education

- **École polytechnique fédéral de Lausanne**
PhD in Chemistry and Chemical Engineering 2019 - present
 - Thesis Title: Synthesis and Characterization of Functionalized Spacer Cations for the Incorporation in Layered Perovskite
 - Extensive experience in organic chemistry synthesis and perovskite thin-film fabrication
 - Characterization of organic compounds with NMR, HR-MS, and UV-vis absorbance and photoluminescence spectroscopy
 - Structural and electrochemical characterization of new semiconductor materials
 - Responsible for groups safety management as Safety correspondent (CoSec) for 1.5 years
- **Helmholtz-Zentrum für Energie und Materialien**
Doc.mobility PhD-exchange 2022 - 2023
 - 6 month research stay in the institute for Solar fuels under the supervision of Dennis Friedrich and Roel van de Krol
- **École polytechnique fédéral de Lausanne**
MSc. in Molecular and Biological Chemistry 2017 - 2019
 - Specialisation modules: organic, inorganic and computational chemistry
 - Master Thesis: Synthesis and Characterization of Novel Hybrid 2D Semiconducting Materials, Supervisor: Prof. Kevin Sivula, Grade: 5.75/6
- **University of Bern**
BSc. in Chemistry and Molecular Sciences 2014 - 2017
 - Undergraduate Thesis: Crystal and Electronic Structure of Perovskite ATiO₂N Oxynitrides (DFT-calculations), Supervisor: Prof. U. Aschauer, Dr. S. Ninova, Grade: 6/6
 - Graduated magna cum laude

Projects and Research Experience

- **GMF - EPFL, Prof. Nazeeruddin**

Master internship

09/2018 - 01/2019

- Synthesis of new organic hole-transporting materials (HTM) for perovskite solar cells

- **LCOM - EPFL, Prof. Dyson**

Semester project

02/2018 - 05/2018

- Investigating the catalytic efficiency and optimum reaction conditions of different ionic liquids for the reduction of CO₂ using phenylsilane as reducing agent

Research Interest

- Organic and inorganic functional materials for photovoltaic and light emitting applications
- Synthesis of organic electronics materials

Skills

Languages

German (mother tongue)

English (fluent)

French (fluent)

Italian (beginner)

Programming

Python, C, L^AT_EX, Microsoft office (experienced)

Bash, R (intermediate)

Publications

- S.Nussbaum et al. *Free Charge Carrier Generation by Visible Light Absorbing Chromophore Spacer in Ruddlesden-Popper Type Perovskites* (manuscript under preparation)
- S.Nussbaum, E. Socie, G. Fish, N. Diercks, H. Hempel, D. Friedrich J. Yum, J. Moser, K. Sivula, *Photogenerated charge transfer in Dion-Jacobson type layered perovskite based on Naphthalene diimide* (Chem. Sci., 2023, accepted manuscript)
- S. Nussbaum, E. Socie, J. Yum, J. E. Moser, K. Sivula, *Tuning naphthalenediimide cations for incorporation into Ruddlesden-Popper type hybrid perovskites*, Chem. Mater., 2022, **34**, 8, 3798–3805
- R. A. Wells, N. Diercks, V. Boureau, Z. Wang, Y. Zhao, S. Nussbaum, M. Esteve, P. I. Shouwink, M. Caretti, A. Kis, K. Sivula *Composition-Tunable Transition Metal Dichalcogenide Nanosheets via a Scalable, Solution-Processable Method* (Manuscript under preparation)
- Y. Liu, M. Xia, D. Ren, S. Nussbaum, J. Yum, M. Grätzel, N. Guijarro, K. Sivula *Photoelectrochemical CO₂ Reduction at a Direct CuInGaS₂/Electrolyte Junction*, (ACS Energy Lett. 2023, **8**, 4, 1645–1651)
- M. Caretti, E. Mensi, R. Kessler, L. Lazouni, B. Goldman, L. Carbone, S. Nussbaum, R. A. Wells, H. Johnson, E. Rideau, J. Yum, K. Sivula, *Transparent Porous Conductive Substrates for Gas-Phase Photoelectrochemical Hydrogen Production*, Adv. Mater. 2023, **35**, 2208740

- M. Caretti, L. Lazouni, M. Xia, R. A. Wells, S. Nussbaum, D. Ren, M. Grätzel, K. Sivula, *Transparency and morphology control of Cu₂O photocathodes via an in-situ electro-conversion*, (ACS Energy Lett. 2022, **7**, 5, 1618–1625)
- M. Hulla, S. Nussbaum, A. R. Bonnin, P. Dyson, *The dilemma between acid and base catalysis in the synthesis of benzimidazole from o-phenylenediamine and carbon dioxide*, Chem. Commun., 2019, **55**, 13089-13092

Conferences

- S. Nussbaum (2023, March), Towards Organic-Inorganic Hybride Nano-Heterostructures, ChemMatSus Spring meeting Valencia (oral presentation)